Towards Cooling Nanoelectronic Devices
to
Microkelvin Temperatures

- Design, Construction and Test of a Novel Type of Refrigerator -

Inauguraldissertation

zur

Erlangung der Würde eines Doktors der Philosophie
vorgelegt der
Philosophisch-Naturwissenschaftlichen Fakultät
der Universität Basel

von

Kai Kurt Schwarzwälder

aus Staufen im Breisgau, Deutschland

UNI
BASEL

Basel, 2011

Genehmigt von der Philosophisch-Naturwissenschaftlichen Fakultät auf Antrag von

Prof. Dr. Dominik M. Zumbühl

Prof. Dr. George R. Pickett

Basel, den 26. April 2011

Prof. Dr. Martin Spiess
Dekan

Contents

List of Symbols

A_0	AVOGADRO number
$\mathcal{D}$	density of states
Δ_0	superconducting energy gap
E_F	FERMI energy
γ	SOMMERFELD coefficient
I	nuclear spin, current
k	thermal conductance
κ	thermal conductivity, KORRINGA constant
$\mathcal{L}$	LORENZ number
$\bar{\ell}$	mean free path
Λ_e	electronic CURIE constant
λ_F	FERMI wavelength
Λ_n	nuclear CURIE constant
μ_B	BOHR magneton
μ_n	nuclear magneton
μ	mobility
m^*	effective mass
Q	heat
$\dot{Q}$	heat flow
R	universal gas consant, electrical resistance
ρ	electrical resistivity
σ	electrical conductivity, STEFAN-BOLTZMANN constant
τ_ϵ	electron-phonon relaxation rate
τ_1	spin-lattice relaxation
τ_2	spin-spin relaxation, decoherence time
τ_2^*	spin-spin relaxation, dephasing time
v_F	FERMI velocity

Introduction

1.1. Miniaturisation and Temperature

The second half of the 20th century saw an enormous development of miniaturisation and progress of electronic and data processing devices. The first computer had the size of a room, whereas the same computing power nowadays can be fit into a pocket-size gadget. To a large extend this progress is based on the integration of transistors in semi-conductor circuits. Already 1965, Gordon Moore predicted surprisingly precisely the present state of electronics and computer technology [1, 2]. He also stated a law that describes the development of computing power: the number of transistors per unit area doubles about every two years.

Apart from technological limits, this evolution will eventually run into a fundamental physical limit. As the circuits approach the size of atoms, quantum mechanical effects start to become important. But quantum mechanics is not only a limit, it is also an opportunity. In contrast to a classical computer that stores information in a bit which is for example represented by the on and off state of a transistor, it is possible to store the information in a system of two combined quantum mechanical states. This allows for using algorithms that can solve certain tasks, e.g. the factorisation of large integers with Shor's algorithm, faster than any known algorithm on a classical computer [3].

Several systems can be used to physically implement such a quantum computer. Generally such a system has to provide coherence of the quantum mechanical states to maintain the stored information. One particular system are the electron

spins in a Gallium-Arsenide (GaAs) quantum dot [4]. Science has learned a lot about the physics in such devices [5, 6]. It was found that the major source of decoherence is the influence of fluctuations of the magnetic field created by nuclear magnetic moments of the GaAs host nuclei. An obvious way to eliminate these fluctuations is to polarise the nuclei, either by cooling or applying a large external field. Braunecker, Simon and Loss predict a 'built-in' solution [7, 8]. Below a certain temperature the GaAs nuclei enter a new state: They order ferro-magnetically. This phase transition is caused by an interaction between the nuclear spins which is mediated by electrons. The electron-electron interactions however, elevate the transition temperature into a range which is orders of magnitudes higher than the nuclear phase transitions found for instance in copper or silver [9]. Thus, the phase transition shows new physics besides the positive effect on spin coherence. The transition temperature can be tuned by changing the electron density, a phenomenon which has not yet been observed in nature. The phase transition is yet supposed to occur at temperatures below those that can currently be achieved with cooling techniques established in mesoscopic physics. Therefore we need to break new ground in cooling nanoelectronic devices such as GaAs quantum dots.

One way to go relies on the well-known technique of nuclear adiabatic demagnetisation. It allows for cooling nuclear spins in metals far into the sub-microkelvin regime [9]. The new idea that is pursued within this thesis is to incorporate such a nuclear refrigerator in each measurement lead of a low temperature set-up that is used for nanostructure research and thus - in principle - enables us to find the predicted phase transition. In a more general view, other questions could be examined, effects that are still masked in the currently accessible temperature range. The new type of refrigerator could lead to the discoveries of new states in the fractional quantum hall regime [10] or insight in the Kondo effect [11, 12]. Moreover, it is also possible that new, unexpected effects show up upon cooling nanostructures into new temperature ranges. The goal of this thesis was to plan, build and test a prototype refrigerator consisting of a parallel network of nuclear refrigerators. The outline is as follows.

1.2. Outline of this thesis

The first chapter is this introduction, whereas the second chapter is intended to give an overview on the basics in mesoscopic physics. A focus is put on quantum point contacts and quantum dots. Chapter three provides the basics of low-temperature physics with an emphasis on aspects relevant for this work. In chapter four I discuss the present status of cooling nanoelectronic devices and layout the concept of the novel refrigerator. Chapter five deals with the experimental set-up and in chapter six the single constituents of the refrigerator are discussed. Then, in chapter seven, the overall performance of the refrigerator is analysed whereas the following chapter eight contains measurements done on a quantum dot. Finally, chapter 9 summarises our findings, presents a brief look at the second generation refrigerator of this type and gives further outlook.

Mesoscopic Physics

2.1. Introduction: Mesoscopic Physics and Nanostructures

Classical theories of transport such as the DRUDE model rely on some implicit assumptions. All mechanisms that cause resistance are summarised in a general friction which scales linearly with velocity acting on the electron travelling in a device. The resistance can then be described by one single microscopic parameter τ, which can be interpreted as the average time between two scattering events [13]. The electron propagates at an average speed $\bar{v}$ and the mean free path, the distance travelled between two scattering events, is given by $\bar{\ell} = \bar{v}\tau$.

Scaling the size of a device further and further down brings us into a regime where these dimensions become comparable to certain length scales of importance. One scale is given by the FERMI wavelength λ_{F}, which is the DE BROGLIE wavelength of the electrons at the FERMI energy. It depends on the charge carrier density n only, as $\lambda_{\mathrm{F}} \sim n^{-1/d}$ where d is the dimensionality of the device. If the device length is comparable to λ_{F} size quantisation appears. The mean-free-path is another important length scale. In the DRUDE model it is assumed to be much smaller than the length of the device. Transport is called diffusive. If that is no longer the case, i.e. the length is comparable or even smaller than $\bar{\ell}$, transport becomes ballistic. The average speed $\bar{v}$ mentioned above has to be replaced by the FERMI velocity v_{F}. Furthermore, the energy required to add one more electron

into a device becomes larger as the dimensions are reduced. That is because the device capacitance C decreases and therefore the charging energy e^2/C goes up. If the thermal energy of the electron is much smaller, single electron charging effects can be observed. All these quantum mechanical effects are fundamental limits for an arbitrary miniaturisation of electronic devices. But quantum mechanics opens new ways of computation, so-called quantum computation, which is briefly discussed in section 2.2.

The physics that examines the effects in such devices is called mesoscopic physics. The devices have dimensions smaller than a few micrometer and larger than nanometres, that means more than the size of a single atom. The new cooling scheme presented in this thesis allows in principle to examine many types of devices at lower temperatures. Hence, the term 'nanostructure' in the context of cooling refers almost all device designs and host materials. It is far beyond the scope of this work to discuss all in detail.

2.1.1. 2D Electron Gases in GaAs

The primary goal is to cool 2-dimensional electron gases (2DEGs) in GaAs/AlGaAs heterostructures. This base material has experienced an enormous progress within the last 30 years. Nowadays, it is possible to fabricate devices which have a mean free path that exceeds the device dimensions by an order of magnitude or even more. Electrons are typically confined in one direction in a triangular potential well about 100 nm below the surface. At low enough temperatures only the lowest mode of the potential is occupied and the electrons form a 2D system.

Figure 2.1 shows a sketch of GaAs heterostructure that contains such a 2DEG. 50 nm of GaAs are deposited on a GaAs wafer. Afterwards a superlattice is put which smoothens the surface and reduces the stress. Then 800 nm of GaAs are added and followed by 100 nm of $Al_{0.3}Ga_{0.7}As$ which means that 30% of the gallium is replaced by aluminium. In a depth of 70 nm a layer of silicon is added. Its thickness is about one atom thick. This delta layer dopes the material. On top a last layer of 10nm GaAs is deposited to prevent the Aluminium from oxidising. The electrons gather in the potential well in the AlGaAs/GaAs interface. Their wavefunction spreads typically ~ 10 nm perpendicular to the layer sequence. Modern molecular beam epitaxy (MBE) techniques including super clean growth environments and modulation doping which puts the ionised donor atoms a distance away from the 2DEG provide samples with extremely high electron mobility.

An advantage of semiconductors over metals is their smaller, and in particular controllable, charge carrier density. This leads to a larger Fermi wavelength, typically about a factor of ~ 100, and therefore, size quantisation can be seen in comparatively large devices. Furthermore, metallic gates can be attached on the surface of semiconductor materials resulting in the opportunity to tune charge
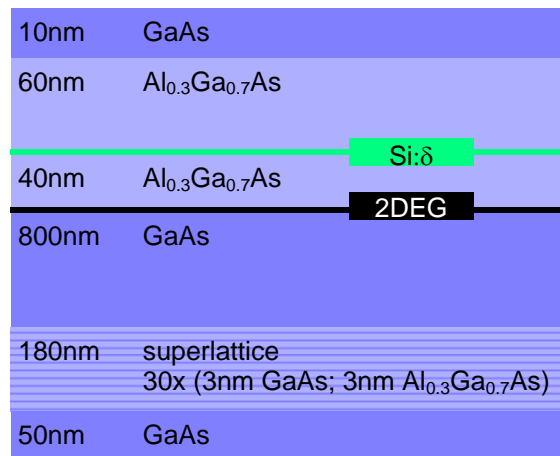
10nm	GaAs
60nm	Al$_{0.3}$Ga$_{0.7}$As
	Si:δ
40nm	Al$_{0.3}$Ga$_{0.7}$As
	2DEG
800nm	GaAs
180nm	superlattice 30x (3nm GaAs; 3nm Al$_{0.3}$Ga$_{0.7}$As)
50nm	GaAs

Figure 2.1.: A GaAs heterostructure that comprises a 2DEG. It is 110 nm below the surface. The Si:δ layer dopes the material.

carrier density and local electrostatic potentials. Modern micro-fabrication procedures, such as electron beam lithography, structures of the size of the FERMI wavelength can be made. If a large enough (negative) voltage, typically a few hundred mV, is applied on a top gate the 2DEG underneath is depleted. An area is established which is forbidden for electrons. The extension of this area can be tuned with the gate voltage. Besides the confinement in the triangular well, this enables us to confine the electrons also in the remaining two dimensions. Among others, we can form one-dimensional wires or zero-dimensional quantum dots.

I will now discuss some fundamental concepts of mesoscopic physics which is followed by a treatment of quantum point contacts (QPCs) and quantum dots (QDs) as examples of nanoelectronic devices.

2.1.2. Electronic Structure of Semiconductors

A characteristic property of solids is the presence of energy bands. The tight-binding model explains how they are formed out of atomic orbitals. Consider the orbital wave functions of two atoms, ϕ_A and ϕ_B, each with energy $E_{n,A} = E_{n,B}$. If the atoms are brought closer together the wave function overlap and the two combinations $\phi_A + \phi_B$ and $\phi_A - \phi_B$ form new orbitals the energy of which differ slightly. The energy of $\phi_A + \phi_B$ is smaller than $E_{n,A}$, the energy of $\phi_A - \phi_B$ is larger. In both cases, two atom cores share one electron. The probability density function for the '+'-states is finite in between the atoms, i.e. the binding energy is increased. Extending this approach to N atoms results in N new orbitals. Since the energy splitting of the orbitals is small and N is large, the energy levels are

regarded as a quasi-continuous band. For small enough spacing the band arising from the n-th orbital overlaps with orbitals arising from orbitals adjacent in energy. An equilibrium configuration is given if the repelling Coulomb forces of the atom cores balance out the attracting forces which arise through the gain of binding energy of the '+'-states. In semiconductors the energy bands exhibit a gap of the order electronvolt (GaAs: 1.4 eV, Si: 1.1 eV) in this equilibrium and the Fermi energy is within this gap. A proper application of the tight-binding model gives maxima and minima in k-space. Since a semiconductor has a small charge carrier density compared to the number of available electronic states, the charge carrier reside in the minima. The band can hence be approximated by a parabola and the Taylor expansion is [14]

$$E(\vec{k}) = E_0 + \frac{1}{2}\vec{k}\left(\frac{\partial^2 E}{\partial k_i \partial k_j}\right)\vec{k} \tag{2.1}$$

where $\vec{k}$ is the electron wave vector. If we compare this expression with the dispersion relation of the free electron gas $E(\vec{k}) = \hbar^2 \vec{k}^2/2m$ with $\hbar$ Planck's constant divided by 2π and m the mass of the free electron the tensor of the second derivative can be regarded as an effective mass

$$\frac{1}{\hbar^2}\left(\frac{\partial^2 E}{\partial k_i \partial k_j}\right) = \left(\frac{1}{m^*}\right)_{ij} \tag{2.2}$$

A diagonalisation of the effective mass tensor enables us to describe the behaviour of electrons with their effective mass along the crystal axis. The electron can be treated as a free electron with effective mass m^*

Electrons are fermions and hence they are distributed according to the Fermi-Dirac distribution in equilibrium.

$$f = \frac{1}{e^{\frac{E-\mu}{k_B T}} + 1} \tag{2.3}$$

It gives the probability of a state at energy E to be occupied. T is the temperature, k_B the Boltzmann constant and μ denotes the chemical potential. Figure 2.2 shows the Fermi-Dirac distribution for different temperatures. The black solid line is for zero temperature. The distribution is then a sharp step at the Fermi energy below which all states are occupied and above which all states are empty. For finite temperatures, electrons can access higher energy levels due to thermal energy. The step is smoothened more and more as the temperature is increased (blue and green curve).

Besides the occupation probability f, the density of states (DOS) is required to calculate the density of electrons n. The DOS is the number of states per unit
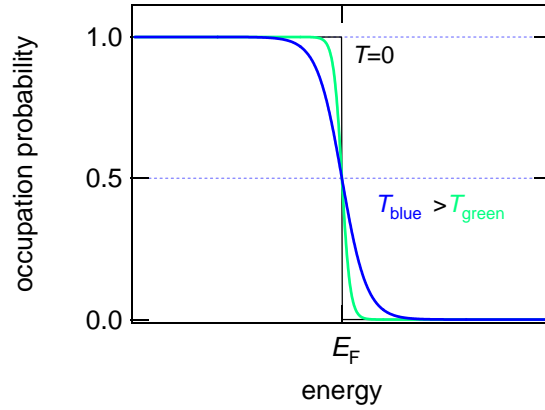
Figure 2.2.: FERMI-DIRAC distribution for different temperatures.

volume in an energy interval $[E, E + dE]$. It depends on the dimensionality of the system and the dispersion relation. Since we are primarily interested in 2D systems, I calculate the DOS for 2D and $E(\vec{k}) = \hbar^2 \vec{k}^2 / 2m^*$. Consider a 2D cube with base length L along the x- and y-axes. In a simple picture we assume plane waves Φ with periodic boundary conditions. Hence we can conclude

$$\Phi(\vec{r}) = \Phi(\vec{r} + \vec{L}) \quad \Longrightarrow \vec{k} = \frac{2\pi}{L}(n_x, n_y) \tag{2.4}$$

with n_i being integer quantum numbers. All allowed wave vectors form a cubic lattice in k-space resulting in one wave vector per unit area $V_k = 2\pi/L$ in k-space. All wave vectors of equal length $|\vec{k}|$ form a circle and so the total number of states N can be written

$$N = g\frac{1}{V_k}\pi k_F^2 \tag{2.5}$$

Here, g denotes the degeneracy and $\vec{k}_F$ the FERMI wave vector. Plugging in the dispersion relation gives

$$N = g\frac{L^2 m^*}{2\pi\hbar^2}E_F \tag{2.6}$$

With this the DOS in 2D $\mathcal{D}_2$ reads

$$\mathcal{D}_2 = \frac{1}{L^2}\frac{\partial N}{\partial E} = g\frac{m^*}{2\pi\hbar^2} \tag{2.7}$$

Accordingly, the calculation for 1D and 3D give

$$\mathcal{D}_1 = g\frac{\sqrt{2m^*}}{2\pi\hbar}\frac{1}{\sqrt{E}} \qquad\qquad \mathcal{D}_3 = g\frac{(2m^*)^{3/2}}{4\pi^2\hbar^3}\sqrt{E} \tag{2.8}$$

For $d = 0$, we cannot use the ansatz (2.4), in that case the DOS is given by discrete energy levels.

The interaction parameter r_S is a measure of the interaction strength in an electronic system. It is the ratio of the COULOMB energy of two electrons at average distance r, and the kinetic energy at the FERMI energy. Hence, it reads [14]

$$r_S = \frac{E_{\text{Coulomb}}}{E_{\text{kinetic}}} = \frac{\frac{e^2}{4\pi\epsilon_0\epsilon_r r}}{\frac{m^* v_F^2}{2}} = \frac{e^2 m^*}{\epsilon_0\epsilon_r r h^2}\frac{1}{\sqrt{n}} \tag{2.9}$$

For $r_S \ll 1$, the interactions between the electrons can be disregarded. However, if $r_S > 1$ this becomes questionable [14]. Note that in two dimensions, the FERMI wavelength λ_F is proportional to r_S.

2.1.3. Quantum Point Contacts

Conductance Quantisation

One of the most fundamental nanostructures is the quantum point contact (QPC). Simply speaking it is a narrow channel that connects two reservoirs. In the ballistic transport regime it exhibits quantised conductance steps as function of channel width [15, 16]. The steps are in multiples of $2e^2/h = 2G_0 \approx 1/25.8\,\text{k}\Omega$ where e is the elementary charge and h is PLANCK's constant. Such a QPC can be realised by putting two split gates on top of a GaAs heterostructre. If a negative voltage is applied the 2DEG beneath the gates is depleted and a channel is formed between the gates as depicted in figure 2.3 a).
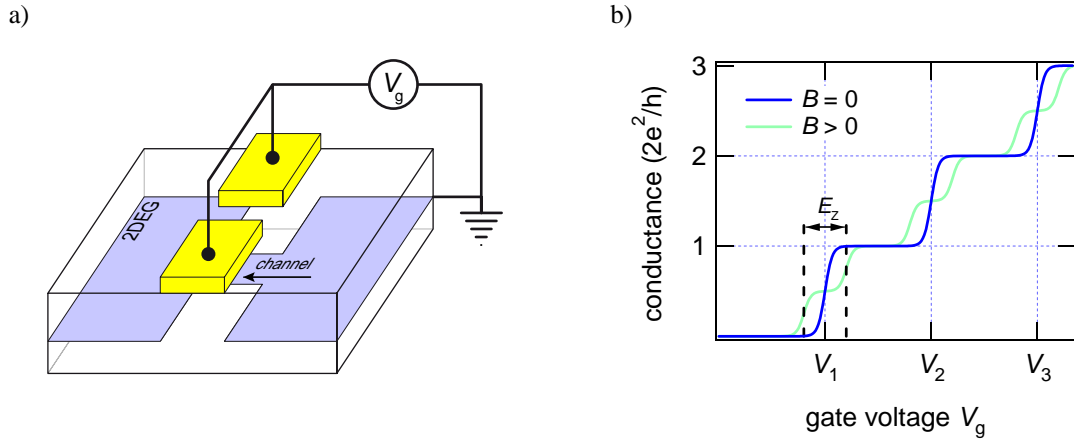

Figure 2.3.: a) Schematic of a split gate QPC b) Qualitative illustration of conductance quantisation.

Adiabatic Approximation

In the adiabatic approximation, a QPC is treated as a potential barrier. For simplicity electrons are treated as incoming plane waves with transverse modes ϕ_n. They are scattered through the QPC with an transmission amplitude t_n.

The quantum mechanical current density is given by $j = -\frac{|e|\hbar}{2im^*}\left(\phi_n^* \nabla \phi_n - \phi_n \nabla \phi_n^*\right)$ which leads to

$$dj = -\frac{|e|}{2\pi}\left|\phi_n\right|^2 \left|t_n^2\right| \underbrace{\frac{\hbar k}{m^*}}_{v} e_x dk \tag{2.10}$$

We can write the group velocity v as

$$v = \frac{\hbar k}{m^*} = \frac{\sqrt{2m^* E}}{m^*} = \sqrt{\frac{2}{m^*}}\sqrt{E} \tag{2.11}$$

and we can replace

$$dk = \frac{\partial k}{\partial E}dE = -\sqrt{\frac{m^*}{2}}\frac{1}{\hbar}\frac{1}{\sqrt{E}}dE \tag{2.12}$$

Plugging (2.11) and (2.12) into (2.10) and writing $\mathcal{T}_n(E) = |t^2|$ gives

$$dj = \frac{g\,|e|}{h}\mathcal{T}_n(E)\left|\phi_n\right|^2 dE \tag{2.13}$$

where g denotes the degeneracy. Integration over the whole cross section gives the spectral current

$$dI = -\frac{g\,|e|}{h}\mathcal{T}_n(E)dE \tag{2.14}$$

In order to obtain the current we have to take into account the FERMI-DIRAC distribution (2.3) and integrate

$$I = \frac{g\,|e|}{h}\sum_n \int_{E_n}^{\infty} \mathcal{T}_n(E)(f_{\mathrm{S}}(E) - f_{\mathrm{D}}(E))\,\mathrm{d}E \tag{2.15}$$

$f_{\mathrm{S,D}}(E)$ is the FERMI-DIRAC distribution in source and drain, respectively. In case of a small source-drain voltage, i.e. $\mu_{\mathrm{S}} - \mu_{\mathrm{D}} = eV_{\mathrm{SD}} \ll k_{\mathrm{B}}T$ the difference in the FERMI-DIRAC distribution can be expanded, hence (2.15) can be re-written

$$G = \frac{I_{\mathrm{QPC}}}{V_{\mathrm{SD}}} = g\frac{e}{h}\sum_n \int_{-\infty}^{\infty} \mathcal{T}_n(E)\left(-\frac{\partial f_{\mathrm{S}}(E)}{\partial E}\right)\,\mathrm{d}E \tag{2.16}$$

In the limit of zero temperature the derivative of the FERMI-DIRAC distribution becomes a delta peak around the FERMI energy E_F and hence (2.16) simplifies to

$$G = g\frac{e}{h}\sum_n \mathcal{T}_n(E_F) \qquad (2.17)$$

In summary, the conductance quantisation shows up for two reasons. On the one hand, it is a finite number of transverse modes in the narrow channel. On the other hand, $\frac{\partial k}{\partial E}$ in (2.12) can be identified with the 1D DOS (apart from a constant factor) which cancels the group velocity (2.11) and hence the energy dependence disappears. The exact transition from one conductance plateau to another depends on the transmission probability, i.e. the potential in the constriction. Even for zero temperature the steps show smooth transitions instead of a sharp step as one would expect from simple FERMI edge considerations.

Finite Field

So far external magnetic fields were neglected. Electron spins align parallel or antiparallel to an applied magnetic field, they occupy states called ZEEMAN levels. The energy difference is $E_Z = g\mu_0 B$ which is $25\,\mu$eV/T in case of GaAs. The conductance steps in a QPC now show plateaus at $1e^2/h$. This is indicated in figure 2.3 b) by the green curve. The lower ZEEMAN level is populated first and hence contributes to conductance before the upper ZEEMAN level. The displacement of the steps in the gate voltage corresponds to the ZEEMAN energy.

2.1.4. Quantum Dots

In general, a quantum dot is a structure in which electrons are confined in all three directions. The confinement can be formed in a heterostructure during the growth of the material itself, e.g. in InGaAs [17] or InAs [18, 19]. Vertical QDs are fabricated by etching circular pillars into the 2DEG material [20]. The electrons are then confined in a disc within the pillar. The QDs used in this thesis are formed with electrostatic gates on top of a GaAs heterostructure containing a 2DEG. The pattern of the gates is shown in figure 2.4 a). A QD, indicated by the ellipse, forms if the potentials on the gates are chosen right. The contact to the dot is controlled with QPCs. In our device, the QPCs are formed between the left wall (LW) and the nose gate (N), and between right wall (RW) and (N) respectively.

On the one hand, the QPC can be tuned such that that the conductance of the dot is small, $G_{QD} \ll 2e^2/h$. In this closed dot regime, the electrons enter or leave the QD in tunnelling processes. On the other hand, the QPCs can be tuned such that one or more modes of conductance are available. In this open dot regime electrons can travel through the dot without tunnelling.

Since we conducted measurements on closed dots I will focus on this regime only. I will also treat double quantum dots (DQDs) afterwards to explain some of the observations shown in section 8.
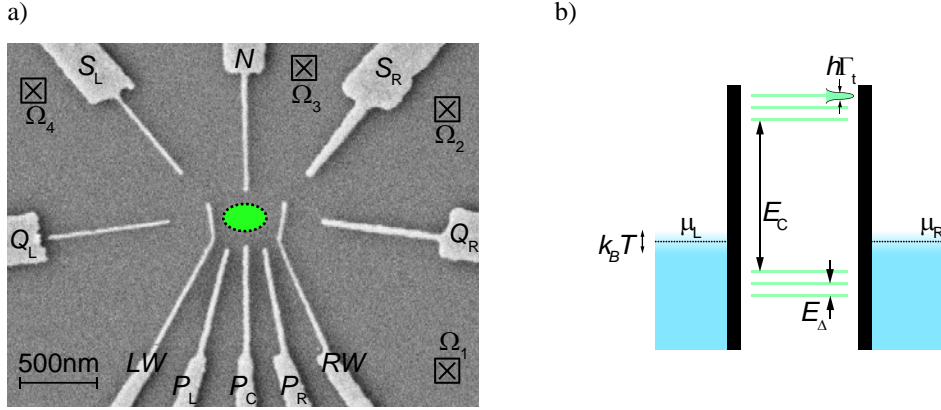

Figure 2.4.: a) SEM picture of a quantum dot. The ellipse indicates a quantum dot. b) Schematic illustrating the energies in a quantum dot, charging energy E_{C}, level spacing E_Δ, temperature T, natural linewidth Γ_{t}, and the chemical potentials of the reservoirs $\mu_{\mathrm{L,R}}$.

Single Quantum Dots in the Closed Regime

Transport through a closed QD can occur only if the QD has a state which lies within the chemical potentials of the source and drain reservoirs. This energy window can be tuned with a source-drain voltage V_{SD}. In the linear response regime ($V_{\mathrm{SD}} \to 0$) lock-in techniques allow the measurement of conductance G which is finite if an energy level of the QD is in resonance. Transport measurements can be used to examine the spectra of QDs. They exhibit many effects that are also present in natural atoms [21], in particular shell filling and Hund's rule [22, 23]. The advantage of QDs is that it is possible to probe them through leads and to tune the confinement potential whereas the confinement of electrons in atoms is set by the COULOMB potential of the nucleus.

However, the number of electrons in the QD is an integer, N. Due to COULOMB repulsion between electrons it requires energy to bring an additional electron of charge e on the dot. This charging energy reads

$$E_{\mathrm{C}} = \frac{e^2}{C_\Sigma} \tag{2.18}$$

C_Σ is the total capacitance of the dot. It is known from classical electrodynamics that the capacitance scales with the size of an object. For a thin disc with radius

r the capacitance is $C = 8\epsilon_0\epsilon_r r$ [24] where ϵ_0 is the permittivity of free space and ϵ_r the relative permittivity of the material. From figure 2.4 a) we can estimate the radius of the dot as $\sim 100\,\mathrm{nm}$ and ϵ_r is of the order of 12 for AlGaAs [25]. The capacitance is then $\sim 85\,\mathrm{aF}$ hence the charging energy is of the order $\sim 2\,\mathrm{meV}$ which corresponds to $23\,\mathrm{K}$.

The total capacitance is a sum of capacitances as described by the capacitance model [14]. It describes the COULOMB interactions between the electron in the dot and source, drain and gate by a capacitive coupling.

$$C_\Sigma = C_S + C_D + C_g + C_r \tag{2.19}$$

with mutual capacitances between the dot and source C_S, drain C_D, and plunger gate C_g. C_r is a residual capacitance to other parts which is often neglected.

Starting from the 2D DOS (2.7) we can estimate the average level spacing of the confinement energy of a single particle [14]. In an area A there are $A \cdot \mathcal{D}_2$ states per unit energy. Hence, the average level spacing is

$$E_\Delta = \frac{2\pi\hbar^2}{gm^*A} \tag{2.20}$$

With the effective mass in GaAs, $m^* = 0.067m_e$ [25], and a spin degeneracy of $g = 2$ the average level spacing is $E_\Delta \approx 110\,\mu\mathrm{eV}$ corresponding to $1.3\,\mathrm{K}$ for a radius $r = 100\,\mathrm{nm}$ like above.

The third energy scale is set by the natural line width. The QPCs tune the tunnel barriers through which the electrons can enter or leave the dot resulting in tunnel rates $\Gamma_{S,D}$ between source and drain, respectively. The total tunnel rate is then $\Gamma_t = \Gamma_S + \Gamma_D$ and the line width is $h\Gamma_t$ with h being PLANCK's constant.

Finally, the thermal energy, $k_B T$, broadens the FERMI edges in the reservoirs. Figure 2.4 b) depicts a QD and the energies. The blue areas are the left and the right electron reservoir. $\mu_{L,R}$ are the corresponding chemical potentials. The FERMI edges are broadened by temperature. The black areas represent the tunnel barriers created by the QPC. The green lines are the energy levels in the QD.

Coulomb Blockade

If the thermal energy is larger than all other energies it can always excite an energy level in the dot and hence the conductance is always finite, whereas for $k_B T \ll E_C$ COULOMB blockade is observed. If an energy level in the dot is available with an energy below the FERMI energies in the reservoirs, such as the lower levels in figure 2.4 b), an electron from one of the reservoirs can tunnel onto the dot but it cannot leave because all states in the reservoirs which are energetically available are occupied. Since the next higher energy level in the dot can not be excited

thermally, tunnelling is suppressed. In the resonant case, $\mu_\mathrm{L} \approx E_\mathrm{dot} \approx \mu_\mathrm{R}$ the electron can tunnel onto the dot and on to the next reservoir, hence the conduction is finite. I am now explaining COULOMB blockade (CB) with the help of figure
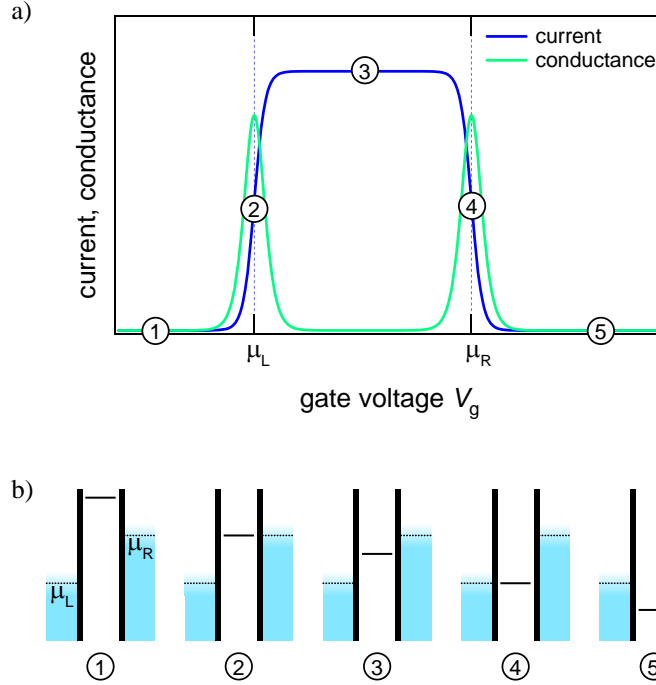

Figure 2.5.: Schematic on COULOMB blockade. a) Current and differential conductance through the dot. b) Energy diagram of the dot's levels E_dot.

2.5 for finite dc bias. In a) the current and the differential conductance $\partial I/\partial V$ of the QD is plotted against plunger gate voltage. The numbers (1) to (5) refer to the situations depicted in the level diagrams in b) which shows the dot for a finite bias voltage between left and right reservoir. The plunger gate voltage is increased from left to right, i.e. the energy level of the dot E_dot is lowered. Within this picture the current is proportional to the number of occupied states in the source and proportional to the number of available states in the drain. Hence we can write

$$I \sim f_\mathrm{S}(E_\mathrm{dot}) \cdot (1 - f_\mathrm{D}(E_\mathrm{dot})) \tag{2.21}$$

where $f_\mathrm{S,D}$ are the FERMI-DIRAC distributions in source and drain, respectively.

In (1) the the energy level of the dot is above both, chemical potentials of source and drain. In this case $f_\mathrm{S}(E_\mathrm{dot}) = 0$ and hence $I = 0$. As the plunger gate voltage is increased the energy level of the dot gets into resonance with the source and

electrons can tunnel onto the dot (case (2)). The Fermi-Dirac distribution of the drain is ≈ 0 and therefore the current is $I \sim f_{\mathrm{S}}(E_{\mathrm{dot}})$. If the energy level is half-way between the chemical potentials of the two reservoirs (3) essentially all states in the source are occupied, $f_{\mathrm{S}} = 1$, and all states in the drain are empty $f_{\mathrm{S}} = 0$. The current is constant. When E_{dot} gets into resonance with the drain we get $I \sim (1 - f_{\mathrm{S}}(E_{\mathrm{dot}}))$. Finally in (5), all states in either reservoir are occupied and hence the second factor in (2.21) vanishes such that $I = 0$. In this simple picture that neglects spin degeneracy the current does not depend on the bias voltage. The tunnelling through the barriers sets the current according to [26]

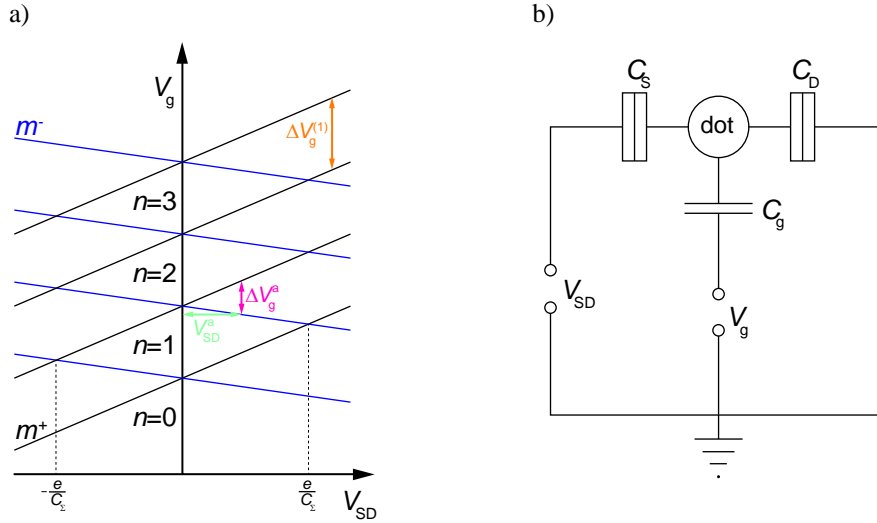$$I = |e| \frac{\Gamma_{\mathrm{S}} \Gamma_{\mathrm{D}}}{\Gamma_{\mathrm{S}} + \Gamma_{\mathrm{D}}} \tag{2.22}$$

Figure 2.6.: a) schematic of a Coulomb diamond. The black and blue lines indicate lines of finite conduction. Furthermore the charging energy E_{C} and the lever arm $\alpha = V_{\mathrm{SD}}^a / \Delta V_{\mathrm{g}}^a$ are indicated. b) Model circuit of a quantum dot. The double rectangle is a tunnel contact. It can be regarded as a capacitance and a resistor in parallel.

Figure 2.6 a) shows a schematic of a so-called Coulomb diamond. The black and blue lines indicate the peaks of conductance as function of bias voltage V_{SD} and gate voltage V_{g}. Figure 8.5 shows a measurement. The numbers $n = 0, 1, 2, \ldots$ represent the numbers of electrons on the dot relative to a neutrality point. The lever arm is a factor that converts the plunger gate voltage into the energy of the dot level. Since in the closed dot regime the applied bias voltage drops across the dot the energy difference between source and drain reservoir is $\mu_{\mathrm{S}} - \mu_{\mathrm{D}} = eV_{\mathrm{SD}}$.

This corresponds to the voltage difference of the inflection points in figure 2.5 a). Hence, the lever arm reads

$$\alpha = \frac{V_{\mathrm{SD}}^a}{\Delta V_{\mathrm{g}}^a} \qquad (2.23)$$

where $V_{\mathrm{SD}}^a, \Delta V_{\mathrm{g}}^a$ are defined in figure 2.6 a). The capacitance model introduced in equation 2.19 is reflected in the slopes of the diamonds.

The consideration so far are based on classical electrodynamics and the capacitances involved are assumed to be constant. This model of constant interaction suffices to understand the basic physics in quantum dots. It neglects electron-electron interactions or screening effects. Furthermore, the electron spins and related effects such as spin-orbit coupling and the influence of magnetic fields were not considered either. However, within this simple picture and the confinement potential we can denote the Hamiltonian for a single quantum dot (SQD) [25]

$$\mathcal{H}_{\mathrm{SQD}} = \frac{|e|^2}{C_\Sigma} \frac{N(N-1)}{2} + N \frac{|e|}{C_\Sigma} \left(C_{\mathrm{g}} V_{\mathrm{g}} + C_{\mathrm{S}} V_{\mathrm{S}} + C_{\mathrm{D}} V_{\mathrm{D}} \right) + \sum_n \epsilon_n \qquad (2.24)$$

The first term is the energy required to bring N electrons onto the dot due to their COULOMB repulsion. The second term describes the interaction between the electrodes. For simplicity, only one plunger gate, source and drain are considered. The single particle levels ϵ_n can be deduced from the confinement potential.

Coulomb Blockade Thermometry

CB is a temperature dependent effect. As explained in figure 2.5 the current as function of the gate voltage reflects directly the FERMI distributions in the reservoirs. The picture above gives a qualitative understanding of CB. For a quantitative description of a conductance peak through a QD we have to distinguish different regimes. They are determined by the energies $h\Gamma$, E_Δ, $k_{\mathrm{B}}T$ and E_{C}. A fundamental pre-requisite for CB to occur is that the dot has energy states with a spacing which is larger than temperature. Otherwise higher energy states can be populated by thermal excitations, hence, $k_{\mathrm{B}}T \ll \max(E_\Delta, E_{\mathrm{C}})$ [27]. Furthermore, the QD has to be operated in the tunnelling regime. If the QPCs that define the QD comprise several modes, the conduction through the QD is determined by the QPCs in series. In other words, $h\Gamma_{\mathrm{t}} = h(\Gamma_{\mathrm{S}} + \Gamma_{\mathrm{D}}) \ll E_\Delta, k_{\mathrm{B}}T, E_{\mathrm{C}}$ [27].

In the metallic or classical COULOMB regime where $h\Gamma_{\mathrm{t}} \ll E_\Delta \ll k_{\mathrm{B}}T \ll E_{\mathrm{C}}$ all states in the QD are populated according to the FERMI distribution in the reservoirs. In the limit of $V_{\mathrm{SD}} \to 0$ each energy level contributes to the conductance $G = I/V$ according to [27]

$$G \simeq \frac{e^2 \mathcal{D}_2}{2} \frac{\Gamma_{\mathrm{S}} \Gamma_{\mathrm{D}}}{\Gamma_{\mathrm{S}} + \Gamma_{\mathrm{D}}} \frac{1}{\cosh^2 \left(\frac{e\alpha V_{\mathrm{g}}}{2.5 k_{\mathrm{B}} T} \right)} \qquad (2.25)$$

where α is the lever arm, $\mathcal{D}_2$ the 2D density of states, and V_g is the plunger gate voltage.

In the quantum COULOMB blockade regime where $h\Gamma_t \ll k_B T \ll E_\Delta$ only one confinement level facilitates transport and the conductance peak as a function of plunger gate voltage V_g is given as [27]

$$G = \frac{e^2}{4k_B T} \frac{\Gamma_S \Gamma_D}{\Gamma_S + \Gamma_D} \frac{1}{\cosh^2\left(\frac{e\alpha V_g}{2k_B T}\right)} \qquad (2.26)$$

Note, that the amplitude in (2.26) holds, irrespective of the ratio of E_Δ/E_C [27].

Both conductance peaks, (2.25) and (2.26), follow the same qualitative behaviour, $\cosh^{-2}$. However, the regimes can be clearly distinguished. In both cases, the full width at half maximum $\Delta E_{1/2}$ scales linearly with temperature. It is $\Delta E_{1/2}^{(m)} \simeq 4.35k_B T$ in the metallic regime and $\Delta E_{1/2}^{(qc)} \simeq 3.5k_B T$ in the quantum COULOMB regime [28]. Furthermore, the temperature dependence of the amplitudes are different. The amplitude in (2.25) is independent of temperature whereas in the quantum COULOMB regime, the amplitude goes as $1/T$.

If the natural line width is comparable to temperature, $h\Gamma_t \approx k_B T$, the conductance peak starts to become life-time broadened. Disregarding electron-electron interactions, but considering different scattering mechanisms, the so-called Breit-Wigner form can be derived [29, 30]

$$G = g\frac{e^2}{h} \frac{\Gamma_S \Gamma_D}{\Gamma_S + \Gamma_D} \frac{\Gamma_t}{\left(\frac{e\alpha V_g}{\hbar}\right)^2 + \left(\frac{\Gamma_t}{2}\right)^2} \qquad (2.27)$$

where g denotes the degeneracy of the single level. This Lorentzian line shape of the COULOMB peaks was shown experimentally [31] despite the simple picture of a non-interacting 2DEG.

Double Quantum Dots

The gates of the device presented in figure 2.4 a) can be tuned such that two QDs adjacent to each other are formed. The model circuit of such a double quantum dot (DQD) is depicted in figure 2.7 a). It is essentially an expansion of the model circuit of the SQD in figure 2.6 b). The new key feature is the coupling between the two dots which is controlled by the voltages on gates (N) and (P_C). Starting

from the Hamiltonian of the SQD the Hamiltonian of the DQD can be written [32]

$$
\begin{aligned}
\mathcal{H}_{\mathrm{DQD}} \quad = \quad & \underbrace{\frac{|e|^2}{C_{\Sigma\mathrm{L}}}\frac{N_{\mathrm{L}}(N_{\mathrm{L}}-1)}{2}}_{(1)} + \frac{|e|}{C_{\Sigma\mathrm{L}}}\Big(\underbrace{N_{\mathrm{L}}}_{(2)} + \underbrace{N_{\mathrm{R}}\frac{C_{\mathrm{m}}}{C_{\mathrm{R}}}}_{(3)}\Big)(C_{\mathrm{gL}}V_{\mathrm{gL}} + C_{\mathrm{S}}V_{\mathrm{S}}) + \sum_{n}\epsilon_{\mathrm{L}n} \\
+ \quad & \frac{|e|^2}{C_{\Sigma\mathrm{R}}}\frac{N_{\mathrm{R}}(N_{\mathrm{R}}-1)}{2} + \frac{|e|}{C_{\Sigma\mathrm{R}}}\Big(N_{\mathrm{R}} + N_{\mathrm{L}}\frac{C_{\mathrm{m}}}{C_{\mathrm{L}}}\Big)(C_{\mathrm{gR}}V_{\mathrm{gR}} + C_{\mathrm{D}}V_{\mathrm{D}}) + \sum_{m}\epsilon_{\mathrm{R}m} \\
+ \quad & N_{\mathrm{L}}N_{\mathrm{R}}\frac{|e|^2\,C_{\mathrm{m}}}{C_{\mathrm{L}}C_{\mathrm{R}} - C_{\mathrm{m}}^2} + \sum_{nm}t_{nm} \qquad\qquad\qquad\qquad\qquad\qquad (2.28)
\end{aligned}
$$

where the (1) denotes the charging energy of the left(right) dot. The total capacitances of the left(right) dot $C_{\mathrm{L(R)}}$ dot is rescaled with a factor that accounts for the coupling:

$$
C_{\Sigma\mathrm{L(R)}} = C_{\mathrm{L(R)}}\left(1 - \frac{C_{\mathrm{m}}^2}{C_{\mathrm{L}}C_{\mathrm{R}}}\right) \qquad\qquad (2.29)
$$

with C_{m} the mutual capacitance between the two dots. (2) couples the left dot to the left plunger gate and the source and (3) couples the right dot to the left plunger gate and the source. Note that this is an indirect coupling. The direct couplings of the left dot to the right plunger gate and the drain are neglected (see figure 2.7 a)). All three terms are analogue for the centre row.

The first term in the third row describes the mutual charging energy which is the additional energy required to put an electron onto the dot due to an electron present in the other dot. Finally, t_{nm} is a general tunnel coupling that couples the wave function in the left dot to the wave function in the right dot.

The state of a DQD is typically denoted as $(N_{\mathrm{L}}, N_{\mathrm{R}})$ where $N_{\mathrm{L(R)}}$ is the number of electrons in the left(right) dot. It is primarily tuned with the corresponding plunger gate voltage $V_{\mathrm{gL(R)}}$. The two plunger gate voltages span a parameter space which exhibits regions of stable charge configuration, hence the name charge stability diagram. Starting from the Hamiltonian (2.28) the shape of the stable charge areas can be explained.

In the the limit of small coupling $(C_{\mathrm{m}}, t_{mn} \to 0)$ (2.28) is the sum of two Hamiltonians each describing a SQD coupled to one reservoir and to one plunger gate. Each plunger gate tunes the level of one dot regardless of the potential of the other gate or the number of electrons on the other dot. This leads to the charge stability regions as indicated by the dashed line in figure 2.7 b). If, for instance, V_{gL} is increased the dot is charged with an additional electron each time a dashed line is crossed. Due to the absence of coupling, this is independent of V_{gL}. In the quadruple points where the vertical and the horizontal lines cross, each dot is in resonance with its reservoir and the four adjacent charge state are degenerate. Transport through the DQD can occur only in such a quadruple point.
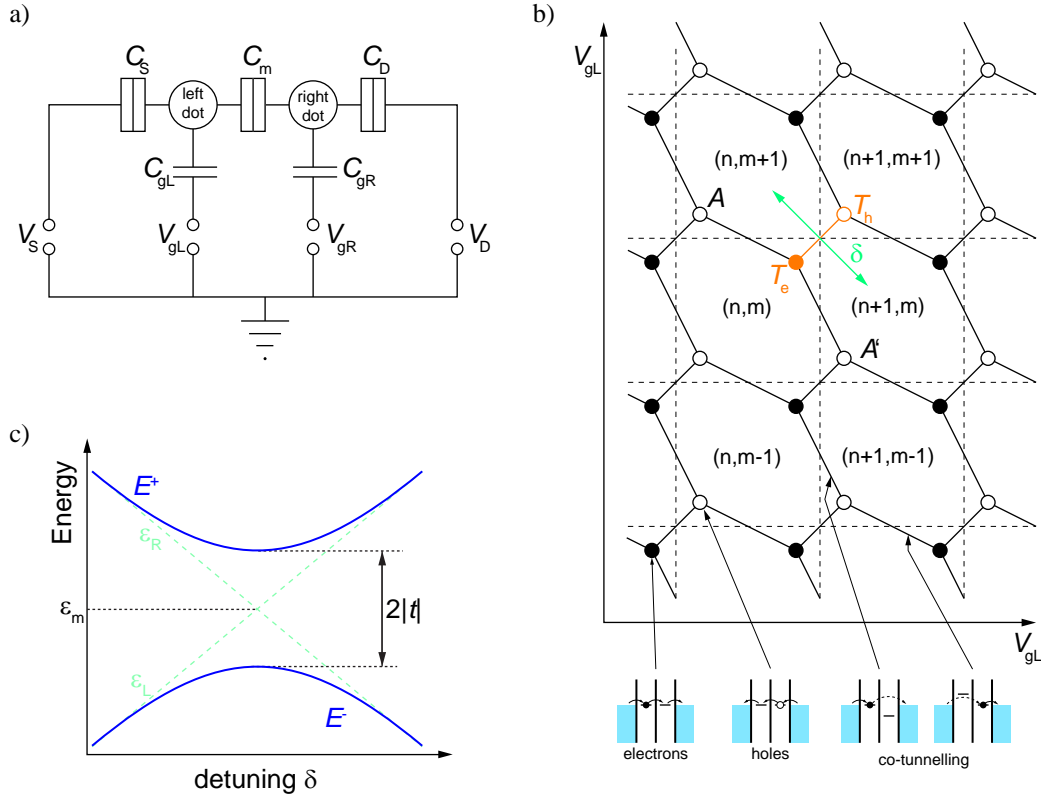
Figure 2.7.: a) Model circuit of a double quantum dot. b) Charge stability diagram. c) Energy of hybridised charge states.(partially adopted from [33])

In the case of finite capacitive coupling the electron on a dot feels the presence of an additional electron on the other dot. The degeneracy in the quadruple point is lifted and splits into two called triple points where three charge states coexist. One can distinguish two types of triple points. The electron-type, one of which is labelled T_e in figure 2.7 b), allows transport through the whole system by a sequential tunnelling process of electrons. The hole-type (T_h in figure 2.7 b)) allows transport through a sequential tunnelling of a hole. The following transfer processes are depicted below the charge stability diagram.

$$T_e \quad : \quad (n,m) \to (n+1,m) \to (n,m+1) \to (n,m)$$
$$T_h \quad : \quad (n+1,m+1) \to (n+1,m) \to (n,m+1) \to (n+1,m+1)$$

On the line $\overline{T_e T_h}$ the states $(n, m+1)$ and $(n+1, m)$ are degenerate. The mutual inductance allows interdot coupling but tunnelling into or out of the DQD to either reservoir is energetically forbidden. Along $\overline{T_e A}$ (n,m) and $(n,m+1)$ are

degenerate i.e. the chemical potential of the right dot is in resonance with the right reservoir. Increasing V_{gL} lowers the energy level in the left dot. Due to the coupling, the energy level in the right dot is lower, too, and V_{gL} has to be lowered to compensate for the coupling and maintain the resonance of the right dot level with the right reservoir. $\overline{T_e A'}$ is explained analogically interchanging 'left' and 'right'.

Currents along the honey comb edges can be experimentally observed, although forbidden within this picture. As sketched in the third picture below the honey comb diagram an electron can tunnel into the left dot in a regular process. Subsequentially, it might tunnel through an energetically forbidden region in a virtual process. The latter could appear first as shown in the fourth diagram. Transport between the triple points can occur if one electron leaves the DQD to one side while simultaneously another one enters the DQD from the other side. These processes are referred to as co-tunnelling.

Finally, at very strong coupling $(C_m \to C_{L(R)})$ the Hamiltonian in (2.28) recovers essentially the SQD Hamiltonian (2.24). The first term in the third line goes to infinity which reflects the fact that it requires an infinite amount of energy to localise two point charges in the same spot. However, the DQD passes over to a SQD and the charge stability now shows parallel lines only which go from top left to bottom right. They correspond to COULOMB blockade peaks.

In order to explain the effects of the tunnel coupling we consider one energy level in each uncoupled dot, denoted ϵ_L and ϵ_R, that can be tuned with plunger gates. The coupling t then leads to eigenstates of this two level system with energies that can be written as [32]

$$E^{\pm} = \epsilon_m \pm \sqrt{\frac{\delta}{4} + |t|^2} \qquad (2.30)$$

Here, $\epsilon_m = (\epsilon_L + \epsilon_R)/2$ is the mean energy and $\delta = \epsilon_L - \epsilon_R$ is called detuning which is measured along the axes shown in Figure 2.7 b). Figure 2.7 c) shows the energy for these two states as function of detuning. The effect of coupling is strongest for zero detuning where the two coupled states are $|t|$ higher or lower in energy than the uncoupled states.

This model is a strong simplification. It neglects for instance electron-electron interaction (apart from COULOMB interaction) or the role of the spins. DQDs were proposed to be used as fundamental building blocks for quantum computers. This could be the spin degree of freedom [4] or the charge degree of freedom [34, 35].

2.2. Quantum Coherence and Quantum Computing

Next I will give a brief introduction and overview on quantum computing based on the book by Nielsen and Chuang [3].

The fundamental unit of a classical computer is a bit. It can be in one of two possible states, '0' or '1'. Its physical realisation is typically accomplished by a transistor. Any data processing leaves the bit in one of the two states. Accordingly, the fundamental unit of a quantum computer is called a quantum bit, or shorter qubit, denoted $|0\rangle$ or $|1\rangle$. Unlike classical bits, the qubit can also be in a state $|\Psi\rangle$ different than these two. It can be in a linear combination or superposition of the two:

$$|\Psi\rangle = \alpha_0 |0\rangle + \alpha_1 |1\rangle \qquad \alpha_i \in \mathbb{C}, |a_0|^2 + |a_1|^2 = 1 \qquad (2.31)$$

The probabilistic character of quantum mechanics draws an important distinction to classical computation. Assume one initialises a bit in a certain state, performs a computation process and reads out the result. The final state of the bit is always the same, no matter how often the sequence initialisation - process - read out is repeated. In a qubit the situation is different. You can do the same sequence as in the classical case but the result varies. The final outcome can be written as in (2.31). A repetition of the sequence gives $|0\rangle$ with a probability of $|\alpha_0|^2$ and $|1\rangle$ with a probability of $|\alpha_1|^2$.

Single qubit states can be depicted on the BLOCH sphere (figure 2.8). Equation (2.31) can be re-written

$$|\Psi\rangle = \left(\cos\frac{\theta}{2} |0\rangle + \mathrm{e}^{i\phi} \sin\frac{\theta}{2} |1\rangle \right) \mathrm{e}^{i\gamma} \qquad (2.32)$$

$\mathrm{e}^{i\gamma}$ is a phase factor which doesn't have any observable effect. The meanings of θ and ϕ are given in figure 2.8. Any superposition $|\Psi\rangle$ is represented by a point on the sphere. The other way round every point of the BLOCH sphere corresponds to a qubit state. However, a classical bit can only 'live' on either one of the poles of the sphere.
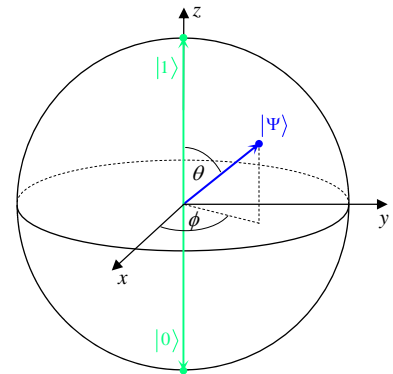
Figure 2.8.: BLOCH sphere.

A classical computer has one non-trivial operation on a single bit, the negation. Operations on classical bits are called logic gates. Operations on qubits are called quantum gates, accordingly. In comparison to classical computing, quantum computing provides more quantum gates than just one. Any unitary operator can be seen as such. In the BLOCH sphere picture such quantum gates represent an effective tilt of the initial state about a corresponding axis into a final state. In case of a single qubit they can be written as 2×2 matrices.

Such as a classical computer is composed of an array of bits, several qubits can be combined to form a quantum computer. In that case it is no longer possible to depict the state as easy as for a single qubit. A register of N bits can be in 2^N states, accordingly the state of N qubits is a superposition of 2^N states. Each factor $|\alpha_{i_1 \cdots i_N}|$ then represents the probability to find the state in $|i_k\rangle$. A remarkable phenomenon can be explained looking at 2 qubits. Their state is then

$$|\Psi\rangle = \alpha_{00}\,|00\rangle + \alpha_{01}\,|01\rangle + \alpha_{10}\,|10\rangle + \alpha_{11}\,|11\rangle \tag{2.33}$$

With appropriate unitary operations the double qubit can be brought into a superposition of the first and last state, a state which is called EPR (EINSTEIN-PODOLSKY-ROSEN) or BLOCH state.

$$|\Psi_{\mathrm{EPR}}\rangle = \frac{1}{\sqrt{2}}\left(|00\rangle + |11\rangle\right) \tag{2.34}$$

Measuring this state gives a 50% chance to measure either of the two states. Now assume we establish this state in a two-qubit system and subsequently take them spatially apart, we keep one and take the other further away. If we now measure once the state collapses either into $|00\rangle$ or $|11\rangle$. That means that both qubits are in the same state which in return tells us that the distant qubit is in the same state as the one that we kept. This type of correlation is not possible with classical bits.

This consideration has so far been premising an ideal qubit. Quantum mechanics provides a mighty calculus but it also sets prerequisites. In principle any quantum mechanical two-level system could be regarded as qubit. However, two major issues have to be considered. First, the single state itself has to persist. An ensemble of spin-$1/2$ particles in an external magnetic field will for example evolve into a population of the two ZEEMAN levels which is given by the BOLTZMANN distribution. This is usually referred to as spin-lattice relaxation with a general decay time τ_1. The second issue is coherence. The quantum mechanical states that constitute the qubits are in fact waves, in particular they have a phase. The phase information of a qubit, and the phase relation between qubits, has to persist as well. Eventually, all quantum computations have to be carried out before the phase information, i.e. coherence, is lost. The inevitable loss mechanisms depend on the particular systems under consideration. In general two time parameters describe the decoherence, τ_2^* and τ_2. The difference is that τ_2 describes the complete randomisation of phase, whereas τ_2^* comprises mechanisms such as inhomogeneities which can be eliminated by echo-techniques. The meaning of these two time parameters is depicted in figure 3.10.

Up to date numerous proposals have been made on which two-level system can be used for quantum computations. They are as different as superconducting charge,

flux or phase qubits, nuclear Zeeman states (NMR), optical lattices or qubits based on Bose-Einstein condensates, to mention but a few. One particular approach was proposed by Loss and DiVincenzo [4]. They suggested to use the spin in an GaAs quantum dot in an external magnetic field as the two-level system. Ever since, many experiments have been conducted towards such systems [6]. It was found that the major source of decoherence is hyperfine interaction between the electron spin and fluctuating magnetic fields created by the nuclear spins within the envelope of the electron wave function, the so-called Overhauser field. It is of the order of a few mT [36–39].

2.3. Nucelar Spins in Solids

2.3.1. Hyperfine Interaction

The mutual interaction between nuclear and electronic spins is called hyperfine interaction. Nuclear spins create an effective magnetic field that acts on the electrons. This gives rise to the hyperfine structure in the absorption spectra of atoms. In turn, the atom shell creates an effective magnetic field that acts on the nuclear spins. As a consequence, the peaks in nuclear magnetic resonance (NMR) spectra are shifted. This is referred to as Knight shift.

Unlike electrons that have a spin of $1/2$, nuclear spins can be zero such as the spin of the most abundant carbon isotope ^{12}C in carbon nanotubes but also as large as the spins of germanium or indium, which are $9/2$. GaAs is composed of three stable, natural isotopes ^{69}Ga, ^{71}Ga, and ^{75}Ga, all of which have nuclear spin $I = 3/2$.

If we take a QD with a radius $r = 100\,\mathrm{nm}$, like above in section 2.1.4, and a extension of $10\,\mathrm{nm}$ perpendicular to the 2DEG we have a volume of $\pi \cdot 10^{-22}\,\mathrm{m}^3$. The lattice constant of GaAs is $5.6\,\mathrm{\mathring{A}}$, hence $\approx 2 \cdot 10^6$ nuclear spins are within the electron wave function.

The hyperfine interaction of the electronic spin with the host nuclei is a contact hyperfine interaction. The electron has a finite probability to reside in the site of the nucleus which facilitates a spin-spin interaction. In GaAs it can be written as [40]

$$\mathcal{H}_{\mathrm{HF}} = \frac{2}{3}\mu_0 g \mu_{\mathrm{B}} \gamma_{\mathrm{n}} \hbar \vec{I}\vec{S}\,|\psi(0)|^2 \tag{2.35}$$

where g denotes the g-factor of the free electron, μ_{B} the Bohr magneton and γ_{n} the gyromagnetic ratio of the nucleus. $\vec{I}$ and $\vec{S}$ are the nuclear and electronic spins and $|\psi(0)|^2$ is the probability density of the electronic wave function in the site of the nucleus.

This can be expressed as an effective field that the nuclei exert on the electrons. An electron in the orbital state q experiences a so-called Overhauser field [40]

$$\vec{B}_{\text{OF}}^q = \frac{2\mu_0}{3} \frac{g}{g^*} \hbar \sum_i \gamma_i \vec{I}_i \, |\psi_q(r_i)| \tag{2.36}$$

where g^* is the effective electron g-factor. The sum is over all nuclear spins I_i. The fluctuations of the Overhauser field that cause electron spin decoherence are of the order of a few mT [36–39]. However, it is possible to polarise the nuclear spins in GaAs resulting in an Overhauser field of the order $4\,\text{T}$ [41]

2.3.2. Nuclear Ordering

The history of polarised nuclear spins dates back to the middle of the 20th century [42]. At that time nuclear and particle physicists conducted experiments on polarised nuclei. Nuclear magnetism has grown into its own field of research since. Theory and experiment accompanied each other. Various magnetic phase transitions were discovered, in metals as well as in insulators. A comprehensive review focussing on metals is given by Oja and Lounasmaa [9], a wider range of nuclear magnetism is covered by Abragam [43].

In particular the nuclear magnetic ordering of copper shows that spin-spin interaction can be far more complicated than a simple dipole-dipole interaction that is known from macroscopic dipoles. The spin-spin interaction can even be strong enough and anisotropic so that stable spin configurations are not restricted to spins that are aligned parallel or anti-parallel to an applied magnetic field. Figure
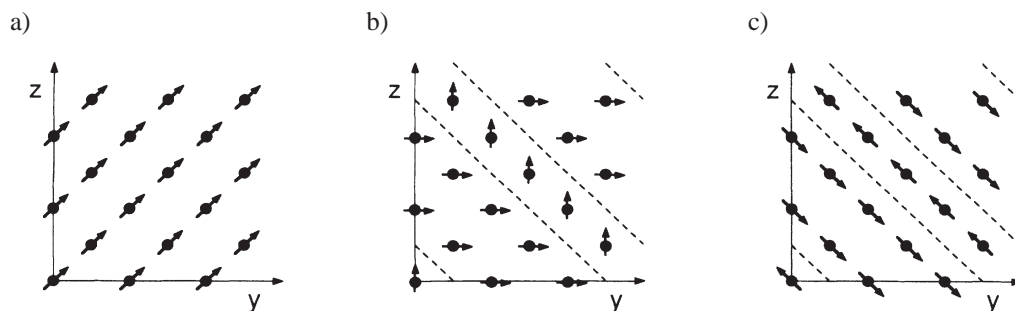
Figure 2.9.: Spin structures of copper for different ranges of external magnetic field along the $[01\bar{1}]$ axis (taken from [44]).

2.9 shows the nuclear ordering of copper [44] for a field which was applied along the $[01\bar{1}]$ axis. The structure in a) is a sequence of alternating anti-ferromagnetic planes, in the shown plane all spins point in the $[011]$ direction whereas in the next

plane they point along $[0\bar{1}\bar{1}]$ (the opposite way). The magnetic field is $|B| = 0$. In b) the structure is shown for $0 < |B| < \frac{1}{3}B_{\mathrm{c}}$, where B_{c} is the critical field above which the ordering vanishes. For c) the magnetic field is $B = \frac{1}{3}B_{\mathrm{c}}$. The nuclear ordering was discovered below a critical field $B_{\mathrm{c}} = 0.25\,\mathrm{mT}$ and below a NÉEL temperature of $T_{\mathrm{N}} = 58\,\mathrm{nK}$ [45]. Both, the low B_{c} and the low T_{N} reflect the comparatively small nuclear magnetic moment compared to ferromagnetism in electronic systems. Viertiö and Oja [44] explain the experimental discoveries with a highly anisotropic interaction among the nuclear spins.

Since the nuclear moments are or can be rather well isolated from the lattice it is possible to create a population inversion of the ZEEMAN levels which gives rise to the concept of negative spin temperatures. Indeed it is possible to observe nuclear ordering at negative spin temperatures. The orders of silver are even different, depending if you are at positive or negative temperature. At $T_{\mathrm{N}} = 0.56\,\mathrm{nK}$ silver orders anti-ferromagnetically whilst it orders ferromagnetically at a CURIE temperature of $T_{\mathrm{C}} = -1.9\,\mathrm{nK}$. Nuclear order can also be found in insulators like CaF_2, LiF_2 or LiH. The latter for example exhibits an anti-ferromagnetic order for positive as well as negative temperatures [42].

2.3.3. Ferromagnetic Phase Transition in GaAs

Simon, Braunecker and Loss predict a nuclear magnetic phase transition [7, 8] for nuclei within a 2DEG. On the one hand the phase transition shows interesting physics itself. Unlike the nuclear phase transitions mentioned above, the transition temperature would be tunable. Besides the fundamental physics, the phase transition can suppress the nuclear field fluctuations that cause electron spin decoherence in GaAs. Therefore it could be a step forward in quantum computation with electron spins in GaAs.

Fröhlich and Nabarro showed that the nuclear CURIE temperature of a bulk 3D metal is in the range $\mu\mathrm{K}$ or below [46]. Applying the same method to a typical 2DEG in GaAs yields a surprisingly high CURIE temperature of $1\,\mathrm{mK}$ [7]. The theoretical methods employed are questionable for two reasons [8]. On the one hand, it does not take into account dimensionality effects and on the other hand, electron-electron interactions are disregarded. In [7], Simon and Loss derive a CURIE temperature of the order $1\,\mu\mathrm{K}$ with a simple mean-field theory for GaAs.

However, electron-electron interaction in a 2DEG elevates the CURIE temperature. Like in metals, the nuclear spins interact with the electron spins through hyperfine interaction. The electrons themselves are subject to a long-range RKKY (Rudermann-Kittel-Kasuya-Yosida) interaction. Thus, the electrons mediate an interaction between nuclear spins resulting in a stronger coupling between the nuclei which manifests in a higher CURIE temperature. The interactions between the electrons can be tuned with a gate electrode. Hence, the strength of the interaction

and so the CURIE temperature can be adjusted.

The theoretical derivation starts with a Kondo lattice Hamiltonian which reads [8]

$$\mathcal{H} = \mathcal{H}_0 + \frac{1}{2} \sum_{j=1}^{N} A_j c_{j\alpha}^{\dagger} \vec{\sigma}_{\alpha\beta} c_{j\beta} \cdot \vec{I}_j + \sum_{i,j} v_{ij}^{\alpha\beta} I_i^{\alpha} I_j^{\beta} \qquad (2.37)$$

$$= \mathcal{H}_0 + \mathcal{H}_{\mathrm{HF}} + \mathcal{H}_{\mathrm{dd}} \qquad (2.38)$$

$\mathcal{H}_0$ denotes the regular conduction electron Hamiltonian. $\mathcal{H}_{\mathrm{dd}}$ is the regular dipole-dipole interaction between nuclear spins. This interaction ($E_{\mathrm{dd}} \,\widehat{=}\, 100\,\mathrm{nK}$) is the weakest involved and is therefore neglected. $\mathcal{H}_{\mathrm{HF}}$ is the hyperfine interaction between nuclear and electronic spin. A_j is the hyperfine coupling constant and $\vec{I}_j$ the nuclear spin at site $\vec{r}_j$. $c_{j\alpha}^{\dagger}$ creates an electron at site $\vec{r}_j$ with spin α and N denotes the number of lattice sites. Assuming, time reversal symmetry of $\mathcal{H}_0$, translational and rotational invariance as well as spin isotropy, they calculate an effective Hamiltonian

$$\mathcal{H}_{\mathrm{eff}} = -\frac{1}{2} \sum_{\vec{r},\vec{r}'} J_{\vec{r}-\vec{r}'}^{\alpha\beta} I_{\vec{r}}^{\alpha} I_{\vec{r}'}^{\beta} \qquad (2.39)$$

with interaction strength

$$J_{|\vec{r}|}^{\alpha\beta} = -\left(\frac{A^2}{4n_{\mathrm{S}}}\right) \chi_{\alpha\beta}\left(|\vec{r}|\right) \qquad (2.40)$$

The hyperfine constant is assumed to be $A_j = A$, n_{S} denotes the nuclear spin density and χ denotes the electronic spin susceptibility. The latter quantity is the key parameter that can be changed to control the nuclear magnetism. Further theoretical analysis yields finally the CURIE temperature

$$T_{\mathrm{C}} = \frac{IA}{2k_{\mathrm{B}}} \sqrt{\frac{3I}{\pi}} \frac{A}{\Pi} \qquad (2.41)$$

Π can be regarded as screened potential due to interaction effects. It can be tuned by the interaction parameter r_{S}, hence the electron density can be used to tune T_{C}. The estimates for the CURIE temperature deviate. On the one hand, it is estimated that the phase transition occurs in the millikelvin regime, $0.4\,\mathrm{mK}$ for $r_{\mathrm{S}} \sim 5$ and $1\,\mathrm{mK}$ for $r_{\mathrm{S}} \sim 8$ [8]. On the other hand, it is $25\,\mathrm{mK}$ for $r_{\mathrm{S}} \sim 5$ [7]. However, Π depends exponentially on r_{S}.

The ordering occurs on two length scales. On a length of the lattice spacing, the nuclei order parallel, i.e. ferromagnetically. But on a length scale of the FERMI wavelength the magnetisation rotates yielding a helical order.

However, these temperatures are on the verge of what powerful dilution refrigerators can achieve nowadays. It is thus more likely to discover the phase transition using the new cooling scheme presented in this work.

2.3.4. Detecting the Ferromagnetic Phase Transition

Assume that the phase transition exists and that we can cool the 2DEG below the nuclear CURIE temperature. The question that consequently shows up is: How do we detect it?

The probability density of electrons in GaAs at the sites of the nuclei is finite. Therefore, one can use the Overhauser field to detect the phase transition. Thus, a simple nanostructure that could serve as sensor is a QPC. The steps of the conductance as function of the gate voltage should separate due to the ZEEMAN splitting, such as it is shown schematically in figure 2.3 b) by the dashed line. However, two issues have to be considered upon using a QPC as a detector.

On the one hand, the 2DEG is partially depleted to form the QPC. In the depleted area there are no electrons that mediate the interaction and hence, the phase transition is inhibited. Furthermore, the QPC forms a 1D constriction that can be comparable to the FERMI wavelength. There are two questions that remain to be answered. First, does the lack of mediating electrons give rise to a, possibly negative, back-action on the phase transition. Second, does it influence the helical order if the QPC width is comparable to the FERMI wavelength.

On the other hand, the electron density within the QPC is reduced with respect to the density in the 2DEG further away from the QPC. This would actually increase the CURIE temperature locally, i.e. the phase transition would be facilitated.

Note, that the quantum HALL effect is unsuitable because it relies on the coupling of the electrons' momenta to a magnetic field but the Overhauser field couples to the electron spin only.

Another method would be to employ a superconducting quantum interference device (SQUID) fabricated on top of the heterostructure as a detector. We start with an estimate of the magnitude of the magnetic field of the nuclei assuming an average nuclear moment of $\mu \approx 2.4\mu_\mathrm{n}$ for GaAs [47] where the nuclei are weighted according to their occurrence in GaAs. The field in the direction of the dipole is given by $B_\mathrm{d} = \mu/2\pi r^3$ with r being the distance on-axis. We obtain a field $\sim 2 \cdot 10^{-12}\,\mathrm{T}$ for one nucleus at a distance of $100\,\mathrm{nm}$ which corresponds to a typical 2DEG depth. The actual field is the sum over all nuclei corrected with an appropriate angle. Since the ordering is helical on a scale of λ_F, the field at distance r far away, $r \gg \lambda_\mathrm{F}$ is zero because the field of each nucleus is cancelled by the field of a nucleus at a distance $\lambda_\mathrm{F}/2$ which is about $130\,\mathrm{nm}$ in GaAs for $r_\mathrm{S} = 5$. However, if we take that number we have about 10^5 nuclei within a square of $(\lambda_\mathrm{F}/2)^2$ and hence a field of $\sim 2 \cdot 10^{-7}\,\mathrm{T}$ which should be detectable with a SQUID [48]. The FERMI wavelength, however, sets a limit for the size of the SQUID. If the SQUID is too large the net field would be zero due to the the helicity of the magnetic dipoles.

Low-Temperature Physics

This chapter gives an introduction to techniques, methods and materials at cryogenic temperature. It goes far beyond the scope of this thesis to deal with all aspects of (ultra) low temperature physics. Nevertheless, the physics which is relevant for this work will be discussed. One can find all that in more or less detail in common literature on the topic like [49–52]. A summary concentrating on rather technological aspects is given by [53], [54] does the same, but above 1 K. Besides these text books, reviews on adiabatic demagnetisation were written by G.R.Pickett [55, 56] and on cooling below 300 mK by G. Frossati [57].

3.1. Heat Transport

Someone who wants to design a low temperature apparatus has to consider the flow of heat e.g. the distribution of temperatures within the whole set-up. There are three mechanism of heat flow: convection, conduction and radiation.

In the temperature range below $\sim 1\,\mathrm{K}$ convection is negligible over the other two mechanism for two reasons. On the one hand, spaces are pumped down to maintain an isolation vacuum and on the other hand, all gases, except helium, are solid. Hence, in summary there is no significant amount of gas to circulate. However, it is important when designing a liquid helium dewar that often includes a superconducting magnet. In that case, the evaporated helium cools the the magnet leads and structural parts of the magnet.

3.1.1. Radiative Heat Transport

The radiative heat emitted by a black body at temperature T is given by the
STEFAN-BOLTZMANN law, $\dot{Q}_{\mathrm{SB}} = \sigma T^4$ where $\sigma = 5.67 \cdot 10^{-8}\,\mathrm{W/m^2 K^4}$ is the
STEFAN-BOLTZMANN constant. The spectral distribution of blackbody radiation
is given in figure 4.5 (in terms of frequency). Unlike a black body, a real surface
does not absorb all radiation. It has an emissivity ϵ and a reflectivity r such that

$$r + \epsilon = 1 \tag{3.1}$$

Therefore, the net heat flow between two surfaces is given by [51]

$$\dot{Q} = \sigma F(\epsilon_1, \epsilon_2) \left(T_1^4 - T_2^4 \right) \tag{3.2}$$

where $T_{1,2}$ are the temperatures of the two bodies. F denotes a factor which takes
account for the emissivities of the bodies as well as the geometries.

A reduction of this heat flow can be achieved in different ways. Due to the power
of four in the temperature dependence, it is common to divide the space between
the two bodies with intermediate shields on different temperature stages. In order
to reduce F the reflectivity of the low temperature part has to be increased and
the emissivity of the high temperature part needs to minimised. Due to (3.1)
highly polished metals are perfect candidates to achieve that [51]. Since oxidation
decreases the reflectivity, it is advisable to gold-plate the metal to avoid oxidation.
From the DRUDE model one can derive a wavelength-dependent emissivity [54]

$$\epsilon \sim \sqrt{\frac{\rho}{\lambda}} \tag{3.3}$$

where ρ is the electrical resistance of the material and λ the wavelength of the
radiation. According to (3.1) this means that the reflectivity goes up at lower
temperature for two reasons. First, the resistance for metals goes down at low
temperatures. Second, the maximum of the power distribution is shifted to larger
wavelengths according to WIEN's law

$$\lambda T = 2900 \mu\mathrm{m\,K} \tag{3.4}$$

which is the product of the black body's temperature T and the wavelength for
which the power emission is maximal (see figure 4.5).

3.1.2. Thermal Conduction

Conduction in Gases

The heat conduction in a gas depends on temperature and pressure. It is divided in two regimes: the diffusive regime where the mean free path $\bar{\ell}$ of a gas atom is smaller than the dimension d of the vessel, $(\bar{\ell} \ll d)$, and the free molecule regime, where $(\bar{\ell} \gg d)$ [51, 54]. In the the diffusive regime the conduction is $\kappa \sim n\bar{\ell}\bar{v}_{\text{th}}$, where $\bar{v}_{\text{th}}$ is the mean thermal velocity and n the density of the gas. As a consequence κ is independent of pressure P because $\bar{\ell} \sim 1/P$ and the density of atoms is $n \sim P$, so these two dependencies cancel each other. On the other hand, there is a dependence on temperature through the mean thermal velocity $\bar{v}_{\text{th}}$. In the free molecule regime, the conductance becomes independent of temperature but follows pressure linearly, such that $\kappa = \kappa_0 P$. The constant κ_0 contains mainly gas properties.

In low temperature physics one takes advantage of this by using gases as heat switches. Typically a dilution refrigerator is cooled to $4\,\text{K}$ by a gas in the inner vacuum chamber. Once the temperature is reached, the gas is removed again. For this procedure one typically uses helium whereas ^4He is cheaper than ^3He but more difficult to remove due to its lower vapour pressure and more absorption on surfaces at $4\,\text{K}$.

Conduction in Solids

The thermal conductivity of a solid is given by

$$\dot{Q} = \kappa(T)A\frac{\mathrm{d}T}{\mathrm{d}x} \tag{3.5}$$

Here $\dot{Q}$ is the heat flow, A the cross-section of the solid and $\mathrm{d}T/\mathrm{d}x$ the temperature gradient across it. For a qualitative description we re-write (3.5) and integrate on either side

$$\int_0^L \dot{Q} \,\mathrm{d}x = \int_{T_1}^{T_2} A\kappa(T) \,\mathrm{d}T \tag{3.6}$$

On the left we have to integrate from 0 to L, which is the length of the sample, and on the right we integrate from $T = T_1$ at $x = 0$ to $T = T_2$ at $x = L$. Hence we get

$$\dot{Q} = \frac{A}{L}\int_{T_1}^{T_2} \kappa(T) \,\mathrm{d}T \tag{3.7}$$

This equations tells us that is not necessary to know the temperature distribution along the specimen. All information required is the temperature at the two ends,

the dimensions of the object and the thermal conductivity $\kappa(T)$. The microscopic mechanisms that contribute to κ will be discussed in section 3.2. In practice, results for (3.7) can be found in tables for various materials, certain geometries like rods or tubes and for typical hot and cold temperatures like $4\,\mathrm{K}$, $77\,\mathrm{K}$ or $300\,\mathrm{K}$ [54].

3.1.3. Boundary Resistance

A common problem in low temperature physics is thermal transport between a metal and liquid helium. Since there is no conduction electrons in helium, the heat transport across this interface is done by phonons. The very high resistance, as compared to bulk material, arises for two reasons. The acoustic mismatch theory explains it partially [58, 59]. This boundary resistance arises in general at the interface of two materials with different indices of refraction.

On the one hand the soundwave travelling across the interface is refracted according to Snell's law

$$\frac{\sin \alpha_{\mathrm{He}}}{\sin \alpha_{\mathrm{M}}} = \frac{c_{\mathrm{He}}}{c_{\mathrm{M}}} \tag{3.8}$$

The parameters can be taken from the right hand side picture. That means that a phonon that wants to propagate from helium into the metal can be totally reflected. Consequently there is a critical angle α_{crit} of about $3°$ and any wave that impinges at a larger angle is totally reflected. The cone spanned by this angle accounts for about 0.2% of the solid angle of 2π in the helium. Upon that the two different sound velocities give rise to low transmission propability, $t \approx 0.3\%$. In the end the fraction of the phonons that can be transmitted from helium into the metal is $< 10^{-5}$, the other way it is $\sim 10^{-3}$. The resistance according to this theory is then

$$R_{\mathrm{K}} = \frac{C}{AT^3} \tag{3.9}$$

C is constant expressing the sound velocities and densities of the two materials. This so-called Kapitza resistance increases strongly for decreasing temperature T but decreases with larger contact area A. More details on that theory can be found in [58], it matches experimental data well between $0.02\,\mathrm{K}$ and $0.2\,\mathrm{K}$ [49]. Anyway, the only way to overcome this problem is to make A as large as possible. This is usually achieved with porous media such as sintered metal powders.
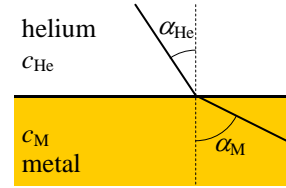
3.2. Solids at Cryogenic Temperatures

Material-specific properties become more and more significant as the temperature is reduced, properties which are veiled by thermal excitations at higher temperatures. I will now discuss some important properties of solids at cryogenic temperatures.

3.2.1. Phase Transitions

One has to be aware of phase transitions if settling for a certain material of a low temperature apparatus. In the construction of cryogenic equipment two phase transitions are of utmost importance: superconductivity and ferromagnetism. Their impact shall briefly be discussed.

Superconductivity

Some materials enter a new state which has some surprising attributes. First of all, the electrical resistance vanishes. This implies also that current can flow without dissipating heat. Superconducting magnets can therefore achieve much higher fields than resistive electromagnets. Second, a superconductor is a perfect diamagnet. It expels magnetic fields from its inside which can be used for magnetic screening of a certain volume.

Superconductors are characterised by mainly three parameters. The critical temperature is the temperature below which the material is superconducting and above which it is in its normal state. Superconductivity can be found in pure metals such as aluminium, in alloys such as NbTi or even in ceramics such as yttrium barium copper oxide (YBCO). The second critical parameter is the magnetic field. If it exceeds a certain value superconductivity breaks down. Superconductors are divided in two types with respect to the critical field. Type I superconductors are described by one critical field whereas type II superconductors are described by two, B_{c1} and B_{c2}. Below B_{c1} the material is an ideal diamagnet. In between B_{c1} and B_{c2} magnetic field lines can penetrate the material and the specimen is in a complicated state mixed between superconducting and normal. Eventually, above B_{c2}, superconductivity is completely destroyed. The third critical parameter is the current density. If it is too large superconductivity disappears as well. The three parameters are given considering the other two to be zero. In a good approximation, the phase separation line in the $T - B$ plane can be described as a parabola, i.e. at finite field the critical temperature is decreased and vice versa.

A problem about superconductors is their low thermal conduction. Electrons condense into a new state in which they contribute less to the heat transport the colder the superconductor is. As far as I know all soft solders turn superconducting

in the kelvin regime [54], hence a solder joint might be inappropriate although easy to make. On the other hand this fact opens the possibility to fabricate heat switches since the material can be driven from normal to superconducting by controlling the applied field. This is the underlying idea of the heat switches in section 6.3.

Ferromagnetism

The transition temperature at which a material turns ferromagnetic is called the Curie temperature. In some materials it is well above room temperature such as in iron ($T_\mathrm{C} = 1033\,\mathrm{K}$) [60]. But some materials show it at low temperatures like dysprosium at $88\,\mathrm{K}$ [60]. Attention has to be paid in the case of steels. Due to their mechanical strength they are very popular for various construction tasks. But they can turn ferromagnetic at low temperatures. Machining and welding can introduce such a ferromagnetic behaviour [54]. A good steel in that sense is for instance 316LN. Ferromagnetica can lead to hysteresis effects and enormously strong forces in the structural parts that can even destroy a set-up.

3.2.2. Heat Capacity

The heat capacity is a measure for the amount of energy required to heat a body from a lower to a higher temperature. Microscopically the amount of heat that a body can store depends on the available excitations. Hence, the heat capacity reflects the quantum mechanics of the specimen. The specific heat depends on the subsystem under consideration and the total specific heat is the sum of single contributions. Figure 3.1 shows the specific heat of the electrons and phonons in copper. Moreover, it plots the specific heat of copper nuclei for a magnetic field of $800\,\mathrm{mT}$.

Phonons

At room temperature the contribution of the lattice vibrations is constant. According to the Dulong-Petit law it is three times the universal gas constant. At low temperature, when the equipartition theorem no longer holds, the Debye model describes the specific heat much more accurate. From a periodicity argument, which goes along the same line that lead to the electron DOS (2.8), on a cube of volume V and with a linear dispersion $\omega = ck$ the phonon density of states is given by [60]

$$\mathcal{D}_\mathrm{ph} = \frac{V}{2\pi^2 c^3}\omega^2 \qquad (3.10)$$

The thermal energy is then the integral over the product of $\mathcal{D}_\mathrm{ph}$, the occupation probability which is in this case given by Bose-Einstein statistics and the energy
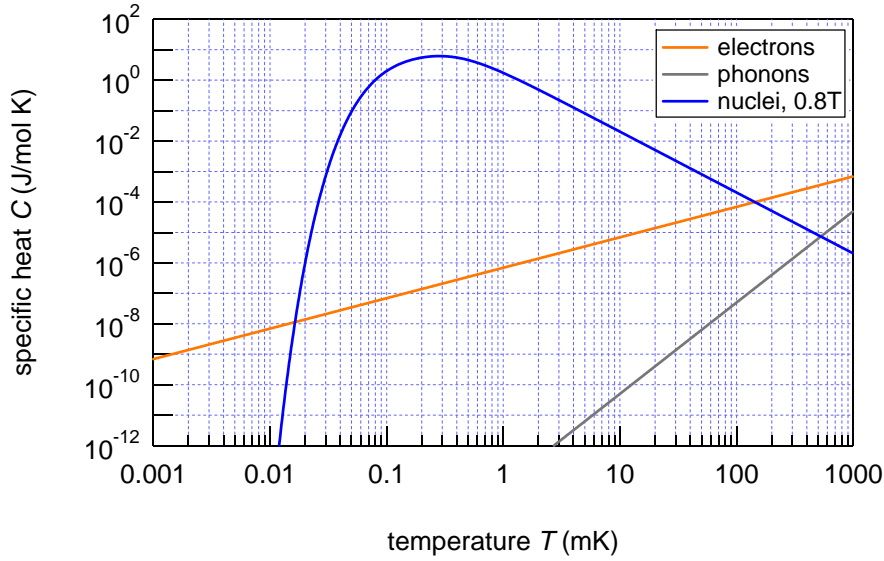
Figure 3.1.: Specific heat of electrons, phonons and nuclei at 800mT in copper

of a single phonon $\hbar\omega$. The integral has to be calculated from zero to the so-called DEBYE frequency ω_{D}. Simply speaking ω_{D} is given by the fact that it is unreasonable to allow wavelengths shorter than twice the lattice spacing. The DEBYE frequency is associated to the DEBYE temperature Θ_{D}. It is a material constant which expresses the mass of the atoms and the binding energy. It ranges from 2000 K for rather light, strongly bound atoms, as for instance in diamond, to 95 K for heavy, weakly bound atoms as in lead. However, within the scope of this thesis we are interested in low temperatures where $T \ll \Theta_{\mathrm{D}}$. Hence, the specific heat of the phonons is given by [49]

$$C_{\mathrm{ph}} = 1944 \frac{\mathrm{J}}{\mathrm{mol\ K}} \left(\frac{T}{\Theta_{\mathrm{D}}} \right)^3 \qquad (3.11)$$

This law hold very well for solid argon [49]. Possible deviations can be taken into account by making the DEBYE temperature a function of temperature.

Electrons

In metals conduction electrons form another system that can be excited. The same considerations about the FERMI distribution and the density of states as in section 2.1.2 apply here. In metals electrons occupy states up to a FERMI energy of typically $\sim 1\,\mathrm{eV}$ [60, 61] which corresponds to a temperature of about $T_{\mathrm{f}} = 10^4\,\mathrm{K}$. Thus, even at room temperature it is $T \ll T_{\mathrm{f}}$ and the FERMI-DIRAC

distribution can be approximated linearly in an interval of $k_\mathrm{B}T$ around E_F. In order to warm the system from T_1 to T_2 an energy $\Delta E \sim T^2$ has to be introduced. A detailed calculation, taking into account the density of states and the Fermi-Dirac distribution yields for free electrons [61]

$$C_\mathrm{e} = \frac{\pi^2 n_\mathrm{e} k_\mathrm{B}^2}{2E_\mathrm{F}} T = \gamma T \tag{3.12}$$

Here, n_e is the electron density, hence γ is a material constant, the Sommerfeld coefficient. The theoretical value given for γ can be altered by electron-phonon interaction or electron-electron interaction which is reflected by the effective mass approach [49].

Superconductors

In a superconductor electrons condense into a new state they form cooper pairs. The number of electrons decays exponentially with temperature due to the superconducting gap. This implies that they are no longer available as a thermally excitable system. Hence, below the critical temperature the specific heat of the electrons decays with temperature T as[1]

$$C_\mathrm{e,sc} = 1.34\gamma T_\mathrm{c} \left(\frac{\Delta_0}{k_\mathrm{B}T}\right)^{3/2} \mathrm{e}^{-\frac{\Delta_0}{k_\mathrm{B}T}} \tag{3.13}$$

with γ the Sommerfeld coefficient, T_c the critical temperature and Δ_0 the superconducting energy gap. The specific heat of a superconductor exhibits an abrupt jump to a higher value which is proportional to $1.34\gamma T_\mathrm{c}$. Such a sudden change can in general indicate a phase transition.

As the temperature is lowered this specific heat diminishes and the phonon system becomes dominant.

Spins

If a magnetic field splits the Zeeman levels of a spin system we obtain excitable states i.e. a heat capacity. For a simple spin-$^1/_2$ system such as electrons the specific heat is given by [59]

$$C_{1/2} = R \left(\frac{\Delta E}{k_\mathrm{B}T}\right)^2 \frac{\mathrm{e}^{\frac{\Delta E}{k_\mathrm{B}T}}}{\left(1 + \mathrm{e}^{\frac{\Delta E}{k_\mathrm{B}T}}\right)^2} \tag{3.14}$$

---

[1]Literature gives different formulas for the specific heat of superconductors [49, 59, 61]. However, the formula here is based on a derivation by [61].

where R denotes the universal gas constant and ΔE is the level splitting i.e. the ZEEMAN energy. For larger spins (3.14) goes over to (3.36) with appropriate replacement of the spin quantities. Figure 3.2 shows the heat capacity for electron
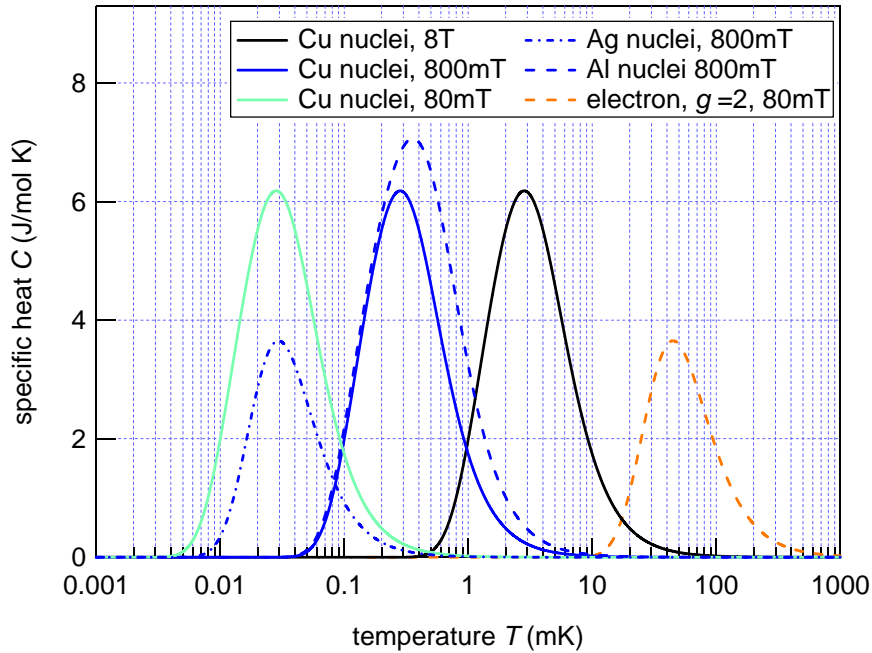
Figure 3.2.: Specific heat of spin systems. Nuclear spins of copper for $80\,\mathrm{mT}$, $800\,\mathrm{mT}$ and $8\,\mathrm{T}$, silver and aluminium for $8\,\mathrm{T}$ and localised electron spins with $g{=}2$ and $80\,\mathrm{mT}$.

spins and copper nuclei at $1\,\mathrm{T}$. In both cases a clear maximum can be seen. The fact that the specific heat exhibits a maximum in temperature is referred to as SCHOTTKY anomaly. Well below the maximum C goes as $\mathrm{e}^{\frac{\Delta E}{k_\mathrm{B} T}}$ whereas for $T \to \infty$ it goes as $1/T^2$. The maximum value of heat capacity is a function of spin but it is independent of magnetic field [49]! This can be understood considering entropy. A higher field implies a larger splitting but the disorder, i.e. the number of states or degrees of freedom is not increased. More ZEEMAN levels on the other hand provide more states, more degrees of freedom, hence a larger entropy and therefore a larger specific heat. The temperature for which the specific heat is maximal depends on spin as well as on magnetic field. It goes up as one of the two quantities is increased. The stored heat Q, however, goes up for larger fields and larger spins, because Q is the integral over C. Since the nuclear and electronic spin differ by roughly a factor of 1000 the corresponding maxima of the specific heat are in completely different temperature ranges.

Amorphous Solids

Last but least non-ideal solids have to be considered. Some materials lack a long-range order such as some glasses. The atoms can be in two sites. The energy required to 'hop' from one site to another is rather small which in return offers an additional mode of excitation and hence a contribution to the specific heat. It is given by [49]

$$C_{\mathrm{a}} = \alpha T^{\eta} \tag{3.15}$$

with a material-specific pre-factor α and an exponent η which is close to 1. In some non-crystalline solids the contribution of this heat reservoir can be significant. In addition to the fact that these materials show a small heat conduction, they can be a source of heat release in (ultra-)low temperature apparatus. Examples for various materials can be found in [49] and the references therein.

3.2.3. Thermal Expansion

In a first idealised approximation the ions that constitute the solid are assumed to rest in a fixed position. However, thermal expansion can't be explained within this model. The potential that an ion experiences in a lattice, looks qualitatively as depicted in figure 3.3. Often the so-called LENNARD-JONES potential is assumed.
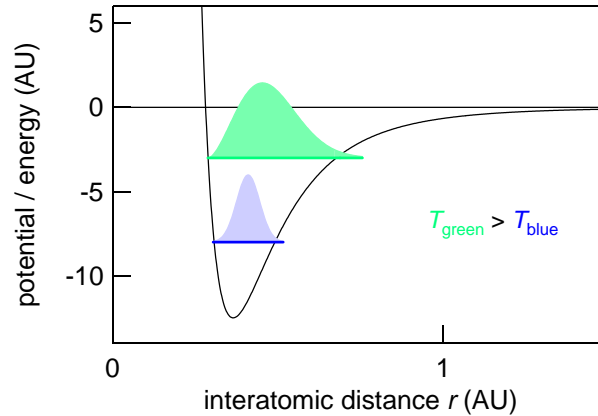
Figure 3.3.: Schematic description of the LENNARD-JONES potential of an ion within a lattice as a function of interatomic distance. The waves illustrate the probability density of the ions as function of inter-atomic distance for two different temperatures.

The attracting forces for larger distance r follow a $1/r^6$ law, whereas the repelling forces at $r \to 0$ are most often assumed to go as $1/r^{12}$ [60, 61]. Given this potential we can understand thermal expansion in a simple intuitive picture [49]. At low

temperatures the system is in a ground state, depicted in blue in figure 3.3. Higher temperatures allow for the system to be excited to a higher state, upper, green level in figure 3.3. As illustrated, the atom wave function spreads to higher interatomic distances due to the smaller potential at higher distances. This results in a higher expectation value to reside at a larger spacing which means that the solid eventually expands for higher temperatures. Within this model the change of the expectation value is larger for higher temperatures. For lower temperatures, the potential can be approximated by a parabola within which the expectation value does not change. Thus, thermal expansion is stronger at higher temperatures.

A general description can be found in [60, 61]. For the purposes within this work it is enough to simply characterise thermal contraction with the thermal expansion coefficient

$$\alpha = \frac{1}{\ell} \left(\frac{\partial \ell}{\partial T} \right)_P \tag{3.16}$$

It is the relative length change upon changing temperature while keeping the pressure P constant. Values for various materials are listed [49, 54]. In general, α is a function of temperature but below a few Kelvin it can be assumed to be constant. The length change from room temperature to that temperature range can be as small as $\lesssim 0.1\%$, for instance for Invar$^{\text{TM}}$ or tungsten, or as large as $\sim 2.1\%$ for Teflon$^{\text{TM}}$ [54].

The fact that different materials can contract very differently upon cooling has a strong impact on the design and the construction of a low temperature apparatus. Neglecting this can result in strong tension and stress at low temperature that in turn can cause cracks such as we encountered for the Araldite$^{\text{TM}}$ beam of the prototype or the sample holder in the second generation stage. To some extend the thermal contraction of a piece can be tuned by using a 'sandwich structure' of layers of different materials. Adding a strongly-contracting material increases the contraction of the the whole sandwich, e.g. we used molybdenum washers to increase the pressure on a screw joint. The brass screw contracts more than the molybdenum and hence the pressure gets larger upon cooling down.

3.2.4. Thermal Conductivity

A crucial property of solids at low temperature is their capability to conduct heat. We now recall equation (3.5) in order to look at the thermal conductivity κ in more detail. In general heat can be carried by electrons and phonons and their contributions simply add up. In a very basic picture we regard the two systems as gases in the solids. Kinetic gas theory then gives [49]

$$\kappa = \frac{1}{3} \frac{C}{V_{\text{mol}}} v \bar{\ell} \tag{3.17}$$

This can be interpreted as follows: The factor $1/3$ is due to the fact that we are interested in transport in one dimension only. V_{mol} is the molar volume, hence C/V_{mol} represents the quantity which propagates, in this case heat. v is the velocity of the propagation which is the speed of sound for phonons and the FERMI velocity for electrons. Eventually, $\bar{\ell}$ is the mean free path, i.e. the average distance the carrier can travel without scattering. In order to examine the temperature dependence of κ we have investigate each factor. The velocities can be assumed to be independent of temperature at low temperatures. The heat capacity was discussed in section 3.2.2. The mean free path is by far more complicated. Both, electrons and phonon can scatter at other phonons or electrons as well as with defects and impurities. Since the number of phonons goes down with temperature all scattering processes involving phonons get more unlikely at lower temperatures. The thermal resistance introduced by impurities and defects depends on the temperature range of consideration. At temperatures of interest, i.e. below $1\,\mathrm{K}$, this type of scattering is independent of temperature. A more precise treatment is given in [49] and references therein.

Phonons

At low enough temperatures, here $T \ll \Theta_D$, we plug (3.11) into (3.17) and get

$$\kappa_{\mathrm{ph}} = \frac{1}{3} \frac{\beta}{V_{\mathrm{mol}}} v_{\mathrm{snd}} \bar{\ell} T^3 =: \kappa_\beta T^3 \tag{3.18}$$

(3.7) becomes

$$\dot{Q} = \frac{A\kappa_\beta}{4L} \left(T_2^4 - T_1^4 \right) \tag{3.19}$$

with appropriate constant κ_β.

Electrons

For electrons ($T \ll T_{\mathrm{f}}$) we plug (3.12) into (3.17) and get respectively

$$\kappa_{\mathrm{e}} = \frac{1}{3} \frac{\gamma}{V_{\mathrm{mol}}} v_{\mathrm{F}} \bar{\ell} T =: \kappa_\gamma T \tag{3.20}$$

and (3.7) becomes respectively

$$\dot{Q} = \frac{A\kappa_\gamma}{2L} \left(T_2^2 - T_1^2 \right) \tag{3.21}$$

with appropriate constant κ_γ.

Superconductors

In the case of superconductors the situation depends on the state. In the normal state, electrons conduct according to (3.20) or (3.21) if it is a metal. Below the critical temperature the electrons condense into cooper pairs that do not carry entropy. That means that the number of available heat carriers diminishes with temperature which is expressed by the exponential term in (3.13). On the other hand it is reasonable to assume that the thermal conductivity is proportional to the remaining unpaired electrons and the corresponding specific heat respectively, hence [49]

$$\kappa_{\mathrm{e,sc}} = \kappa_\Delta T \mathrm{e}^{-\frac{\Delta_0}{k_\mathrm{B} T}} \tag{3.22}$$

If one simply plugs (3.13) into (3.17) the polynomial term changes its exponent. Other approaches simply apply an empirical equation [62]

$$\kappa_{\mathrm{e,sc}} = \kappa_{\Delta,T_c} \mathrm{e}^{\alpha\left(1-\frac{T_c}{T}\right)} \tag{3.23}$$

κ_{Δ,T_c} is the thermal conductivity at the critical temperature and α is a material parameter that can be determined by fitting the equation to a dataset. As for the specific heat of superconductors, literature gives different expression for the electronic heat conductivity in the superconducting state and furthermore the corresponding integral (3.7) is rather cumbersome. Anyway, the dominating physical mechanism is in any case the superconducting gap and therefore the exponential term.

3.2.5. Electrical Conductivity

Electrical conductivity depends on the system under examination. I will focus on metals here. With similar thoughts that led to (3.17) we can state the electrical conductivity. We essentially have to replace the specific heat by the charge. However, we write the Drude conductivity

$$\sigma = en\frac{e\tau}{m} \tag{3.24}$$

e is the elementary charge and n the electron density. The parameter $e\tau/m$ is called mobility μ which is the ratio of the electron drift velocity over the applied electric field. m is the electron mass. In this simple model τ can be regarded as the only temperature dependent quantity. It stands for the average time between two scattering events. For metals there are two scattering mechanisms. At temperatures above $\sim 10\,\mathrm{K}$ electron-phonon scattering dominates. The conductivity follows a rough linear trend (Matthiesen's rule [54]). At lower temperatures the phonon contribution to scattering becomes negligible and what remains is determined by scattering on defects and impurities, a contribution which is independent of temperature.

Purity and RRR

Whereas the conductivity at room temperature depends mostly on the type of material rather than on the purity, the low temperature conductivity is clearly dominated by the purity. Measurements show that most metals exhibit a constant conductance below several Kelvin [54]. The conductance value depends on the purity and can be used as a measure of purity. A quantity which is typically used is the residual resistance ratio or RRR. It is defined as

$$RRR \equiv \frac{R_{\mathrm{RT}}}{R_{\mathrm{4K}}} = \frac{\rho_{\mathrm{RT}}}{\rho_{\mathrm{4K}}} \tag{3.25}$$

which is the ratio of the resistance at room temperature, R_{RT}, and that at $4\,\mathrm{K}$, R_{4K}. Geometric quantities are cancelled out, i.e. it is a material property only. The RRR is essentially determined by two parameters, first, by the concentration of contaminants and second, by the crystal quality. The latter gets worse with machining or even welding. It can be improved by annealing which cures defects. High purity materials achieve RRRs up to a few thousand.

Wiedemann-Franz Law

In practice, it is much easier to determine an electrical than a thermal conductance. Since in metals mostly electrons carry both, charge as well as heat, we calculate the ratio of the conductivities, (3.17) over (3.24). The result is

$$\frac{\kappa}{\sigma} = \frac{1}{3} \frac{C_{\mathrm{e}} v_{\mathrm{snd}} \bar{\ell}_{\mathrm{e}}}{e n \mu} \tag{3.26}$$

Everything said about the temperature dependence of the specific heat and the electrical conductivity applies and the expression can be complicated. But it simplifies for very low and high temperatures, i.e. $T \ll \Theta_{\mathrm{D}}$ or $T \gg \Theta_{\mathrm{D}}$ [49]. For very low temperatures σ is constant and C_{e} is proportional to T whereas in the high-temperature case the electrical conductivity is proportional to $1/T$ and the specific heat is independent of T. However, in both cases this leads to the Wiedemann-Franz law.

$$\frac{\kappa}{\sigma} = \mathcal{L}T \tag{3.27}$$

$\mathcal{L}$ is the Lorenz number. A detailed derivation gives $\mathcal{L} = (\pi k_{\mathrm{B}}/e\sqrt{3})^2 \approx 2.4 \cdot 10^{-8}\,\mathrm{W\Omega/K^2}$. Although this is a simple method to get information about the thermal conductivity, one has to pay attention. The law holds accurately for copper at low temperatures but other materials show deviations like aluminium or silver, the latter about a factor of 10 [49]! Data on different materials is given for instance in [63]. Furthermore, $\mathcal{L}$ can depend on magnetic fields [62]. Despite these discrepancies, the Wiedemann-Franz law, in particular in combination with the RRR, is commonly used in low temperature physics.

3.3. Dilution Refrigeration

Since its arrival in the 1960s the dilution refrigerator (DR) has become the workhorse in mesoscopic physics for essentially two reasons. On the one hand it can be operated in a continuous mode whereas other techniques such as demagnetisation of paramagnetic salts, POMERANCHUK cooling, or some ^{3}He cryostats are at least partially one-shot techniques. Furthermore, it can provide lower base temperatures than for example ^{3}He cryostats. I am now briefly discussing dilution refrigeration. A schematic of a DR set-up is shown in figure 3.4.

3.3.1. Helium Dewar

The DR itself is operated in a liquid helium bath inside a dewar (figure 3.4). The helium volume is thermally isolated from the environment by a vacuum (outer vacuum chamber, OVC). Furthermore, the walls of the vessel have to be built from materials with low thermal conductance. Many liquid helium (LHe) dewars, such as ours, are also equipped with a liquid nitrogen (LN$_2$) bath which surrounds the helium bath. On the one hand, the LHe volume is shielded against thermal radiation from the outer wall which is at room temperature, on the other hand, some of the heat that flows down the inner wall of the bath volume is absorbed by the liquid nitrogen. Nitrogen has two advantages over liquid helium. First, it is cheaper, second, it has a higher latent heat of evaporation [54] which gives longer refilling periods.

A further protection against thermal radiation are baffles in the bath volume. They are cooled to temperatures significantly below room temperetaure by cold helium vapour. According to the STEFAN-BOLTZMANN (equation 3.2) law the irradiated power is reduced.

The DR is put inside the liquid helium which serves three purposes. First, it is a bath at 4 K. Hence, the dilution unit is cooled to that temperature and the wall of the inner vacuum chamber (IVC) emits thermal radiation at the corresponding power. Second, the helium is a reservoir for the 1K pot of DR. The helium volume is larger above the 1K pot inlet to ensure that the reservoir holds for a sufficiently long time. Finally, such a set-up typically comprises a superconducting magnet and the helium cools the magnet below the superconducting transition temperature.

Such a helium dewar is is equipped with several flanges and ports. Helium gas is typically recovered for economic reasons, thus the dewar is hooked up to a recovery system. Furthermore, safety devices such as over pressure valves are mounted. If a magnet quenches, large amounts of helium are evaporated and the gas has to be able to leave the vessel.

3.3.2. Dilution Refrigerator

^{3}He/^{4}He Mixtures

The cooling source inside a DR is the phase separation boundary of a mixture of ^{3}He and ^{4}He . Figure 3.5 shows a phase diagram in the temperature T versus concentration x_3 plain, i.e. the concentration of ^{3}He is displayed on the x-axis. Above $2.2\,\mathrm{K}$ the two isotopes are mixable at any concentration and they are normal fluid. At that temperature and $x_3 = 0$ the liquid turns superfluid. The transition temperatures decreases with increasing x_3 down to $0.86\,\mathrm{K}$ or $x_3 \approx 2/3$. Below this temperature, the two liquids cannot be mixed at arbitrary concentrations, i.e. the blue area is not accessible. The following example illustrates the behaviour. We start with a certain concentration at point A and decrease temperature. In point B at the corresponding temperature the mixture turns superfluid. Cooling the system further, the mixture starts to separate into a ^{3}He rich (concentrated) and into a ^{3}He poor (dilute) phase (C, C'). At yet lower temperatures, the concentrated phase floats on top of the dilute phase (D and E). For $T \to 0$ the concentrated phase approaches $x_3 \to 100\%$. However, the dilute phase tends to a finite concentration, $x_3 = 6.6\%$! This finite concentration is of great importance for the dilution refrigerator to work. It shows that the binding energy of a ^{3}He atom in ^{4}He is higher than for a ^{3}He atom in ^{3}He [49].

The ^{3}He/^{4}He mixtures are often treated as Fermi liquids whereas the bosonic, superfluid ^{4}He is referred to as 'inert background' [49] or 'mechanical vacuum' [51], i.e. the properties are determined by the fermionic ^{3}He . Therefore, mixtures follow qualitatively the same laws as conduction electrons. But the striking difference is the Fermi energy E_F, or temperature T_F respectively. In the case of conduction electrons it is around $10^4\,\mathrm{K}$ but for ^{3}He atoms it is of the order $1\,\mathrm{K}$. This analogy holds for example for the specific heat C_3 of ^{3}He. It goes as $C_3 \propto T/T_\mathrm{f}$ if $T \ll T_\mathrm{F}$.

Mixing Chamber

In the mixing chamber (MC) of a DR a ^{3}He/^{4}He mixture is cooled such that the two liquids separate. As a helium-3 atom crosses the phase boundary it experience a change in enthalpy, i.e. cooling. The cooling power is determined by the properties of helium-3 and the ^{3}He/^{4}He mixture. The specific heat and hence the enthalpy is a function of temperature and in in the mixture also of concentration. But at low enough temperatures ($\lesssim 40\,\mathrm{mK}$) the specific heat is linear in a good approximation [49]. The cooling power in Watts is then given by [49]

$$\dot{Q} = \dot{n}_3 \left(95 T_\mathrm{MC}^2 - 11 T_\mathrm{HE}^2 \right) \tag{3.28}$$

where $\dot{n}_3$ is the flow oh helium-3 in [mol/s], T_MC is the temperature of the mixing chamber and T_HE the temperature of the liquid after leaving the heat exchangers
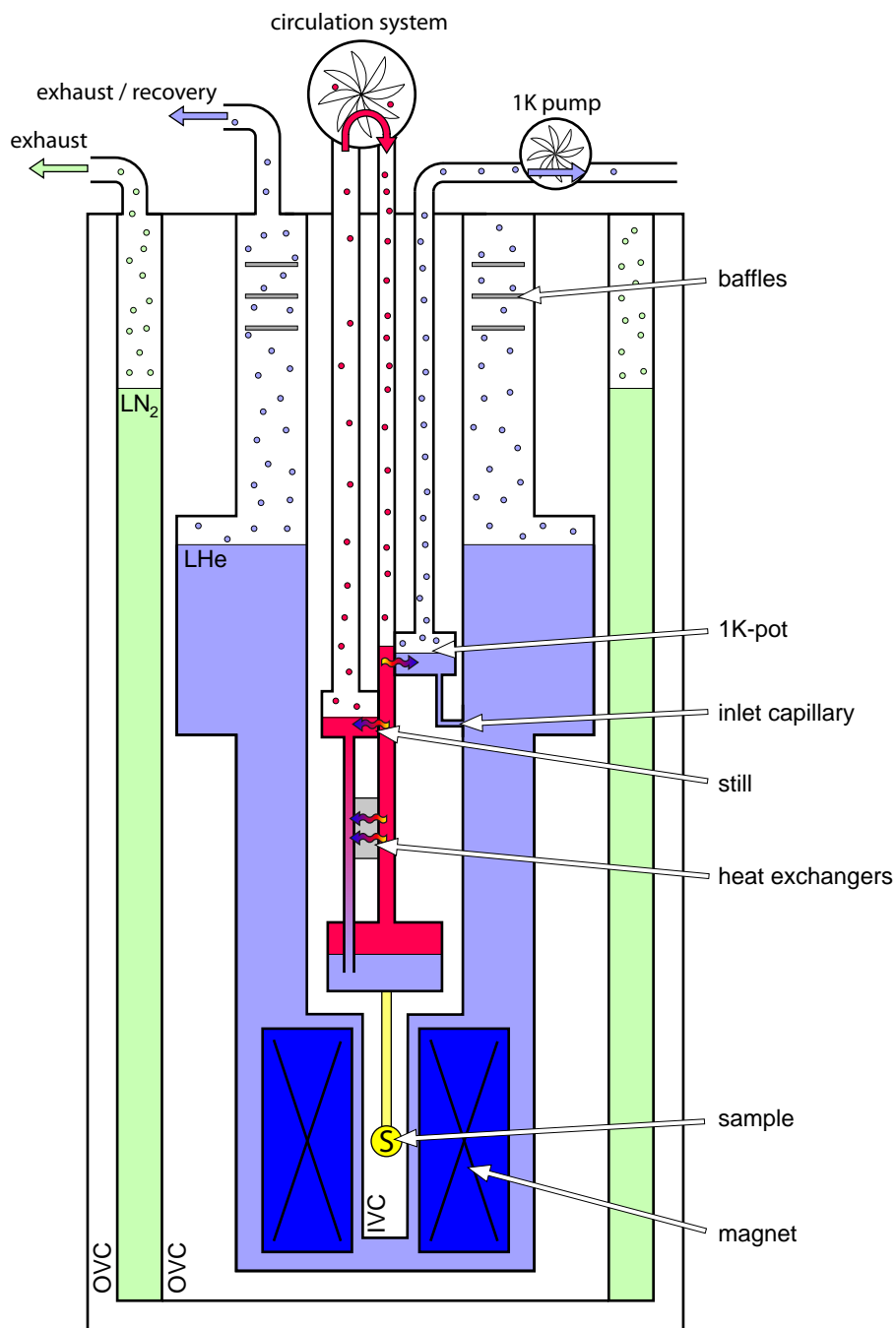
Figure 3.4.: Schematic of a dilution refrigerator and a helium dewar. See text for details.
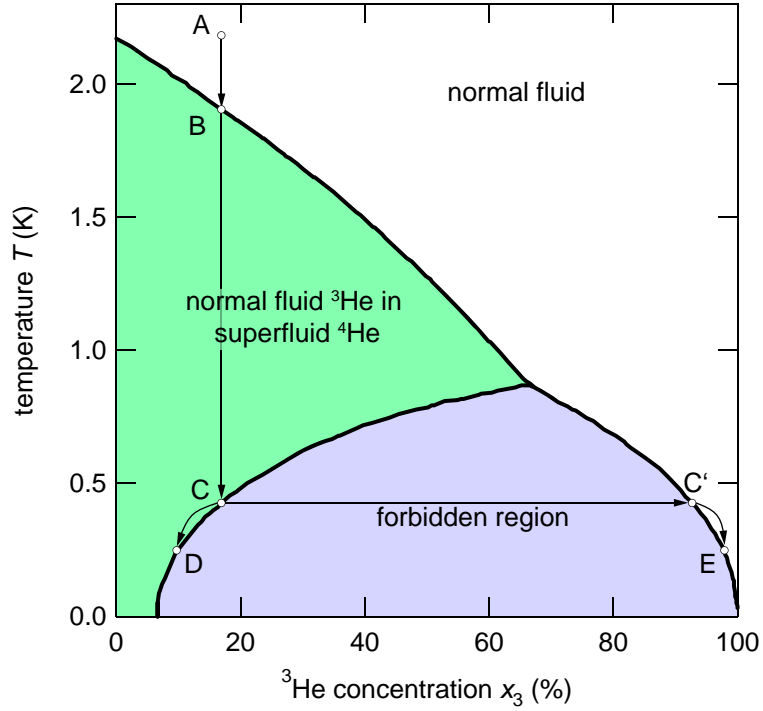
Figure 3.5.: Phase diagram for a ^{3}He/^{4}He mixture. (Adopted from [49])

(explained below), both in [K]. From this equation two limits can be calculated. First, any DR has a finite heat leak on the mixing chamber. If we assume perfect heat exchangers, $T_{\mathrm{MC}} = T_{\mathrm{He}}$, we can calculate a the lowest achievable temperature as a function of the heat load $\dot{Q}_{\mathrm{hl}}$

$$T_{\mathrm{MC,min}} = \sqrt{\frac{\dot{Q}_{\mathrm{hl}}}{84\dot{n}_3}} \tag{3.29}$$

Second, (3.28) shows the necessity of good heat exchangers. Assuming a very low heat leak ($\dot{Q} = 0$) equation (3.28) becomes

$$T_{\mathrm{MC}} \gtrsim \frac{1}{3} T_{\mathrm{HE}} \tag{3.30}$$

Thus, the temperature of the mixing chamber can only be a factor of three lower than that at the end of the last heat exchanger.

In order to transfer the cooling power to an experiment the mixture needs to be coupled to a good thermal conductor. Since only metals provide good thermal conduction at MC temperatures the heat flow has to overcome the boundary

resistance (equation (3.9)) between the metal and the liquid helium. This is accomplished by using metal powders which can be sintered directly on the wall of the MC if it is made of metal. The surface areas are of the order several 10 to several $100\,\mathrm{m^2}$ [49].

The sample (S) is typically mounted on a coldfinger which in turn is attached to and thermally anchored at the mixing chamber. The coldfinger serves two purposes. On the one hand, it is supposed to hold the sample in the centre of a magnetic field. On the other hand, the sample has to be cooled. Details of thermal anchoring are discussed in chapter 4.

Circulation

In order to maintain a permanent cooling ^{3}He needs to be circulated. Starting from the MC the cycle is as follows. The ^{3}He atom crosses the phase boundary, thereby cooling the mixture. Driven by a concentration gradient, the ^{3}He atom flows to the still. On its way it exchanges heat with the ^{3}He atoms that are on their way to the MC. This heat exchange, indicated by the yellow-red-blue arrows, is accomplished in heat exchangers. In order to overcome the thermal boundary resistance they contain sinters with large surface areas. In the still, the ^{3}He atom evaporates and so cools the remaining ^{3}He . The temperature in the still is limited by the vapour pressure of ^{3}He to typically around $700\,\mathrm{mK}$. The still also serves as precooling stage for the ^{3}He that returns to the MC. A circulation system, consisting of powerful pumps, tubes and pumping lines, pumps the ^{3}He back into the dilution unit.

On its way back, the ^{3}He cools and eventually condenses back to its liquid state. The cooling is achieved in two ways. On the one hand, the return line is equipped with flow impedances behind which the gas expands and thereby cools. On the other hand, the so-called 1K pot provides a temperature of $\gtrsim 1\,\mathrm{K}$. The temperature is maintained by evaporative cooling. ^{4}He flows from the bath into the 1K pot where it is evaporated and pumped away. The ^{4}He flows through a thin capillary to make sure that a temperature gradient between the bath at $4\,\mathrm{K}$ and the 1K pot can be established. The lowest achievable temperature of the 1K pot is limited by the vapour pressure of ^{4}He to $\gtrsim 1\,\mathrm{K}$.

Once the ^{3}He is re-condensed, it exchanges heat with the ^{3}He which is on its way from the MC to the still. As shown above, the efficiency of the heat exchangers is a crucial parameter in the performance of the whole DR. After passing the heat exchangers, the ^{3}He arrives back in the MC and the cycle starts over.

Lowest Achievable Temperature

Given the simple consideration which led to (3.28) it looks like it is easy to built arbitrarily strong DRs. One simply has to circulate enough helium-3 and needs to have good enough heat exchangers. Along with a higher flow rate the heat of condensation also increases. That means that the helium enters the heat exchangers at a higher temperature and due to the finite efficiency of heat exchange it will also leave the heat exchangers at a higher temperature. According to (3.29) and (3.30) the minimum achievable temperarture is limited.

Furthermore, there is technological limits set by the pumping conditions such as tube diameters and pumping power. The finite vapour pressure of ^{3}He in the still, and ^{4}He in the 1K pot respectively, constitute limits for the lowest achievable temperatures, too. The cooling power of the 1K pot can be increased by flowing more ^{4}He through the capillary but that has to be filled into the ^{4}He bath and so transfers have to be done more often.

Besides physical and technical limits, it is more expensive to run more powerful DRs. On the one hand, the consumption of LHe is higher, on the other hand, a larger amount of ^{3}He has to be circulated. This is very expensive, but also hard to obtain [64].

3.4. Adiabatic Demagnetisation

3.4.1. Magnetism and Spins

Magnetism is a phenomenon known for centuries maybe even millenniums. The fact that you get two bar magnets if you break one in two can be explained by so-called elementary magnets. These are so small that any macroscopic bar magnet still consists of a large number of them and the summed-up field generated by each of these little magnets creates the magnetic field of the bar magnet. This field can easily be visionalised by iron filings.

Nowadays magnetism is described in a more complex way. The magnetic behaviour of materials is divided in essentially three classes: diamagnetic, paramagnetic and ferromagnetic. The quantity describing the effects is called magnetic susceptibility χ. Diamagnetism has its origin in small orbital currents induced in a material by an external field. According to LENZ's law these currents themselves generate a field that is anti-parallel to the external field such that this gets reduced, hence $\chi < 1$. Superconductors are perfect diamagnets that repel a field completely from their inside. Paramagnetism ($\chi > 1$) on the other hand, arises if permanent magnetic moments in the material are present. They are given due to uncancelled micro-currents in atomic or molecular orbits or by the magnetic moments of the particles themselves. Under the influence of an external field they line up and

therefore enhance the field whereas without field they are randomly oriented by thermal fluctuations and so the vector sum is zero. In ferromagnets ($\chi \gg 1$) these permanent magnetic moments additionally couple strongly to each other such that the material can be magnetised even if there is no external field. Two other classes of materials, anti-ferromagnetic and ferri-magnetic, are neglected at this point.

The magnetic moment of a particle is closely related to another quantum mechanical property of the particle, the spin. A particle with a spin I has a magnetic moment $\mu = g_I \mu_\mathrm{n} I$. g_I is the dimensionless g-factor which depends on the specific particle. μ_n is the nuclear magneton for nuclei, and the BOHR magneton if the particle is an electron. In analogy to classical physics the spin is sometimes regarded as an angular momentum that describes a rotation of the particle about its own axis. If the particle is charged the magnetic moment is then a consequence of a circular current. The spin behaves in fact as an angular momentum but the picture of a rotating charged particle is incorrect. For instance, some neutral particles, such as neutrons, have a magnetic moment and a spin which cannot be explained in this classical picture.

3.4.2. Magnetic Cooling - Qualitative Picture

Classically, a magnetic moment aligns parallel to an applied magnetic field. The magnetic moments of a microscopic particle with spin I however, can take up to $2I + 1$ orientations with respect to an external magnetic field, hence the particle can be in $2I + 1$ possible states. The energy splitting of the states in a magnetic field B is given by

$$E_m = -m_I g_\mathrm{n} \mu_\mathrm{n} B \qquad m_I = (m_I = -I; -I+1; \cdots; I-1; I) \qquad (3.31)$$

m_I denotes the spin quantum number, g_n the nuclear g-factor and μ_n is the nuclear magneton. For electron spins these quantities have to be replaced by their electronic counterparts. In both cases, this energy is called ZEEMAN energy. At zero temperature, all spins occupy the lowest ZEEMAN level. At a finite temperature T thermal energy enables the spins to occupy higher levels. The resulting population distribution reflects temperature and is given by the BOLTZMANN factor

$$p = \mathrm{e}^{-\frac{E_m}{k_\mathrm{B} T}} \qquad (3.32)$$

where p states the probability to find a spin in state $E_m = m g_\mathrm{n} \mu_\mathrm{n} B$. Figure 3.6 illustrates the ZEEMAN levels for two sets of magnetic fields and temperatures for a $I = {}^3/_2$-system, e.g. copper. If the magnetic field is increased, the spins on the higher ZEEMAN levels gain energy. According to (3.32) this no longer reflects temperature, hence the system warms up. In order to return to the initial
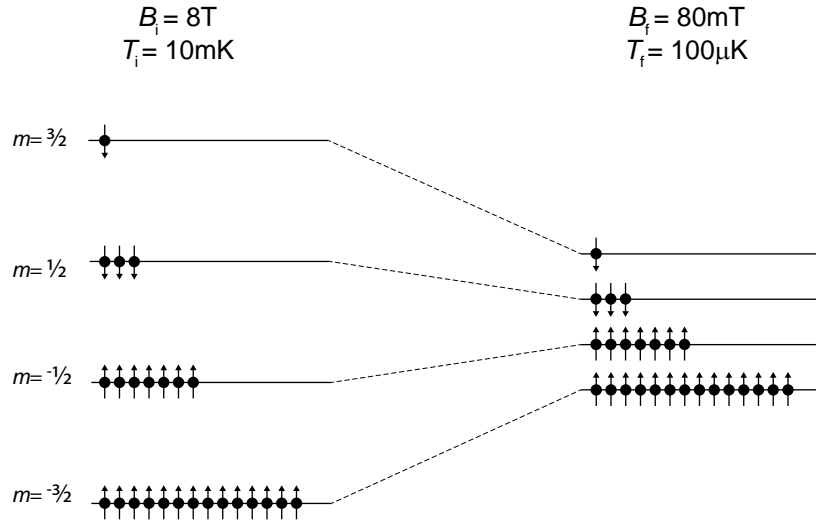
Figure 3.6.: Zeeman levels of a spin-3/2 nucleus. The left-hand side illustrates
the population prior to demagnetisation. During the adiabatic de-
magnetisation, the population is preserved. That corresponds to a
reduction of temperature.

temperature, this heat, the heat of magnetisation, has to be removed. The spins
then occupy preferably lower levels than before at lower field.

The cooling now works as follows. Assume the system is at an initial field, say
$B_i = 8\,\text{T}$, and an initial temperature, say $T_i = 10\,\text{mK}$, as shown in figure 3.6 this
corresponds to a certain population. The system is then thermally decoupled from
the environment and the field is reduced slowly, i.e. adiabatically, to a final field
T_f. Since this is done adiabatically, the population is preserved which means that
the Boltzmann factor p is constant. In turn, this implies that the temperature
has to go down by the same factor as the magnetic field. Hence,

$$T_f = \frac{B_f}{B_i}T_i \qquad (3.33)$$

In figure 3.6 this is shown for a final field of 80 mT. This corresponds to a reduction
by a factor of 100 and so the final temperature is $T_f = 100\,\mu\text{K}$.

The temperature which is reduced this way is the temperature of the nuclei.
The equilibration of both, nuclei and electrons among themselves, is faster than
the relaxation between the two systems at these low temperatures [51]. Hence,
the two system can be regarded as individual baths with individual temperatures.
After demagnetisation the nuclear spin bath is at a low temperature. It undergoes
mutual flip-flop processes with the electron spins, thereby the nuclei warm up and
the electrons are cooled.

3.4.3. Thermodynamic Basics of Paramagnets

A particle with spin I can occupy $2I+1$ possible states which leads to the following partition function:

$$Z = \left(\sum_{k=-I}^{I} \exp \frac{-m_I g_{\mathrm{n}} \mu_{\mathrm{n}} B}{k_{\mathrm{B}} T} \right)^{A_0} \tag{3.34}$$

where A_0 is the AVOGADRO number. This is the starting point to compute the required thermodynamic quantities entropy S, (nuclear) heat capacity C_{B} [49] and magnetisation M [13]

$$\frac{S}{R} = \frac{\beta}{2} \left[\coth\left(\frac{\beta}{2}\right) - (2I+1) \coth\left(\frac{\beta(2I+1)}{2}\right) \right] + \ln \left[\frac{\sinh\left(\frac{\beta(2I+1)}{2}\right)}{\sinh\left(\frac{\beta}{2}\right)} \right] \tag{3.35}$$

$$\frac{C_{\mathrm{B}}}{R} = \left(\frac{\beta}{2}\right)^2 \frac{1}{\left(\sinh\left(\frac{\beta}{2}\right)\right)^2} - \left(\frac{\beta(2I+1)}{2}\right)^2 \left(\frac{1}{\sinh\left(\frac{\beta(2I+1)}{2}\right)} \right)^2 \tag{3.36}$$

$$\frac{M}{M_{\mathrm{S}}} = \frac{2I+1}{2I} \coth\left(\frac{\beta(2I+1)}{2I}\right) - \frac{1}{2I} \coth\left(\frac{\beta}{2I}\right) \tag{3.37}$$

where the ratio of ZEEMAN and thermal energy was used: $\beta = \mu_{\mathrm{n}} g_{\mathrm{n}} \frac{B}{k_{\mathrm{B}} T}$. R denotes the universal gas constant and M_{S} the saturation magnetisation. At this point it should be emphasised that these properties are functions of the B/T ratio only once the material, e.g. I, is given. Figure 3.8 shows the entropy of copper nuclei as a function of temperature for different magnetic fields whereas figure 3.7 shows the polarisation $P = M/M_{\mathrm{S}}$. The functions $P_I(\beta)$ are called BRILLOUIN functions.

These rather cumbersome expressions can be simplified by the so-called high temperature approximation [49]. For $g_{\mathrm{n}} \mu_{\mathrm{n}} B \ll k_B T$ we can expand equations (3.35), (3.36) and (3.37), resulting in

$$S = R \ln(2I+1) - \frac{\Lambda_{\mathrm{n}} B^2}{2T_{\mathrm{n}}^2} \tag{3.38}$$

$$C_{\mathrm{n}} = \Lambda_{\mathrm{n}} \frac{B^2}{T_{\mathrm{n}}^2} \tag{3.39}$$

$$M_{\mathrm{n}} = \Lambda_{\mathrm{n}} \frac{B}{T_{\mathrm{n}}} \tag{3.40}$$

$\Lambda_{\mathrm{n}} = A_0 I(I+1) \mu_{\mathrm{n}}^2 g_{\mathrm{n}}^2 / 3k_{\mathrm{B}}$ is called the molar CURIE constant. From (3.40) it is easy to derive CURIE's law.

$$\chi_{\mathrm{n}} = \frac{\mu_0 \Lambda_{\mathrm{n}}}{T_{\mathrm{n}}} \tag{3.41}$$
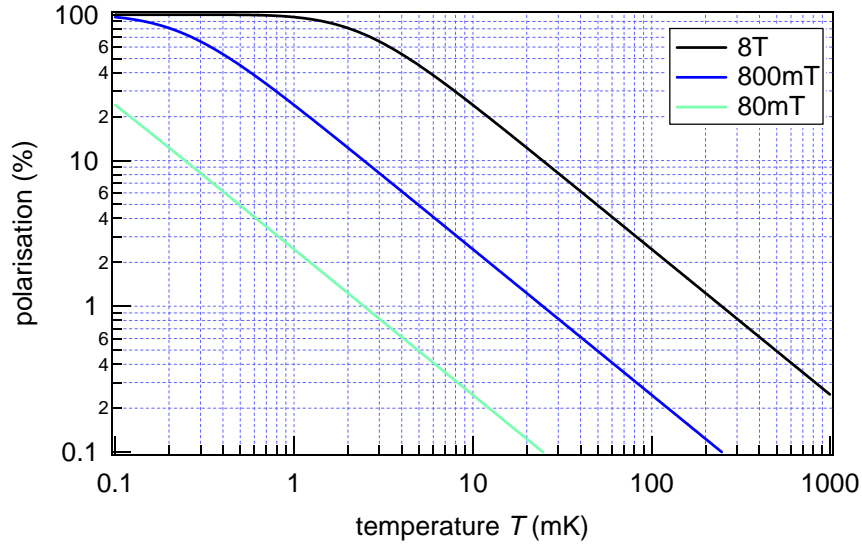
Figure 3.7.: Polarisation (equation (3.37)) of copper nuclei for $80\,\mathrm{mT}$, $800\,\mathrm{mT}$ and $8\,\mathrm{T}$ as function of temperature.

3.4.4. Magnetic Cooling - Quantitative Picture

In this section I am discussing the mechanism presented in section 3.4.2 in a more quantitative way. The thermodynamic processes during the cooling cycle are illustrated with arrows in figure 3.8. Along $\overline{\mathrm{AB}}$ the system is isothermally magnetised. The arising heat is given by [49]

$$Q = nT_{\mathrm{i}} \left[S(0, T_{\mathrm{i}}) - S(B_{\mathrm{i}}, T_{\mathrm{i}}) \right] \tag{3.42}$$

In the entropy diagram this corresponds to the rectangle which is defined between $\overline{\mathrm{AB}}$ and the entropy axes. From the high temperature approximation we get

$$Q\Big|_{T} = -\frac{n\Lambda_{\mathrm{n}}B_{\mathrm{i}}^{2}}{2\mu_{0}T_{\mathrm{i}}} \tag{3.43}$$

In practice, the nuclei are polarised at constant magnetic field and cools the system along the entropy curve from A' to B. This gives an additional heat that corresponds to the yellow-shaded area defined by $\overline{\mathrm{AB}}$, $\overline{\mathrm{A'A}}$ and the entropy curve between A' and B. It is calculated as [49]

$$Q\Big|_{B} = n \int_{\infty}^{T_{\mathrm{i}}} C_{n}\ \mathrm{d}T \tag{3.44}$$
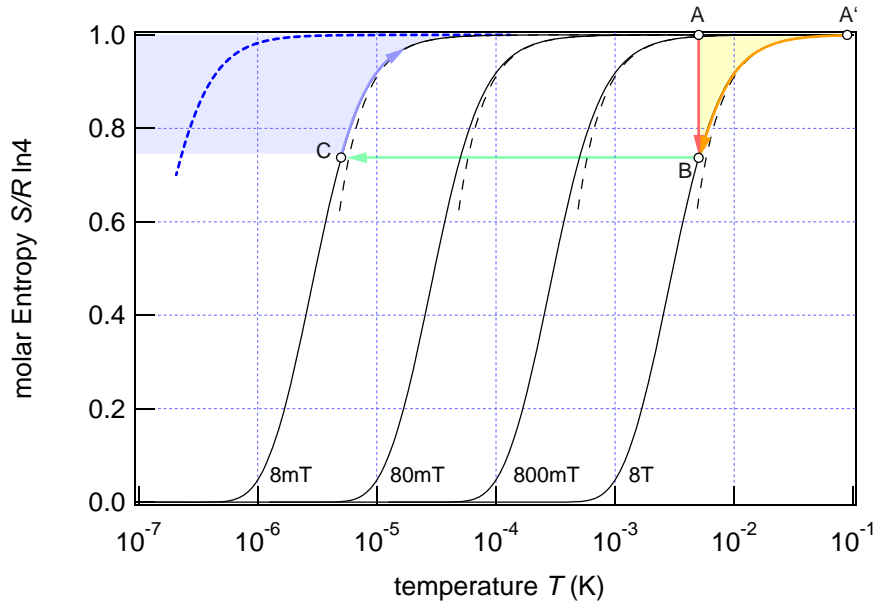
Figure 3.8.: Entropy of copper nuclear spins as a function of temperature for different magnetic fields (black solid lines). The dashed black lines are the corresponding hight temperature approximations (3.38). The dashed blue line is based on an internal field of $0.3\,\mathrm{mT}$ but zero applied field (equation 3.63).

Plugging in (3.39) we get

$$Q\Big|_B = -\frac{n\Lambda_{\mathrm{n}}B_{\mathrm{i}}^2}{\mu_0 T_{\mathrm{i}}} = 2Q\Big|_T \tag{3.45}$$

Although this is twice as much heat as in the isothermal case, it is advisable to cool along the entropy curve. The time required to arrive in B is faster because one can seize the higher cooling power of a dilution refrigerator which is approximately quadratic in temperature [49] (see also section 5.3.2).

The cooling is accomplished along $\overline{\mathrm{BC}}$ along which the entropy is constant. Since the entropy of the nuclei (3.35) is a function of B/T only we can deduce that the ratio has to be constant and we obtain (3.33).

Once the final field is reached, the system warms up along the entropy curve as indicated by the light blue arrow in figure 3.8. The heat that can be absorbed is given by the blue-shaded area in figure 3.8. In analogy to the heat of magnetisation, we can derive this heat in the high temperature approximation. We get [59]

$$Q = \int\limits_{T_{\mathrm{f}}}^{\infty} C_{\mathrm{n}}\,\mathrm{d}T = n\int\limits_{T_{\mathrm{f}}}^{\infty} T\left(\frac{\partial S}{\partial T}\right)_B\,\mathrm{d}T = n\Lambda_{\mathrm{n}}\frac{B_{\mathrm{f}}^2}{\mu_0 T_{\mathrm{f}}} = n\Lambda_{\mathrm{n}}B_{\mathrm{f}}\frac{B_{\mathrm{i}}}{T_{\mathrm{i}}} \tag{3.46}$$

For the last '=' we used (3.33). This result shows us that we need a compromise for the final demagnetisation field. According to (3.33) we get lower temperatures for lower final fields, on the other hand, according to (3.46), higher final demagnetisation fields give a higher cooling potential.

3.4.5. Thermal Performance

In a process where a paramagnetic salt is used as a refrigerant the electrons are cooled directly. Nuclear demagnetisation leads to a bath of cold nuclei. And if one is not interest directly in the properties of cold nuclei, and within this project we are interested in cold electrons, this bath has to cool the electrons. That means the heat has to be transferred from the electrons to to the nuclei.

The nuclei and the electrons exchange energy according to the Korringa law. For this discussion a short summary suffices. A more detailed derivation is given in [43]. The Korringa process explains the behaviour in metals and to some extend in semiconductors [43]. The electrons with a high probability to be located in the site of the nucleus, mainly s-electrons, interact with the nucleus.

The nucleus and the electron exchange energy through hyperfine interaction, they undergo a mutual spin flip. The electron needs an empty state within the range of the exchanged energy. The electrons involved lie within a range of $k_{\mathrm{B}}T_{\mathrm{e}}$ around the Fermi energy. Hence, the exchange rate of energy is proportional to T_{e} within this simple picture. The result is the Korringa law:

$$\tau_1 T_{\mathrm{e}} = \kappa \tag{3.47}$$

κ is called Korringa constant, it is characteristic for a certain metal. τ_1 is referred to as spin-lattice relaxation. Strictly speaking, it is the time that the nuclei need to come into equilibrium with the conduction electrons. But since electron-phonon coupling is strong the nuclei come into equilibrium with the lattice at nearly the same rate.

The temperature dynamics can be calculated by looking at the magnetisation of the nuclei. In this way the spin lattice relaxation is given by:

$$\frac{\mathrm{d}M_{\mathrm{n}}}{\mathrm{d}t} = -\frac{1}{\tau_1}\left(M_{\mathrm{n}} - M_{\mathrm{e}}\right) \tag{3.48}$$

M_{n} is the magnetisation of the nuclei and M_{e} is the magnetisation once the nuclei have reached equilibrium with the lattice. With the Curie law (3.41) and the fact that lattice and electron temperatures are equal due to strong coupling and small heat capacitances we can write:

$$\frac{\mathrm{d}}{\mathrm{d}t}\left(\frac{1}{T_{\mathrm{n}}}\right) = -\frac{1}{\tau_1}\left(\frac{1}{T_{\mathrm{n}}} - \frac{1}{T_{\mathrm{e}}}\right) \tag{3.49}$$

Including the KORRINGA law (3.47) this can be expressed as

$$\frac{\mathrm{d}}{\mathrm{d}t}\left(\frac{1}{T_\mathrm{n}}\right) = \frac{T_\mathrm{n} - T_\mathrm{e}}{\kappa T_\mathrm{n}} \tag{3.50}$$

The nuclear temperature changes linearly with the temperature difference between nuclei and electrons, that implies a heat flow $\dot{Q}$. By conservation of energy we can write:

$$\dot{Q} = nC_\mathrm{n}\frac{\mathrm{d}T_\mathrm{n}}{\mathrm{d}t} = -nC_\mathrm{e}\frac{\mathrm{d}T_\mathrm{e}}{\mathrm{d}t} \tag{3.51}$$

Here n is the number of moles. This equation opens the way for two statements. First we plug the right '=' into (3.50) and obtain

$$\frac{\mathrm{d}T_\mathrm{e}}{\mathrm{d}t} = \frac{T_\mathrm{n}}{\kappa}\frac{C_\mathrm{n}}{C_\mathrm{e}}\left(T_\mathrm{n} - T_\mathrm{e}\right) \tag{3.52}$$

Subtracting this from (3.50) results in

$$\frac{\mathrm{d}\left(T_\mathrm{n} - T_\mathrm{e}\right)}{\mathrm{d}t} = -\frac{T_\mathrm{n}}{\kappa}\frac{C_\mathrm{n} + C_\mathrm{e}}{C_\mathrm{e}}\left(T_\mathrm{n} - T_\mathrm{e}\right) \tag{3.53}$$

For comparison we modify (3.50)

$$\frac{\mathrm{d}T_\mathrm{n}}{\mathrm{d}t} = -\frac{T_\mathrm{n}}{\kappa}\left(T_\mathrm{n} - T_\mathrm{e}\right) \tag{3.54}$$

These three equations, (3.52)-(3.54), describe the time scale on which the temperatures come into equilibrium. We get time constants for the relaxation of the electron temperature, the nuclear temperature and their difference:

$$\tau_n = \tau_1 \tag{3.55}$$

$$\tau_e = \tau_1\frac{C_\mathrm{e}}{C_\mathrm{n}} \tag{3.56}$$

$$\tau_{n-e} = \tau_1\frac{C_\mathrm{e}}{C_\mathrm{n} + C_\mathrm{e}} \simeq \tau_1\frac{C_\mathrm{e}}{C_\mathrm{n}} \tag{3.57}$$

The latter simplification is due the fact that the electronic heat capacity is much smaller than the nuclear heat capacity in the region of interest. These equations tell us two things. On the one hand all three processes get slower as the demagnetisation goes on because T_n is reduced, equations (3.52)-(3.54). On the other hand the electrons come into equilibrium with the nuclei fast whereas the nuclear temperature changes very little only $\tau_e = \tau_{n-e} \ll \tau_n$.

We get the second statement by starting with the left '=' of (3.51). Together with the nuclear heat capacity (3.39) we get a heating rate for the nuclear spins.

$$\frac{\mathrm{d}}{\mathrm{d}t}\left(\frac{1}{T_\mathrm{n}}\right) = -\frac{\dot{Q}}{n\Lambda_\mathrm{n}B^2} \tag{3.58}$$

Plugging this into (3.50) gives

$$T_{\mathrm{e}} = \left(\frac{\kappa \dot{Q} + n\Lambda_{\mathrm{n}} B^2}{n\Lambda_{\mathrm{n}} B^2} \right) T_{\mathrm{n}} \tag{3.59}$$

In (3.51) $\dot{Q}$ is defined as the heat that flows between the nuclear and the electronic system. Once the two systems are equilibrated $\dot{Q}$ disappears, the nuclear temperature doesn't change any more (3.58) and the electron temperature is the same as the nuclear temperature. But $\dot{Q}$ could also be seen as heat that leaks into the systems from the environment. That usually flows into the electronic system. Since the electronic heat capacity is so small compared the the nuclear heat capacity, the heat will flow instantaneously into the nuclear bath. In that case the nuclei will warm up according to (3.58) and there will be a temperature gradient between electrons and nuclei given by (3.59). These two equations tell us also that the heat leak must not be too large to make demagnetisation possible at all, hence $\kappa \dot{Q} \ll n\Lambda_{\mathrm{n}} B^2$. In other words the temperature reduction by reducing the field must be larger than a possible heat increase by the heat leak. From these two equations we can write down the dynamic behaviour of the electron temperature directly

$$\frac{\mathrm{d}}{\mathrm{d}t} \left(\frac{1}{T_{\mathrm{e}}} \right) = -\frac{\dot{Q}}{\kappa \dot{Q} + n\Lambda_{\mathrm{n}} B^2} \tag{3.60}$$

The fact that there is an inevitable heat leak in a real system gives rise to an optimum final demagnetisation field $B_{\mathrm{f,min,opt}}$. If we replace T_{n} in (3.59) with (3.33) we get:

$$T_{\mathrm{e}} = \frac{T_{\mathrm{i}}}{B_{\mathrm{i}}} \left(\frac{\kappa \dot{Q}}{n\Lambda_0 B_{\mathrm{f}}} - B_{\mathrm{f}} \right) \tag{3.61}$$

which has a minimum at

$$B_{\mathrm{f,min,opt}} = \sqrt{\frac{\kappa \dot{Q}}{n\Lambda_{\mathrm{n}}}} \tag{3.62}$$

So far we neglected interaction between the magnetic dipoles. We take account of these interactions with an internal field B_{int} which describes the field exerted on a nucleus by other nuclei. Given an external field B a nuclear spin experiences an effective field B_{eff} given as

$$B_{\mathrm{eff}} = \sqrt{B^2 + B_{\mathrm{int}}^2} \tag{3.63}$$

The internal field of copper is of the order of $0.3\,\mathrm{mT}$ [49, 52] but lower values ($\sim 0.07\,\mathrm{mT}$) are reported [52]. In any case this gives a lower limit for the final demagnetisation field and therefore an upper limit for the lowest achievable

temperatures. Electronic paramagnets are subject to higher internal fields limiting temperature range to $\gtrsim 2\,\mathrm{mK}$ in the case of Cerium Magnesium Nitrate (see 3.5.2). If $B \gg B_{\mathrm{int}}$ it is $B_{\mathrm{eff}} = B$ and (3.33) holds. Otherwise, the magnetic fields have to be substituted by (3.63).

3.4.6. Choice of Nuclear Refrigerant

From the Considerations above we can summarise the prerequisites for a 'good' refrigerant [49, 55]

1. Cooling power. In order to have a large cooling power we need a large molar CURIE constant Λ_{n}. Moreover, this should be valid for a large fraction of the element's isotopes.

2. Handling. The material should be easy to handle. It should be machinable and, in particular, weldable with as little effort as possible.

3. The KORRINGA constant should be small for efficient cooling. This limits the choice to metals but rules out all superconductors.

4. Small B_{int}. Magnetic ordering should be absent in both systems, electrons and nuclei. Hence, we must not use ferromagnets. Furthermore, the lattice should be cubic or the spin should be $1/2$.

5. The thermal conductance, i.e. internal equilibration, should be good for two reasons. On the one hand, the precooling time has to be short, on the other hand, we want to couple the refrigerant efficiently to an electronic device.

If we consider all these points and compare them with data [49] we find that there is no ideal material. However, copper has become the 'work horse' [49] of adiabatic nuclear demagnetisation. It provides a good trade-off between the prerequisites and so we decided to use copper. It has a spin of $3/2$, a good electrical and thermal conductivity and it doesn't show any magnetic ordering above $1\,\mu\mathrm{K}$ nor superconductivity above $10\,\mu\mathrm{K}$. Moreover, it is easily available in high purity and has good machining and metallurgical properties.

3.5. Thermometry

So far we have seen that one has to take strong efforts to achieve low or even ultra-low temperatures. But one wants to determine the temperature also. It is important to know the temperature for several reasons. On the one hand, the goal of this project is to achieve sub-millikelvin temperatures in electronic heterostructures and that has to be confirmed experimentally. This also means that certain quantities have to be probed as a function of temperature. But on the other hand, knowing the temperatures on different parts of the whole cryostat tells about the performance and thus helps to localise the origins of problems. Unfortunately our knowledge of temperature is not very precise unlike time or length [49]. In fact thermometry can be as complicated as or even more complicated than the cooling technique itself [49]. John Saunders expressed it the following way "..isn't it the fact that, if we have one thermometer we know temperature, if we have two, we don't." [65].

In the following I will discuss some methods of thermometry focussing on techniques more relevant below 1 K.

3.5.1. Resistance Thermometry

Resistance thermometry is a method that calculates temperature from a measured resistance. This calculation is based on a calibration of the resistor against a known temperature scale, e.g. resistors are secondary thermometers. The advantages of this method are that the resistors are easily obtainable and it is easy to measure a resistance. During the analysis of the performance of the prototype it turned out that the small size of the resistors, of the order 1 mm, is another huge advantage, in particular since we installed several of them. But there are also disadvantages: thermal conductivity, thermal contact, self-heating through the measuring current and rf-absorption [49].

Gap-activated resistors

Semiconductors show a temperature-dependence of their conductance where the dominant mechanism is the loss of charge carriers. At lower temperatures it can be written:

$$R \sim \mathrm{e}^{-\frac{\Delta E}{2kT}}$$

The proportionality factor contains the weakly temperature dependent mobility of the charge carriers [49]. ΔE is the energy gap between valence and conduction band. However, this equation usually doesn't hold, it has to be replaced by an empirical equation.

In essence, there are three resistor types: germanium, carbon and oxide compounds. Germanium resistors offer a temperature range of $0.3\,\mathrm{K}$ to $400\,\mathrm{K}$, whereas the range can be extended down to $30\,\mathrm{mK}$ with an appropriate doping [49]. Their advantage is a stable and reliable resistance value as function of temperature. It is stable over time as well as upon thermal cycling. The carbon resistors on the other hand are cheaper because they don't have to be produced specifically for low-temperature application, they are produced by electronic companies for general applications. Their disadvantage is that one has to take special actions to avoid certain problems like bad thermal contact and long equilibration times [49]. Furthermore, their resistances can vary from chip to chip, from cooldown to cooldown and it can even drift during the same cooldown. Since we used RuO_2 chips as sensor, they shall be discussed in more detail.

Ruthenium Oxide Chips

Like the carbon resistors, the RuO_2 chips are produced as standard electronic components and thus cheap. The comparatively small RuO_2 chip consist of a mixture of conductive RuO_2, Bi_2RuO_2 and silica-glass deposited on alumina. Unlike the carbon resistors they exhibit less magnetoresistance and more stability and reliability [49, 59]. The magnetoresistance is about 4% at $30\,\mathrm{mK}$. It goes down for higher temperatures. However,the behaviours observed deviate in detail [49] and larger magnetoresistances were oberved. The reliability of the calibration is better then for carbon resistors, nevertheless it is recommended to calibrate only after about 60 thermal cycles [49]. Resistors particularly designed for low temperature thermometry are available. Among other things, the film is deposited on sapphire for better thermal contact [59]. The RuO_2 chips have a low temperature limit whereas literature gives different values [49, 59]. We found trustworthy calibrations down to $\sim 8\,\mathrm{mK}$ but below $\sim 25\,\mathrm{mK}$ the equilibration time can be of the order $2\,\mathrm{h}$.

3.5.2. Electronic Susceptibility

Another possibility to measure temperature in the range down to a few millikelvin is to determine the susceptibility of a paramagnetic salt. The most common is cerium magnesium nitrate (CMN)[2].

$$2Ce^{3+}(NO_3)_3 3Mg(NO_3)_2 24H_2O$$

The measured quantity is the magnetisation M of the salt, or the susceptibility χ respectively [49]. Ideally, they follow the Curie law (see also section 3.4.3, in

---

[2]Although other salts are possible this type of thermometer is in general referred to as CMN for simplicity here.

particular (3.41))

$$M = \frac{\Lambda_e B}{T} \tag{3.64}$$

$$\chi = \frac{\Lambda_e \mu_0}{T} = \frac{\lambda_e}{T} \tag{3.65}$$

Note, Λ_e is the electronic Curie constant. This suggests that a CMN is a primary thermometer. But the field in (3.64) is altered which requires a calibration against other thermometers. The magnetic field can be written as [49]

$$B = B_{ext} + B_d + B_i \tag{3.66}$$

where B_{ext} is the applied external field, B_d is called demagnetisation field and B_i is the internal field or Weiss field which is created by surrounding dipoles. The fields are given as

$$B_d = -f\mu_0 \frac{M}{V} \tag{3.67}$$

$$B_i = \alpha\mu_0 \frac{M}{V} \tag{3.68}$$

f is a geometric factor given by the shape of the specimen and α depends on the crystal structure. Since $f, \alpha > 0$, B_d weakens the field whereas B_i enhances it. Plugging (3.67) and (3.68) into (3.66) and that into (3.65) yields the Curie-Weiss law

$$\chi = \frac{\lambda_e}{T - (\alpha - f)\frac{\lambda_e}{V}} \tag{3.69}$$

In practice, it possible to obtain a constant background susceptibility χ_0 which can stem e.g. from parasitic inductances in the measurement leads. However, the temperature is given by

$$\chi = \chi_0 + \frac{\lambda_e}{T - \Delta} \tag{3.70}$$

Δ is called the Weiss constant. It reflects which of the competing effects, (3.67) or (3.68), is stronger.

Such a CMN thermometer is a convenient way to measure temperatures below 1 K. The lower limit is given by the ordering temperature of the specific salt [51]. Below that, the magnetic moments order and the susceptibility becomes insensitive to temperature. The best material in that sense is CMN itself with an ordering temperature of 2 mK. This range can be extended further down by diluting the salt. The cerium atoms are replaces by lanthanum. The average distance between the magnetic moments in such a lanthanum doped CMN (LCMN) is increased and hence the dipole-dipole interaction is weaker and thus the ordering temperature is lowered. A few hundred μK are possible this way.

The signal is detected with AC techniques. The susceptibility is given in terms of the mutual inductance L_M as

$$L_M = L_{M0} \left(1 + \mathcal{F}\chi\right) \tag{3.71}$$

where L_{M0} is the mutual inductance without any sample and $\mathcal{F}$ is the filling factor which tells how much of the secondary coil are filled with the specimen. Figure 3.9 shows a simple circuit that can be used to determine the mutual inductance of a CMN. An ac current source drives the primary coil which creates the external magnetic field B_{ext}. Since it is an ac field it induces a voltage in the secondary coil
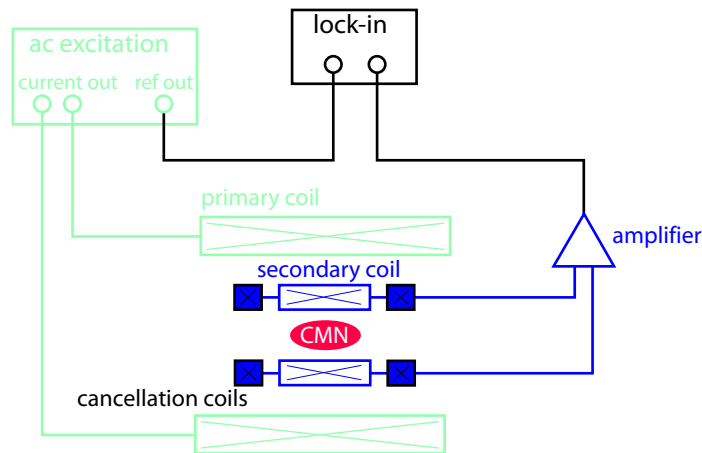
Figure 3.9.: Simple circuit to determine the mutual inductance of a CMN thermometer.

which is than amplified and measured with a lock-in amplifier. The amplifier can be at room temperature but the signal can also be amplified at low temperature, e.g. with a SQUID. The cancellation coil is counter-wound in order to compensate for L_{M0} in (3.71) such that the measured mutual inductance is proportional to to the susceptibility. Aside from such a lock-in technique it is quite common to use an inductance bridge to determine the mutual inductance.

The actual realisation of a CMN thermometer can be very different. Nevertheless, some issues can be said in general. First, a superconducting shield is necessary to prevent stray fields from corrupting the temperature measurement on the one hand, but on the other hand, the ac field of the thermometer must not influence other parts of the set-up. Second, paramagnetic salts are insulators, and thus, bad thermal conductors. Good thermalisation is typically achieved by putting fine metal wires into the salt. The wires themselves have to be connected to the bath that one intends to measure. Another aspect concerning the salt is their water

content. Dehydration can change the Curie and the Weiss constants drastically which can eventually make the thermometer useless [53]. Any material used has to be chosen carefully. As superconducting shields Nb is a good choice. It is type I superconductor and hence doesn't allow flux penetration. Epoxy can be dangerous because it is paramagnetic [53]. Furthermore, as for all thermometers, self-heating has to be avoided.

3.5.3. Nuclear Susceptibility

Instead of the susceptibility of the electrons it is also possible to measure the nuclear susceptibility. It follows the same functional behaviour like the electrons but some facts lead to significant differences. Since the nuclear magnetic moments are about three orders of magnitudes smaller than their electronic counterpart, they order at much lower temperatures. Hence, the low temperature limit is in the microkelvin regime. Furthermore, it is possible to use metals which offer good thermal contact. On the other hand the metal should have a small Korringa constant to provide good thermal contact between the nuclear system and the electrons, and its the temperature of the latter that is usually of interest.

However, the nuclear susceptibility and the magnetisation respectively, can be determined in different ways. Like in the electronic case it is possible to probe nuclear moments with a quasi-dc method. But due to their smallness a SQUID is required to obtain sufficient sensitivity. A substantial drawback is the contributions from sources other than the nuclei. This could be electrons in the specimen but they can also originate from very small amounts of magnetic impurities, the sample holder or even leads [49]. It needs elaborate methods to separate the contributions. The advantage of this method is that it does not introduce heat per se.

Instead, specific nuclei are adressed by resonant radio frequencies, a technique known as nuclear magnetic resonance (NMR). The first method combines the resonant excitation with the static read-out with a SQUID. The latter reads a certain magnetisation which is reduced upon shining a resonant 90° pulse. The reduction is proportional to the magnetisation of nuclear spin species under consideration [49]. This method is usually referred to as SQUID-NMR. In the next step the detection is resonant as well, whereas two methods have to be distinguished. The continuous wave method determines the method by continuously shining a resonant radio frequency. This drives transitions between the Zeeman levels. The required energy is taken from the resonance circuit what can be seen as absorption dip in the spectrum. If the rf amplitude is small the absorption is proportional to the magnetisation.

However, the most common technique for thermometry below 1 mK is the pulsed NMR technique [59] on platinum nuclei. Since we used it to determine the tem-

perature in the the demagnetised copper I describe it in more detail. The topic is treated in standard literature [49, 51, 53, 59] and for Platinum NMR thermometry by Hechtfischer and Schuster [66].
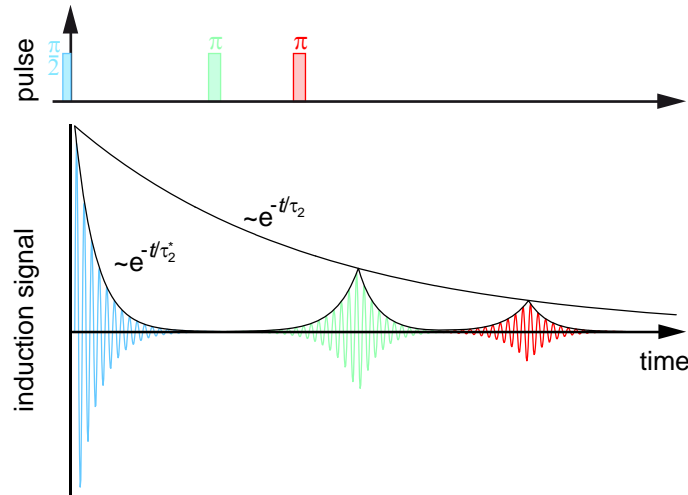
Figure 3.10.: Schematic of a free-induction decay. The top axes shows the pulse sequence, the observed induction signal below. A $\pi/2$ pulse (blue) tips the spins which subsequently start to process and thereby create an induction signal. The signal dephases with a characteristic time τ_2^* (blue). The π-pulses elicit echoes. The green pulse is followed by the green echo, the red signal is accordingly. The echo amplitude decays with a characteristic time τ_2. Note that the spin-lattice relaxation time τ_1 is typically much larger than τ_2.

In an external magnetic field the energy of a nuclear spin I splits into $2I + 1$ ZEEMAN levels with level spacing $E_Z = g_n \mu_n B$. Transitions between the levels can be driven by applying radiation of frequency $\omega = E_Z/\hbar$. If $I = 1/2$ only one frequency is possible otherwise multiples can drive transitions, too. In a spin-$1/2$ system the magnetisation is essentially given by the relative population of the two ZEEMAN levels. In general, the magnetisation is a statistic average of an spin ensemble and hence the spin dynamics of the individual spins determines the dynamics of the magnetisation. Spin dynamics is described by the BLOCH equations. An rf pulse of resonant frequency tips the spins by a certain angle θ which is determined by the amplitude and the length of the pulse. Afterwards the spin precesses about the z-axis defined by the external magnetic field. The precession is superimposed by a return to the z-axis. The arising induction signal can be picked up, e.g. by a coil whose main axis is perpendicular to the external

field. Such a signal is shown schematically in figure 3.10. The magnetisation in the xy-plain decays exponentially with a characteristic time τ_2^*. If the tipping angle is 90° the static magnetisation and hence susceptibility can be inferred from the size of the induction signal immediately after the tipping pulse. If the tipping angle is not 90° a correction of $\sin\theta$ needs to be applied. The signal is given by [49]

$$V(t) = \alpha\omega_\mathrm{L} M_z(T) \sin\theta \sin(\omega_\mathrm{L}t)\mathrm{e} - \frac{t}{\tau_2^*} \tag{3.72}$$

α is a geometric constant describing the properties of the pick-up coil, $M_z(T)$ is the temperature dependent magnetisation and $\omega_\mathrm{L} = \gamma B$ is the LARMOR frequency, γ the material specific gyromagnetic ratio. The dephasing time τ_2^* is given by the fact that the spins experience different magnetic fields and so the LARMOR frequencies can differ. Some spins precess faster than others and hence their projections into the xy-plain diverge over time. To some extend this effect is reversible, e.g. if the magnetic field is inhomogeneous. If a pulse that tips the magnetisation by 180° is applied the the spins that lag behind and the spins that rotate ahead interchange their roles but their LARMOR frequencies are not affected. That means that the spins now lagging behind 'catch up' and the spins ahead slow down and the magnetisation in the xy-plain re-emerges. Such an echo signal is shown in green and red in figure 3.10. Nevertheless, inevitable effects cause a dephasing of that signal, too, and the characteristic time is denoted τ_2. The dephasing time should be as long as possible for accurate magnetisation reading.

As NMR thermometry is done on metals two fundamental effects have a crucial impact on the technique: the skin effect and eddy current heating. Ac fields have a finite penetration depth δ in conductors which goes as

$$\delta \sim \sqrt{\frac{1}{\sigma\omega}} \tag{3.73}$$

where σ is the conductivity of the material and ω the rf frequency. For this reason the rf field inside the metal is strongly attenuated and the dimensions of the specimen should be smaller than δ. That means that the frequency should be rather small and the conductance bad. The heating power of the the rf pulse goes as

$$P_\mathrm{rf} \sim \omega^2 B^2 \tag{3.74}$$

Therefore the frequency ω has to be chosen small again as well as the amplitude B. But the dimensions of the sample should be minimised also to suppress eddy currents. So both problems demand a small sample. That can be achieved by employing metal powders or thin insulated wires. The problems can also be diminished for lower frequencies but that is in contrast to the signal strength (3.72), so a compromise has to be found.

Besides this, other points have to be considered. The static magnetic field has to be homogeneous to achieve long dephasing times. In addition the magnetic field has to be large for a strong signal on the one hand but on the other hand small to have not too large of a heat capacitance which means fast thermalistion. As the actual sample material platinum is the ideal choice. It has a small KORRINGA constant, hence a fast spin-lattice relaxation, and a long τ_2 time.

3.6. Heat Leaks

Going to lower temperatures requires not only a strong source of cooling power but also a reduction of heat leaking into the system. On the one hand, at some point the heat leak balances out the cooling power (equation (3.28)) but in case of adiabatic demagnetisation the warming rate is determined by the heat leak (equations (3.58) and (3.60)) and hence the cold time. Today, state-of-the-art heat leaks can be of the order of a few pW [56].

Residual Thermal Conduction

Any part of a refrigerator needs some structural support and thus a residual heat flow is inevitable. However, two measures can help to reduce it. First, the materials have to be chosen with care. For electrical leads a trade-off between low ohmic heating and heat conduction needs to be found. Superconductors offer both, no heat dissipation and a negligible amount of heat flow. Second, all wires and tubes running down to the experiment have to be heat sunk at several intermediate temperature stages.

Blackbody Radiation

As already mentioned above, the blackbody radiation needs to blocked. The demagnetisation stage should be surrounded by a shield which is anchored on a stage as cold as possible.

RF Radiation

Besides blackbody radiation, high frequency electromagnetic fields can heat the system. The cryostat itself forms a FARADAY cage but all leads going to the experiment have to be well filtered. A higher level of protection is given by a shielded room which protects against ambient radiation such as radio stations or mobile phones. A serious problem can be noise emitted by certain instrumentation. It might be necessary to put that in a separate shielded box. Ways to build filters can be found in books on general electronics [67] or rf technologies [68]. Attention

has to be paid if the filters (or amplifiers) are intended to be operated at low temperature because electronic components can change their properties.

Vibrations and Sound

A further source of heat are vibrations and sound. Vibrations can stem from building vibrations or more obvious from vacuum pumps driving a DR. Heat arises from frictional effects or eddy current heating if conducting parts shake in a magnetic field (see below). Some guidelines to reduce this source of heat are as follows. The low temperature set-up should be placed in the basement of the building because vibrations are weaker than on higher floors. In general large masses help to reduce the impact of vibrations because resonant frequencies are shifted to less harmful lower frequencies. Damping can also be achieved by passing vacuum lines through a sand box. That provides mass but vibrations are also dissipated by friction between the sand grains. Furthermore, (metallic) vacuum lines should be interrupted by rubber pieces on the one hand. On the other hand, it helps to firmly connect them to a large mass. Besides the pumping lines the electric leads have to be considered. They can also be embedded in a large mass or they can be hung in loose loops. Vacuum pumps should be mounted separately to avoid transmission of vibrations through the floor. Moreover, it is advantageous to attach them to a large mass. The set-up usually rests on air springs to decouple the system from the ground. The actual refrigerator has to be build as rigid as possible where spacers between the radiation shields can increase the stiffness.

Sound can take two paths. It can travel in solids such as vacuum lines or through gas. In the first case some of the measures taken to reduce the effect of vibrations also damp the sound waves. A rubber piece within a vacuum line causes an acoustic mismatch and hence reflects a significant part of the soundwave. In the latter case the sound propagates either through the ambient air or through helium gas. A shielded room constitutes not only a protection against rf radiation it also hinders the transmission of sound. Acoustic noise can enter the system through the exhaust line of the helium bath which is usually connected to a recovery system. Hence, the bath is coupled to sound sources such as 1K pot pumps or helium liquifiers. It can be decoupled with a long rubber hose which damps the transmitted sound significantly.

All these considerations lead to low temperature set-ups which are larger than usual cryostats employed in mesoscopic physics including up to several tens of tons of concrete such as the set-ups in Helsinki [69], Lancaster [55] or Bayreuth [70].

Eddy Currents

Demagnetisation cooling requires a changing magnetic field which induces currents in conducting parts of the cryostat. The heating caused by a changing magnetic field $\dot{B}$ is given by [49]

$$\dot{Q}_{\text{eddy}} = G\sigma V\dot{B}^2 \tag{3.75}$$

where V is the volume of the body and σ its conductivity which can be field dependent. The geometric factor G is calculated as

$$G = \begin{cases} \frac{r^2}{8} & \text{for cylinders of radius } r \\ \frac{d^2}{16}\left(\frac{(w/d)^2}{1+(w/d)^2}\right) & \text{for rectangles of width } w \text{ and thickness } d \end{cases} \tag{3.76}$$

In practice one needs to find a compromise between demagnetising too fast or too slowly. This is on the one hand, because the eddy current, or strictly speaking the corresponding loss of entropy, has to be compared to the gain of entropy due to the actual demagnetisation. On the other hand, inevitable heat leaks accumulate and cause an additional loss of entropy. A guideline is a ramp rate of $\lesssim 1\,\text{T/h}$ [49].

Besides the intended ramp rate, ripples on top of the magnet's current can cause eddy currents as well. Such ripples can be reduced with filters. Induction can also be caused by a conductor shaking within a (inhomogeneous) magnetic field. In this case it should be considered that the magnet can move with respect to the refrigerator.

Ortho-Para Conversion of Hydrogen

At room temperature and below the hydrogen molecule can be described as a wave function composed of the nuclear spin states and rotational states. Electronic and vibrational states are not excited and therefore neglected [49]. The two nuclear spins of the proton ($I = 1/2$) align either parallel or anti-parallel e.g. they couple to a total spin of $I = 0$ or $I = 1$. The rotational state is described by the rotational quantum number J which is a good quantum number. The wave function of the hydrogen molecule has to be anti-symmetric because the single protons are fermions. That means that the symmetric (anti-symmetric) $I = 1(I = 0)$ wave function has to be multiplied with the anti-symmetric (symmetric) wave function of the rotational states. These are symmetric (anti-symmetric) for even (odd) values of J. This results in two different species of hydrogen: para- ($I = 0$) and ortho-hydrogen ($I = 1$). Their energy diagrams are depicted in figure 3.11

At low temperatures only the lowest rotational states are occupied. The molecule tends to relax to the lowest possible energy state which means that all molecules relax from the lowest ortho state to the lowest para state. Each relaxation process releases an energy of $\sim 13\,\text{meV}$. Depending on the starting concentration of ortho-hydrogen this leads to an initial heat release which is of the order of $\sim 1\,\text{kJ/mol}$[49].
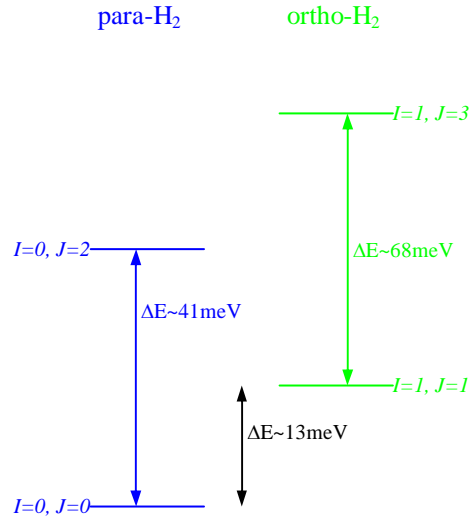
Figure 3.11.: Energy states for para- (blue) and ortho-H$_2$ (green). The degeneracy in m_J is lifted by an electronic quadrupole interaction ($\Delta E \sim 0.2 meV$) and the m_I degenarcy is lifted by nuclear dipole-dipole interaction ($\Delta E \sim 80$ peV).

In order for this transition to occur one of the nuclear spins has to flip. That happens only if they interact with a magnetic field or with each other. Since the nuclear moments are rather small this is unlikely to happen. That is why hydrogen can still release heat after days [49]. The relaxation process can be stimulated by bringing the hydrogen into contact with electronic magnetic moments such as those in iron. This heat release can be a severe obstacle if one wants to enter the microkelvin regime by the mean of adiabatic nuclear demagnetisation. Copper, often used for that purpose, can have small ($\sim 0.1\,\mu$m) hydrogen inclusions that form a heat leak to large for demagnetisation cooling [49].

Heat Release

Even if all external sources of heat are eliminated internal sources persist. One of them is the slow heat release from various materials. The excitations that lead to the specific heat as described by (3.15) give rise to an internal heat leak. Some materials can exhibit a heat release of about $0.1\,$nW/g even days after initial cooldown [49]. Therefore one has to be careful with epoxies, plastics or ceramics. Good materials in that sense are Teflon$^{\mathrm{TM}}$, graphite or alumina. Apart from these insulating materials also metals can release heat e.g. if lattice defects relax. Finally, the exchange gas used to precool the refrigerator needs to be properly removed. Due to its higher vapour pressure ^{3}He should be preferred over ^{4}He .

Cooling Nanoelectronic Devices

4.1. Introduction

The majority of quantum transport experiments to date, such as those in GaAs heterostructures or any other nanoelectronic devices on insulating substrates, have been carried out at electron temperatures T_e significantly greater than those of the host cryostats, which are mostly dilution refrigerators [33, 71–74]. The main challenges to achieve low temperatures is to thermalise the device well to the main heat sink which is the phase boundary in the mixing chamber in case of a DR. Furthermore, radio-frequency noise has to be attenuated and low-frequency interferences such as ground loops have to be minimised. I will now discuss the challenges and the presently most frequently used techniques to achieve low temperatures in nanostructures to be followed by a description of our new approach.

4.2. State of the Art Cooling

Cold 2DEGs

Most nanoelectronic devices are cooled down in a dilution refrigerator. Simple commercially available DRs reach base temperatures of the order 10 mK. Superior models achieve a few millikelvin. Nevertheless, the actual electron temperature in the nanostructure is often significantly higher [33, 71–74]. This can be seen, for
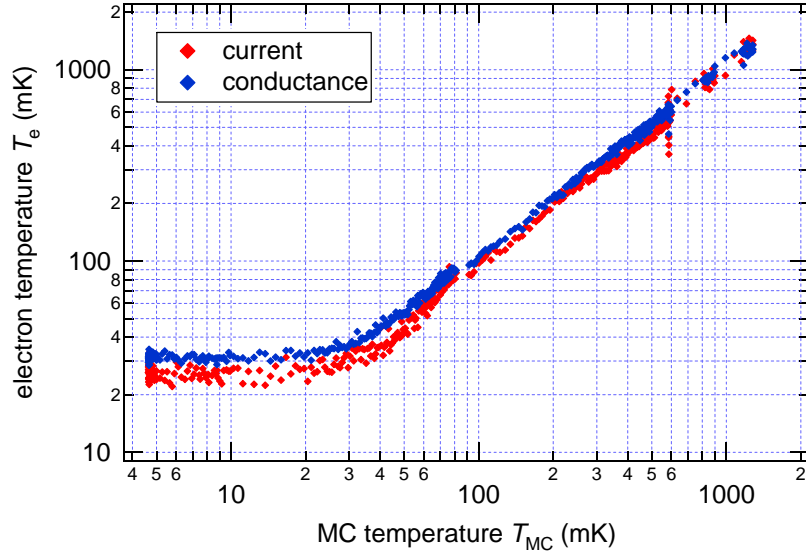
Figure 4.1.: Saturation of electron temperature. The data shows electron temperatures as extracted from a current and a differential conductance measurement as a function of mixing chamber temperature. The electron temperature agrees well for high temperatures but it saturates at values clearly below 25 mK. (Data from [73]).

instance, in a measurement done by Sarah Heizmann and Christian Scheller [73]. While at base temperature of their DR, they gradually reduced the ^{3}He circulation to allow the refrigerator to warm up. During that warm up two temperatures were recorded: the temperature of the mixing chamber and the electron temperature inside a quantum dot in a GaAs heterostructure. The electron temperature was extracted from a current measurement as well as from a differential conductance measurement. Figure 4.1 shows the electron temperatures as a function of mixing chamber temperature. The graph shows that the electron temperature clearly deviates from the mixing chamber temperature below 20 mK. Only above ~ 30 mK the temperatures agree.

In order to understand this insufficient cooling at lowest temperatures, one needs to look at the way how cooling in the nanostructure is achieved. The lowest temperature is achieved when the effective cooling power $\dot{Q}_{\mathrm{ecp}}$ balances out the residual heat leaking into the system $\dot{Q}_{\mathrm{rhl}}$. Note, that this balance has to be calculated for the nancostructure, i.e. the effective cooling power is the heat that is drained away from the nanostructure, in our case the 2DEG, and $\dot{Q}_{\mathrm{rhl}}$ sums up all sources that bring heat into the nanostructure. As a result, two major challenges have to be faced. On the one hand, the effective cooling power has to be increased and on the other hand, the residual heat leak has to minimised.

Energy Relaxation in a 2DEG

As the primary goal is to cool 2DEGs in GaAs heterostructures, we need to discuss how heat can leave such systems. The heat can relax through two channels. The first channel is through the ohmic contacts and the leads, the second mechanism is a relaxation via phonons, i.e. the sample substrate.

If one wants to make contact to such a device one has to bear in mind that the band structure in a semiconductor and a metal are different. The interface between these two types of materials exhibits a SCHOTTKY barrier e.g. the I-V-curve does no longer show ohmic behaviour. The contacts that overcome this problem are based on many different fabrication recipes and have been examined extensively [75–82]. However, as to my knowledge the thermal resistance of such a contact has never been measured. In order to describe the thermal behaviour, I therefore use the electrical resistance as a figure of merit and assume that the WIEDEMANN-FRANZ law (equation (3.27)) holds true. We can then compare the ohmic contact with other contacts. Weld joints that we made were in the range of $\mu\Omega$ whereas the ohmic contacts in our lab are a few hundred ohms to a few kΩ. Good ohmic contacts can be of the order $5\,\Omega$ [82]. Given a typical area of an ohmic contact of $A = 100\,\mu\mathrm{m} \times 100\,\mu\mathrm{m}$ and a typical depth of a 2DEG of $\ell = 100\,\mathrm{nm}$ we can estimate the thermal conductance of an ohmic contact from (3.27) as

$$k = \mathcal{L}\frac{T}{R} \tag{4.1}$$

For an ohmic contact of $R = 100(5)\,\Omega$ this gives $k = 2.4 \cdot 10^{-12}(4.9 \cdot 10^{-11})\,\mathrm{W/K}$ which is plotted in figure 4.2 as a function of temperature.

These estimates can be compared with measurements. Mittal and co-workers measured the thermal resistance between a 2DEG and the mixing chamber [71]. They analysed their data based on the WIEDEMANN-FRANZ law with the internal resistance of the 2DEG being the dominant impedance. Their findings are a factor of ten lower than calculated but self-consistent within a factor of 2. From this we can conclude that the thermal conductance is dominated by electron-like conduction which means that it is linear in temperature. This data is shown in figure 4.2 and extrapolated to lower temperatures for comparison.

However, other channels cannot be excluded [71]. The heat relaxation from the 2DEG into the phonon bath within the sample can be estimated. This is done in a so-called 'two-bath model' [83]. The electrons are at temperature T_e and the phonons at T_ph, respectively. In a steady-state the heat that flows into the electronic system equals the heat that flows out into the phonon bath. Thus, the electrons are at an elevated temperature with respect to the phonons. The heat flow is then

$$d\dot{Q} = \frac{1}{\tau_\epsilon}C_\mathrm{e}dT_\mathrm{e} \tag{4.2}$$
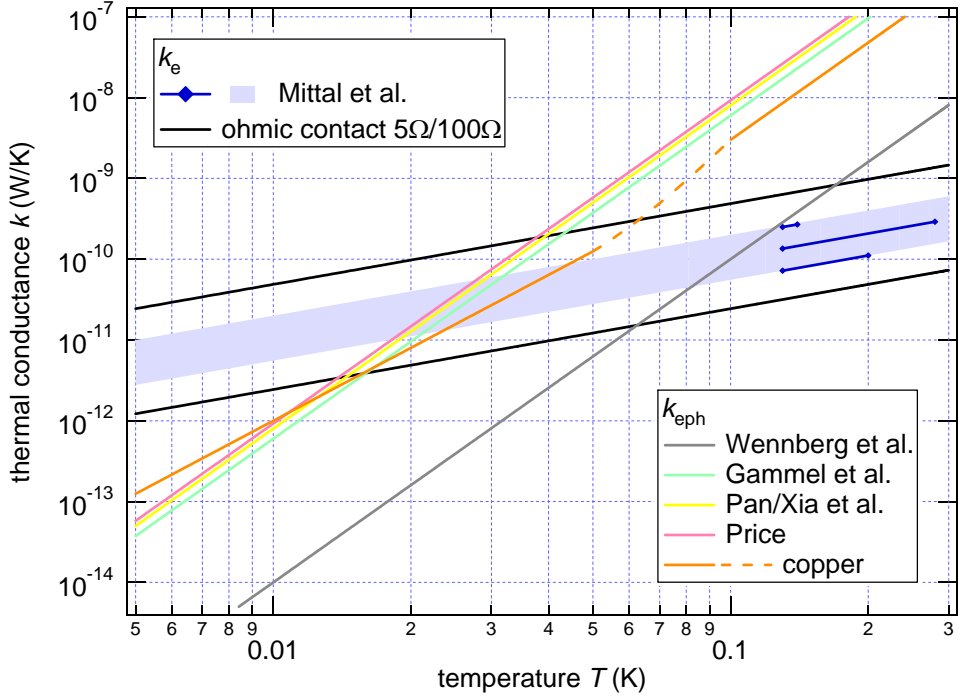
Figure 4.2.: Comparison of thermal conductances $k = \mathrm{d}\dot{Q}/\mathrm{d}T$. The graph shows thermal conductances, electron-like and electron-phonon coupling, as a function of temperature. The electron-like thermal conductances are calculated for ohmic contacts(black)) based on the Wiedemann-Franz law and data from Mittal and co-workers [71] (blue). That data is also extrapolated to lower temperatures (bright blue area). The electron-phonon coupling is based on data by Wennberg et al. [83], Gammel et al. [84] and Pan/Xia et al. [85, 86]. The purple trace is a theory by Price [87] and the orange trace is for copper [49]. The dashed orange line is an interpolation between two temperature regimes. Wennberg et al. measured a multi-quantum-well, the other traces are for 2DEGs.

with $1/\tau_\epsilon$ being the electron phonon-relaxation rate and C_e the electron heat capacitance. $1/\tau_\epsilon$ follows a power law, $1/\tau_\epsilon = \alpha T^3$ [83, 84, 87] and the electron heat capacitance is proportional in T, $C_\mathrm{e} = \gamma T$. Hence, with $\alpha' = \alpha\gamma$ we get

$$k = \frac{\mathrm{d}\dot{Q}}{\mathrm{d}T} = \alpha' T^4 \tag{4.3}$$

or integrated

$$\dot{Q} = \frac{\alpha'}{5}\left(T_\mathrm{e}^5 - T_\mathrm{ph}^5\right) \tag{4.4}$$

Figure 4.2 shows values of thermal conductances as estimated from [83–86]. Price [87] gives a theory that can be written as [72]

$$\dot{Q} = 1.65 \cdot 10^6 \frac{A}{\sqrt{n}} \left(T_{\mathrm{e}}^5 - T_{\mathrm{ph}}^5 \right) \tag{4.5}$$

where A is the sample area and n is the electron density. This theory is shown in figure 4.2 with the sample parameters of [84]. Furthermore, the electron-phonon relaxation for copper [49] is plotted where the dashed section is an interpolation between two given temperature ranges.

Comparing the five traces of k_{eph} in figure 4.2 with that calculated for the ohmic contacts it becomes obvious that below a certain temperature heat predominantly leaves the 2DEG through ohmic contacts. The findings of [71] second this statement. The particular transition temperature depends on several parameters. Besides the details of electron-phonon scattering it is the electronic heat capacitance in (4.3) and (4.4). According to (4.5) it is determined by the charge carrier density n and the sample area A. Note, that it is altered by magnetic fields [88–90] which can be understood considering that LANDAU levels constitute an additional excitable system. Furthermore, the size of the ohmic contact compared to the size of the sample is important.

Mittal and co-workers give a more detailed description [72, 91]. Besides relaxing via electron-phonon scattering, electrons can also diffuse through the ohmic contacts out of the 2DEG into the lead to be replaced by colder electrons. Fitting their theory to their data, they find that at higher temperatures electron-phonon scattering dominates whereas out-diffusion dominates at lower temperatures with the transition temperature to be of the order $100\,\mathrm{mK}$.

Moreover, they find that electron-phonon scattering is stronger for more disorder in the system, i.e. $1/\tau_\epsilon$ goes up with decreasing electron mobility [91].

Note, that Mittal and co-workers consider the internal relaxation in the 2DEG to dominate over the ohmic contact but it is not clear what the limitations are. However, Mittal's calculations as well as mine are based on the WIEDEMANN-FRANZ law (4.1) and thus yield the same result as the resistances used are of the same order of magnitude.

Next, I will discuss the two possible channels of energy relaxation with a focus on the more efficient electron-like path.

Electron-like Cooling Path

Figure 4.3 a) shows a schematic of a typical coldfinger as it is for example used in the MNK-I set-up in our laboratory, appendix E shows a coldfinger that was used to measure a Hall bar [92]. From the mixing chamber a coldfinger is extended down. At its end a sample holder is attached to hold the nanostructure. In our case, a brass can surrounds the sample as an additional radiation shield. The location of the sample is usually chosen to bring the sample into the centre of a

a)

b)

lead

mixing chamber

f

silver coldfinger

nanostructure

brass can

phonons
³He/⁴He mixture

Kapitza

phonons
MC housing/
coldfinger

insulator

phonons
leads

electron-phonon
coupling

electrons
leads

ohmic
contact

electrons
nanostructure

weak parallel phonon channel
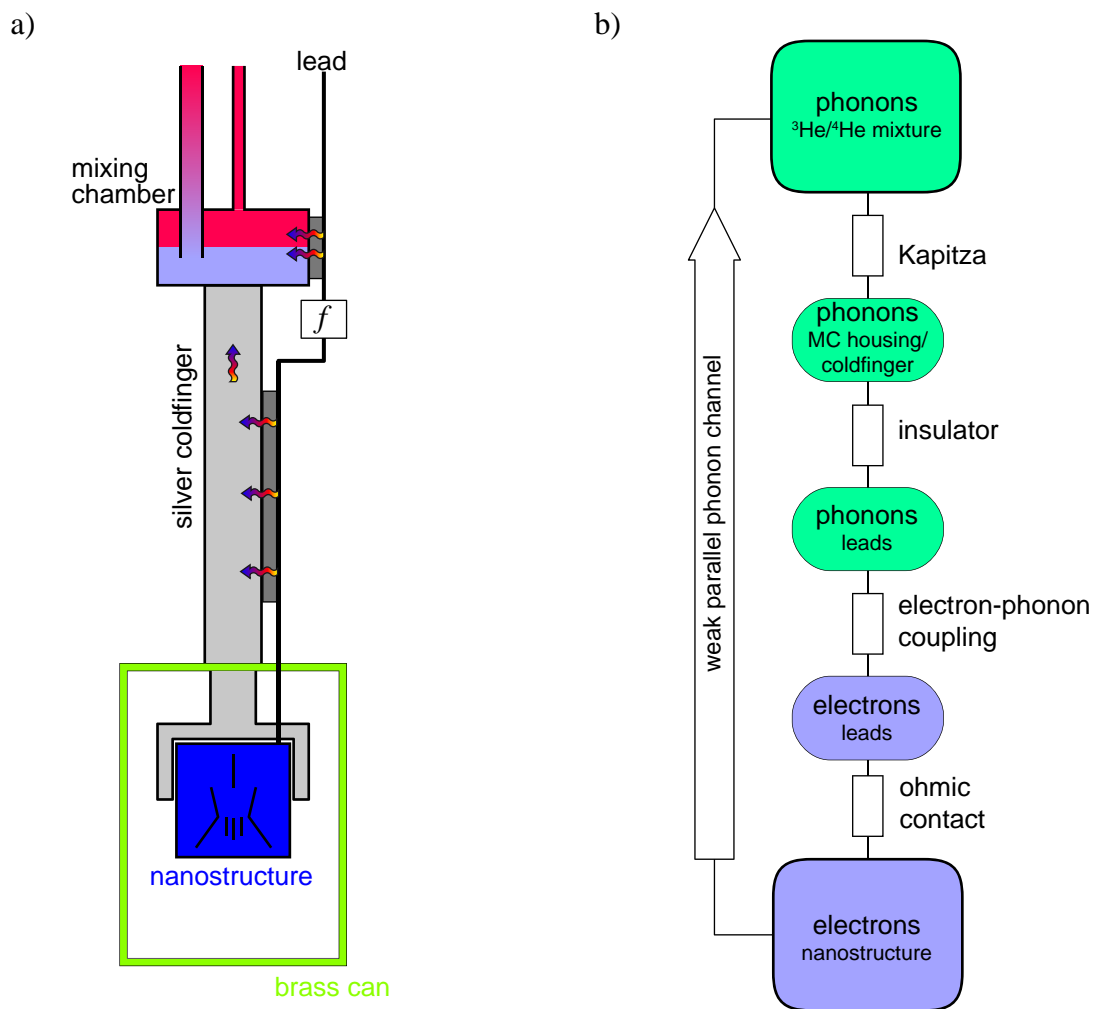
Figure 4.3.: a) Schematic of a coldfinger as it is typically used in the field of mesoscopic physics. b) Simplified heat flow chart depicting the electron-like path which dominates at low temperatures.

magnetic field. The leads run up along the coldfinger, pass the mixing chamber, and finally leave the cryostat.

In such a system, the heat has to propagate the following way from the nanostructure to the phase separation in the ^{3}He/^{4}He mixture which is the source of cooling. In a first step, it has to flow through the ohmic contact and a bond wire to the metal contact on the chip carrier. Next, the heat has to flow through a press contact into the pin of the socket. A wire is wrapped around the pin and soldered afterwards. This joint is the next thermal impedance before the leads. The steps described so far can be followed in figure 4.4.
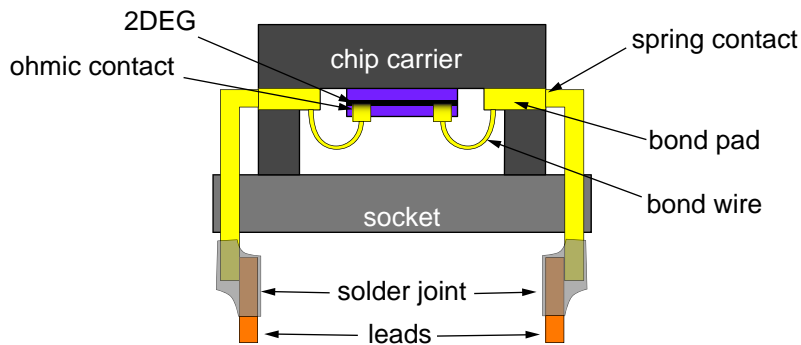
Figure 4.4.: Detailed schematic of a socket as it is typically used in the field of mesoscopic physics.

The leads have to be electrically insulated from one another and from ground. Therefore they are coated with some insulator which inhibits current but inherently also heat flow. Thus, the heat has to flow from the electrons in the leads to the phonons in the leads which in turn propagate through the insulator into the metal of the mixing chamber. Here, the heat has to overcome the KAPITZA resistance between the metal and the ^{3}He/^{4}He mixture. Finally, the heat has to propagate to the phase separation in the mixing chamber.

Figure 4.3 b) shows a simple heat flow chart for the electron-like cooling path. The thermal impedance labelled 'ohmic contact' comprises the ohmic contact itself and for simplicity the thermal impedances of the parts shown in figure 4.4: the bond wire, the metal pad on the chip carrier, the press contact, the pin, and the solder joint to the leads. Bond wire, metal pad, press contact and pin have resistances in the range of mΩ and are therefore much smaller as the ohmic contacts. The solder joint can become significant, though, because standard solders turn superconducting at several Kelvin [54]. In order to overcome the bad thermal conductance of this superconducting section the lead is typically wrapped around the pin several times to ensure a metal-metal contact. Alternatively, one can suppress

superconductivity by applying a magnetic field. Critical fields of solders are of the order $10\,\mathrm{mT}$ to $60\,\mathrm{mT}$ [54].

Within the leads the heat has to flow eventually from the electrons into the phonons. This flow is increased with a larger volume of the leads [49].

Due to the absence of conduction electrons in the insulator the heat has to be carried by phonons across it. On the one hand heat conduction by phonons is weaker than the heat conduction of electrons, but on the other hand the phonon has to propagate across two thermal boundary resistances - once upon entering the insulator, once upon leaving it. As described in section 3.1.3 this leads to an additional suppression of thermal conductance due to acoustic mismatch and total reflexion. In order to reduce this impedance one maximises the contact area. For instance, the lead can be wound many times around a metal post which is thermalised at the mixing chamber. The gaps between the turns can be filled with silver epoxy or grease to improve thermalisation further. Besides their attenuation properties, the cryogenic microwave filters described in [73] provide also a good thermalisation following this concept.

The KAPITZA resistance to the mixing chamber housing is reduced in a similar manner. Sintered metal powders provide contact areas of several 10 to several $100\,\mathrm{m}^2$ between the metal and the ${}^3\mathrm{He}/{}^4\mathrm{He}$ mixture. The KAPITZA resistance (per unit mass and unit area) is typically in the range of $\sim 10^{-5}\,\mathrm{W/Kgm}^2$ at $10\,\mathrm{mK}$ [57, 93]. Hence, the resistance between metal and ${}^3\mathrm{He}/{}^4\mathrm{He}$ mixture is negligible compared to the resistances plotted in figure 4.2.

Phonons

The role of the phonons can be seen from two perspectives. The first is that of an additional cooling path between the 2DEG and the mixing chamber. According to the considerations above electron-phonon relaxation dominates above $\sim 100\,\mathrm{mK}$. However, this phonon channel is further suppressed. On the one hand the bulk conductance of phonons is smaller than that of electrons and on the other hand the phonons have to overcome several thermal boundary resistances on their way to the mixing chamber. The coldfinger and the sample holder are built of different materials and at every interface between two materials a thermal boundary resistance occurs which eventually leads to a very weak phonon channel parallel to the electron-like path described above. This path is depicted in figure 4.3 b). Note, that the phonons can in principle couple to the reservoirs in the electron-like path at various stages along their way to the mixing chamber.

In the second perspective, the phonons constitute a bath to which the electrons can be coupled. In the considerations above, the energy relaxes from the electrons into the phonon bath, i.e. the heat flows from the electron system into the phonon bath. Below a certain (electron) temperature the phonons are hotter and the heat

flow turns around. The temperature dependence of the heat conductance changes. If we replace the electron heat capacitance in (4.2) with its phonon counterpart we get $k \sim T^6$. This is a strong temperature dependence which means that this heat influx gets weaker the colder the systems are. But on the other hand, the whole chip contributes phonons which means that the effective amount of mols is larger for phonons as for electrons. This, in turn, means that the influx can be higher. In consequence, the phonon bath should possibly be cooled, too.

Reducing the Heat Leak

So far I discussed how heat can be carried away from the sample. But one also has to minimise the amount of heat that flows into the sample.

Already in the construction of the coldfinger two things have to be considered. It has to be designed such that eddy current heating is suppressed, e.g. with a slotted geometry. In order to minimise the thermal radiation onto the sample one can surround the sample holder with a metal can (figure 4.3 a) or appendix E).

Besides this, two further sources of heat have to be eliminated, high frequency radiation and low frequency interferences.

The high frequency radiation can originate either from blackbody radiation or from a distinct source such as radio stations, mobile phones or certain electronic devices. Leads and cables connected to the refrigerator can potentially act as antennas for electromagnetic waves. The waves can then propagate along the leads to be absorbed at low temperature causing the temperature to rise.

Blackbody radiation is emitted by an object at finite temperature T. The spectrum is described by PLANCK's law which gives the spectral radiance L as [94]

$$L = \frac{2h}{c^2} \nu^3 \frac{1}{e^{\frac{h\nu}{k_B T}} - 1} \tag{4.6}$$

where h is PLANCK's constant, c the speed of light, and ν the frequency. The maxium of this spectrum at $\nu_{\max}$ is described by WIEN's law (3.4) which reads in frequency

$$\nu_{\max} = 5.8 \cdot 10^{10} \, \frac{\text{Hz}}{\text{K}} T \tag{4.7}$$

Figure 4.5 shows the spectrum of a black body. From this we can deduce that at room temperature a background radiation in the THz regime is present. According to the STEFAN-BOLTZMANN law (3.2) such an object at temperature T emits a power which is $\sim 460 \, \text{W/m}^2$ at 300 K. In order to reduce the amount of radiation that couples to the sample, low-pass filters can be employed. A cut-off frequency of 1 THz eliminates most (see figure 4.5) of the blackbody radiation emitted at 300 K. But even if it is reduced by a factor 1000, the power is still far from being in the desired nanowatt regime (as is derived in section 6.1).
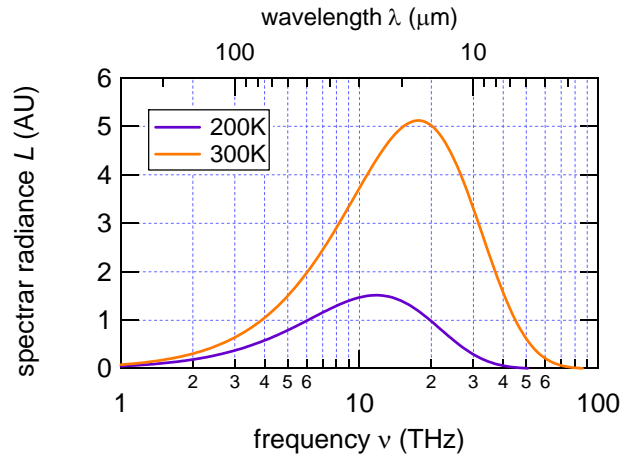
Figure 4.5.: Spectral radiance as a function of frequency. The top axis shows
the wavelength for comparison.

Superimposed on the blackbody spectrum signals of destinct frequencies are
present. They stem from modern telecommunication means such as mobile phones
(around 1 GHz), radio and TV stations (several 10s of kHz to several 100 MHz), or
GPS ($\gtrsim 1$ GHz), to mention but a few. A 100 MHz radio signal can easily increase
the temperature of the mixing chamber by a few mK [72]. In addition, certain
electronic equipment possibly emits radiation at certain frequencies. For instance,
a magnet power supply can also cause heating of of the mixing chamber of the
order 10 mK [72], which would correspond to a heat leak of the order $\sim 10\,\mu$W in
our DR (see figure 5.5). Like the blackbody radiation, this can be reduced by low
pass filters, but typically with lower cut-off frequencies. Furthermore, the whole
cryostat, and in particular the brass can in figure 4.3 a), act as FARADAY cage
provide additional attenuation.

However, low frequency interferences have to be considered, too. A common
problem is noise created by the 50 Hz ac voltage in the power lines. It can manifest
as 50 Hz noise signal and multiples. Furthermore, cables and wires can form loops
that can establish a voltage if the magnetic flux inside changes. Such a voltage can
be induced, for instance, by a transformer in a mains adapter. We observed that on
the Signal Recovery 7265 lock-in amplifier and reduced the noise by wrapping the
amplifier in a mu-metal foil [95]. Another method to minimise the impact of such
loops is to interrupt the current path. Figure 4.6 illustrates the situation. In a) a
voltmeter and a pre-amp are connected through a cable, e.g. a BNC cable, that
carries the signal but also a ground. Furthermore, both devices have an individual
connection to the mains ground. Hence, there is a ground loop that facilitates
a current. In b) the current is inhibited because the ground connection through
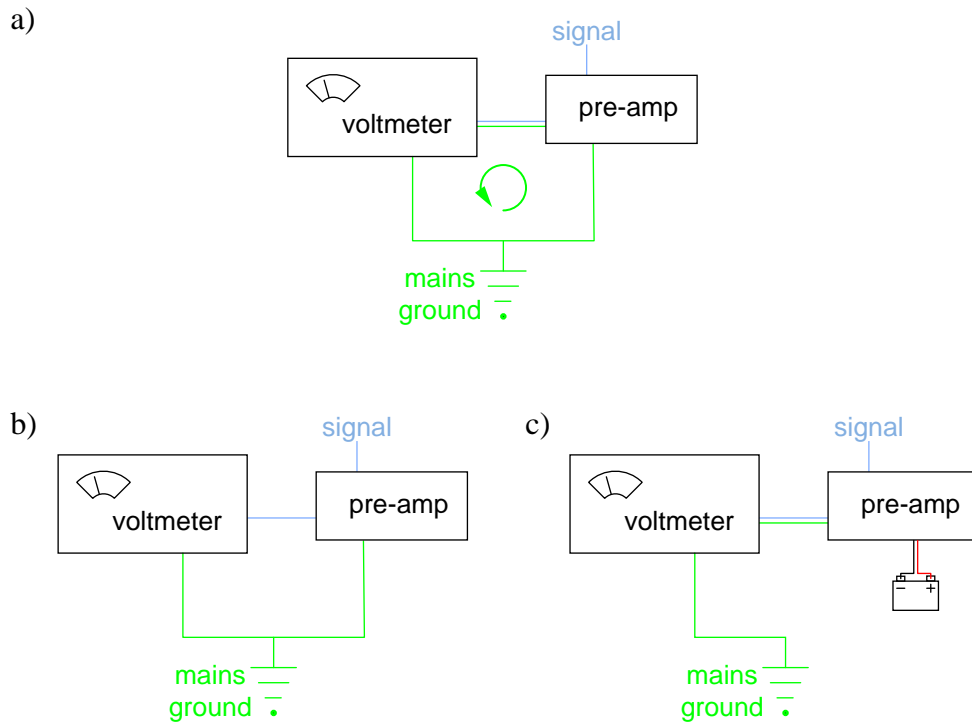
Figure 4.6.: Ground loop. a) The ground constitutes a loop that can carry a loop current. b) The cable connecting the two devices doesn't carry ground. c) The pre-amp runs on battery. It is disconnected from the mains ground.

the cable is interrupted. In c) the pre-amp is no longer connected to the mains ground and the ground loop is interrupted, too. Some devices can be operated in a floating mode, i.e. the circuit is galvanically separated from the mains. This separation can also be accomplished by floating transformers which are simple 1:1 transformers that separate two circuits.

A maximum noise level on the system can be derived from $k_\mathrm{B}T = eV_\mathrm{n}$ with V_n being a voltage noise. For $1\,\mathrm{mK}$ this gives $V_\mathrm{n} = 86\,\mathrm{nV}$. In order to resolve $1\,\mathrm{mK}$ with CBT the noise on the bias voltage has to be smaller than that. For this reason we had special low-noise voltage sources built with a noise level of $\lesssim 500\,\mathrm{nV}/\sqrt{\mathrm{Hz}}$ at an output of $10\,\mathrm{V}$. Since the bias voltage is typically $< 1\,\mathrm{mV}$, this value can be divided by a factor of 10^4 which gives $50\,\mathrm{pV}/\sqrt{\mathrm{Hz}}$ or $V_\mathrm{n} = 5\,\mathrm{nV}$ at a sufficient bandwidth of $10\,\mathrm{kHz}$. Similar considerations hold for gates. Unlike the bias, gates require voltages of the order $1\,\mathrm{V}$. So we can divide by 10 only. The lever arm reduces this further. On our sample we measured a lever arm of ~ 10. Hence, we have $5\,\mathrm{nV}/\sqrt{\mathrm{Hz}}$. In order to achieve the same result as for the bias we can allow

a bandwidth of the order $100\,\mathrm{Hz}$.

Lowest Electron Temperatures

Despite the difficulties in achieving low electron temperatures, values of $T_\mathrm{e} \lesssim 10\,\mathrm{mK}$ are reported [85, 86, 96–98].

Chung and co-workers achieved $9\,\mathrm{mK}$. They grounded the sample partially at low temperature which avoids the poor thermal coupling through an insulator. Potok and co-workers achieved $12\,\mathrm{mK}$. Unlike the typical method they placed their sample inside the mixing chamber of their DR.

However, the record to date, as to my knowledge, was measured in Florida [85, 86] using a method different than the method described above. Their sample was put in a ^{3}He immersion cell which was cooled employing a nuclear demagnetisation refrigerator. Both, electrons and lattice were thermalised. The lead heat exchanger was made by sintering silver powder directly onto a silver wire. The silver wire was then indium-soldered to the sample. To thermalise the lattice they 'glued' the sample on a silver post with gallium. The silver post had silver powder sintered around its tail. Furthermore, they employed RC filters with a cut-off frequency of $10\,\mathrm{kHz}$ to reduce rf heating. With this technique they achieved an electron temperature $T_\mathrm{e} = 4\,\mathrm{mK}$ at a bath temperature of $T_\mathrm{b} = 2\,\mathrm{mK}$.

4.3. A New Concept: Cooling the Leads

Within this work we propose a new scheme of cooling that brings two improvements over the typical scheme as explained above. First, we want to feed the leads through the mixing chamber and equip them with sintered metal powder to couple them well to the ^{3}He/^{4}He mixture. This is similar to the method applied in Florida [86] with the difference that we employ the sinter in a ^{3}He/^{4}He mixture instead of inside a ^{3}He immersion cell. Second, we want to couple each lead to a separate mikrokelvin bath that is based on the well-known and widely-used technique of adiabatic nuclear demagnetisation.

Figure 4.7 a) shows a set-up for a single lead. The ohmic contact and the bond wire are the same as in the conventional cooling scheme. The standard chip carrier and socket have to be replaced by a home-made sample holder where the sample is directly bonded to the silver wire. The heat then propagates along this wire into copper plates . In the plates the heat flows from the electrons into the nuclei mediated by a Korringa process. The nuclei themselves were demagnetised before and hence, they constitute a bath at microkelvin temperatures. In summary, the 2DEG is coupled to a microkelvin bath through essentially two impedances only, the ohmic contact and the hyperfine coupling between electrons and nuclei.
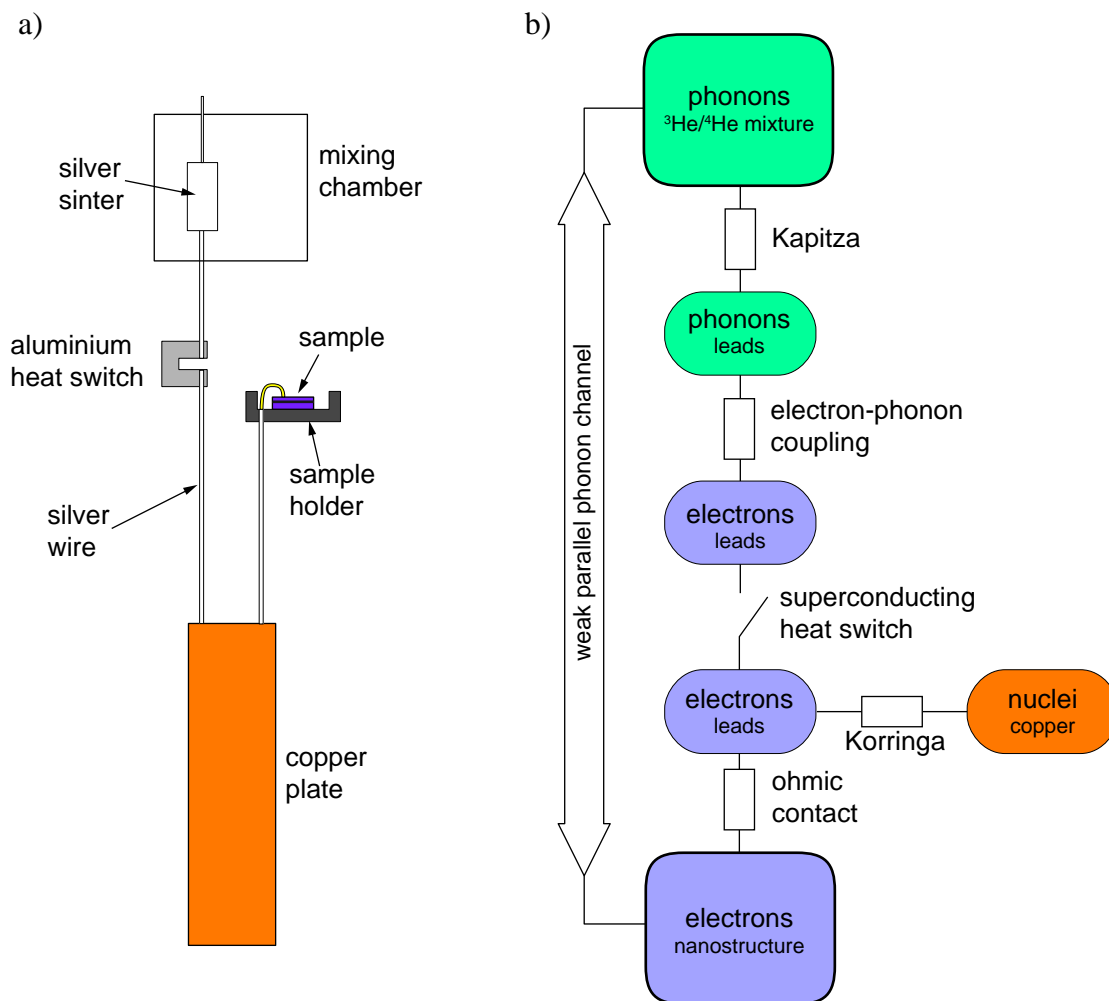
Figure 4.7.: a) Schematic of the set-up based on the approach of demagnetising the leads. b) Simple heat flow chart for for this new scheme.

However, before the lead can be demagnetised it has to be magnetised first which releases the large heat of magnetisation. In order to remove this, the plate has to be coupled well to the phase boundary of the ^{3}He/^{4}He mixture of the mixing chamber. Thus, we attach another silver wire to the plate and run it up into the mixing chamber where sintered metal powder is pressed around the wire providing good thermal contact to the mixture. The wire is interrupted by a piece of aluminium that serves as superconducting heat switch.

Figure 4.7 b) shows the heat flow chart in analogy to figure 4.3 b). In the precooling stage during which the heat of magnetisation has to be removed the heat switch is closed and the heat flow is similar as in figure 4.3 b) with one

significant improvement. The thermal resistance of the insulator is eliminated and thus, the thermalisation is better. During the demagnetisation and the cold time thereafter the heat switch is open and the heat flows as mentioned above, from the 2DEG through the ohmic contact into the electrons of the leads where it is drained into the demagnetised nuclei.

Even without demagnetisation, this scheme provides better thermalisation of the 2DEG through the sintered metal powder attached to the leads inside the mixing chamber. Thus, it should, in principle, be possible to achieve low electron temperatures with dilution cooling only.

Experimental Set-up

5.1. Introduction

Besides designing, constructing and testing the new type of refrigerator, the task was to build the complete experimental set-up. That includes the whole measurement electronics and the entire low-temperature equipment. The set-up was in an old particle accelerator hall among other low-temperature set-ups.

5.2. General Set-up

The floor of the accelerator hall was partially made from wood which was mounted to provide a flat floor level. The other part was a solid concrete floor. Due to space limitations the set-up had to be extended over both, the wooden floor and the concrete. The arrangement we finally chose is shown in figure 5.1. The gas handling system (GHS) contains the pumps for the dilution refrigerator. Since they are a source of strong vibrations, the GHS had to be put onto concrete in order not to transmit vibrations to other parts of the set-up as it would have been the case on the wooden floor. The cryostat was put next to the GHS because it had to be connected to the GHS. On the one hand, the pumps in GHS have to be connected to the dilution refrigerator and on the other hand, the GHS comprises an electronic unit that controls the DR which necessitate connections to valves and pressure gauges on the DR. The measurement rack (left-hand side in figure

5.1) was placed on the other side of the cryostat. Almost all digital multimeters, lock-in amplifiers and other electronic devices where put on the rack. Finally, a desk was put next to the rack. A personal computer was installed on that desk that was used to acquire data electronically.

5.3. Cryogenic Set-up
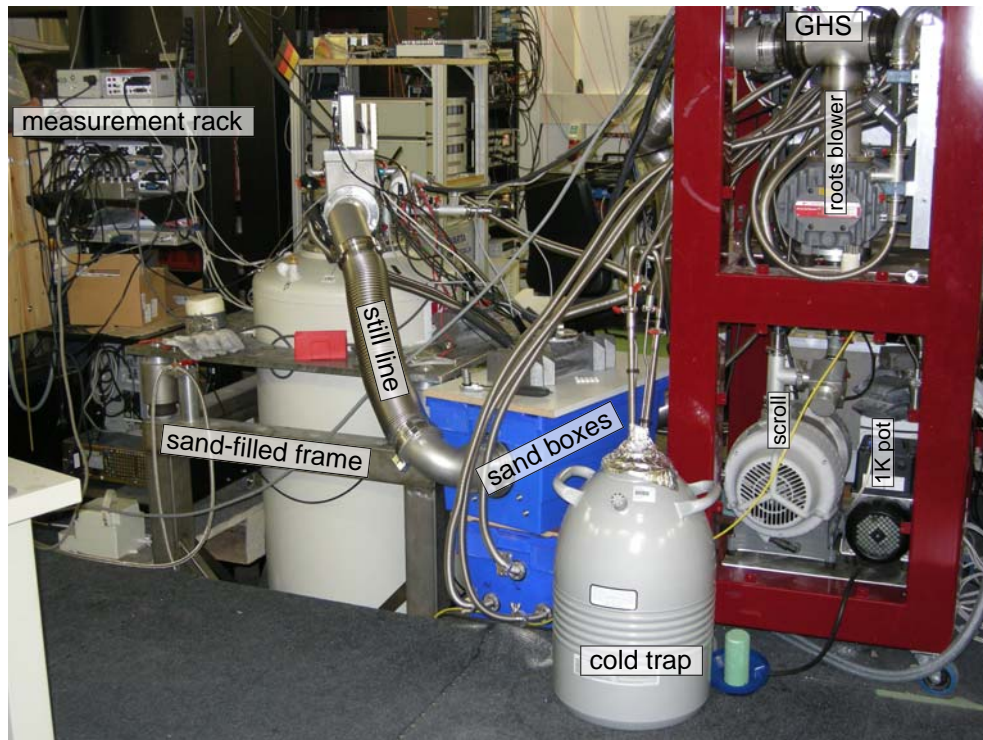
Figure 5.1.: Photograph of the whole set-up. The set-up can be divided in three parts. Data acquisition on the left, cryostat in the centre, and gas handling system on the right.

One requirement for the set-up was a connection to a helium recovery system. This was done with copper tubes and hoses. For the helium bath of the dewar we used a rubber hose with a length of about 10 m. This length is necessary to attenuate the acoustic noise coming on the one hand from the recovery, and on the other hand from the 1K pot pump. We had the possibility to shortcut the rubber hose with a metal bellows during helium transfers because the rubber does not withstand cryogenic temperatures. The second port that was connected was the outlet of the 1K pot pump. In order to avoid an overpressure in the 1K pot,

me mounted a one-way valve and an overpressure valve between the pump and the recovery.

Since vibrations are serious issues in a demagnetisation experiment we had to take care of that problem. Several measures were taken one of which was the sand-filled boxes. We fed all the pumping lines through boxes in which mechanical vibrations from the pumping line are transferred into friction between sand grains and hence, the vibrations are eventually dissipated into heat. Besides the sand-boxes, the pumping lines were clamped on the table except for the large-diameter still line to provide additional vibration damping.

Furthermore, we distributed lead bricks on the system. We had different types, most of them with a mass of around 11 kg each. We put three bricks directly on the 1K pot pump to dampen the vibrations at their origin. We put four on top of the sandboxes and a few inside. All in all we arranged about 12 bricks on the table, three in each corner. Note that the bricks on the table were also used to level the table and to clamp the pumping lines between them. The table rested on four air springs which provided further vibration damping. The table frame below the air springs was assembled from hollow stainless steel profiles which were filled with sand to provide both, a larger mass and dissipation. The table itself was positioned on a level $\sim 1.6\,\text{m}$ below the lab floor. On the one hand this condition was set by the shape of the accelerator hall, but on the other hand, this provides a convenient working height.

5.3.1. Magnets and Dewar

A larger sub-project was to provide magnets for both, the demagnetisation and the heat switches. The task was to adapt a magnet which was the remainder of a disassembled low-temperature set-up to our needs. Besides the main solenoid, we had to incorporate the heat switch magnet. Since a top flange that fitted onto the dewar and that had an appropriate bore for the DR the task simplified to building a structural support and leads for the magnets. The heat switch magnet had yet to be build completely.

The main solenoid consisted of the main coil and two compensation coils. More-over, it had a lambda plate, i.e. it could be pumped on. It provided 8 T in normal operation and 10 T if pumped. In a first step we removed the lambda plate because its diameter was too large to fit into the bore of the dewar. We also had to investigate a cable tree attached to the magnet. Some of the wires were presumably connected to safety diodes on the bottom part of the magnet. One pair of wires was identified as persistent switch heater. This was accomplished by measuring the mutual resistance between the wires one of which was found to have a value $\sim 100\,\Omega$ which is typical for such resistors.

The structural support has to be rigid on the one hand which favours metals.
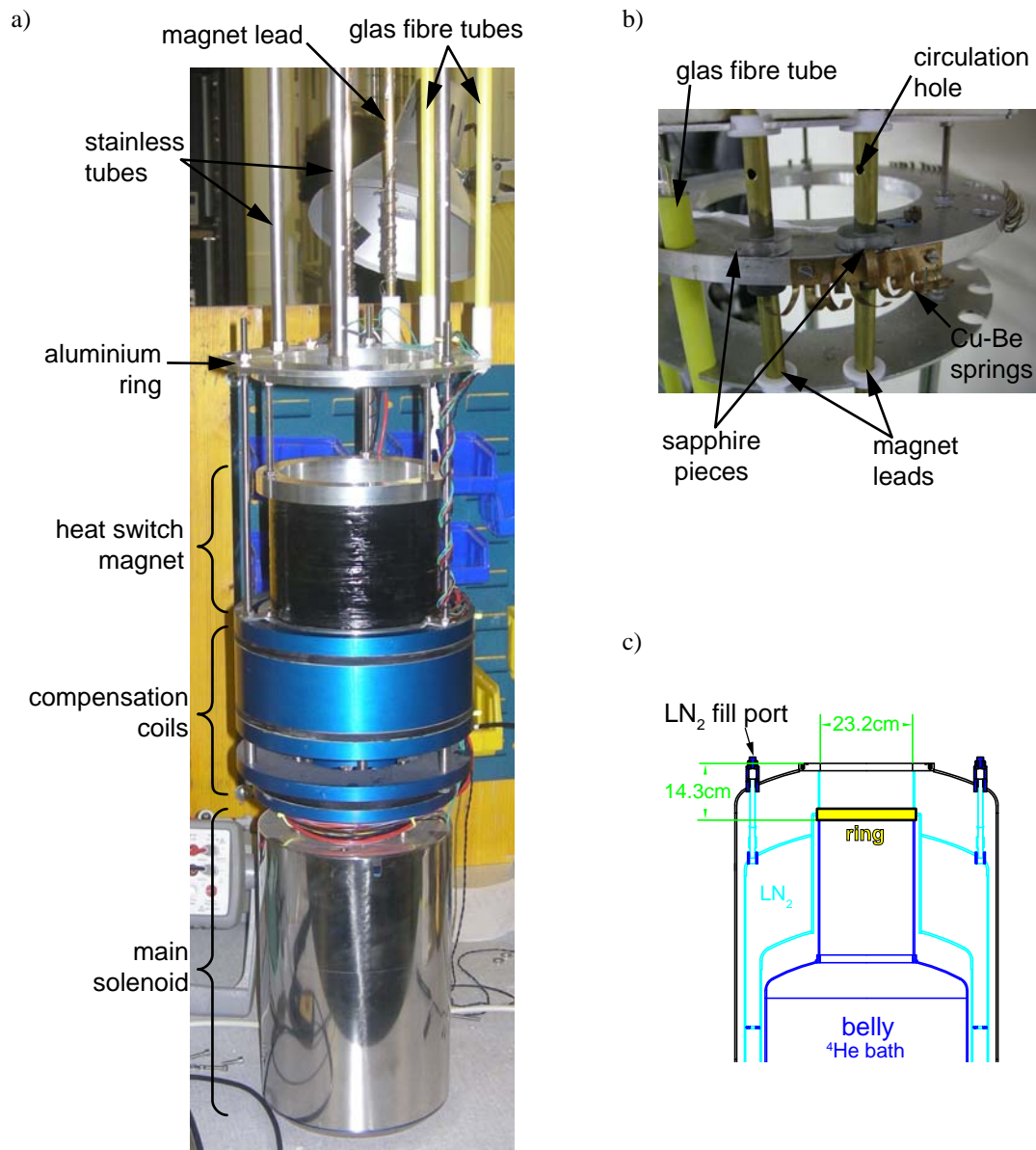
Figure 5.2.: a) Photograph of the magnets. b) Photograph of the baffles. The
CuBe springs were intended to make thermal contact to a metal
ring inside the dewar. c) Technical drawing of the dewar. The
metal ring is highlighted in yellow.

But on the other hand, it should conduct as little heat as possible to keep the
helium consumption low which speaks against metals. We chose stainless steel as
material which is a strong metal but has yet a worse thermal conduction compared

to other metals [54]. The support was divided into two sections. The lower part consisted of three threaded rods (250 mm, M5) that were screwed into pre-existing tapped holes in the top compensation coil of the magnet. The top part was made of three stainless steel tubes (L~ 115 cm, OD 12 mm, ID 11.5 mm) that were screwed onto three threaded rods extending down from the top flange. The two sections were connected by an aluminium ring. In order to reduce the heat load on the helium bath further, we drilled holes into the steel tubes at the bottom and at the top to allow helium circulation inside. Thus, the helium vapour cools the tube from the inside, too.

The magnet leads were made from brass tubes (OD 8 mm, ID 7 mm). Brass has the advantage of a lower thermal conductance over copper. The drawback is that the ohmic heating is higher as long as a current flows. But since the magnet can be put in persistent mode the time during which current actually flows can be minimised. Hence, we preferred a low static helium boil-off over low ohmic heat dissipation. Like the stainless steel tubes, we drilled holes into the brass tubes to allow vapour cooling also from the inside. We soldered terminals, milled out of a solid block of OFHC copper, to the top end of the leads. The bottom ends were arrested in the aluminium ring, from which they were electrically insulated by a Teflon^{TM} piece. In order to contact the superconducting wire of the solenoid, we wound the wire around the brass tube and soldered it with standard Sb/Pb solder. Additional superconducting wires were attached parallel to the magnet leads along the lower ~ 0.5 m of the brass tubes. This shunts the lower parts of the brass tubes and allows the current to flow dissipationless as much as possible if these superconducting wires are immersed in helium.

Besides choosing specific materials and enhancing vapour cooling, we pursued another idea to reduce the helium consumption. The idea was to thermally anchor the leads as well as the support structure to the nitrogen bath. The dewar had a metal ring inside its neck that was in good contact with the nitrogen bath (see figure 5.2c)). We equipped one of the radiation baffles with Cu-Be springs that were pressed against that ring and hence established a metallic connection between the baffle and this ring (figure 5.2 b)). Decent thermal contact between the magnet leads and the baffle was eventually accomplished by inserting a sapphire piece between the two (figure 5.2 b)). Sapphire has a comparatively large thermal conduction around 77 K [49] but it keeps the magnet leads electrically insulated.

We measured the efficiency of this method in two separate cooldowns. In one the Cu-Be springs were attached, in the other they were removed. We determined the helium consumption with a superconducting helium level probe [99]. The consumption with Cu-Be springs removed was $\sim 5 \pm 0.8$ l/d as compared to $\sim 4.5 \pm 0.8$ l/d with them in place. The error is based on the assumption that the level can be read with an accuracy of ± 3 mm and a conversion factor of ~ 0.2 l/mm.

Taking into account that the manufacturer states static boil-off of $4.6\,l/d$ [100], and that the helium boil-off also depends on the nitrogen level which was not recorded, one cannot tell if we achieved a noteworthy improvement.

Eventually we had to incorporate a second magnet in order to operate the heat switches of the demagnetisation unit. Since each lead requires a separate switch each with a size of the order $1\,cm$, the magnetic field has to cover a large volume. It is too large to provide a homogeneous field without building a magnet with complicated compensation coils or shim plates. Hence, we built a simple solenoid. Prior to winding, we did some field estimates for a coil of finite radius and length but for infinitesimally small thickness [101]. Figure 5.3 shows the field factor $|b|$ along the main axis of the coil and in radial direction. These calculations are done based on the dimensions of our coil: length $L = 10\,cm$, effective radius $R = 6.71\,cm$ and a winding density of 9458 turns per $10\,cm$. A more detailed description of the field profile and the dimensions of the coil are given in appendix C. The magnet
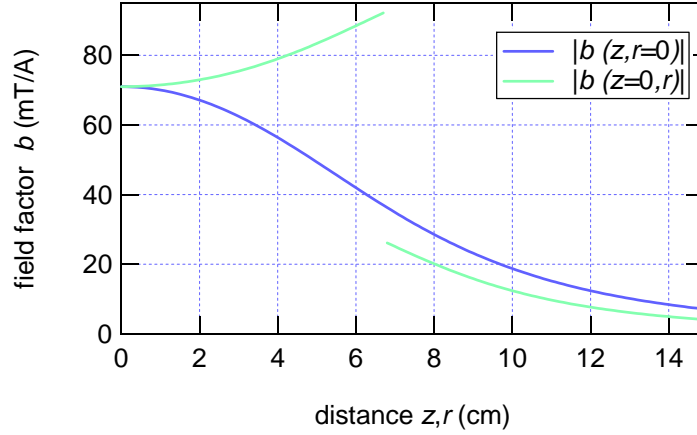
Figure 5.3.: Calculated field factor $|b|$ as a function of distance from the centre of the magnet along the main axis $|b(z, r = 0)|$ and in radial direction $|b|\,(z = 0, r)$. At $z = r = 0$ it is $|b| = 71\,mT/A$. The discontinuity at $r = 6.71\,cm$ reflects the infinitesimally thin thickness of the solenoid.

was wound from a NbTi wire with a diameter of $0.18\,mm$. The leads were made from brass wires with a diameter of $1.27\,mm$. In order to measure the magnetic field we mounted a Hall bar[1] close to the mixing chamber. It was $\sim 19mm$ below the mixing chamber, $\sim 18mm$ off centre and perpendicular to the cryostat's main axis. Thus there is a small angle between the applied field and the measured field. From the Hall resistance R_{H} we calculated the magnetic field according

---

[1]The Hall bar was fabricated by Sarah Heizmann and Kristine Bedner.

to $B_z = neR_H$ where $n = 2 \cdot 10^{11} 1/\text{cm}^2$ is the known charge carrier density. Figure 5.4 shows the measured field factor $|b|_z$ as function of the applied current
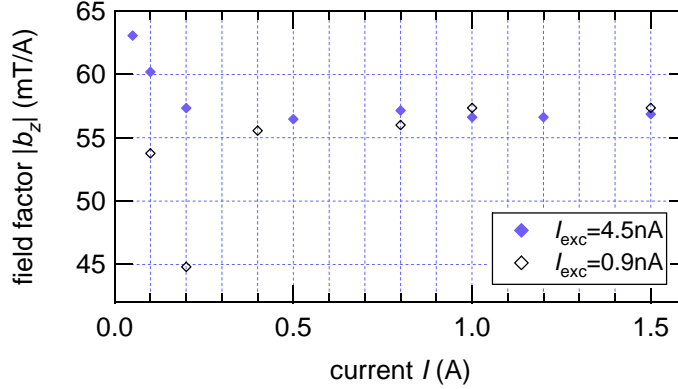
Figure 5.4.: Field factor of the heat switch magnet as measured with a HALL bar. Two different measurements are shown for two different excitation currents in the device as a function of current in the heat switch magnet.

in the heat switch magnet. For currents larger than $400\,\text{mA}$ the field factor is about $57\,\text{mT/A}$. At lower currents the field is small and the reading was probably influenced by a nearby CMN thermometer. However, the calculated value for this location is $\sim 69\,\text{mT/A}$ which is in reasonable agreement with the measured value. Besides the field factor, we determined inductance and resistance of the magnet. At room temperature we measured $4.5\,\text{k}\Omega$ which is in good agreement with a calculated value of $4.2\,\text{k}\Omega$. At low temperature, we measured inductance and resistance by monitoring the voltage V across the magnet terminals as a function of time while ramping the current at a constant rate $\dot{I}$. The voltage is then given by $V(t) = \dot{I}L + RI(t)$ where L is the inductance and R the residual resistance. We obtained $L \sim 9\text{H}$ and $R \sim 140\text{m}\Omega$.

In the same manner we measured inductance and resistance of the main solenoid. We obtained $\sim 15.5\,\text{H}$ and $\sim 5\,\text{m}\Omega$. The resistance is three orders of magnitudes smaller than the value given in the magnets specifications. This is most likely because it was originally equipped with different leads. The specifications state a field factor of $13.26\,\text{mT/A}$ but they do not give any inductance[2].

Apart from the main current leads and the heat switch magnet we installed a base heater and four resistors on the magnet that served as thermometers. They

---

[2]We started the work on the solenoid with very few information about the magnet. Only after a fundamental lab clean-up the manual showed up. It contains many values (homogeneity, resistances, ..) but for whatever reason it doesn't state the magnet's inductance.

were put on the bottom side of the solenoid, on one of the cancellation coils, on the aluminium ring, and on one of the baffles. All the required leads and the two leads for the persistent switch heater were run down in a glass fibre tube which was mounted as protection for the wires (figure 5.2 a)).

5.3.2. Dilution Refrigerator

The dilution refrigerator we used is a MNK126 from Leiden Cryogenics [102]. The key feature of this DR is its removable mixing chamber. Unlike most DRs, it allows to put wires and sinters directly inside as will be described in section 6.2.

However, a crucial property of a DR is its cooling power. We determined it the following way. A defined current is applied to a resistor inside the mixing chamber. The temperature then equilibrates at a temperature at which the removed power P_{rem} balances the applied power P_{app} and the residual heat leak P_0. At higher temperature we assume a simple polynomial for the removed power. Furthermore, we treat the removed power as root mean square of applied power and heat leak. Hence, the phenomenological ansatz

$$P_{\mathrm{rem}} = \sqrt{P_{\mathrm{app}}^2 + P_0^2} = aT_{\mathrm{MC}}^n \tag{5.1}$$

with fit parameters P_0, a and n. The result of the fit is shown in figure 5.5 a) with $P_0 = 2.2 \pm 0.4\,\mu\mathrm{W}$, $n = 1.69 \pm 0.01$ and $a = 0.10 \pm 0.01\,(\mu W/mK)^{1/n}$. Equation (5.1) matches remarkably well to the data. Note that the cooling power of the mixing chamber can also be tuned by changing the current in the still heater, i.e. the molar flow of ^{3}He . This data was taken for a flow that achieved the lowest base temperature. In cooldowns after these initial tests, a CMN thermometer read base temperatures of only $\sim 10\,\mathrm{mK}$ which corresponds to a residual heat leak of $\gtrsim 10\,\mu\mathrm{K}$. Three reasons could explain that discrepancy: (i) possibly the calibrations of the resistor is inaccurate, (ii) the load on the mixing chamber is truly higher because modifications were done and (iii) the resistance measurement is very sensitive to the way the system is grounded. It was observed that the resistance easily changes by a few tens of kΩ simply by changing the grounding at lowest temperatures. However, in order to give an estimate of the precooling time in section 6.1 we can use the cooling power extracted here for mixing chamber temperatures higher than $25\,\mathrm{mK}$ that we trust.

Besides the IVC shield, the DR was equipped with two additional radiation shields: one anchored on the still and the second anchored on the cold plate.

The DR had several leads for measurements. They comprised 2 times 12 twisted pairs some of which were used for thermometry. Furthermore, it provided 28 thermocoax cables. These have a length of $\sim 1.5\,\mathrm{m}$. Two different types were installed giving a resistance of either $\sim 180\,\Omega$ or $\sim 95\,\Omega$. The capacitances of the

a)
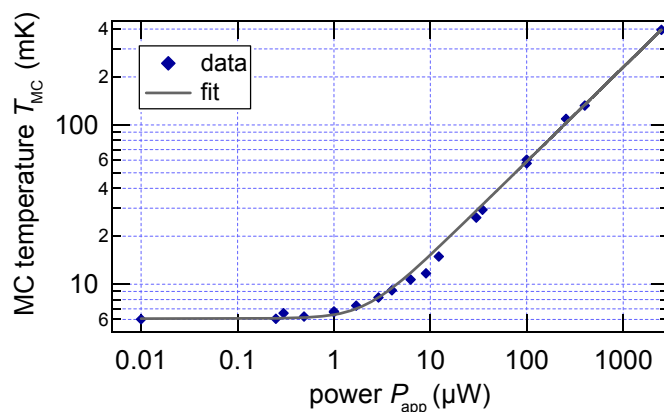
b)
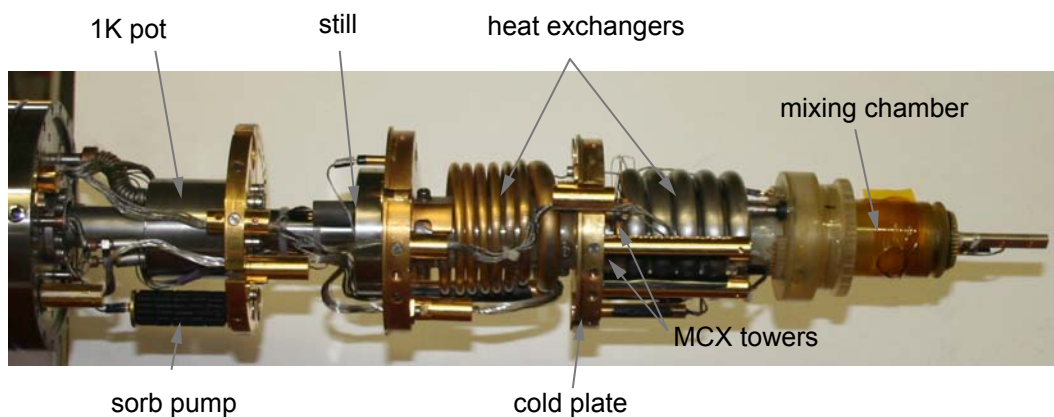
Figure 5.5.: a) Cooling power of the mixing chamber. The graph shows applied power versus equilibration temperature. The fit is according to phenomenological equation (5.1). b) Photograph of the dilution unit. Note that the mixing chamber is removeable at a cone seal. The MCX towers are the low temperature ends of two bundles of thermocoax cables.

coax lines varied between a few and several 100 nF. At the low temperature side of the thermocoax we used low pass filters. Some where obtained from Leiden Cryogenics [102], some where fabricated in-house [73].

5.4. Electronics and Data Acquisition

Another task was to set up the electronic measurement devices and a personal computer for digital data recording.

A basic consideration in such a set-up is grounding. On the one hand a zero potential is needed as reference for measurements but on the other hand it can be a security issue, e.g. magnet power supplies react to magnet quenches automatically by monitoring voltages. We pursued the following concept to define the zero point potential. One point of the cryostat was connected to a ground terminal that we had installed. This was independent from the the ground provided by the public power grid. We then powered all devices through floating transformers to cut them from the ground of the public power grid and grounded them at the reference point on the cryostat. However, grounding straps where used to minimise small voltage differences between the ground terminals of the instruments.

The signals measured through the thermocoax cables were taken from the top of the cryostat through standard d-sub cables onto a break-out-box (BOB) which distributed the signals to single BNC connectors. Each line was equipped with a switch to allow for grounding the lead. This is done to protect nanostructures from being charged electrostatically which could otherwise destroy the sample. Furthermore, a $200\,\Omega$ resistor was mounted in the lead for similar reasons. Most of our instruments where then plugged into the BOB. One of the twisted pair bundles was used exclusively for thermometry. The signals were fed through a splitter box to separate the signals of the resistors from the CMN signals. The CMN was measured with a mutual inductance bridge. Only after moving to the new set-up we changed to measuring it with a lock-in.

In order to record the data digitally we used a personal computer. Data was taken mainly using IGOR [103], except for the CMN thermometer which was read using LabVIEW [104]. The communication between the computer and the instruments was accomplished with GPIB interfaces, except for the CMN thermometer which was read with another bus system. To make sure that the instruments are not grounded through the bus we employed optical isolators to separate the instruments from the computer galvanically.

Besides recording data, the computer could also be used to control the temperature of the mixing chamber. It was connected to a AVS-47 ac resistance bridge and a TS-530 temperature controller [105] which in turn where hooked up to the cryostat.

Finally, one detail of the DR has to be mentioned. The main axes of the cryostat was bent. A plastic tube extended down from the cold plate to the mixing chamber along the main axes to support it structurally. Besides this main structure, the ^{3}He return line and the still line influenced the structure. On the one hand, this led to an overall curvature of the cryostat's main axis but on the other hand the

mixing chamber was not held in place rigidly, i.e. it facilitated vibrations. These effects could be reduced by re-tightening a screw that connected the plastic tube and the mixing chamber. Moreover, we put spacers on the demagnetisation unit which held it against the cold plate shield.

5.5. New Set-up

The department of physics had another nuclear accelerator dismantled. This set new lab space free into which we could expand. We seized the opportunity to build a set-up with fewer limitations. Hence, we did the best we could in a reasonable way to build a new set-up including a shielded room and better vibration damping.

Shielded Room

Although one can purchase shielded rooms commercially and have it installed, we decided to build the room ourselves for economic reasons. The bearing structure of the shielded room is a truss of aluminium profiles. Wooden boards were then put on that frame and the whole room was covered with metal sheets. We used tinplate for most of the coating. In the vicinity of the pit where the magnet was intended to be operated we used non-magnetic copper because we wanted to be sure to avoid large forces on both, the magnet and the magnetic tinplate. However, both materials can be soft soldered which gives a radiation tight but also economic connection. Furthermore, the metal sheets can be bent in almost any shape. Since the floor is exposed to stronger wear and tear, we put two layers down. In the course of the work the vibration isolation table (see below) was set up and the room was built around the table.

The room has two doors: a main door and a trapdoor on top of the room. The latter is needed to lower the refrigerator into the dewar. Both of these doors were bought commercially [106]. From the same supplier we also obtained filters for the magnet leads and so-called attenuvents. The latter are tin-coated metal honeycomb grids. Two of them were mounted to allow for rapid gas exchange in case of a magnet quench.

Vacuum Lines

Besides the shielded room itself we had to design and built the pumping tubes. Since the pumps are obviously further away from the fridge the tubes are longer as they have been before. We calculated the pumping efficiency [53] and found that the required length should not reduce the flow of ^{3}He . As pumps went outside the room feedthroughs had to be incorporated. In order to operate some of the

valves of the DR and to float the vibration isolation table a pressured air line had
to be brought inside, too.

Electrical Feedthroughs

Another part was to plan the electrical feedthroughs
which included the measurement leads, the magnet leads
and the wires for the DR, i.e. valve control, vacuum gauge
read-out etc. The basic concept of filtering is shown in the
schematic on the right. A π-filter is placed in the plane of
the shielded room wall. It consists of two capacitors and
one inductor or resistor (here an inductor). The signal
is fed through the inductor. The two capacitors, one in
front and one behind the inductor, provide a capacitive
coupling to ground. Thus, high frequency signals are attenuated. On the one hand,
high frequency signals have a low impedance to ground ($|Z| = 1/\omega C$) and on the
other hand a high transmission impedance ($|Z| = \omega L$). This way, high frequency
signals in the leads are attenuated but it disturbs the integrity of the Faraday
cage because the leads have to be insulated from the shielded room wall. Hence,
high frequency radiation can enter the cage. In order to allow as little radiation
as possible to enter, the whole feedthrough is enclosed with a metal box (green
shaded area).
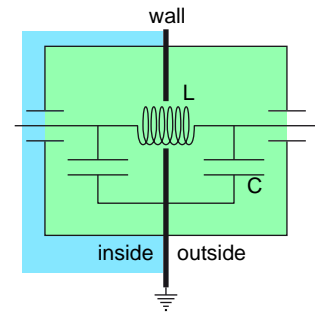
We built eight BNC feedthroughs exactly this way. The same is true for the
magnet leads. For those, we used high current filters [106]. One of the same type
of filters was used for a 220V power line. However, most of the feedthroughs were
made in a simpler way. We purchased standard $\pi-$filters embedded in a d-sub
housing. We then cut slots into a 10 mm thick brass plate to fit in the $\pi-$filters.
The brass plate was in turn soldered to the tin plate. Unlike the concept described
above, these feed throughs do not comprise a metal box. Valve control, vacuum
gauge read-out and the helium level probe were fed through such filters, too.

Attenuation Test

Once we completed the shielded room including all feedthroughs, the doors and the
ventilations, we performed an attenuation test. Two simple methods were applied:
mobile phones do not work properly nor did a transistor radio. However, we did
some more careful tests with a frequency generator and a spectrum analyser. The
signal was simply emitted from an open BNC cable. We used an Agilent E8257D
Analog Signal Generator to create signals at 300 MHz, 400 MHz, and 500 MHz at
a power of 25 dBm which was the maximum available. On the reception side we
employed a single-turn coil wound from a copper wire of diameter 2 mm. The

area of the coil was $\sim 20\,\mathrm{cm^2}$. The signal was analysed in a HP3561A Signal
Analyser. The radiation emitted from the open BNC cable could clearly be seen
in the spectrum of the coil while holding emitter and receiver about 20 to 30 cm
apart with nothing in-between them. Then we emitted the radiation in the vicinity
of the shielded room and tried to receive it inside while attempting to keep the
distance between emitter and receiver at a few tens of cm. We couldn't see any
transmission around the feedthroughs and the doors. But we found tiny leaks
around the attenuvents. After putting some conducting copper tape around their
margins the leaks disappeared. Note, that the hand lever that locks the door has
to be fully closed to ensure radiation tightness. It was observed that only a tiny
gap allows radiation to enter the room. A more careful test is planned with more
suitable equipment.

Vibration Damping

One issue that should be improved as compared to the old system is vibrations.
Several features are intended to suppress them. The first is a vibration isolation
table [107]. The table plate has a lateral dimension of $170\,\mathrm{cm} \times 125\,\mathrm{cm}$ and a
thickness of $\sim 31\,\mathrm{cm}$. It is made of a steel honeycomb core and has a mass of
$\sim 360\,\mathrm{kg}$. In the centre a recess was cut to lower the dewar inside. The dewar was
bolted to the aluminium plate taken from the old set-up which was then put down
onto table with a wooden board (thickness 8mm) in-between.

Like in the old set-up, all tubes were fed through a sandbox. But in contrast to
the old one which had partially collapsed upon the forces exerted by the vacuum
lines we built a more rigid one. Furthermore, we anchored the tubes in a concrete
block on the table. In order to reduce the vibrations of the still pump we mounted
it on a construction of concrete blocks and the line itself was bolted to a wall
of concrete blocks. The still line was interrupted by a rubber piece between the
pump and that wall. Besides the still pump, we also mounted the 1K pot pump
onto a separate concrete block. Beneath the concrete blocks and the pumps we
added rubber mats to prevent the vibrations from travelling through the ground.
Another feature to reduce the vibrations is mass. We put another concrete block
and some lead bricks on the table, on the one hand to increase the mass but on the
other hand they help to level the table. The acoustic noise that can return from
the helium recovery was suppressed by leading the evaporated helium through a
long rubber hose.

Figure 5.6 shows three spectra of vibrations. One was taken on the table of
the old set-up and two were taken on the new table. The trace of the old set-up
was recorded while the DR was in normal operation, i.e. the pumps were running.
The table was floating which means in that case that the air springs were fully
pressurised and the table as pushed against a guiding and arresting mechanism.
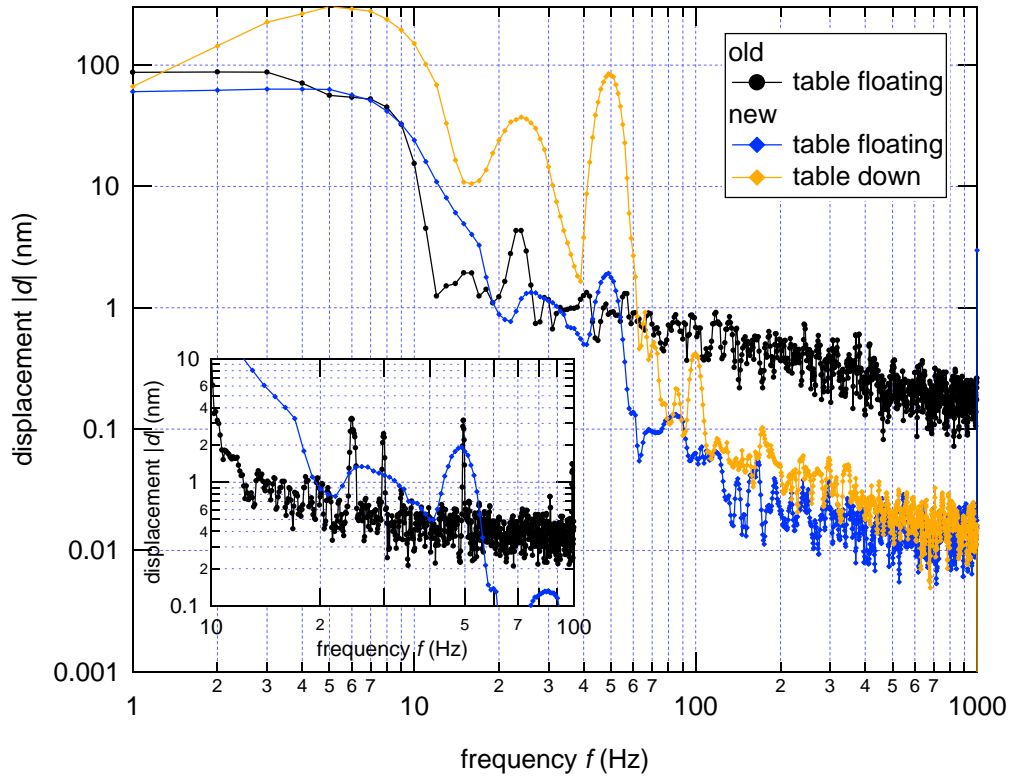
Figure 5.6.: Vibrations spectra the old and the new set-up. The graph shows
amplitude of the displacement $|d| = \sqrt{d_x^2 + d_y^2 + d_z^2}$ as measured on
the table surface. The inset shows the spectrum from 10 to 100 Hz
with a higher resolution. The 50 Hz peak then becomes visible.

The traces taken on the new set-up were also recorded during normal circulation for
both, the table floating and non-floating. The new set-up clearly shows a better
vibration damping for frequencies above 60 Hz. Below, the spectra look similar
except for ~ 23 Hz where the new set-up is better and for ~ 12 Hz where the
old set-up was better. The data in the range of a few Hz suffers from the transfer
function of the sensor (JRS Vibration Analyzer VA-2) which drops to 50% at 1 Hz.
At the upper end of the frequency range it drops to 80% at 1 kHz.

Note, that the spectrum of the old set-up does not show a pronounced peak at
50 Hz. This peak could be resolved for a lower bandwidth from 1 to 100 Hz. The
peak then becomes more pronounced and shows that it has reduced on the new
set-up. Furthermore, the inset shows a peak at 100 Hz which is a multiple of 50 Hz
and two peaks at lower frequencies, one at ~ 23 Hz and a second at ~ 30 Hz. The
23 Hz peak disappeared when we turned off the roots blower pump. The 30 Hz

peak became less pronounced with all pumps off but it didn't vanish completely. The source of that vibration has not been found.

Conclusions

In conclusions we built a shielded room in a simple and economic way. Furthermore, we included different approaches of vibration damping that proved to have reduced the vibrations. Despite the longer pumping lines of the mixture circuit, the performance of the DR did not suffer, as we had expected.

Construction of the Novel Refrigerator

6.1. The Nuclear Refrigerators

The heart of the novel cooling scheme is a nuclear demagnetisation refrigerator incorporated in each measurement lead. As outlined in section 3.4.6 we decided to use copper as nuclear refrigerant. We purchased 5N copper plates from ACI Alloys [108] with a RRR~ 140.

Having settled on a material we need to find a shape. A hexagonal rod takes advantage of space best. On the other hand we have to consider eddy current heating. If we assume a copper plate with a width of 20 mm, a thickness of 2 mm and a length of 100 mm we get a power of 0.6 nW for a ramp rate of 1 T/h, according to (3.75). Calculating the power for the same volume and length but for a cylinder we get 4 nW. For a hexagonal cross-section we would expect approximately the same as for the cylinder, i.e. roughly an order of magnitude more than for the plate. For this reason we chose a plate geometry.

Traditional demagnetisation refrigerators contain one copper body. The electrons in it rest such that they have time to thermalise with the nuclei. If the electrons propagate through the copper due an external voltage, one could argue that they do not have enough time to thermalise. However, a simple consideration based on the DRUDE model shows that the electrons can thermalise easily. The electrons thermalise to the nuclei through the KORRINGA process (3.56). The time scale is set by the KORRINGA constant. If we plug in the heat capacities of the

nuclei (3.39) and the electrons (3.12) into (3.56) we get the thermalisation time:

$$\tau_\mathrm{t} = \kappa \frac{\gamma}{\Lambda_\mathrm{n}} \frac{T^2}{B^2} = 230 \left[\frac{\mathrm{T}^2}{\mathrm{K}^2}\right] \frac{T^2}{B^2} \tag{6.1}$$

where the latter equality is for the values of copper [49], $\Lambda_n = 3.2\,\mu\mathrm{J} \cdot \mathrm{K}/\mathrm{T}^2 \cdot \mathrm{mol}$, $\kappa = 1.2\,\mathrm{K} \cdot \mathrm{s}$, $\gamma = 0.7\,\mathrm{mJ}/\mathrm{K}^2 \cdot \mathrm{mol}$. Furthermore, we assume $T_\mathrm{e} = T_\mathrm{n}$ which is true for sufficiently small heat leaks.

The average or drift velocity of a charge carrier in a solid can be written as [61] $v_\mathrm{d} = I/neA$ with charge carrier density n, current I, elementary charge e, and cross-sectional area of the conductor A. If the conductor has the length ℓ the dwell time of the electron is

$$\tau_\mathrm{d} = \frac{\ell}{v_\mathrm{d}} = \frac{\ell neA}{I} = 54 \cdot 10^3 \,[\mathrm{As}] \frac{1}{I} \tag{6.2}$$

where the latter equality is again for the value of copper, $n = 8.5 \cdot 10^{22}\,1/\mathrm{cm}^3$ [61], and our plate geometry $A = 40\,\mathrm{mm}^2$, $\ell = 100\,\mathrm{mm}$. The current in the plate will be for sure smaller than $1\,\mathrm{mA}$ and the plate will have a temperature in the range of $\sim 10\,\mathrm{mK}$. If we assume that we have demagnetised to a final field of $100\,\mathrm{mT}$ we obtain

$$\begin{aligned} \tau_\mathrm{t} &\approx 2.5\,\mathrm{s} \\ \tau_\mathrm{d} &\approx 5.5 \cdot 10^7\,\mathrm{s} = 1.7\,\mathrm{a} \end{aligned}$$

The electron lingers in the copper for a time span seven orders of magnitudes longer than it needs to thermalise. In other words, the drift velocity must be less than $4\,\mathrm{cm/s}$ if we take τ_t as given. In fact it is $2\,\mathrm{nm/s}$ with these numbers. Note that the drift velocity does not depend on temperature nor on resistance (if the current is given). This estimate shows that the electrons can thermalise to the nuclei, even if they are biased.

Next, we can estimate how long the plates stay cold for a given heat leak. In figure 6.1 we estimate how long it takes to warm up the copper. The above amount of copper corresponds to $0.56\,\mathrm{mol}$. Furthermore, we assume that we precool to $15\,\mathrm{mK}$ to subsequently demagnetise from $8\,\mathrm{T}$ to $80\,\mathrm{mT}$. The traces in figure 6.1 are for heat leaks of 1, 4 and $10\,\mathrm{nW}$, respectively. For $4\,\mathrm{nW}$ the copper has warmed up after $\sim 5\,\mathrm{h}$. Since this a short time to do experiments we can a posteriori justify that the cylindrical/hexagonal geometry considered above was rejected. Instead a heat leak of less than $1\,\mathrm{nW}$ should be achieved to have a reasonable amount of time for experiments. Note, that the $4\,\mathrm{nW}$ calculated above are for a ramp rate of $1\,\mathrm{T/h}$ and the calculations shown figure 6.1 are at constant field. However, we take $1\,\mathrm{nW}$ as a 'magic number' for a tolerable heat leak.
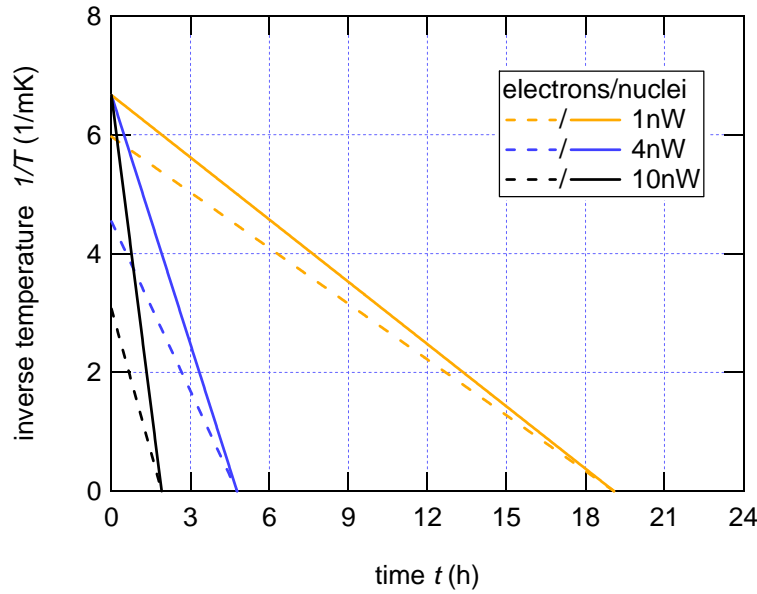
Figure 6.1.: Estimates for the warm-up time based on (3.60) and (3.58). The traces are estimates of the time required to warm up 0.5 mols of copper after demagnetising it from 8 T to 80 mT. The demagnetisation was started at 15 mK, hence the final (nuclear) temperature is 150 μK.

Besides the time the copper stays cold, we can estimate the precooling time. According to (3.45) we have a heat of magnetisation of ~ 10 mJ if we want to precool to 10 mK at 8 T. If we further assume that the cooling power of the DR is the bottle neck we get a precooling time of the order 0.5 h based on (5.1). In fact, we precooled (the electrons) to ~ 30 mK with in ~ 1.5 h (figure 7.7). Below that temperature the cooling power of the mixing chamber gets small and other resistances in the cooling line become increasingly relevant.

Eventually we have to consider how the copper plates are held together and in place. On the one hand, we need a strong structure that can for example withstand magnet quenches but on the other hand, we have to prevent the copper from being in thermal contact with hotter parts in the cryostat. We finally decided to tie the copper plates together [109] with dental floss and have one plate in the centre which was intended to be glued in an Araldite$^{\text{TM}}$ beam to support the whole bundle. We called this plate 'sarcificial' because it was sacrificed to structural purposes and not meant to be part of a measurement lead [109]. The sacrificial plate had a size of 2 mm $\times$ 20 mm $\times$ 140 mm whereas the usual plates had dimensions of 2 mm $\times$ 20 mm $\times$ 100 mm. In order to improve the thermalisation of the electrons
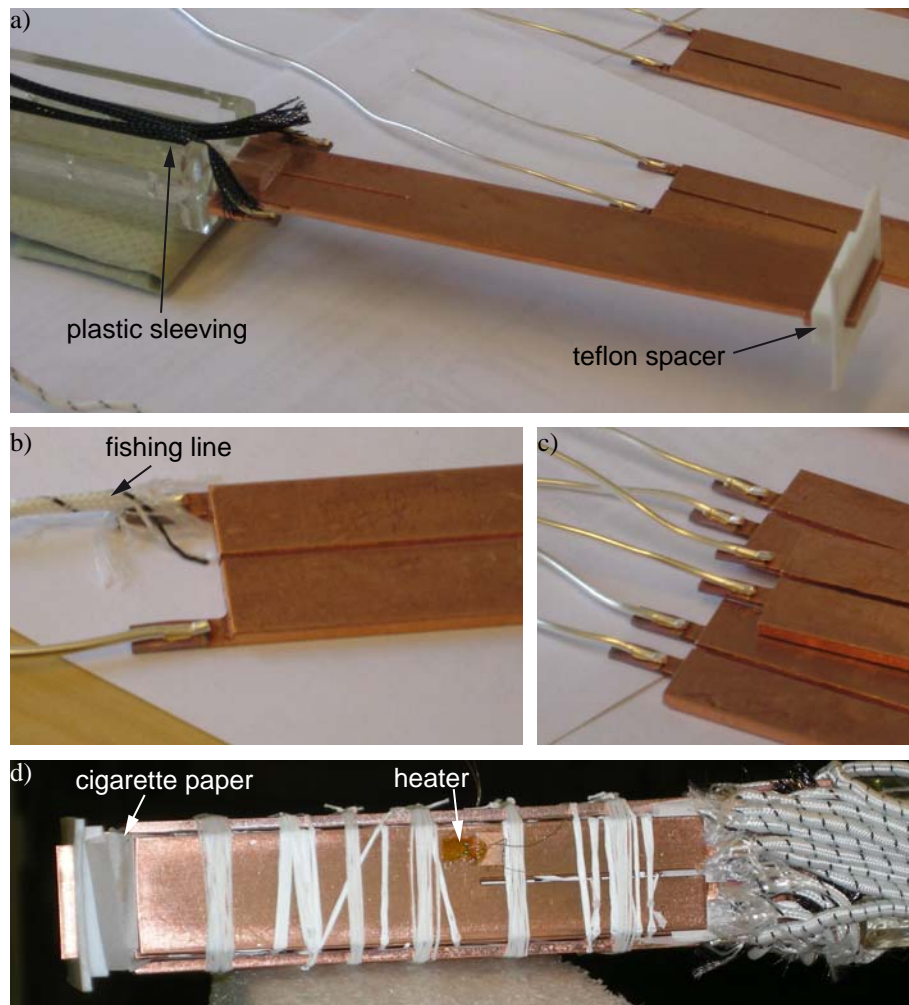
Figure 6.2.: The demagnetisation stage. a) The sacrificial plate which was glued into the Araldite$^{\text{TM}}$ beam for mechanical support. The plastic sleeving was intended to insulate the wires, one from another. b) and c) The two types of plates. In b) you can see a section of fishing line that served as insulation between the wires, too. d) The complete demagnetisation stage. We used strain gauges as heater and cigarette paper as additional insulation.

in the copper and to reduce the eddy current heating we cut 40 mm long and 1 mm wide slits in each plate, including the sacrificial plate.

The copper plates and the complete bundle are shown in figure 6.2. The sacrificial plate, after it was glued into the Araldite$^{\text{TM}}$ beam, is shown in figure 6.2 a). It was equipped with two wires for precooling which were wrapped in black

plastic sleeving. At the bottom a Teflon$^{\text{TM}}$ spacer is mounted which was supposed to prevent the demagnetisation stage from both, touching the innermost radiation shield and vibrating too much. In the centre row some of the plates are shown. There were basically two types which can be grouped according to their welding taps which were towards the outside, b), or to the inside, c). In b) and c) you can also see the silver wires which were welded to the plates before the bundle was tied together. One wire in figure 6.2 b) is wrapped with a commercially available fishing line [110] which we used for all wires to insulate them from one another and from ground. This fishing line is a hose braided from plastic fibres.

The lower most picture shows the complete bundle. We stacked the bundle the following way. We put a plate onto the sacrificial plate and tied it with dental floss. Rolled-up Teflon$^{\text{TM}}$ tape was put in between as insulation. Then the second plate was mounted the same way, but on the other side of the sacrificial plate. Then a plate on the other side again but this time with the other weld tap arrangement. This alternating sequence was repeated until plates 11 and 12 were then tied to the sides (perpendicular to the other plates). In order to prevent the stack from sliding down we had added a small stub on the sacrificial plate. Furthermore, we added cigarette paper between the plates as can be seen in figure 6.2 d) on the left. Although feeling quite rigid to the touch the plates slid. So we frequently added more cigarette paper or sections of shrink wrap in some parts or pushed the plates into position again.

Finally, we added heaters on the plates. For that purpose we employed strain gauges [111] with a resistance of $120\,\Omega$ each. They were connected with superconducting wires of a length of about $50\,\text{cm}$ to prevent the plates from from being in thermal contact with stages of higher temperature . You can see one heater in figure 6.2 d). Two were mounted immediately, two more followed later, as we had realised that they were very useful. They were glued down with GE varnish and insulated from the plate with cigarette paper.

6.2. Mixing Chamber and Sintered Silver Heat Exchangers

A crucial point in our approach is to thermalise the leads well to the mixture of the DR's mixing chamber. Since the mixing chamber of our DR was removable, we could feed the measurement leads through the mixing chamber where they passed through a section of sintered silver for efficient heat exchange. Such a sintered silver heat exchanger (SSHE) is composed of compressed silver powder.

In a first step we built a sinter set-up. Three parameters can be used to control the sinter process: the temperature, the compressing force and the atmosphere.
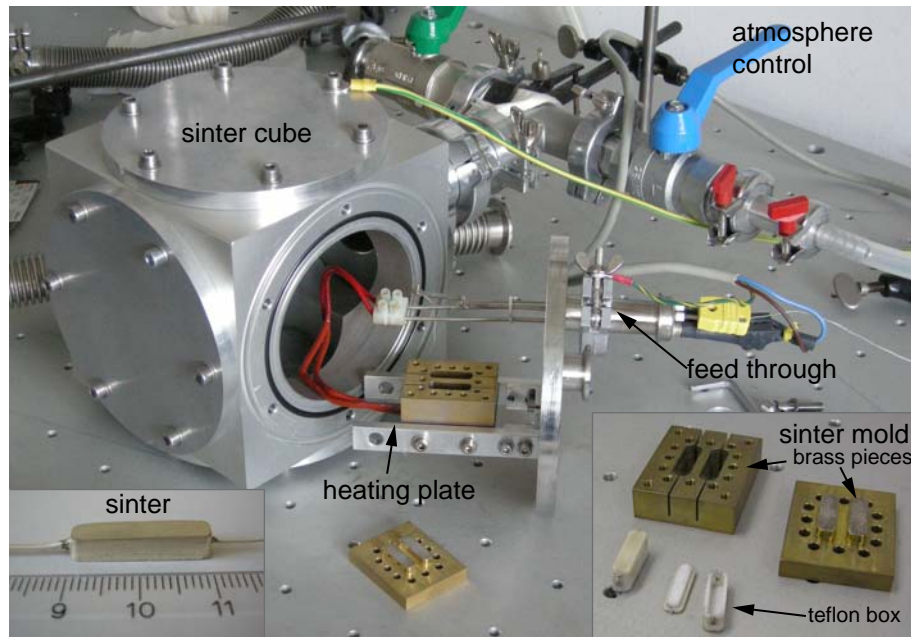
Figure 6.3.: Photograph of the sinter set-up. The sinter cube was adopted from a vacuum set-up. The press was mounted on a plate which was equipped with vacuum flanges. One flange was used to measure the pressure in the cube, the other was used to feed through the heating wires and the thermocouple leads. In the back, some valves can be seen that we used to control the atmosphere. The bottom-right inset shows the brass pieces and the Teflon^{TM} boxes in which the silver was sintered. The bottom-left inset shows a completed sinter.

The latter can be divided again into the pressure and the type of gas. The whole press is mounted on a copper base plate which has a recess where a heating element was plugged in. A thermocouple thermometer is attached on the copper block to measure its temperature. A commercially obtained control unit, a Panasonic AKT4111100J, was used to set a temperature. The actual press was bolted onto the copper plate. It consisted of two brass pieces and two Teflon boxes each with a small lid. Figure 6.3 shows the whole set-up. The lower brass piece was bolted onto the copper plate. The Teflon^{TM} boxes were then placed in the corresponding notches and filled with silver powder. Afterwards, the Teflon^{TM} lids and the upper brass piece were mounted. Tightening the screws applied pressure onto the silver powder. The whole press was mounted in a cube which could be sealed vacuum tight and hence allowed us to control the atmosphere. Based on different recipes [93, 112–114] we tried to bake our SSHEs by trying to find the optimal parameters

[92, 115]. We found that at least 250 °C have to be applied to actually sinter the
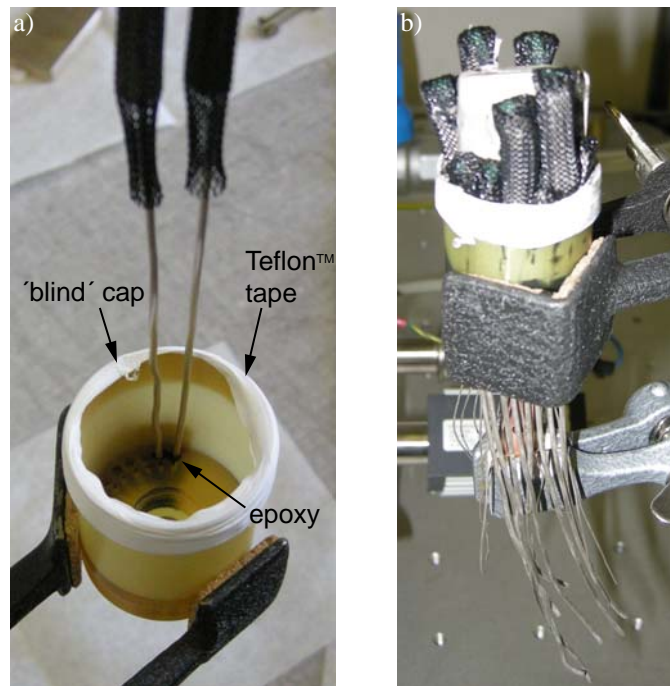
Figure 6.4.: MC plug during the assembly. a) Two silver wires before they were pulled through. A drop of epoxy was put on the through holes before we fed the wires through. Teflon^{TM} tape prevented the cone seal from being accidentally spilled with epoxy during the process. b) The completed MC plug during the curing process. It was held in a clamp throughout, to ensure that the epoxy flows to the bottom.

powder. We choose a 'Silver Nanopowder' with a nominal grain size of ~ 150 nm and a purity of 99.95 % [116]. The surface areas of the sinters were then measured with a standard BET method [115, 117] which is based on gas absorption on the sinter surface. We found surface areas of around $1.9 \, \text{m}^2/\text{g}$ which is in good agreement with values reported elsewhere [112–114]. We finally decided to bake the powder for 1 h in a He atmosphere at 1 bar and at 260 °C.

The leads had been put into the silver powder when we were filling it into the Teflon^{TM} box. This way the sinter could be firmly attached to the leads. We made the leads from silver wire of 5N purity obtained from ESPI [118]. On the low temperature side the diameter was 1.27 mm on the other side 0.5 mm. The wires were annealed at ~ 820 °C for 5 to 7 hours in a constant flow of about 0.5 l/min of nitrogen prior to sintering. The RRRs achieved were almost 2000. We tried to

avoid cold work on the wire during processing as much as possible because it can reduce the RRR significantly (~ 400). Figure 6.3 shows a SSHE in the lower-left inset. The cross-sectional area is 4 mm by 4 mm, the length 20 mm.

Once the sinter production was done the mixing chamber had to be built. We had a 'blind' cap for the mixing chamber available. In that sense 'blind' means that it was a cap that closed the mixing chamber so that it was possible to circulate the mixture but there was no possibility to thermally anchor any device or apparatus. This blind cap was modified to house 16 SSHEs as described above and a coldfinger. The latter was meant to hold the weight of the whole demagnetisation stage and to provide a cold stage at mixing chamber temperature. The recipe was adopted from [93]. It was basically a copper piece with through holes on one side and a slab on the other. We sintered silver powder onto the slab to thermalise it in the mixing chamber [92]. The slab was electroplated with a 10 μm layer of silver before. The dimensions of the copper slab were 25 mm $\times$ 35 mm $\times$ 1 mm and the sinter was 1.5 mm high on each side. The other side of the coldfinger was a flattened rod of 8 mm diameter.

Figure 6.4a) shows the first steps of the mixing chamber assembly. In the bottom of the blind cap you can see the holes for the silver wires and the large hole for the coldfinger. We put some black Stycast 2850 epoxy onto the holes before feeding the wires through. The sinters were covered with plastic sleeving to prevent them from touching each other. This way all wires and the coldfinger were pushed into the beaker. Finally, we poured more epoxy onto the bottom of the beaker intending to make the bottom leak tight. The whole assembly was left to cure the epoxy while the beaker and the coldfinger were held in place with clamps, as can be seen in figure 6.4b).

The mixing chamber was then tested where the first test was a vacuum leak test. Therefore the MC plug was mounted on the DR and we pumped with a leak checker. Since helium diffuses through the plastic of the MC plug the DR was hanging over a bath of liquid nitrogen and hence the MC plug was in evaporating nitrogen near 77 K. This way no signs of vacuum leaks could be observed.

In the next step we added two RuO_2 chips, each connected to two of the 1.27 mm wire extending out of the MC plug. We soldered a short section of copper wire on the smaller wire and MCX connectors to the other end of that copper wire. The MCX connectors were then plugged in the MCX towers. Thus we could measure the resistance of the chips. We then cooled down the whole DR and found that the chips read 18.2 kΩ corresponding to ~ 10 mK where a CMN thermometer mounted on the coldfinger read ~ 9.5 mK. In conclusion, the MC plug performs well. The electrons in the wires thermalise completely through the SSHE and the coldfinger cools also. Furthermore, the MC plug did not leak and in particular there was no superleak.

Within his masters project Tobias Bandi could measure electron temperatures of $T_e = 28 \pm 4\,\text{mK}$ in a HALL bar sample [92]. The sample was mounted on a 'conventional' coldfinger but the leads were thermally anchored through the above MC. The electron temperature measured is an upper limit which is set by the mobility of the sample.

6.3. Heat Switches

In a demagnetisation stage the heat switch is placed between the nuclear refrigerator and the precooling bath. It can be shifted between good thermal conductance to allow for efficient precooling and thermally isolating for sufficient adiabaticity. Different approaches are reported [69, 119–122] whereas the basic idea is the same throughout. A metallic superconductor is placed in a magnet allowing to switch between superconducting and normal conducting by applying zero field or a field above the critical field.

The figure of merit of a heat switch is the switching ratio which is the ratio of thermal conductance κ_e in the normal state to the thermal conductance in the superconducting state, κ_s. Using (3.20) and (3.22)we get

$$\mathcal{K} = \frac{\kappa_e}{\kappa_s} = \frac{\mathcal{K}_0}{T^2} \tag{6.3}$$

with $\mathcal{K}_0$ being a constant. This means that we assuem $T \ll T_c$ where the heat conductance in the superconductor is dominated by phonons. Note, that this ratio is independent of geometry which means that it holds for conduct*ance* as well as for conduct*ivity*. It is desirable to have a κ_e as large as possible and a κ_s as small as possible, hence it is desirable to have a $\mathcal{K}$ as large as possible.

In the approaches reported, different superconducting materials were used. Aluminium was found to show the largest switching ratios $1600\,\text{K}^2/T^2$ [121] as compared to $65\,\text{K}^2/T^2$ for indium [122]. Further candidates are tin or lead. Table 6.1 summarises the properties of some superconducting materials. From this table one can read that aluminium is the best choice. It has the best thermal conductivity and is mechanically the strongest material. The critical field is the lowest which means that the heat switch magnet does less likely interfere with other parts of the set-up. The critical temperature is roughly a factor 100 larger than the expected temperature range of operation as recommended [49]. A drawback of aluminium is its native oxide layer. Unlike the other three materials which can be soldered, it takes more effort to contact aluminium such as etching and plating techniques [121] or welding [119, 124].

This leads to the next question: how to make contact between the superconductor and the lead. The latter is usually copper or silver both of which can

Material	T_c(K)	B_c(mT)	elasticity (GPa)	κ(W/cm K)
aluminium	1.14	11	71	2.37
lead	7.2	80	16	0.35
tin	3.7	31	50	0.67
indium	3.4	29	11	0.82

Table 6.1.: Properties of superconducting materials that can be used as heat switch: critical temperature, critical field and thermal conductivity (300 K) [60]. Elasticity [123] exemplifies the mechanical strength of the materials.

be soldered easily. The disadvantage of a solder contact is that the joint can be contaminated with flux [53]. Some fluxes, in particular those for aluminium soldering, contain very aggressive chemicals which can lead to slow, long-term corrosion. Furthermore, most solders are superconducting with critical fields of $\sim 100\,\text{mK}$ [54] which is ten times higher than aluminium. Alternatively, a press contact is possible in any case. The pressure has to be high which can be achieved with a high pressure right at the start and a choice of materials that are stacked up such that the joint gets compressed even more by thermal contraction upon cooling down. Another method would be welding. Different welding techniques can be applied. But due to the oxide layer of aluminium it takes in any case an elaborate process. The fourth technique is a process [120, 125] that can be applied to join silver and aluminium. The two materials are brought into contact and a large current across the joint is applied. Joule heating melts the aluminium locally and the still solid silver is then pushed into the liquid aluminium. Subsequently, the current is interrupted and the pressure is released. The aluminium then solidifies around the silver wire whereas the native oxide layer was penetrated when the silver was pressed into the aluminium.

Since we used aluminium-silver switches which were 'fused' together this way for the demagnetisation stage, I discuss production and characterisation. We also tested indium which is briefly presented at the end of this section.

Lay-Out

Although aluminium is a type I superconductor magnetic flux can be trapped [49], e.g. in impurities. Along the magnetic field line the material is normal-conducting, i.e. a good thermal conductor. If the flux line connects the terminals of the switch the superconducting material is thermally shortcut. As a consequence the switch does not or only insufficiently close. This can be avoided by orienting the switch in an appropriate way or using a certain shape. That is why we chose a 'C'-shape in

which it is unlikely that a magnetic flux line connects the two silver wires at each end of the 'C'. Figure 6.5 a) shows a photograph of a heat switch. It was milled out of a solid piece of aluminium. We used grade 5N aluminium purchased from ESPI [118]. The dimensions can be read from figure 6.5 b). It has a base square of 7 mm by 7 mm. The cross-sectional area is 3 mm by 3 mm. The gap has a width of 1 mm and a nominal depth of 4 mm. As a result of milling it has a round end, indicated by the dashed semi-circle.
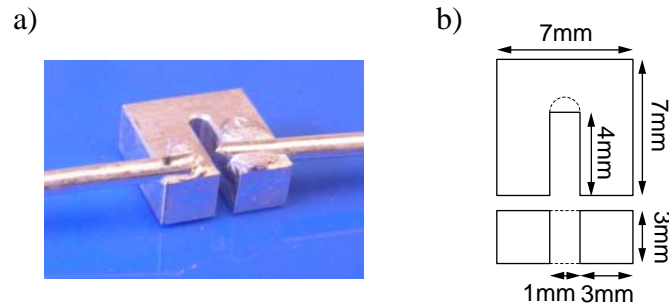
Figure 6.5.: a) Photograph of a silver-aluminium heat switch. b) Schematic including dimensions.

Production

In order to produce the switches we had to build a set-up which is described as follows and shown in figure 6.6. A standard press, as it could be used to make projections for projection welding, available in our in-house workshop, was modified to be used as a fuse press. The top chuck of the press was replaced by a Teflon^{TM} chuck to electrically isolate the press from the top electrode. An OFHC copper piece was mounted in the chuck. A copper clamp and the cable shoe of a current lead were screwed into that copper piece. The copper clamp held a graphite rod, 6 mm in diameter, that served as top electrode. On the bottom, a Teflon^{TM} plate was used as electrical insulator. On top of that, a cylindrical copper block was set. A graphite disc, serving as bottom electrode, was laid into a trough milled into the copper block. The current was supplied by a home-built source capable to provide 100 A/30 V.

Before the actual fusion process the silver was cleaned in a 50% nitric acid solution, the aluminium in 50% caustic soda. Since graphite is a brittle material, the top-electrode should frequently be filed or sanded into shape again to prevent graphite fragments from contaminating the joint.

The 'C'-shaped aluminium piece was put on the bottom graphite piece. The silver wire was then clamped between the aluminium and the top electrode. In

a)

b)
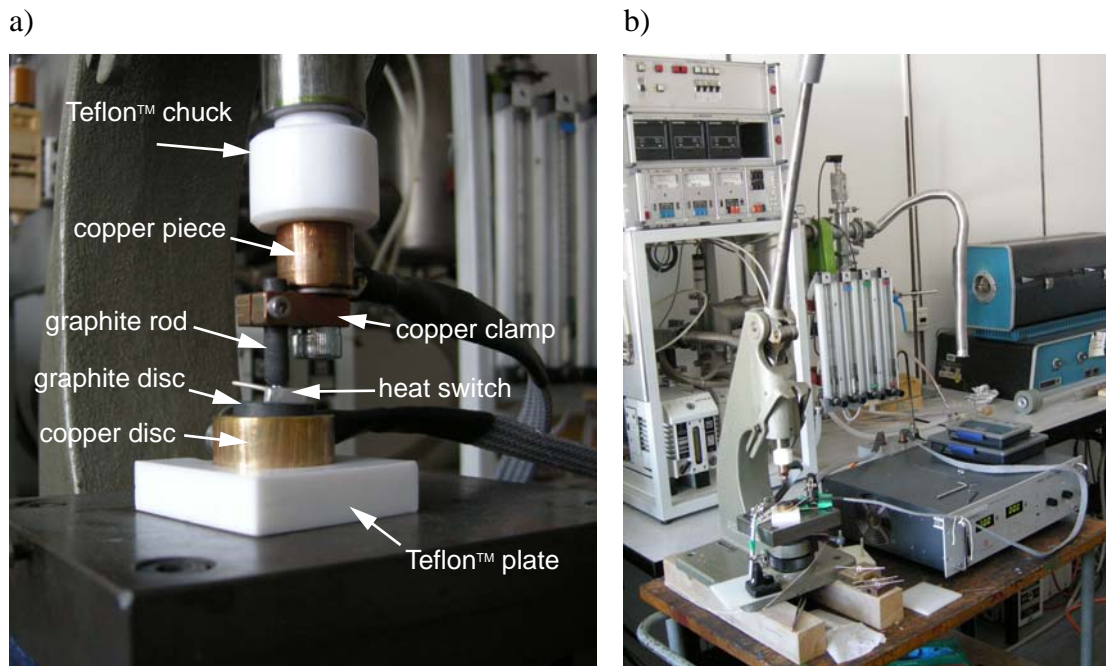
Figure 6.6.: Fuse set-up used to produce the heat switches. a) Close-up of the actual fusing electrodes made from graphite (see text for details). b) Overview, showing the fusing press and the power supply to the right.

the next step the current was ramped up to values of 80 A to 100 A within a few seconds. Once a high enough temperature was reached the aluminium melted and the silver was pushed down. The weight of the plunger was almost sufficient to fuse the silver and the aluminium together. Too much pressure gave bad results because the liquid aluminium squirted away. The heat arises mainly in the graphite electrode and flows down to the aluminium. Therefore, the first two or three attempts usually resulted in useless switches because the top electrode needs to be pre-warmed. The switches were then produced in a regular rhythm to keep the set-up in a hot quasi-static state. Attention has to be paid after the process, the workpiece is hot and can easily injure people.

Quick Testing Method

In a traditional demagnetisation stage one can test a switch elaborately because only one switch is needed. A stage as described in section 4.3 has to be equipped with several switches - 14 in the case of the prototype. A rather quick and simple method is required. We performed three tests to tell if a heat switch is 'good'

or 'bad'. We measured the electrical resistance, inspected the switch under optical microscopes and we had some switches analysed with energy dispersive x-ray spectroscopy (EDX) in the Basel microscopy centre ZMB [126].

In order to determine the resistance we sourced a current of a few $100\,mA$ to $\sim 1\,A$ with a Keithley 2400 SourceMeter and measured the voltage with a Keithley 2182A Nanovoltmeter. We took several data points to correct for offsets and thermal voltages. The electrical resistances were in the range of a few hundred $n\Omega$ for good joints and a few $\mu\Omega$ for bad joints.

Another simple test is an inspection under the optical microscope. A good fuse joint exhibited clear, straight interfaces between the two materials. Since, the focus depths of the optical microscopes were insufficient for good photographs I cannot show any pictures. However, the straight interface can be seen in the SEM image figure 6.7a). Bad joint showed signs of alloying as indicated by the arrows in figure 6.7b). Under an optical microscope, one could discriminate on the basis of different shades of grey and the texture of the surface. Some joints show gaps between the silver wire and the aluminium as shown in figure 6.7 d) - another sign of a bad joint.

Finally, we had three of our switches and one from Lancaster [127] analysed with EDX. They were mounted on the stage of a scanning-electron microscope with black conductive tape. Figures 6.7 a) and b) show the two joints of one switch. The image was taken using back-scattered electron (BSE) contrast which offers a good material contrast. The black region on top of the silver wire is due to some accidentally deposited conductive tape. Otherwise figure 6.7 a) shows an excellent joint. The other joint shows signs of alloy formation indicated by small arrows. In figure 6.7 c) you can see an BSE image of the heat switch from Lancaster. The three spots labelled A,B and C mark the areas where the spectra shown in 6.7 e) were recorded. These spectra are examples for the x-ray spectra of the switches. The electron beam had an energy of $20\,keV$, the spectra where cut at $4\,keV$ because we saw no peaks at higher energies. The elements displayed are proposals given by the automatic element detection of the EDX microscope. Obviously silver and aluminium are present in every case. The system detected also oxygen and silicon in all three spectra. Carbon and manganese were proposed in case C. Carbon and oxygen could originate from the conductive tape. If silicon and manganese were truly present can be doubted. It needs to be said that these measurements gave a rough estimate of the elementary constitutions of the switches only. The spectra in the three spots confirmed what we expected. One peak only around $1.5\,keV$ indicating pure aluminium in spot A and one twin peak around $3\,keV$ in spot B indicating pure silver. In spot C both peaks are pronounced which shows that both elements, hence an alloy, were present. Figure 6.7 d) shows a 'bad' heat switch. The arrow points at a gap inside which it is possible to see how the
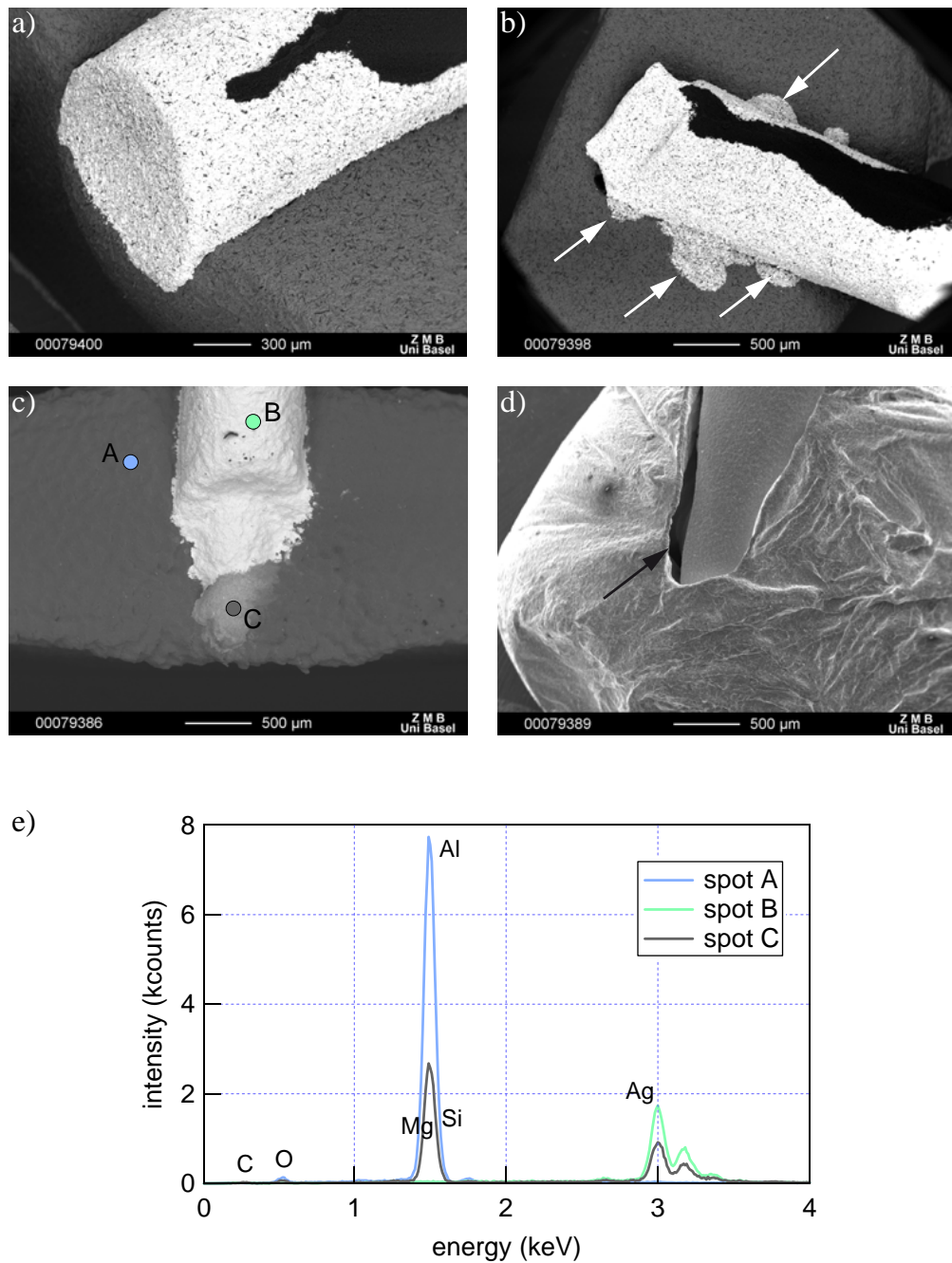
Figure 6.7.: a)-d) Scanning electron microscope images of some heat switches a)-c) show a back-scattered electron (BSE) contrast, d) shows secondary electron (SE) contrast. e) Example of an EDX spectrum.

liquid aluminium dissolved the silver. Table 6.2 summarises the results of the EDX analysis. We could correlate the EDX results to observations made with optical microscopes and electrical resistance measurements.

Switch	Figure	Contrast	Remarks
B0	6.7 d)	SE	strong alloy formation, up to 15% O_2, 76% Al, 8% Ag in some parts
B5			similar as B6
B6	6.7 a)	BSE	good joint
	6.7 b)	BSE	strong alloy formation
Lancaster	6.7 c)	BSE	some alloy formation

Table 6.2.: Summary of the EDX analysis. We had three of our switches and one from Lancaster analysed. The elementary composition of B0 was determined by the EDX automatically. The numbers are only rough estimates since for example topography effects of the switches were neglected.

As a summary I can say that the examinations confirmed the expectations I had in advance. A low-resistance fuse joint does not show any or only little signs of alloy formation which can be seen in an EDX analysis as well as under a microscope. Thus, it was sufficient to inspect the switches under an optical microscope for a production of a larger number of switches.

Thermal Conduction

We measured thermal conductance of two switches, labelled #4 and #7. The silver wire on one end was partially rolled flat to provide a flat surface. A $100\,\Omega$ metal film resistor was tied to the outermost end. Between that resistor and the switch, still on the flat section, chip thermometers with a manufacturer's calibration were mounted. It was electrically insulated from the silver with cigarette paper soaked in GE varnish [128] and additionally tied down. The other wire was spot welded to a copper rake. This rake was screwed down to the coldfinger of our dilution refrigerator. Figure 6.8 b) shows a schematic of the set-up. In figure 6.8 a) one can see a photograph of the rake after the resistors and chips had been removed, they were needed for other measurements. All leads that contacted the chips as well as the resistors were phosphor-bronze wires of diameter $125\,\mu$m. It was made sure that they are not in thermal contact to any cold part below the cold plate. We then flew a current I through the resistor. The generated heat $I^2 R$ in the resistance R can flow two ways. It can be drained through the heat switch or flow through the phosphor-bronze wires. However, we measured the temperature of the

a)

b)
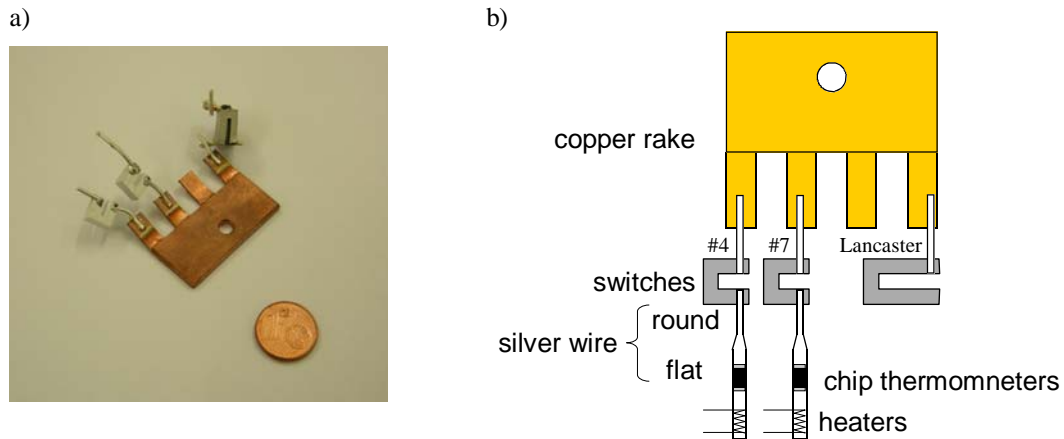
Figure 6.8.: a) Photograph of the switches #4, #7 and a switch from Lancaster [127]. We welded the silver wires to a copper rake which was bolted on the coldfinger of the DR. The wires on one side of the Lancaster switch were too short to make (weld) good contacts on both sides. b) Schematic of the set-up. The silver wire was partially rolled flat which facilitated to mount the chip resistors. We used phosphor-bonze wires (length ~ 25 cm, diameter $125\,\mu$m) to connect the resistors and the heaters.

mixing chamber and the hot side of the switch using a calibration given by the supplier [102]. In order to obtain a temperature dependence, the mixing chamber was heated with a separate heater. For each data point we assumed that the heat flows through the heat switch only, i.e. we neglect the flow through the phosphor-bronze wires. This assumption will be justified a posteriori further below. We divided the power by the calculated temperature difference between hot and cold side of the switch. This way we obtain thermal conductances which are an average in the range between the two temperatures.

Figure 6.9 plots these thermal conductances as a function of the mean between the two temperatures for the normal conducting and the superconducting state. The points of switch #4 in the normal conducting state (open blue diamonds) curve slightly down what we allocate to the switches being partially superconducting. The points of switch #7 (open green diamonds) show a behaviour that goes linear with temperature, as expected for electrons. The solid green line is a fit based on that assumption. The solid triangles are the conductances in the superconducting states. The measurements follows roughly some behaviour that expresses the decrease of thermal conductance due the superconducting gap above 100 mK. Phonons in aluminium are known to show a thermal conductance that deviates from the cubic law due to dislocations [129]. Instead, this anomalous con-
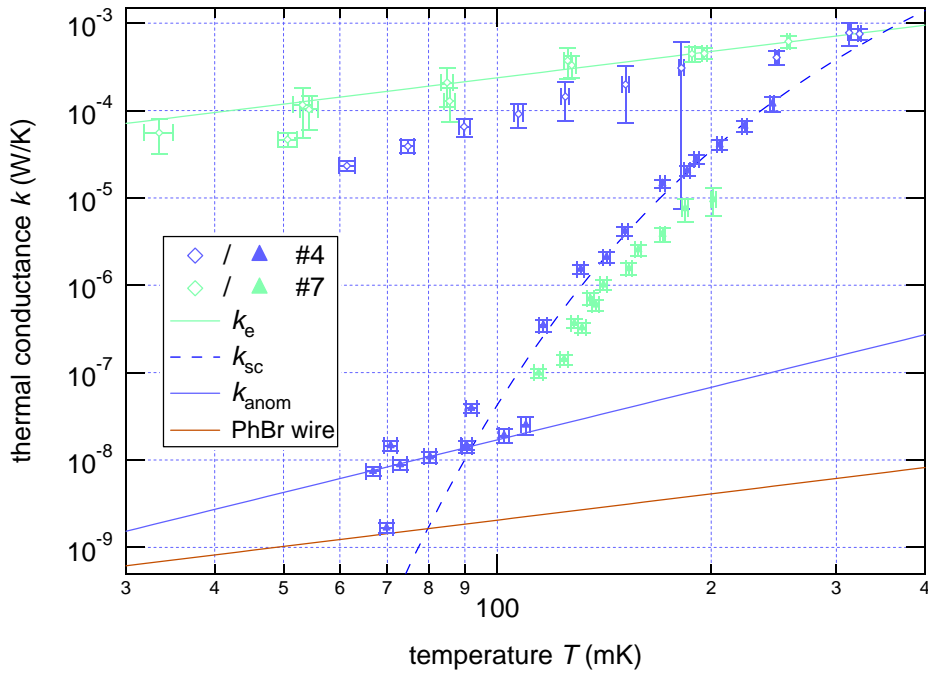
Figure 6.9.: Thermal conductance k of heat switches #4 and #7 in the normal
conducting state (open diamonds) and in the superconducting state
(solid triangle) as function of average temperature. The large error
bar in the data of #4 at 180 mK is because the temperature gradi-
ent is comparable to the estimated uncertainty of the temperature
measurements. For the next data point ($T \sim 250$ mK) we increased
the power and hence the temperature gradient. The solid lines are
fits according to $k_e \sim T$ in the normal conducting state, $k_{anom} \sim T^2$
for phonons in the superconducting state and $k_{sc} \sim T \exp(-T_c/T)$
for the quasi-particles in the superconducting state. Furthermore,
the thermal conductance for a phosphor-bronze wire of length 25 cm
is plotted as calculated based on the WIEDEMANN-FRANZ law.

ductance depends quadratically on temperature. Hence, one can fit a quadratic
curve, $k_{anom} \sim T^2$ (solid blue line) which is in decent agreement with the data
between ~ 66 mK and ~ 110 mK.

The following equations summarise the theoretical lines displayed in figure 6.9 quantitatively.

$$k_{\mathrm{e}} = 2.4 \cdot 10^{-3} \left[\frac{\mathrm{W}}{\mathrm{K}^2}\right] T \tag{6.4}$$

$$k_{\mathrm{sc}} = 7 \cdot 10^{-2} \left[\frac{\mathrm{W}}{\mathrm{K}^2}\right] T \, \mathrm{e}^{-\frac{1.2[\mathrm{K}]}{T}} \tag{6.5}$$

$$k_{\mathrm{anom}} = 1.7 \cdot 10^{-6} \left[\frac{\mathrm{W}}{\mathrm{K}^3}\right] T^2 \tag{6.6}$$

Furthermore, figure 6.9 shows the thermal conductance of a phosphor-bronze wire of length $25\,\mathrm{cm}$ and diameter $125\,\mu\mathrm{m}$ as calculated from the WIEDEMANN-FRANZ law based on the resistivity of the wire which is $11.5\,\mu\Omega\,\mathrm{cm}$ [130] and assuming a RRR$\lesssim 2$ [131]. Taking into account that the solder joints were superconducting in that temperature range [54] which inhibited heat flow even more the thermal conductance of the wire was at least about a factor of 10 smaller than the thermal conductance of the switch. This justifies our initial assumption of the heat flowing exclusively through the switch a posteriori. The phosphor-bronze wire was thermally anchored on the cold plate on which we didn't have a thermometer at that time. However, it must have been hotter than the mixing chamber, hence the heat flow from the hot side of the switch through the wire to the cold plate is negligible. On the other hand, the heat flow from the cold plate to the hot side of the switch can be assumed to be neglibile, too. The mixing chamber was around $\sim 50\,\mathrm{mK}$ and the hot side of the switch read $\sim 100\,\mathrm{mK}$. In order to get a comparable heat flow in the phosphor-bronze wire, the temperature gradient across it has to be $\sim 500\,\mathrm{mK}$, hence the coldplate needs to be at $\sim 550\,\mathrm{mK}$ which is unrealistic.

Figure 6.10 compares the measured conductances with calculations done for some parts of the measurement set-up. The dark grey line is an estimate based on the known aspect ratio of the aluminium. The light grey line assumes a silver wire with length $3\,\mathrm{cm}$ and diameter $1.27\,\mathrm{mm}$. The RRR values assumed were 400 for the silver and 100 for the aluminium, respectively, which is in good agreement with RRRs that we measured. Although the best RRR that we achieved for silver was ~ 1800, the assmuption of RRR=400 is still justified because bending, and in particular rolling flat the wire reduces it easily. From these estimates we can conclude that the silver wire is the bottleneck of heat flow in the normal conducting state. In the demagnetisation stage the silver wire will be even longer which probably cancels the better RRR.

Finally, figure 6.11 compares our data with the data of Müller and co-workers [121]. Note, that this graph plots conductivity. We can convert the conductances in the superconducting states into a conductivity because in that case the aluminium is the largest thermal resistance and we know its dimensions. However, in the
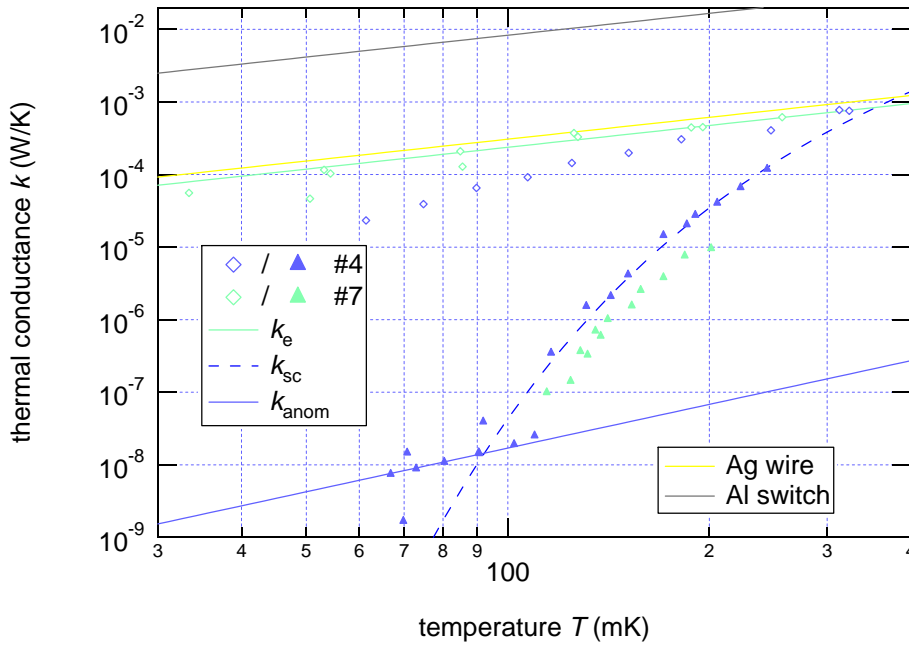
Figure 6.10.: Thermal conductances as function of temperature. This graph compares the measurements (figure 6.9) with calculations for the aluminium switch (RRR=100) and a silver wire (RRR=400) of length 3 cm and diameter 1.27 mm. The calculated conductance of the silver wire is smaller than the conductance of the aluminium switch but comparable to the fit. From this we can deduce that the silver wire is the bottleneck.

normal conducting state it is not clear which dimensions to choose. Hence, I omitted that data and displayed the calculations of the aluminium in the normal conducting state instead. In the superconducting state, our thermal conductances are one to two orders of magnitudes smaller than the data by Müller and co-workers. This is most likely due the different RRR. They state their RRR to be 1400 whereas ours is about 100.

Switching Ratio and Residual Heat Leak

From the equations given above, (6.4) and (6.6), we can estimate the switching ratio $\mathcal{K}$. Dividing the two equations gives

$$\mathcal{K} \sim \frac{1400\,\mathrm{K}}{T} \tag{6.7}$$
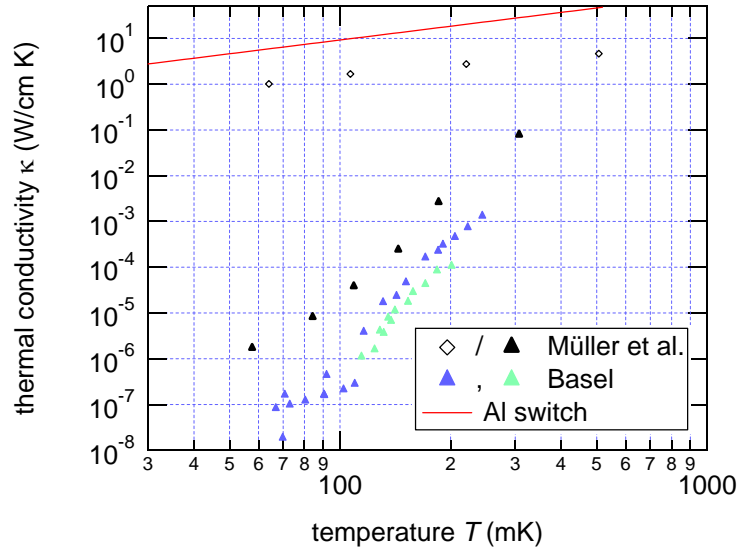
Figure 6.11.: Comparison of our data with [121]. The graph plots thermal con-
ductivity as a function of temperature. The conductivity was cal-
culated from the conductance measurement based on the dimen-
sions given in figure 6.5. The solid line is converted from figure
6.10.

Strictly speaking (6.4) is for switch #7 and (6.6) for switch #4. The thermal con-
ductances in the normal conducting states agrees above ~ 200 mK. The deviation
below can be attributed to switch #4 being partially superconducting. So we can
assume that (6.4) is a decent description of #4 in the normal state.

Since the mixing chamber provides a temperature of ~ 10 mK, the switching
ratio at that temperature gives a lower limit for $\mathcal{K}$ during a demagnetisation cycle.
This gives $\mathcal{K} \geqq 10^5$ for our switches. Müller and co-workers achieved $\mathcal{K} \approx 10^6$
at ~ 10 mK [121] whereas Ho and Hallock achieved $\mathcal{K} \approx 6 \cdot 10^5$. Taking into
account that the thermal conductance is limited by the silver wire in the normal
state, and based on the estimates for the aluminium in figure 6.10 we can assume
the switching ratio that we achieved (equation (6.7)) to be at least a factor of ten
larger. Thus, our switching ratio at 10 mK is comparable to the data of Müller and
co-workers. Note, that their theory is based on the assumption that phonons in
aluminium conduct heat according to $k \sim T^3$ which can easily introduce a factor
of ten at 10 mK [1].

From (6.6) the conductance in the superconducting state can be estimated as
$k \leqq 2 \cdot 10^{-10}$ W/K below 10 mK. If we assume the demagnetised copper to be at

---

[1] I estimated this from a 'pencil-and-ruler-analysis' of one of their graphs.

zero temperature we calculate an upper limit for the heat that leaks through the closed switch. Thus, the heat leaking through a closed switch is

$$\dot{Q} < k \cdot T_{\mathrm{MC}} = 2\,\mathrm{pW} \tag{6.8}$$

which fulfils the requirement stated in section 6.1. This heat flow is clearly below 1 nW.

Indium Switch

For some time we were considering to use indium as switching material. One particular design that we tried is shown in figure 6.12. The idea is based on the alternating sequence of foils used by Bunkov [119] who used a stack of copper and aluminium foils. Figure 6.12 b) is a schematic explaining the switch itself. In our approach the lowermost part is a copper block. On that we put cigarette paper as electrical insulation. Then the first copper foil is added. It goes to the right where it is clamped to the coldfinger (see 6.12 a)). Afterwards, the first layer of indium is laid down. We used an indium wire of 5N purity and 0.75 mm diameter [118] that we rolled up like a spiral. The next piece is again a copper foil but this time it goes to the left. This copper foil was equipped with a heater and a ruthenium oxide chip, i.e. this copper foil is the hot side of the switch. Subsequently, we put a second indium layer and a third copper foil which is bolted to the coldfinger like the first foil. Eventually, another layer of cigarette paper insulates the switch from the top copper bar. Brass screws were used to bolt down the whole construction. A brass and a molybdenum washer were used. Molybdenum has a smaller thermal contraction than the other materials and the washer makes sure that the pressure on the switch persisted at low temperatures.

We then measured the thermal conductance across the switch. Like in the measurements above we assumed that the heat flows exclusively from the heater through switch to the mixing chamber. With these assumptions we get the thermal conductance shown in figure 6.13. It was determined in the same way as the data above for the aluminium-silver switch. The open green diamonds are the data with an applied magnetic field of nominally 44 mT. That's well above the critical field of indium which is about 28 mT. The solid green triangles is data taken at zero field, hence with the indium being superconducting. The two solid green lines are fits for conduction proportional to temperature, $k \sim T$. The dashed green line is again a theoretical curve for the exponential decay of thermal conduction of a superconductor. It is drawn such that it matches the data around 315 mK. From the facts that the conductance looks electronic and the theoretical curve for the transition region does not match either, we conclude that the indium was not fully superconducting in both measurements. The slight curvature of the 'superconducting' trace above 100 mK suggests that the indium was partially superconducting.
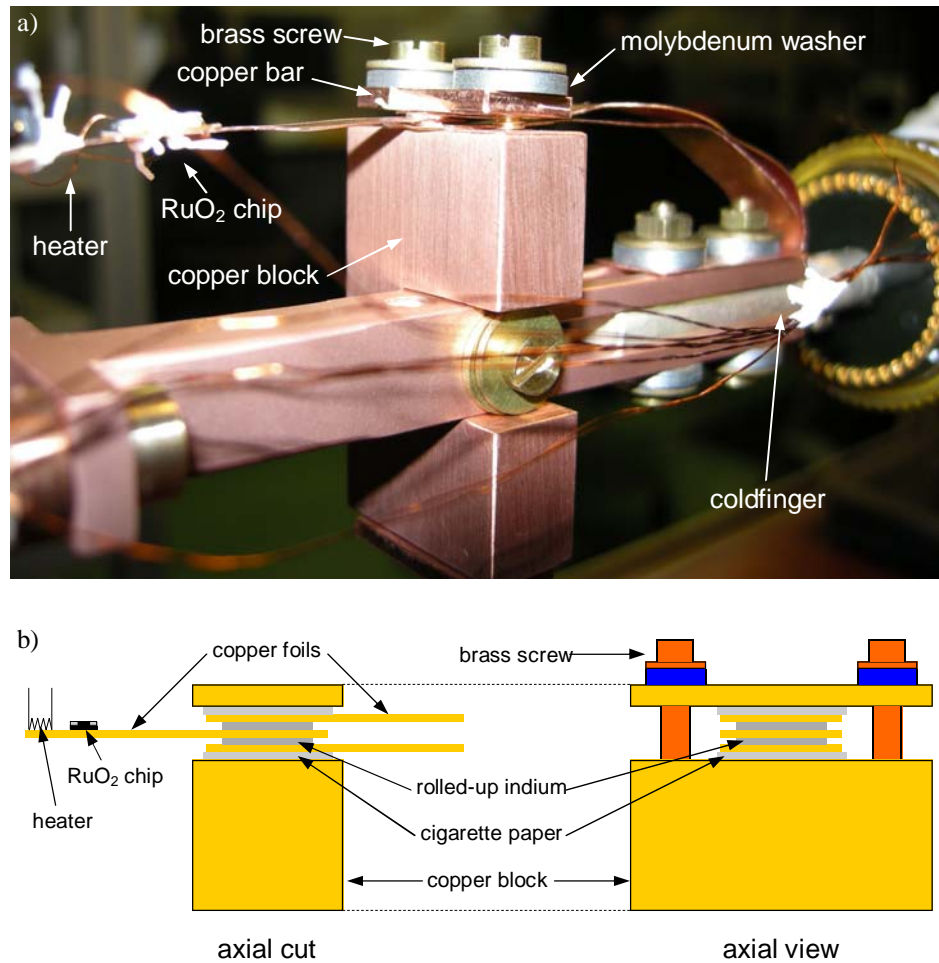
Figure 6.12.: a) Photograph of the indium switch. It was bolted on a copper block which in turn was screwed down to the coldfinger. b) Schematic that explains the switch. An interchanging sequence of copper and indium was stacked and bolted between two copper plates.

This mixed state could have been due to trapped magnetic flux. However, from this graph we can read a switching ratio of 10 at most.

There are two more comments that should be made about this approach. For the switch we intended to use more than three copper foils which would have been even more cumbersome as this attempt. Furthermore, the whole demagnetisation stage required 14 switches, and since one switch of this type is comparatively large, it would have been difficult to fit 14 on the demagnetisation stage.
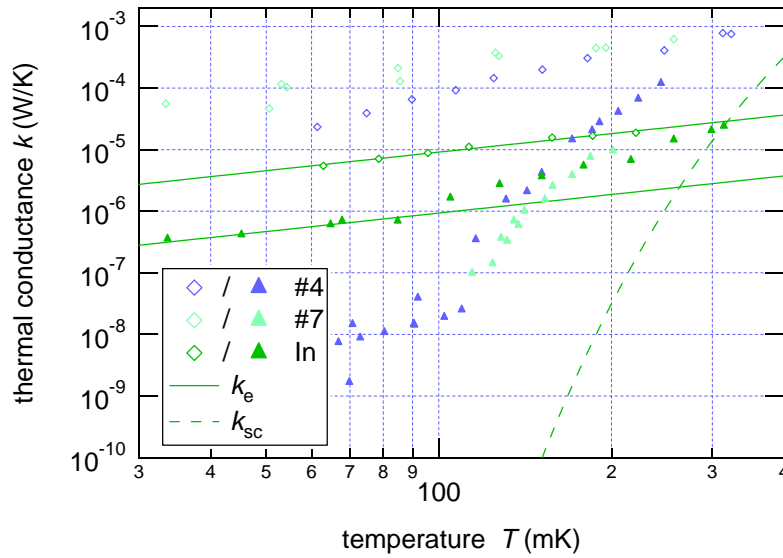
Figure 6.13.: Thermal conduction of the indium heat switch in the superconducting (solid triangles) and the normal conducting state (open diamonds) as a function of temperature. For comparison, the graph shows also the conductances of the aluminium-silver joints. The two solid green lines are theoretical curves based on electronic thermal conduction, $k_e \sim T$. The dashed green curve is again for the superconducting quasi-particles, $k_{sc} \sim T \exp(-T_c/T)$, $T_c = 3.4\,\text{K}$. It is drawn such that it matches the data point at $315\,\text{mK}$.

Conclusions

With everything said above, I can conclude that the fusing process is a reliable method to produce heat switches. The measurements of the thermal conduction show that the switching ratio and the isolation in the closed state are sufficient for demagnetisation. We also saw that the bottleneck for precooling is the silver wire. Furthermore, the switches are rigid and stable and each of them is small enough to fit 14 of them on the demagnetisation stage.

6.4. Sample Holder

An essential part of a cryostat designed for investigating nanostructures is the sample holder. Usually a commercially available socket holds a chip carrier into which the sample is glued. The sockets that we use on other systems in our laboratory are made of plastic and contact is achieved through gold-plated Cu-Be

pins that are simply pressed against their mating pieces on the chip carrier. The thermal contact achieved this way is bad for two reasons. First, the press contact does not provide good thermal contact and second, the leads are soldered to the pins and most solders turns superconducting already at temperatures of several Kelvin [54]. In order to minimise the thermal resistance between the copper plates and the the nanostructure we therefore decided to built our own sample holder based on a discussion with Richard Haley [132].
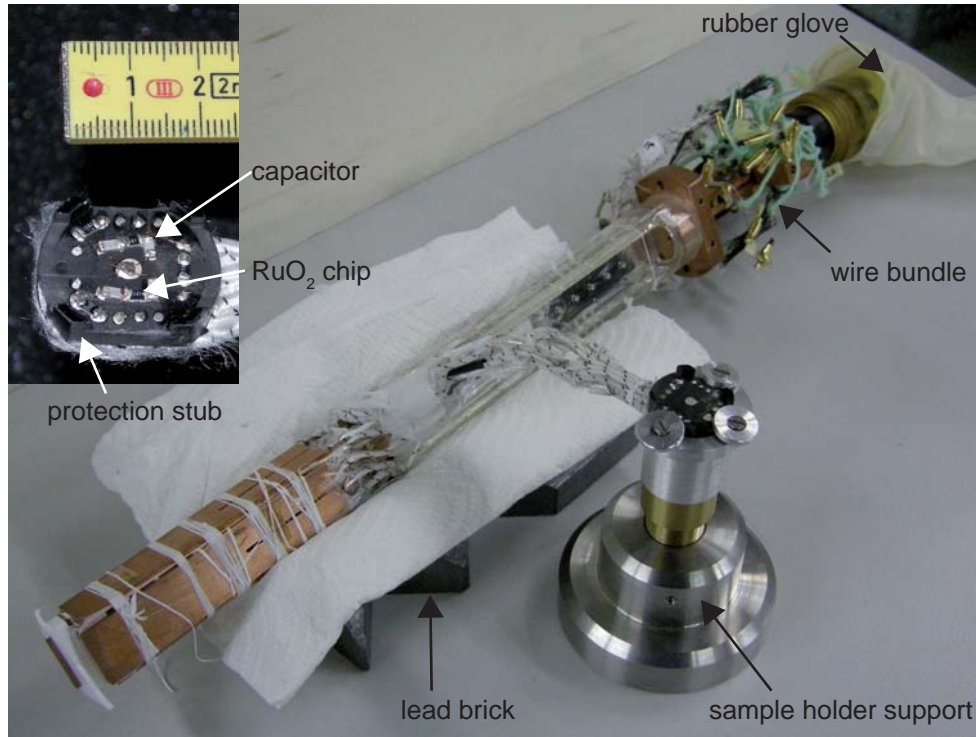
Figure 6.14.: The final sample holder and the set-up for bonding. The inset shows the actual sample holder equipped with four RuO_2 chips for thermometry. Two of the chips were capacitively connected to ground for additional filtering. The heavy sample holder support held the sample holder during wire bonding while the lead brick secured the stage. The rubber glove was intended to protect the mixing chamber from getting dusty.

We had a mould made into which the silver wires were placed [133]. Afterwards Stycast 2850 was poured into the mould. Once the epoxy was cured the piece was machined into its final shape, the result is shown in the inset of figure 6.14. The flat sides were cut such that the holder fits into the groove of the Araldite^{TM} beam. The 4×4 contact pads were made by polishing the ends of of the silver wires. The

central pad was the 'ground plane'. It was machined out of solid piece of silver. Furthermore, we left protection stubs in the four corners of the sample holder which acted as spacers to prevent the sample from touching the Araldite$^{\text{TM}}$. The visible chips are RuO_2 chips and capacitors used in one of the early cooldowns. They were connected with a thin $(125\,\mu\text{m})$ copper wire and silver epoxy.

During the work with this sample holder we realised some drawbacks. We had to built a sample holder support to which the sample holder could be clamped during wire bonding. But it was useful in general to keep the sample holder in the support also when we changed RuO_2 chips.

In the course of wire bonding, the sample carrier has to be rotated with respect to the wire bonder. Due to the mass distribution and the geometry, large torques acted on the stage and hence the sample holder. Therefore the sample holder support had to be heavy enough to compensate for these torques. Additionally, the stage itself was put into the groove of a lead brick for stabilisation. Two more problems showed up during bonding. First, the washers that clamped down the sample holder were an obstacle for the bonding needle which made the process cumbersome. Second, one side was completely inaccessible because there was not enough space to rotate the whole stage arbitrarily.

Finally, every time we modified something on the sample holder we had to bend it out of the groove. This bending decreased the RRR of the silver wire and hence its thermal conduction. This undermined the whole efforts to achieve good thermal contact. Instead of having the bottle neck in the press contact and the solder contact of the pins, it was now most likely in the wire. Besides that, the motion can cause the wires to touch each other and hence short them.

A nanostructure is very susceptible to static charges. Thus, all the contacts must always have a defined voltage, if not in use they are grounded. In order to achieve that during wire bonding, we wove a de-soldering braid between the wires in the bundle (see figure 6.14) to connect all the wires together and grounded the braid in a spot with a defined potential. This process is tricky because one easily overlooks a wire. The first quantum dot we mounted was destroyed. Most likely that happened when we walked from the wire bonder back to the laboratory. During that short time the potentials of the wires were undefined. After bonding the second quantum dot we had the wires always connected to the house ground through extension cords. However, this dot was destroyed as well. In summary, the wire bonding is very cumbersome using this sample holder.

6.5. Structural Support

The parts described so far need also some mechanical support. It had to provide structural stability on the one hand but on the other hand, it had to be designed such that the copper plates and the silver wires are electrically insulated from one another and from ground. Furthermore, we had to plan it such that the residual heat leak on the plates is as low as possible. Eventually, the structural support can be divided into two parts.

MC Temperature Stage

On the one hand the part below the mixing chamber was a mechanical support, but on the other hand, we used that part as thermal or structural anchor point. The central image of figure 6.16 shows this stage. A fork-like copper piece was bolted to the coldfinger of the mixing chamber. In order to ensure good contact, we used molybdenum washers to compensate for different thermal contraction coefficients. Another copper piece was attached below it and a silver crossbar was screwed to it. The MCX towers were then anchored on the crossbar. Furthermore, a CMN thermometer was bolted on the crossbar. The static coil of a PtNMR thermometer was anchored here, too.

Araldite Beam

Below the MC temperature stage we had to find a structure that served the following purposes. We needed a structural support for the stage, that means something that carries the weight of the copper. Furthermore, it had to have the right length, such that the copper plates were centred in the solenoid field. The material should be isolating, both thermally and electrically. The first because the copper plates needed to be thermally isolated for the demagnetisation process, the latter to minimise the probability for shorts. This rules out all metals and superconductors. We decided to test Araldite[TM] [134]. We found that it can be easily machined and it can withstand slow cooldowns, i.e. a sudden dip in liquid nitrogen caused our test pieces to crack. Figure 6.15 shows a schematic of the design which is to scale and was generated from CAD drawings. At the top (to the left in figure 6.15) we added a cylindrical trough to glue the whole beam to a copper piece which was part of the MC temperature stage. The cross section is chosen as an I-beam for structural stability. The two troughs of that I-beam were also planned to house the silver wires and the sample carrier. In the central wall we had a pattern of threaded holes made for general purposes and to attach the sample carrier. At the bottom (to the right in figure 6.15) the beam ended in a cylinder with a slit which was supposed to hold the sacrificial plate (see section 6.1). For the beam
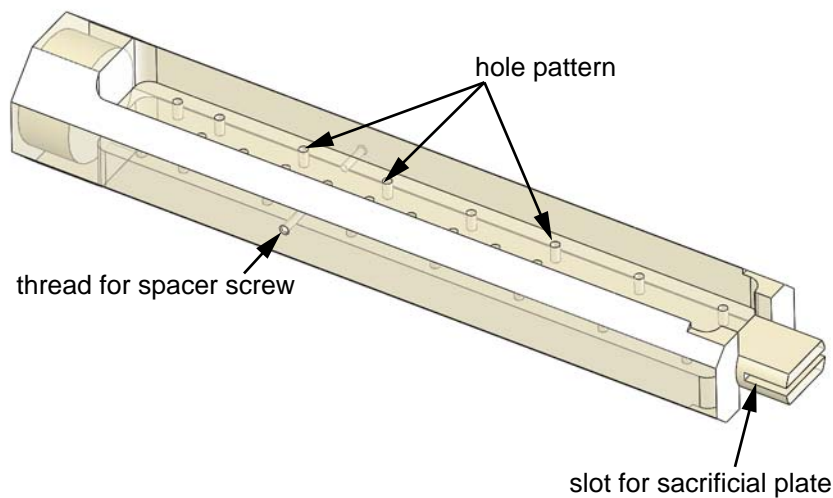
Figure 6.15.: Technical drawing of the Araldite beam.

itself we poured the Araldite^TM into a brass mould, cured it and took it back out of the mould. Afterwards the Araldite^TM block was annealed and then machined into shape. Eventually, we painted the piece with Stycast 1266 Epoxy to minimise the probability of cracking. Details and parameters of production can be found in appendix B.

6.6. Assembly of the Stage

After all parts had been made and tested, we had to assemble the whole stage. In two parallel steps we built the copper bundle including the silver which had been welded to the plates before and we welded the switches to the MC plug. Then the copper piece was glue into the upper end of the Araldite^TM beam. In the next step the second fork-like copper piece was screwed down to the other copper piece and then the MC plug was bolted to the rest of the stage. Finally, the wire between the heat switches and the plates were welded. On the sample side of the plates, the sample holder wires were also welded to the plates' wires. In later steps we welded the Pt NMR thermometer and a silver base plate to one wire. The latter served to anchor a CMN thermometer.
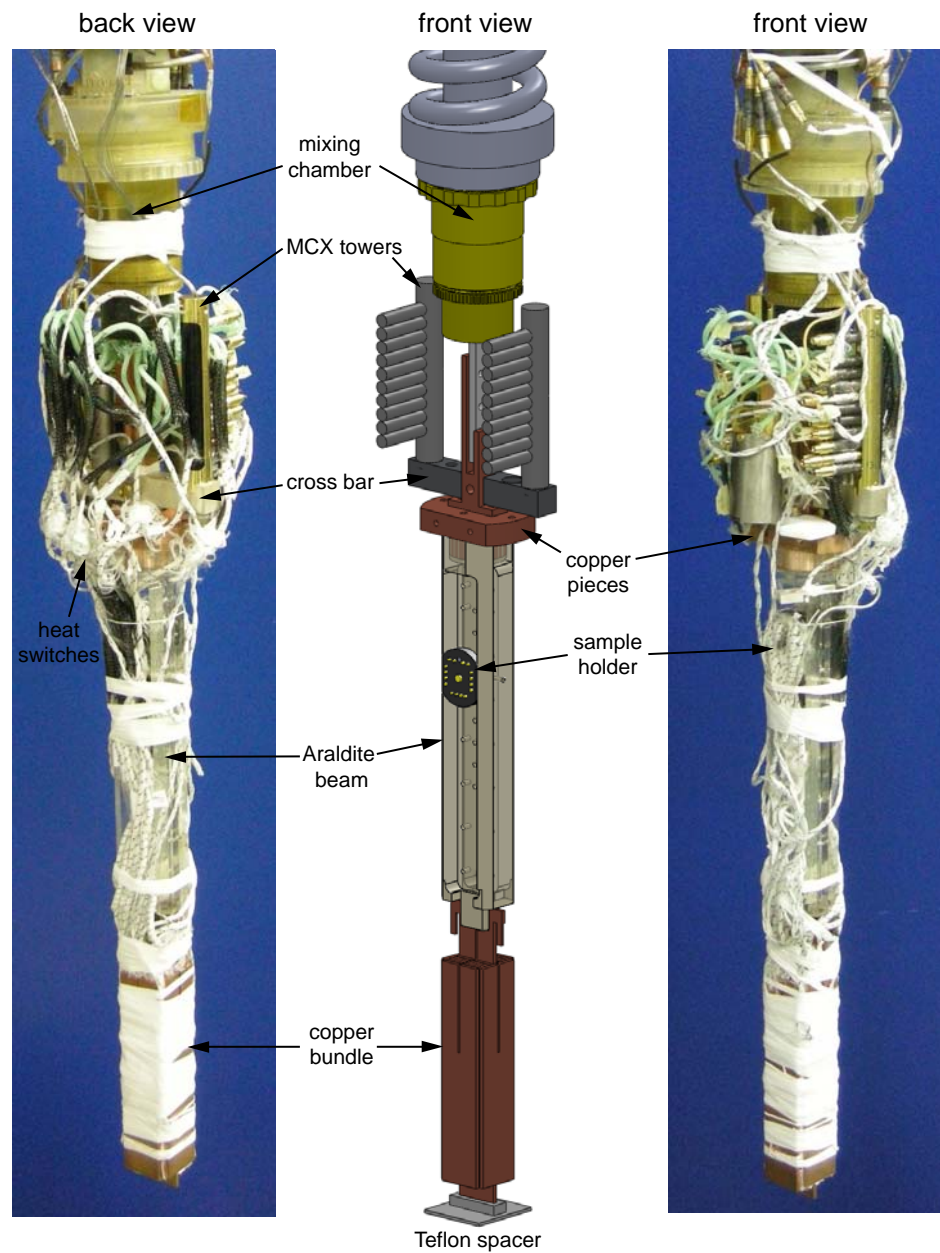
Figure 6.16.: The demagnetisation stage. The centre shows a simplified schematic. On the sides front and back view are shown, respectively. (An enlarged, un-fold version of this picture can be found in the back of the printed version.)

Performance of the Refrigerator

Having discussed the single constituents of the refrigerator I will now discuss the performance of the whole stage as a unit.

7.1. Thermometry

A basic quantity needed to determine the performance of the refrigerator is temperature. We tried three methods to acquire this information: resistance thermometry with RuO_2 chips and susceptibility measurements with both, paramagnetic salts and platinum nuclei.

7.1.1. Ruthenium Oxide Thermometers

Despite the known fact that RuO_2 chips become temperature insensitive at temperatures of the order $\sim 10\,mK$ [49], they were very easy to handle and turned out to be the most helpful thermometers in the course of our work. Eventually, all plates could be monitored (except for one) and we could determine the achieved temperature indirectly as described in section 7.5. Figure 7.1 shows how the chips were arranged and which chips measured which plate. The chips prepared for the first demagnetisation cycle (details of which are described further down in section 7.2) are shown in figure 7.1 a). We evaporated gold onto the contact pads and wire bonded it to the silver pads on the sample holder with a gold wire of $32\,\mu m$

diameter. As the first demagnetisation cycle did not show satisfying results, we found [135] that the contact pads contain superconducting material that we made, at least partially, responsible for not achieving the expected low temperatures. Afterwards, the contact pads were removed with sand paper and we used silver epoxy E4110 [136] to establish contact to the silver pads [135]. If the distance between the silver pad and the contact pad was long we bridged it with a short section of copper wire. Besides that, the contacts of chips A and B were capacitively coupled to ground (plate G) for additional filtering (figure 7.1 b)). Chips
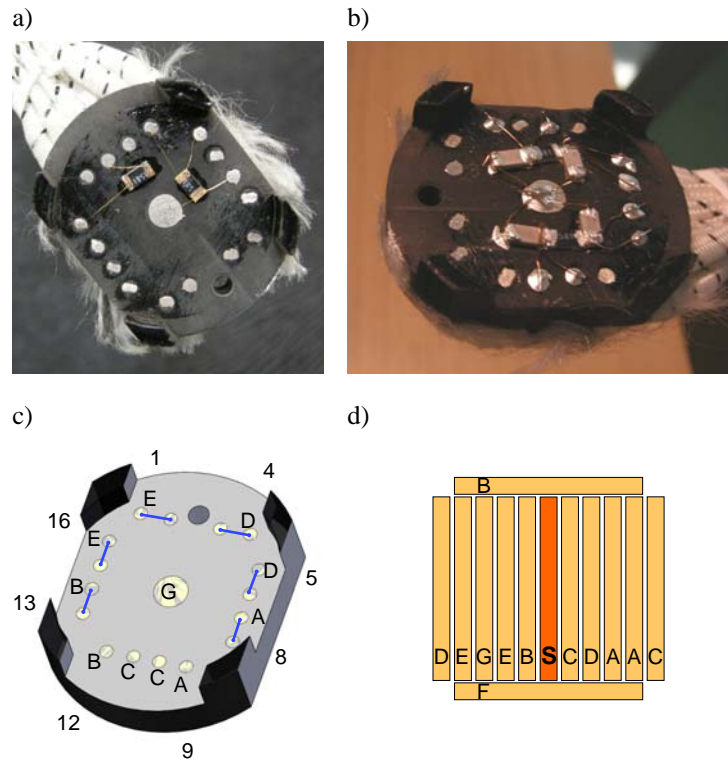
Figure 7.1.: a) Chip thermometers during the very first and the b) second demagnetisation cycle. c) Labelling of the chips and their contacts on the sample holder. d) Cross-sectional arrangement of the plates. The letters indicate the connected chips.

A-E are mounted on the sample holder this way and connected to 10 of the 13 plates with each chip using a pair of plates as its leads. The resistance reading in these cases reflects an 'average' temperature of each pair. Two more chips, F and S, were directly mounted onto individual plates (S on the sacrificial plate), with the second contact of each electrically connected to, but thermally isolated from, the outside world by a bare NbTi superconducting wire. The final plate (G) was

left unmonitored, serving as electrical ground for the chip capacitors across A and B.

We calibrated the RuO_2 thermometers between $12\,mK$ and $120\,mK$. Figure 7.2 shows the resistance of the seven RuO_2 chips at $B = 0$ as a function of mixing chamber temperature T_{MC} with the aluminium switches closed. T_{MC} was measured by a CMN thermometer bolted to the crossbar. Before measuring each data point, an appropriate amount of time for thermalisation was allowed. There is no apparent saturation down to $T_{MC} = 12\,mK$ for thermometers A-F, which all exhibit qualitatively the same temperature dependence. Moreover, on two separate cooldowns a second CMN was mounted directly onto one of the plates (first A, then F), verifying that T_e measured by the RuO_2 chips is indeed equal to T_{MC}. We therefore use the data in figure 7.2 as electron temperature calibrations for plates A-F. The sacrificial plate thermometer S displays some saturation for $T_{MC} \lesssim 30\,mK$, presumably due to a heat leak. Besides, we considered self-heating
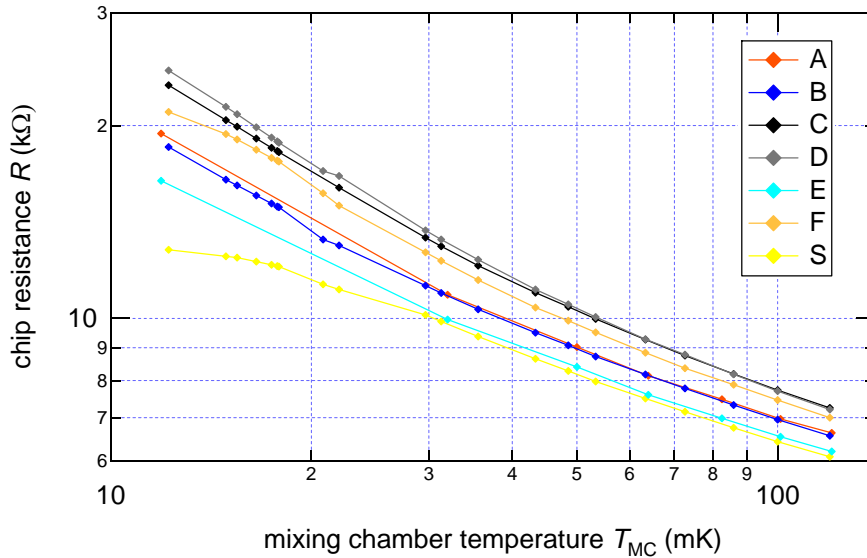
Figure 7.2.: This graph shows the resistances of the RuO_2 chips as a function of mixing chamber temperature. Chips A-F show qualitatively the same behaviour. Chip S deviates below $30\,mK$.

of the chips. We could not see any temperature increase for currents up to $\sim 5\,nA$. However, we biased the chips at 1nA at the base temperature of the DR and above. During the demagnetisation cycles we sourced $\sim 1/4\,nA$ as a precaution.

Since we have a trustworthy calibration of the chips only above the base temperature of the DR, I present data in that temperature range as converted from the calibration whereas I give resistance for temperatures below.

7.1.2. Paramagnetic Salt

We also employed a CMN thermometer to measure the temperature of the plates. First we measured the temperature on plate A, later we attached it to plate F. In both cases we could confirm that the temperature read with the RuO_2 chips equals that read with the CMN thermometer. However, with the CMN thermometer mounted on the system, no matter if on A or on F, we could always observe heat leaks ranging from several nW to several tens of nWs, as read from the power curves (see section 7.4). With this heat leak, it was impossible to achieve low temperature upon demagnetising. But once the CMN thermometer was removed, the heat leak was absent. The reason why the CMN thermometer introduced such an amount of heat is unclear.

7.1.3. Platinum NMR Thermometry

In order to measure the temperature of the electrons in the copper plate we wanted to employ a platinum NMR thermometer (PtNMR) obtained from Leiden Cryogenics [102]. We used the all-integrated electronic device 'PLM-5 Platinum Thermometer' from Picowatt [105]. The sensor is described in figure 7.3. In a) the dimensions are given. b) shows the sensor as it was mounted on the stage. The static coil was wound from a superconducting wire. A superconducting scroll shield was added between the former and the coil to improve homogeneity [137]. A Nb shield was also put around the coil to prevent the coil to interfere with other magnets. c) shows the low temperature stage.

The pick-up coil is made to fit around the bundle of Pt wires. Its wires are glued onto the silver base piece to enhance thermalisation. The signal was read by plugging some leads into the miniature connector. The cold stage was attached to the static coil through three Vespel rods of a length of about 2 cm. Vespel was used to ensure as little thermal contact as possible. With this thermometer we tried to determine the electron temperature of plate F. In the course of time, we also attached a LCMN thermometer and a RuO_2 chip. The latter was glued directly onto the wire with one end, whereas on the other end we soldered a section of superconducting wire to ensure electrical but to suppress thermal contact.

We essentially didn't find useful signals until we wound our own coil. It took us a few attempts to be successful but eventually we had a recipe. We had a Teflon former made around which the coil was wound. The diameter was chosen to match that of the Pt bundle, ~ 3.4 mm. We sprayed some Teflon^{TM} lubricant onto the Teflon^{TM} rod prior to winding. We then wound the coils with copper wire of $30\,\mu$m diameter and 4N purity purchased from Elektrisola [138]. During the process we put Stycast 1266 between the windings to keep them together. Afterwards the epoxy was cured at moderate temperatures ($\sim$40 °C). To take the coil off the rod
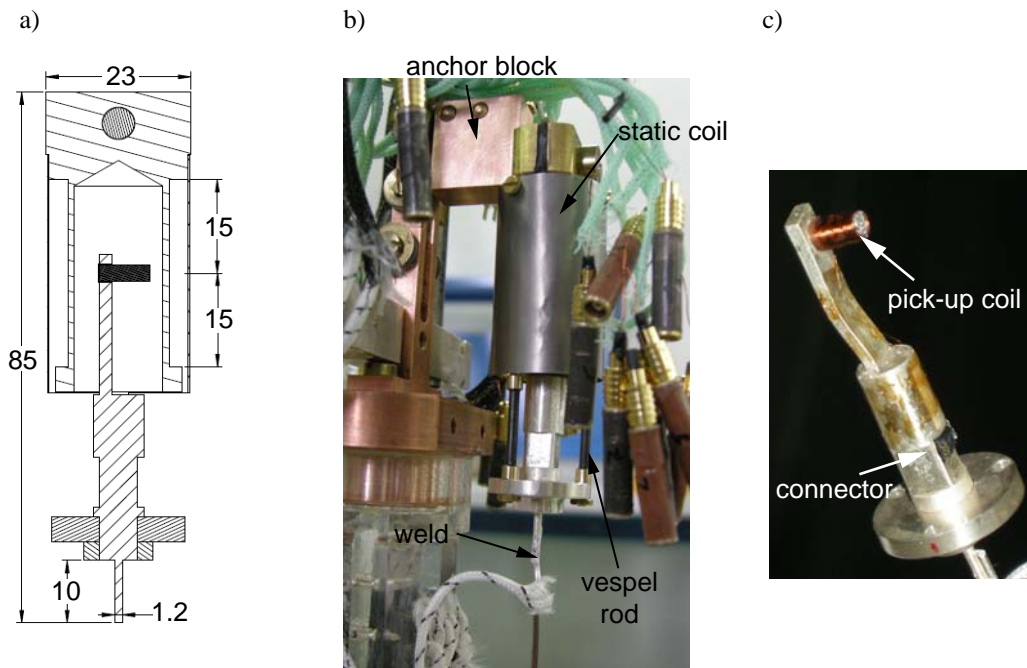
Figure 7.3.: The PtNMR temperature sensor. a) A technical drawing including the dimensions in mm. b) The sensor as mounted on the stage. c) The silver base piece. The pick-up coil surrounds the Pt wires .

it was dipped in liquid nitrogen which causes the Teflon$^{\text{TM}}$ to shrink more than the coil. We then had a coil with $\sim$1215 turns and a Q-factor of 28 at 77 K. The resistances were $350\,\Omega$ at room temperature and $46\,\Omega$ at 77 K. Figure 7.4 b) shows a coil on a rod.

The new coil enabled us to finally find a signal. We could always go through the standard process with the PLM-5: First, the frequency is swept to find the resonance of the coil at zero static field. From this, resonance frequency and Q-factor can be determined. Subsequently, a bandpass filter is adjusted. Then, the magnetic field is ramped up until a clear NMR resonance shows up. But we never achieved a consistent temperature measurement below mixing chamber temperature. However we could manage to calibrate the thermometer against a CMN thermometer between 15 mK and 20 mK as shown in figure 7.5. Besides the new coil, we tried to improve the thermometer with different shield configurations. We tried to cool down without Nb shield and with two home-built shields that were longer than the default shield. We built them from Nb foil [118] which we rolled up and spot welded to form a cylinder. The shields are shown in figure 7.4 a). From left to right in order as they were made. First, the default shield, in the centre one

Figure 7.4.: Improvements that we tried. a) Extended niobium shields. b) A home-built coil wound on a Teflon former.
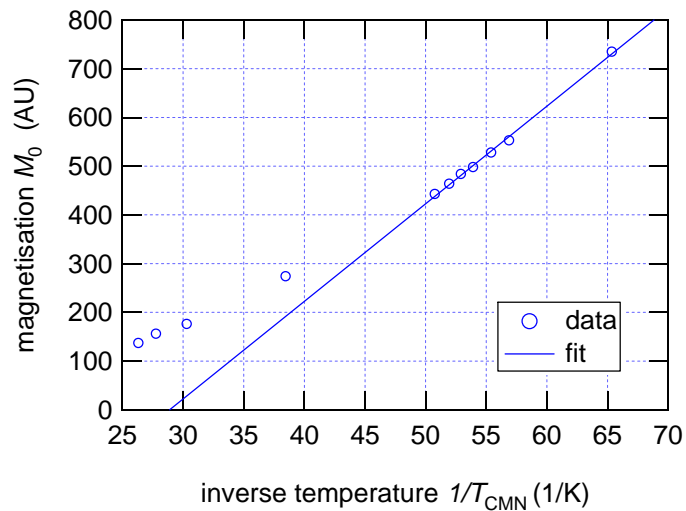
Figure 7.5.: Magnetisation of the Pt wires as read from the PLM-5 as a function of inverse mixing chamber temperature. We could fit a Curie law (3.69) between 15 mK and 20 mK.

that is extended down. For the third one, which was additionally extended upward we had to use another anchoring block for the static coil (see figure 7.3). Although an influence of the solenoid field could be seen the shields did not improve the situation. That influence could be seen in the magnetic field sweeps during the

search for the resonance. Ideally, the resonance should be symmetric in the static coil current. But it was not a priori. We think that is was most probably to the solenoid field but it could also be trapped magnetic flux in the static coil. Anyhow, warming up above the critical field of Nb and making sure that all fields are zero upon cooling down again we could overcome that problem and the resonance was symmetric in the current.

However, figure 7.6 show a photograph of the PLM-5 display with a free-induction decay (FID) of the platinum. The peak at the beginning of the FID is the ringdown of the excitation pulse. It could be seen at all temperatures. The area highlighted in white is the area that the PLM-5 used to determine the magnetisation M_0 of the Pt. On the one hand it is clearly non-exponential and on the other hand the signal should be longer [105]. The reasons for that behaviour is unclear. It could

Figure 7.6.: Photograph of the PLM-5 display showing a free-induction decay of the platinum.

be inhomogeneities. Even small amounts of magnetic impurities such as iron can introduce small local fields [66]. Furthermore, we cannot say with certainty that the Pt bundle is in the centre of the static field.

Another reason that we couldn't measure a PtNMR signal at low temperatures might be that the thermometer itself introduced heat into the plate. When we had the LCMN thermometer and the chip mounted at the same time we saw a heat leak of several tens of nW onto the plate. It did not disappear after removing the Pt sensor but it did so after removing the LCMN. Nevertheless, we cannot say with certainty that the Pt sensor did not have some contributions. However, the Pt wires are not insulated from one another which facilitates eddy currents. Furthermore, it is possible that the rf pulse didn't excite all nuclear spins because the skin

effect screened the nuclear spins further inside the bundle, at least partially. That situation could be improved by putting an insulation between the wires, e.g. SiO_2 or GE varnish[66]. Besides eddy currents, the ohmic resistance of the coil could be the source of heat which was observed elsewhere [139]. Taking a typical voltage of a pulse, 20 V, and the resistance of the leads ($\sim 500\,\Omega$) and the resistance of the coil we get a power or 70 mW for a continuous ac current. If we further consider the length of a pulse (of the order 200 kHz) we get an average power of 5 to 10 10 nW for a pulse repetition time of 5 s. That is roughly in agreement with our observations.

7.2. Typical Demagnetisation Cycles

Before the system can actually be demagnetised the magnetic field has to be ramped up first. This causes the electrons in the plates to heat up for two reasons. On the one hand, the large nuclear heat of magnetisation is released, on the other hand, eddy currents induce heat. However, we typically ramped up the field within about 20 min. The plates then warmed up depending on the ramp speed but within 1 h they cooled back to below 30 mK. Figure 7.7 shows a typical development of temperature after magnetising the copper. The lowest achievable precooling temperatures depended also on the performance of the DR. Given a well-balanced mixture we could achieve $\sim 12\,\text{mK}$ within $\sim 2\,\text{d}$.
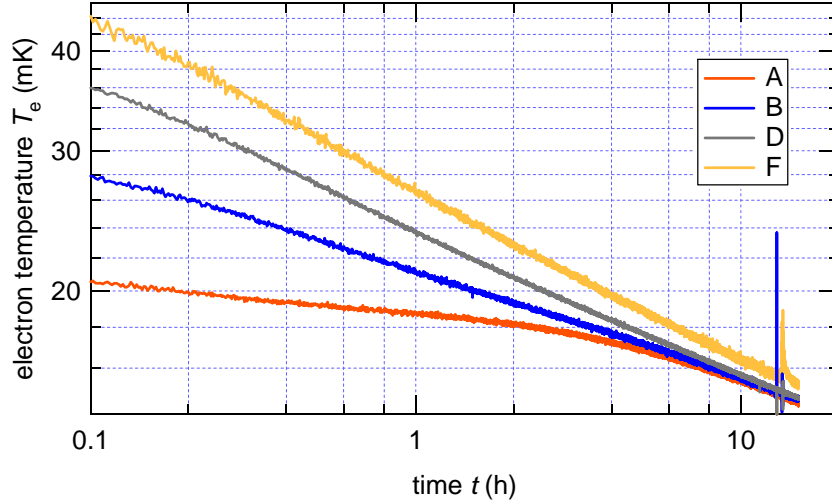
Figure 7.7.: Electron temperature of the RuO_2 chips as a function of time after magnetising to 8 T. After one hour the plates usually cooled to below 30 mK.
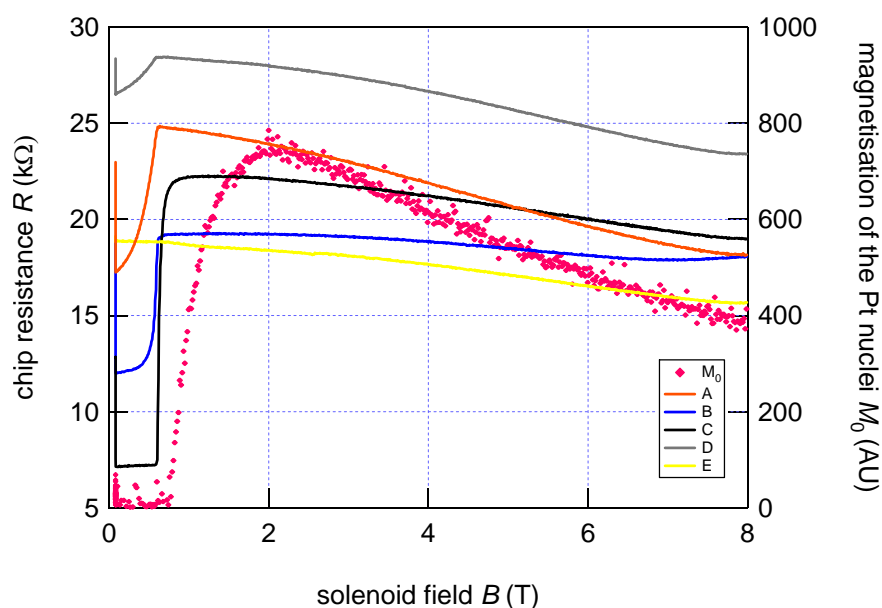
Figure 7.8.: A demagnetisation from $8\,\mathrm{T}$ to $80\,\mathrm{mT}$ with a ramp rate of $1\,\mathrm{T/h}$. The graph plots the chip resistance and the magnetisation of the Pt nuclei which reflects the temperature of plate F as a function of magnetic field. All thermometers show initial cooling in order to warm up below a certain field, except E . At the final field the resistances drift up again as a function of time.

From the demagnetisation cycles two basic issues became evident. First, the process is ramp rate dependent and second, the plates are most likely (thermally) coupled.

Figure 7.8 shows the Resistance of the chips as a function of magnetic field during a demagnetisation done at a ramp rate of $1\,\mathrm{T/h}$. All chips, except B, exhibit cooling when the demagnetisation is started at $8\,\mathrm{T}$. Chip B first warms up by a small amount and exhibits cooling afterwards, too. This behaviour of chip B is also visible in figure 7.9. In those demagnetisation cycles we stopped at $4\,\mathrm{T}$ and $2\,\mathrm{T}$ to readjust the current in the heat switch magnet. When the demagnetisation was continued B first warmed up before it continued to cool. Besides this particular behaviour of chip B, all chips eventually warmed up around $1\,\mathrm{T}$ to temperatures much higher than the precooling temperature. The highest temperature to which the plates warmed up was higher for faster ramp rates. Chip B for instance warmed up to $58\,\mathrm{mK}$, $65\,\mathrm{mK}$, and $75\,\mathrm{mK}$ for ramp rates of $1\,\mathrm{T/h}$, $2\,\mathrm{T/h}$, and $4\,\mathrm{T/h}$.

In figure 7.8 the PtNMR thermometer is the first to show warming. The second to follow is chip C. Afterwards, chips A, B, and D start to warm up also but more

abruptly than C. Chip E does not warm up. One possible explanation is that the plate connected to the PtNMR warms up first and at some point heat leaks into the plates of chip C and eventually also into the plates monitored by chips A, B, and D. Since, E doesn't warm up it seems not to be coupled to the other plates. However, comparable behaviour was also observed with the PtNMR thermometer absent.

A coupling can also be inferred from the following observation. Figure 7.10 shows that the sacrificial plate lacks both, cooling and warming. Since, chip C does not exhibit an overall trend of cooling in figure 7.9 it is possibly coupled to the sacrificial plate. Moreover, chip C is connected to one plate which is next to the sacrificial plate.
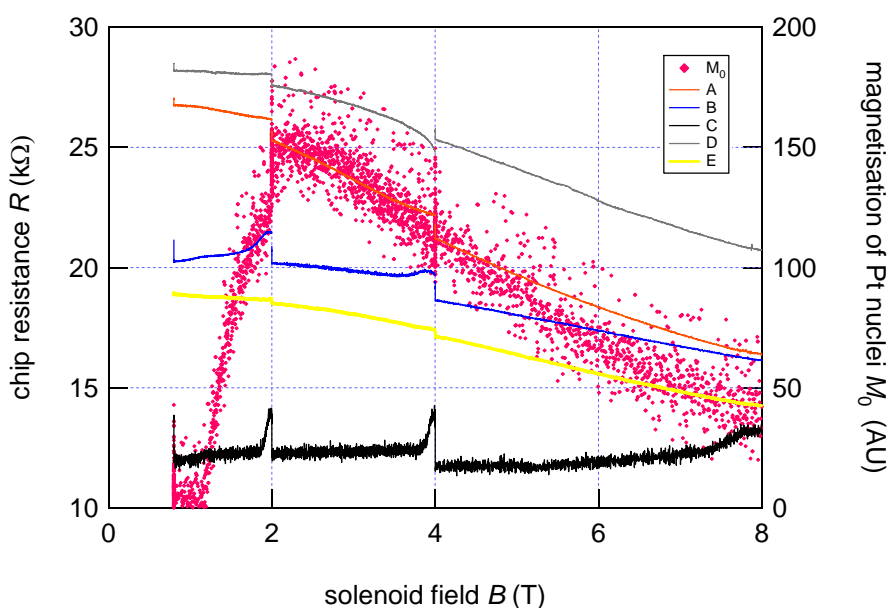
Figure 7.9.: A later demagnetisation from 8 T to 4 T to 2 T to 0.8 T at rates of 1 T/h, 0.5 T/h, 0.5 T/h. Chips A,B, D and E show an overall trend of cooling. The magnetisation reading is qualitatively as in figure 7.8. Chip C warms up when the the field changes and saturates. At 4 T, 2 T, and 0.8 T, when the field is not ramping, it cools again.

Figure 7.10 shows the chip resistances during the demagnetisation that we did before the heating curves shown in figure 7.14. It was done to a final field of 1 T at rates of 1 T/h, 0.5 T/h, and 0.5 T/h, respectively. Chips A, B, and D exhibit cooling. Chip F warms up towards the end of the demagnetisation. This apparently high heat load seems to be associated with vibrations as we could see a dip in resistance of chip F also when the cryostat was tapped, more than for other
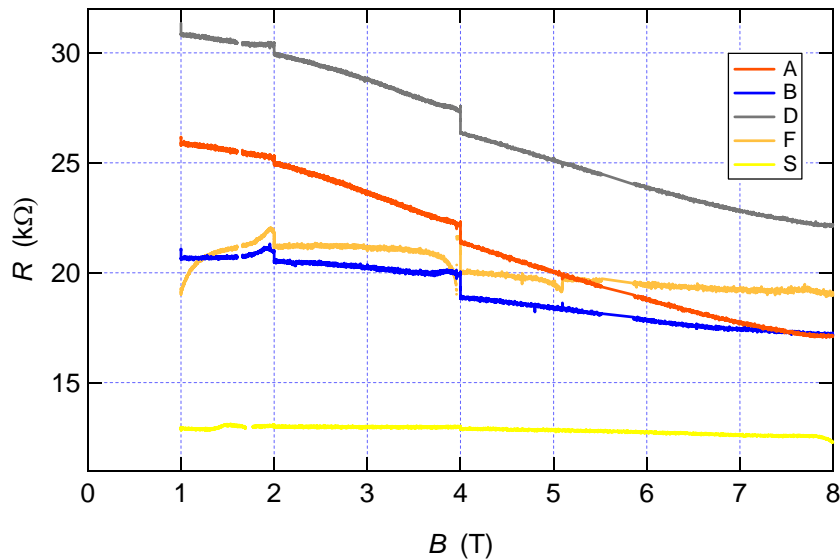
Figure 7.10.: Resistance of the chips versus magnetic field during the demag-
netisation done before the heating curve shown in figure 7.14 a).
It was ramped from 8 T to 4 T to 2 T to 1T T at rates of 1 T/h,
0.5 T/h, 0.5 T/h. Chips A, B, and D exhibit cooling whereas chip
S lacks both, cooling and warming. Chip F warms up towards the
end of the demagnetisation.

chips. That's most likely also the reason for the feature at $\sim 5\,\mathrm{T}$, the resistance
dip at 4 T, and the feature of F in the pre-cooling graph above 10 mK (figure 7.7).
Chip S lacks both, cooling and warming which suggests that the sacrificial plate
is significantly coupled to a temperature bath.

7.3. Heat Switch Maps

During the demagnetisations we realised that the switches open/close at different
current values of the switch magnet. That can be seen in the heat switch maps
(figure 7.12) which plots the switching points as a function of heat switch current
and the solenoid field. With the help of figure 7.11 I explain how we determined
the switch points. The switch magnet was at zero current, hence the plates were
decoupled. Then we ramped the solenoid to a chosen setpoint which warmed up
the plates to temperatures between 100 mK and 200 mK due to eddy currents.
Subsequently, the switch magnet was ramped. When a switch opened the thermal
coupling suddenly improved and the temperature dropped faster. The results were
kinks in the graph. The value of the temperature doesn't matter, we were only
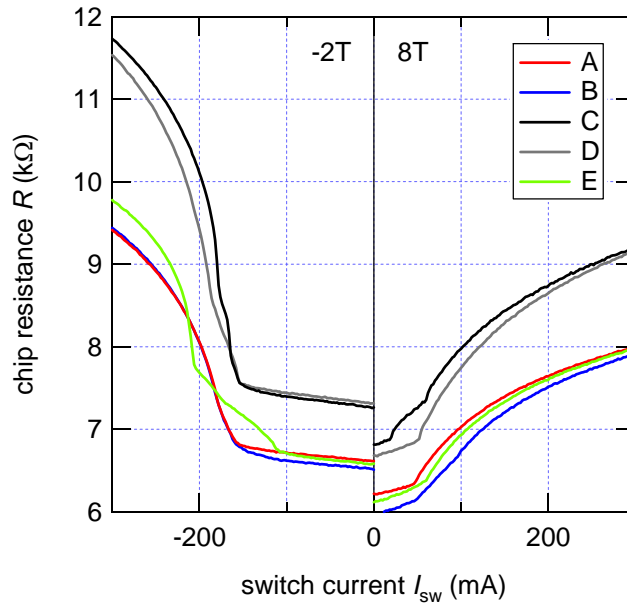
Figure 7.11.: Chip resistances as a function of switch current. The kinks indicate the switch points. The solenoid fields are -2 T and 8 T, respectively.

interested in the value of the switch current. Repeating this for various solenoid fields, e.g. -2 T and 8 T as shown in figure 7.11, and both current directions of the switch current yields the maps shown in figure 7.12. Figure 7.12 a) shows the map before we re-arranged the switches. There is no obvious systematic pattern. In order improve that situation we re-arranged the switches such that they have approximately the same distance from the centre axis of the cryostat and approximately the same height. Afterwards, we determined the switching points again. The result is plotted in figure 7.12 b). It is a clear improvement over the situation before. The points now exhibit a systematic pattern indicated by the solid lines.

Intuitively, one would expect the switches to fall on a straight line, as indicated by the dashed traces. That is because the switch field, about 10 mT, gets altered by the stray field of the solenoid. It is unknown where these inhomogeneities originate that cause this deviation. However, the map is roughly symmetric and we decided first to operate the switches in the centre between the two switch points which means that we adjusted the switch current during demagnetisation cycles. Second, we decided to pay attention not to move the switches any more.
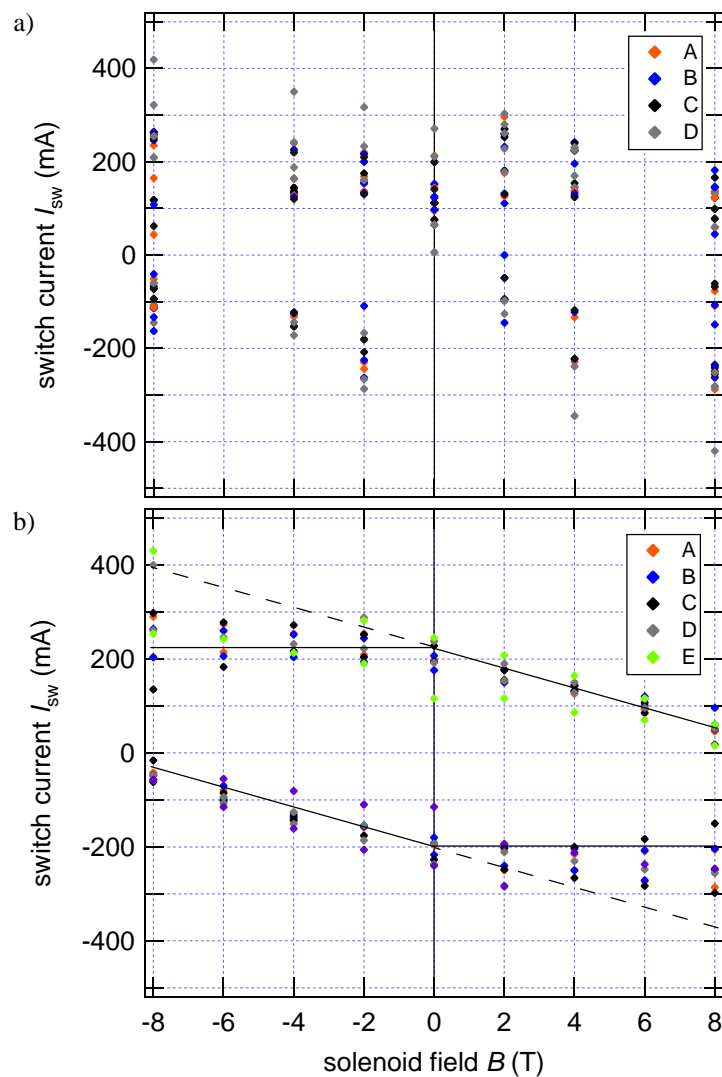
Figure 7.12.: The heat switch maps before a) and after re-arranging the switches
b). The data represent the switching point of the aluminium
switches as function of solenoid field and switch magnet current.
The black solid lines in b) indicate a regular pattern. The dashed
lines indicate what one would expect if the fields simple added up
vectorially.

7.4. Power Curves

Nuclear demagnetisation requires adiabaticity, i.e. zero heat leak. However, there will be an inevitable heat leak which can be quantified as follows. The heaters mounted on the outside plates B, D and F enabled us to apply defined amounts of power P_{app}. We apply that while the plates are decoupled from the the mixing chamber. The power is ultimately drained away by the mixing chamber where we assume that the superconducting heat switch is the primary path. We then recorded the equilibration temperature T_{e} as a function of applied power and plot T_{e} vs P_{app} as shown in figure 7.13. The thermal conductance of the aluminium
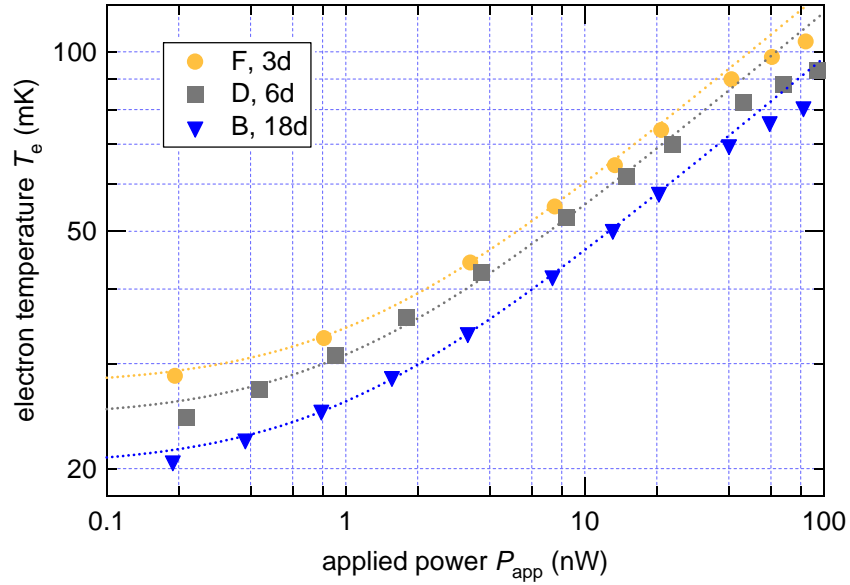
Figure 7.13.: Power curves for chips F, A and B taken 3, 6 and 18 days after
initial cooldown. The graph plots the temperature at which the
chips equilibrate for a given power in the heater.

heat switches is dominated at low temperature by phonon-dislocation scattering processes, obeying the relation [129]

$$P_{\text{app}} = nA\left(T_{\text{e}}^3 - T_{\text{MC}}^3\right) - P_0 \tag{7.1}$$

where P_{app} is the applied power, $n = 0.57\,\text{mol}$ of Cu, A is a prefactor, and P_0 is the intrinsic heat leak to the plate. The dashed lines in figure 7.13 are the fits to this equation. They are in very good agreement with the experimental data, excepts for $T_{\text{e}} > 70\,\text{mK}$ where parallel channels of heat flow become accessible. On the one hand, superconducting quasi-particles start to contribute which can be seen in

figure 6.9. On the other hand, there is some heat flow through the Teflon$^{\text{TM}}$ spacers between the plates at higher temperatures. However, this method enabled us to quantify the heat leak P_0 which improved over time as indicated by the decrease in T_{e} (which holds true for all chips) as $P_{\text{app}} \to 0$ in the power curves obtained 3, 6, and 18 days after cooling down. We conclude that the typical intrinsic heat leak to the demagnetisation stage at $B = 0$ is $P_0 \lesssim 1\,\text{nW/mol}$ which is sufficiently low but clearly above the state of the art value of $\lesssim 5\,\text{pW/mol}$ [56].

All the power curves were taken at zero field. At finite field the equilibration times become extremely long due the large nuclear heat capacity. However, we quantified a heat leak at $B = 2\,\text{T}$ which is $\sim 7\,\text{nW/mol}$. This could be due to small vibrations of the plates in the non-uniform field that induced eddy currents. Another possible cause could be the magnet power supply.

Furthermore, the power curves allow us to convert a saturated temperature into an effective heat input, hence a leak. From such a chart one can easily read at least the order of magnitude of a heat leak.

7.5. Heating Curves

In the absence of a direct measurement at lowest temperatures, we had to measure the achieved temperatures indirectly. We extract T_{f} and $T_{\text{e}} \gtrsim T_{\text{f}}$ of the plates reached after demagnetising to B_{f} by recording the time t necessary for a Cu plate to 'completely' $(1/T_{\text{e}} \to 0)$ warm up under a known, applied power, using (3.58) and (3.60).

In figure 7.14 we plot time traces of $1/T_{\text{e}}$ for chip D for $P_{\text{app}} = 25\,\text{nW}$, $50\,\text{nW}$, and $100\,\text{nW}$. The other thermometers give consistent results, except for F, which appears to heat up during demagnetisation. Due to poor internal thermalisation $1/T_{\text{e}}$ increases for the first several hours despite the influx of heat, only showing significant signs of warming once the Cu is hotter than $\sim 10\,\text{mK}$. Since the temperature gradient between the chip and nuclear refrigerator will vanish at $1/T_{\text{n}} = 1/T_{\text{e}} = 0$, we fix this point (blue line figure 7.14 b)) of the theoretical $1/T$ curves (solid and dashed lines) and extrapolate back to $t = 0$. As expected, larger P_{app} results in faster warm up times.

With this, we find that the final obtained temperature after the demagnetisation is $T_{\text{f}} = 3.0 \pm 0.3\,\text{mK}$ for all three P_{app}, demonstrating the reliability of achieving a particular minimum temperature for a set of demagnetisation parameters. The uncertainty in T_{f} is dominated by the inhomogeneity of B_{f}. Note that in the temperature range explored here, $T_{\text{n}} \approx T_{\text{e}}$ before the power is turned on since $P_0 \ll P_{\text{app}}$.

Figure 7.14 b) shows a final test, a demagnetisation from $8\,\text{T}$ to $0.32\,\text{T}$ starting at $13.3\,\text{mK}$ and cooling to $1.2 \pm 0.1\,\text{mK}$ which was extracted using the method
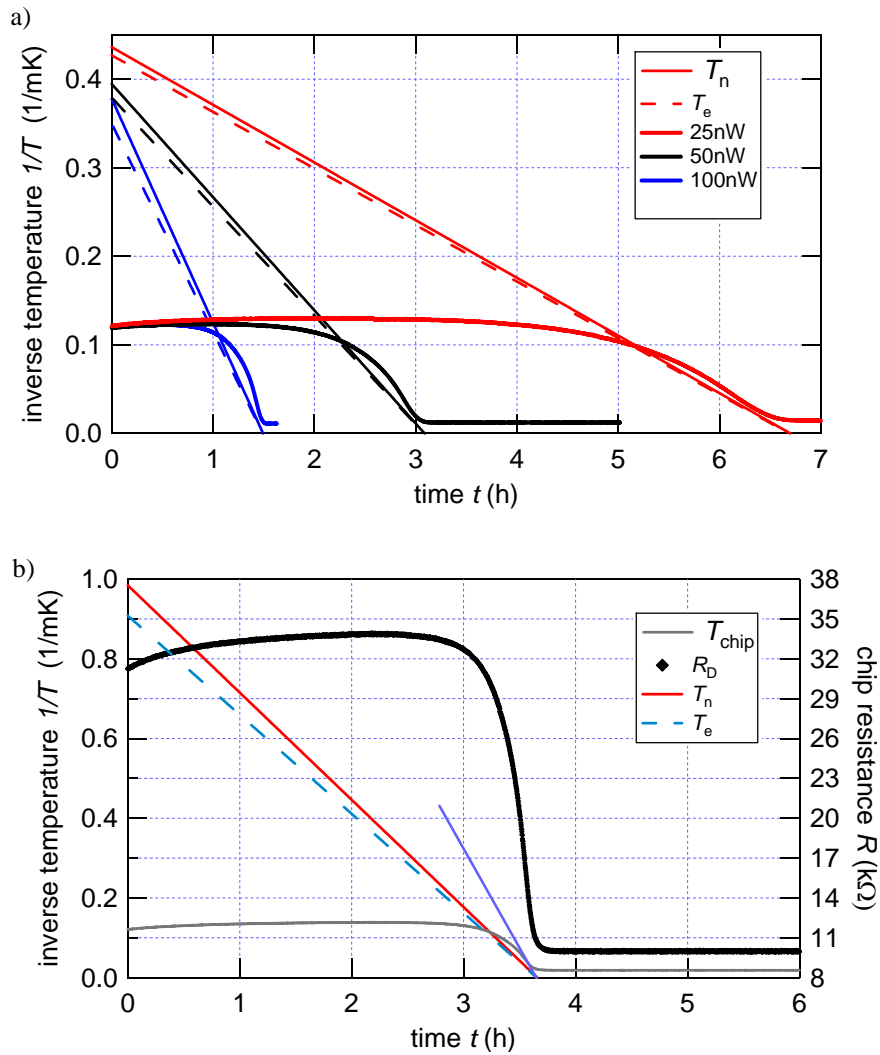
Figure 7.14.: Heating curves for chip D. The electron temperature is measured while a known amount of heat flows into the plate. The blue line in b) extrapolates to 'infinite temperature'. From this point we extrapolate back to $t = 0$ which gives the starting temperature. a) shows the chip temperatures at a final field of 1 T at 25 nW, 50 nW, and 100 nW. b) shows it at 0.32 T applying 10 nW. It also shows a comparison of inverse temperature with the underlying chip resistance on the vertical axes. Both quantities show qualitatively the same behaviour.

described above. This demonstrates a reduction in temperature upon demagnetisation by a factor of 10. The other chips perform similar to D, thus substantiating

the overall cooling scheme proposed here for reaching submillikelvin temperatures on multiple measurement leads.

7.6. Heat Leaks

Ideally, T_i of the Cu nuclei will be reduced by the same factor x as the B-field. To characterise the demagnetisation process we introduce the efficiency

$$\xi = \frac{B_f/T_f}{B_i/T_i} = \frac{B_f T_i}{B_i T_f} \tag{7.2}$$

where B_i, T_i are initial field and temperature, and B_f, T_f are final field and temperature, respectively. We started our demagnetisation cycles at $8\,\mathrm{T}$. The initial or precooling temperature varies and depends on the precooling time allowed. The efficiency can be divided into a total and a sequential efficiency. The first refers to the initial field whereas the second analyses single demagnetisation steps. In figure 7.15 the two efficiencies are plotted. The total efficiency always refers to the parameters at $8\,\mathrm{T}$. The sequential efficiency expresses the quality of one sequence which is from $8\,\mathrm{T}$ to $4\,\mathrm{T}$ from $4\,\mathrm{T}$ to $2\,\mathrm{T}$, and so forth. Total and sequential efficiency are equal for $4\,\mathrm{T}$ by definition but the difference at $2\,\mathrm{T}$ shows that the loss from $8\,\mathrm{T}$ to $4\,\mathrm{T}$ must be larger than that from $4\,\mathrm{T}$ to $2\,\mathrm{T}$. In fact at $4\,\mathrm{T}$ we slow down the ramp rate, and hence the eddy current heating is reduced.

We determined the influence of the ramp rate also in another way. The plates were decoupled (switches superconducting) and the magnet was ramped from an initial field B_i to a final field B_f. We recorded the temperatures T_i and T_f respectively. The temperature rose and we assumed the only source to be eddy current heating or other mechanisms related to a changing magnetic field. Since we knew all parameters, we could calculate the heat capacities from integrating (3.36) and (3.12). Hence, the heat balances for nuclei and electron are given by

$$\Delta Q_n \sim \frac{B_i^2}{T_i} - \frac{B_f^2}{T_f} \tag{7.3}$$

$$\Delta Q_e \sim T_i^2 - T_f^2 \tag{7.4}$$

where the proportionality factors contain natural constants and material parameters. From the sum $\Delta Q = \Delta Q_n + \Delta Q_e$ and the time it took $\Delta t = t_f - t_i$ we can deduce a heat leak

$$\dot{Q} = \frac{\Delta Q}{\Delta t} \tag{7.5}$$

We obtained $\sim 2\,\mathrm{nW}$ at $0.9\,\mathrm{T/h}$ and $\sim 10\,\mathrm{nW}$ at $2.7\,\mathrm{T/h}$. Note that we scanned between 0 and $100\,\mathrm{mT}$ to keep the influence of the nuclear heat capacity and the
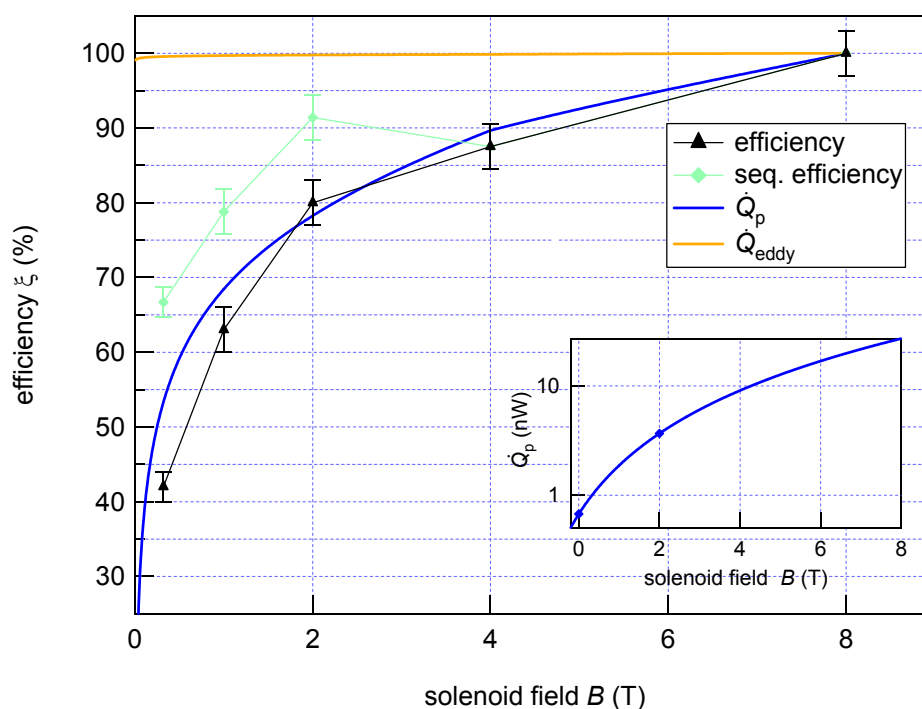
Figure 7.15.: Efficiency as a function of magnetic field. The efficiency is calcu-
lated with respect to the starting conditions at 8T. The sequential
efficiency is calculated from one step to the next. The two theory
traces,$\dot{Q}_{\mathrm{eddy}}$ and $\dot{Q}_?$ are calculations from data point data point
of how much a given heat warms up the plate. $\dot{Q}_{\mathrm{eddy}}$ plots the
efficiency if we assume eddy currents, (3.75), only, where as $\dot{Q}_?$
which is shown in the inset, is quadratic in B and matches the
observations made at 0T and 2T.

heat of magnetisation small. However, we scanned both direction and the heat
leak was slightly larger for ramping the field down.

In another test we ramped the magnetic field, again around $B = 0$. We recorded
the temperature and compared the value at which the temperature saturated with
the power curve chart (figure 7.13). This way we determined magnitudes of $\sim$
$35\,\mathrm{nW/mol}$ at $1\,\mathrm{T/h}$ and $\sim 18\,\mathrm{nW/mol}$ at $0.5\,\mathrm{T/h}$, which are 20 and 40 times
greater than expected from simple eddy current calculations, (3.75).

Furthermore, we tried to find a model that can explain the efficiency. Therefore,
we calculated from data point to data point how much a given heat leak will warm
up T during the increment of time. We assumed a quadratic heat leak $\dot{Q}_{\mathrm{p}}$ that
matches the observations made at 0 and 2 T where we measured 0.5 nW and 4 nW,
respectively. This heat leak is shown in the inset of figure 7.15. Integrating this

gives the theoretical curve in figure 7.15. It matches the measured efficiencies much better then the integrated heat that is explained by eddy currents, $\dot{Q}_{\text{eddy}}$.

Though we can quantify the heat leaks we cannot locate the source. One possible reason could be vibrations. In order to reduce that we tried to fix the magnet with respect to the IVC. We added Teflon$^{\text{TM}}$ pieces on the magnet. On the one hand Teflon$^{\text{TM}}$ shrinks when cooled but on the other hand it is flexible and exerts a pressure on the IVC. We added three finger pieces on the hight of the cancellation coils and a slotted ring at the bottom of the magnet. However, we could not observe any change.

Another source could be inhomogeneities. Any factor that changes the field locally, goes directly into the ramp rate. The field factor is a function of position. Starting from the centre of the solenoid it goes up towards the wall of the solenoid. In order to explain the factor of ten larger eddy currents the field factor needs to be more than a factor of three larger than the given value. Plugging reasonable numbers for the solenoid into (C.1) and (C.2) shows that this seems unrealistic.

From the field profile of the magnet we know that the field on the centre axis drops from 8 T to about 7 T at the edges of the plates. This would lead to a slower ramp rate, though.

Inhomogeneities play an important role if one considers the impact of vibrations. The field is quite inhomogeneous in particular in the region between the main solenoid and the cancellation coils where the field drops comparatively fast from full field to zero. Considering our set-up (see appendix D), it is more likely that the plates are located more in the inhomogeneous region of the lower part of the magnet. In summary, inhomogeneities in combination with vibrations can possibly partially explain the heat leak.

However, our measurements clearly show that the heat leak is triggered by a changing magnetic field which suggests that intrinsic vibrations alone cannot explain the observations. In conclusion the origin of the heat leak remains an open question.

Quantum Dot Measurements

So far all measurements determined the performance of the nuclear refrigerators. And we can say that we achieve millikelvin temperatures upon demagnetisation. Once the nuclear refrigerators proved to perform satisfyingly we were able to cool down a quantum dot - the first nanoelectronic device.

Samples

We cooled down two quantum dots, labelled #2.2 and #4.3, fabricated by Sarah Heizmann [140] and Kristine Bedner on a waver grown in the group of A.C. Gossard. In both cases, we glued the sample with silver paint ('G302 Leitsilber') onto the chip carrier. Standard gold wire bonds ($\varnothing\, 32\,\mu$m, RRR~ 39) were used to contact six top gates and two ohmic contacts. Thus, we had four gate voltages: the nose V_{N}, left V_{L} and right wall V_{R}, and the plunger gate V_{P}. The layout of the quantum dot is given in figure 8.1, the numbers are labels of the wiring path used to measure #4.3.

The attempt to measure #2.2 failed. We could not find any gate configuration to to form a quantum dot. An inspection of the nanostructure with an electron microscope proved that the surface gates were completely disintegrated (figure 8.3). In some step of the mounting and cooldown procedure the gates where overcharged and hence destroyed.

However, the attempt to measure #4.3 was more successful. Although, it turned out to be broken, too, we could form a quantum dot. Figure 8.2 shows an electron
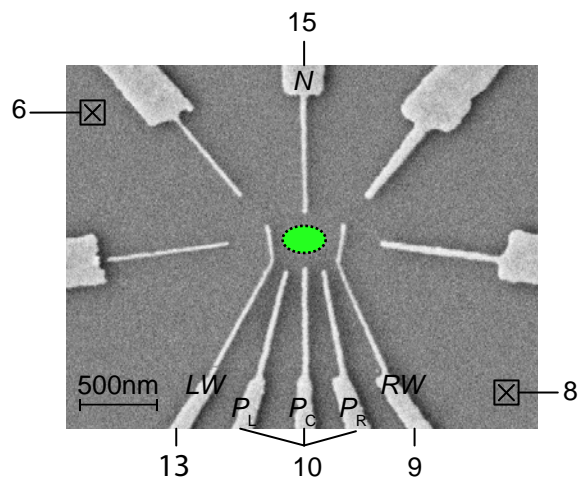
Figure 8.1.: Layout of the quantum dots. Both dots #2.2 and #4.3 were nominally the same, the distance between the walls is $\lesssim 500\,\text{nm}$, the fine sections of the surface gates is $\sim 30\,\text{nm}$. The three plunger gates were, in either case, bonded to one contact, hence acting as one plunger. The numbers indicate the wiring path of #4.3. Contacts 6 and 8 are the ohmic contacts of source and drain, respectively.
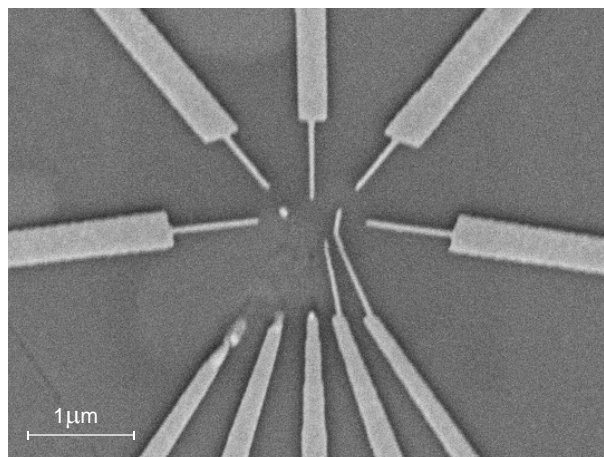
Figure 8.2.: Electron micrographs of quantum dot #4.3 which proves that the dot was destroyed.
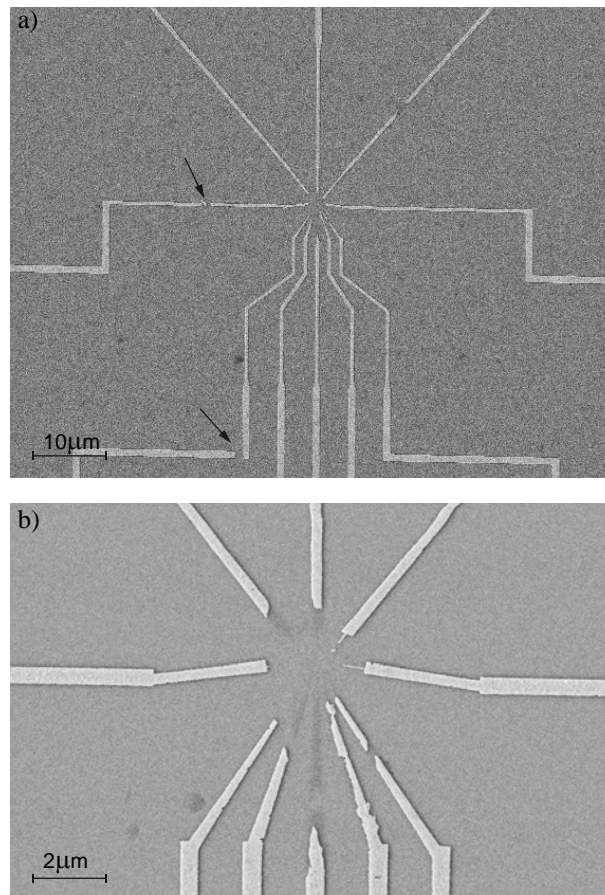
Figure 8.3.: Electron micrographs of quantum dot #2.2 after the cooldown. a) Large-scale image. The arrows point at disruptions that were even visible under good optical microscopes. b) The close-up clearly proves that the sample was destroyed.

micrograph of #4.3 after it had been warmed up. The left wall and two of three plunger gates have disappeared. Despite the destruction, we were able to form a dot and measure a so-called wall-wall scan as shown in figure 8.4. It displays the current as a function of the voltages on the walls. Plunger gate and nose gate were at constant voltages, $V_N = -1300 \, \text{mV}$ and $V_P = -380 \, \text{mV}$ where we measured at a purely dc bias of $V_{DC} = 200 \, \mu\text{V}$.

In the lower third on the right-hand side, one can see current peak lines - a clear sign of a single quantum dot. The plot also shows traces of a double quantum dot as described in figure 2.7 b). The anti-crossing is clearly visible near $V_L \sim -1300 \, \text{mV}$ and $V_R \sim -650 \, \text{mV}$. In the upper right section the features are very broad but
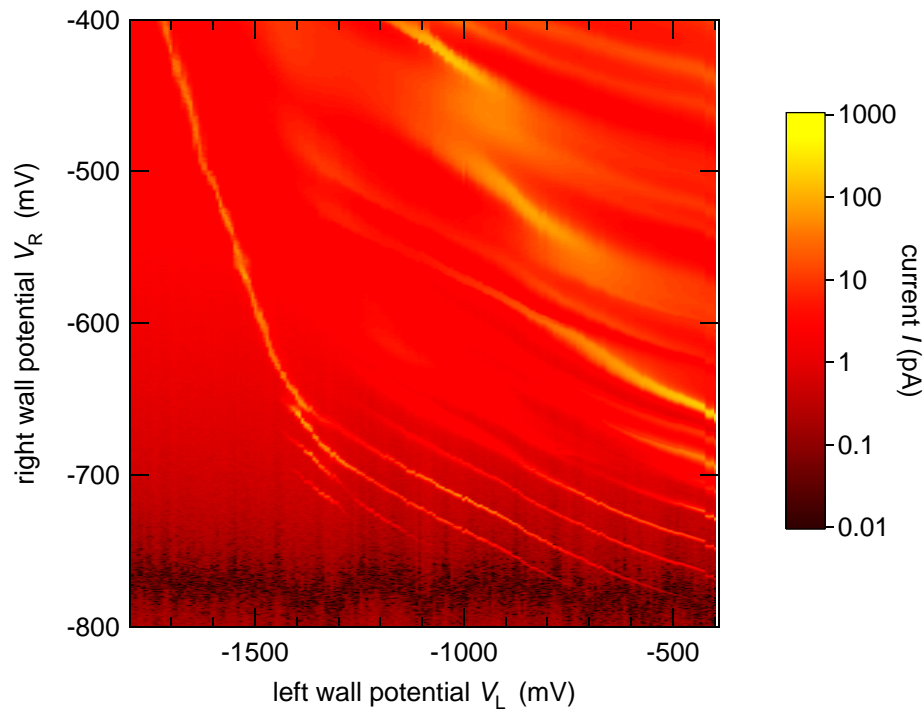
Figure 8.4.: Wall-wall scan at constant bias voltage of $200\,\mu\text{V}$. In the lower third on the right-hand side, the current peak lines suggest a quantum dot. The features in the upper right corner faintly exhibit anti-crossings. Around ($V_\text{L} \sim -1300\,\text{mV}$, $V_\text{R} \sim -650\,\text{mV}$) the anti-crossing is more obvious.

they show also faint hints on a double dot. Since the sample was destroyed, we could speculate that the remaining gates and some metal fragments formed an electrostatic configuration which in turn formed a double quantum dot.

Coulomb Diamond

However, we also recorded the current as a function of plunger gate voltage and bias voltage for fixed wall voltages. The result was a COULOMB diamond displayed in figure 8.5 for $V_L = -575\,\mathrm{mV}$ and $V_R = -743\,\mathrm{mV}$. Despite the broken sample, the diamonds are surprisingly clearly distinct. The diamonds in the upper half are fairly symmetric with respect to $V_{DC} = 0$. We can extract a lever arm of $\alpha \sim 11$ and a charging energy of the order $2\,\mathrm{meV}$. In the lower half the diamonds are asymmetric, likely because of the broken sample.
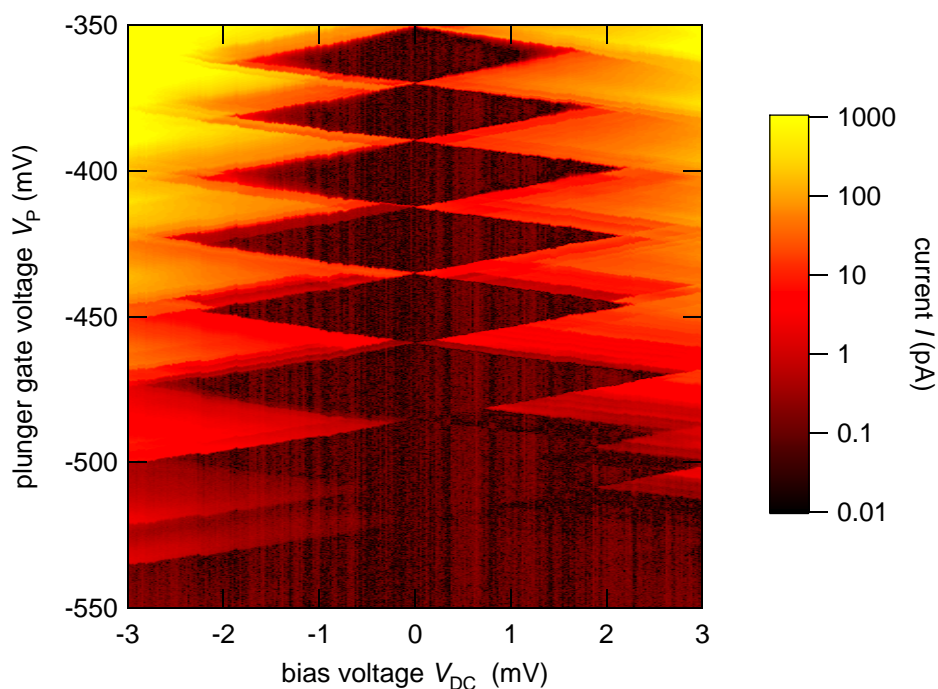
Figure 8.5.: COULOMB diamonds measured on #4.3. It plots the current through the dot as a function of bias voltage V_{DC} and plunger gate voltage V_P for constant wall potentials, $V_L = -575\,\mathrm{mV}$, $V_R = -743\,\mathrm{mV}$.

Coulomb Blockade Steps

Having made sure that COULOMB blockade can be observed, we tried to measure electron temperatures. We recorded many COULOMB steps during the experiment. A choice is plotted in figure 8.6. In such a measurement, we recorded the current
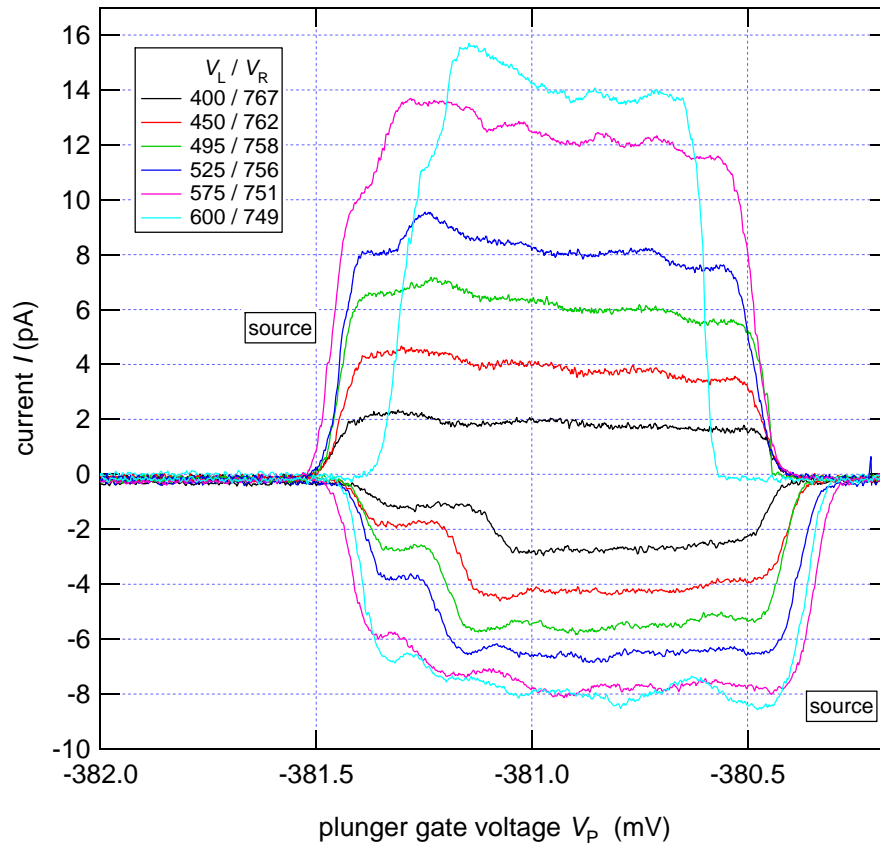
Figure 8.6.: Choice of COULOMB steps for various combinations of left and right wall potentials (measured in mV) and positive and negative bias voltage $V_{DC} = \pm 200\,\mu V$. The graph plots dc current as a function of plunger gate voltage. The traces were taken at base temperature of the mixing chamber. 'source' labels the flank that reflects the source electrode, the other flank is the drain, correspondingly.

while sweeping the plunger gate voltage across a current peak in the lower right corner of figure 8.4. Each current step was taken in another spot but on the same peak line. The wall voltages were tuned such that we could measure a section along that line. The graph shows that the current differs for positive and negative bias of the same magnitude and for the same wall configuration. Furthermore, we

tuned the left wall from 400 mV to 600 mV, whereas the right wall voltage spanned only 18 mV. This is an order of magnitude different which can also be attributed to the broken sample.

Electron Temperatures

However, we extracted temperature from the Coulomb steps. We fitted Fermi-Dirac (2.3) steps to their flanks. The lever arm was extracted from the width of the current steps. Figure 8.7 shows the obtained electron temperatures as a
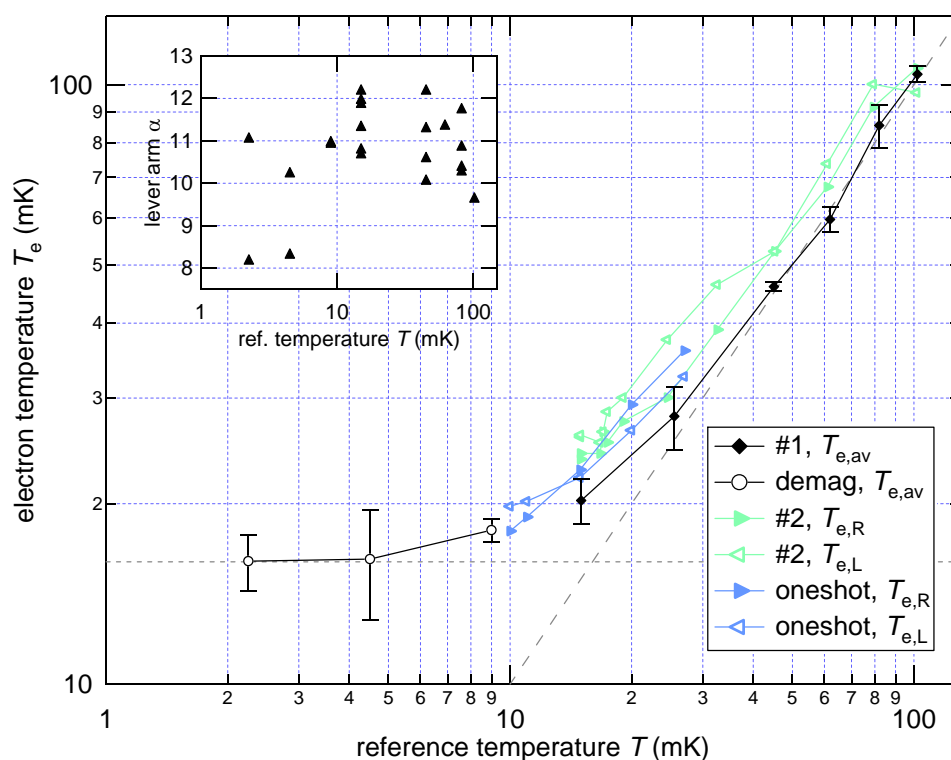
Figure 8.7.: Results of different electron temperature measurements. The graph plots electron temperature in the quantum dot as function of reference temperature. The inset shows the scatter of the lever arm.

function of reference temperatures. For traces #1, #2 and the 'oneshot' traces we refer to the mixing chamber temperature as measured with a CMN thermometer. Traces #1, #2 were measured while controlling the temperature of the mixing chamber whereas the 'oneshot' trace was measured during a oneshot of the mixing chamber, i.e. we interrupted the re-condensation of ^{3}He . For temperatures below the base temperature (trace 'demag') we demagnetised. The reference temperature

is obtained by dividing the precooling temperature prior to demagnetisation by the field reduction factor. Trace #1 and the 'demag' trace display the average temperature of the two reservoirs. The other four traces show the temperature for the left and the right reservoir separately.

For temperatures above $\sim 25\,\mathrm{mK}$, trace #1 shows very good agreement between the two temperatures. The dashed line is a guide for the eye. The green traces read higher temperatures, but follows roughly a linear trend. The electron temperatures upon demagnetisation saturate at $\sim 17\,\mathrm{mK}$ at lowest temperatures, indicated by the dotted line. The saturation is confirmed by the lowest temperature point of #1 and the oneshot data.

The inset in figure 8.7 shows the scatter of the lever-arm, one source of uncertainties for the temperature reading.

Life-Time Broadening

In order for Coulomb blockade thermometry to work the tunnel rates $\Gamma_{\mathrm{S,D}}$ have to be smaller than temperature, $h\Gamma_{\mathrm{S,D}} \ll k_{\mathrm{B}}T$. If $h\Gamma_{\mathrm{S,D}} \approx k_{\mathrm{B}}T$ the current flanks become life-time broadened (see section 2.1.4). The current through the dot can be written [26]

$$I = 2\,|e|\,\frac{\Gamma_{\mathrm{D}}\Gamma_{\mathrm{D}}}{2\Gamma_{\mathrm{S}} + \Gamma_{\mathrm{D}}} \tag{8.1}$$

where e is the elementary charge and the factor 2 in the denominator is due to spin degeneracy. However, if one tunnel barrier is more permeable than the other, say $\Gamma_{\mathrm{S}} \gg \Gamma_{\mathrm{D}}$, the smaller tunnel rate limits the current and we get

$$I = 2\,|e|\,\Gamma_{\mathrm{D}} \tag{8.2}$$

This corresponds to a temperature according to

$$\Gamma_{\mathrm{D}} = \frac{I}{2\,|e|} = \frac{k_{\mathrm{B}}}{h}T \tag{8.3}$$

with h being Planck's constant. The currents we measured is of the order $10\,\mathrm{pA}$. This gives $\Gamma_{\mathrm{D}} = 31\,\mathrm{MHz}$ or $T = 1.5\,\mathrm{mK}$. On the other hand, the saturation temperature, $17\,\mathrm{mK}$, can be converted to $\Gamma = 360\,\mathrm{MHz}$. According to the Breit-Wigner form (2.27), the higher tunnel rate limits the temperature resolution. Looking at the broken sample (figure 8.2) and considering that we need an 'asymmetry' of $\Gamma_{\mathrm{S}}/\Gamma_{\mathrm{D}} \sim 10$ only, we can say that the temperatures read are upper bounds. Thus, and considering the broken sample, the question of the lowest achieved electron temperature remains unsolved.

Summary, Conclusions and Outlook

9.1. Summary

We built a network of parallel nuclear refrigerators each part of the single leads of a low-temperature measurement set-up for mesoscopic devices. As to my knowledge we were the first in the world to accomplish this approach. We were able to achieve temperatures of about $1\,mK$ in the copper plates. Furthermore, we developed versatile tools to analyse and characterise the performance of such a network. We also showed that it is actually possible to measure nanostructures with this novel type of refrigerator. Despite the overall success we also encountered some problems. Besides vibration and noise issues, the main limitation is a ramp rate and field dependent heat leak which cannot be explained with simple eddy current considerations.

9.2. 2nd Generation Stage

Guidelines and Set-up

After performing measurements with the prototype stage for about one year we decided to built another stage, the second generation stage. With the experiences made with the prototype we laid down some guidelines for the construction. I will give a brief overview only, a detailed explanation is given in [133]. Figure 9.1

shows a technical drawing and a photograph of the 2$^{\text{nd}}$ generation stage. In the
following I present some considerations and issues.

1. Materials.
   Since we cannot exclude the Araldite$^{\text{TM}}$ to be the source of time-dependent
   heat release on the sacrificial plate we decided to avoid plastics as much as
   possible. That means that ceramics and metals remain as materials of choice.

2. Sample Holder.
   A second major change is the way to mount the sample. We decided to
   pursue the idea of a home-built plug-in chip carrier as it is usually used in
   the field. On the one hand, the mounting process changes that it is no longer
   necessary to carry the whole stage to a bonding facility which means that
   it is easier to bond but also over-charging the gates on the sample is easier
   to avoid. On the other hand, the mixing chamber can stay closed. The
   latter point includes avoiding possible leaks in the cone seal as well as saving
   pump-down time.

3. Nuclear Refrigerators.
   The prototype comprised 12 demagnetisable leads each containing about
   0.5 mols of copper. Increasing the amount of copper per plate should increase
   the cold time as well as the cooling power. The number of plates on the other
   hand increases the versatility. Since we had more available space, we could
   fulfil both wishes: 21 plates of about 1 mol of copper each. Furthermore, we
   picked a raw material with higher purity. The RRR is ∼450.
   The basic idea of a stack of plates is kept. But instead of tying the bundle
   against a sacrificial plate, we tied the plates together and employed two
   nylon screws to bolt the whole bundle against a gold-plated silver plate. We
   added Teflon$^{\text{TM}}$ discs between the copper plates to keep them apart from
   each other. Ceramic disc proved to be too brittle.

4. More Rigidity.
   The 'banana effect' described in section 5.3.2 should be eliminated by mount-
   ing a strong tripod construction anchored in the cold plate. Taking a tripod
   structure along the whole stage should improve the stiffness of the whole
   stage. Later we even put a tripod between the still and the 1K pot be-
   cause we realised that we have moved the weakest point from right above
   the mixing chamber to the section between still and 1K pot.

5. Heat Switches.
   The first heat switch generation achieved on/off ratios of around 10^5. Chang-
   ing the geometry of the switches should increase that value and decrease the
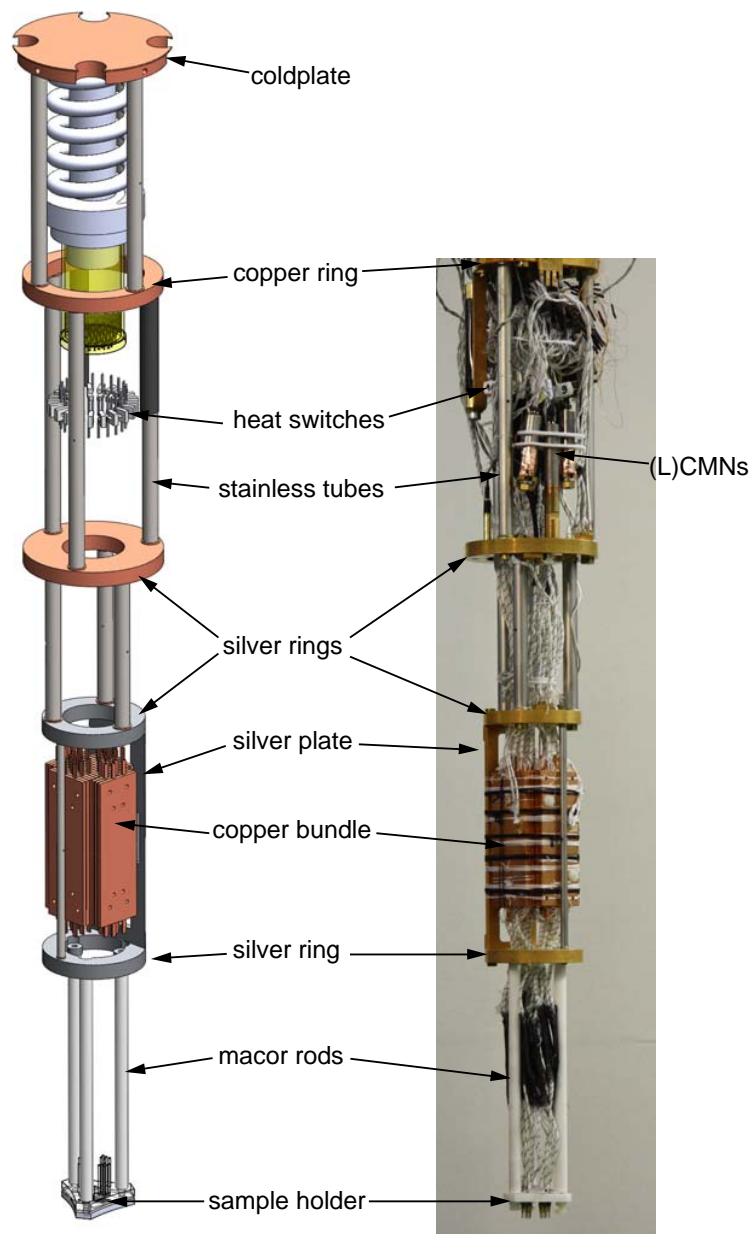
Figure 9.1.: The 2nd generation stage. Technical drawing on the left and a photograph on the right. The fundamental concept is the same as on the prototype. The copper plates are bolted against a silver plate. A tripod structure, made of rings and stainless tubes provides more rigidity. Copper and silver parts are gold plated. The bottom parts, rods and sample holder, are made of Macor^{TM} .

residual heat leaking through the switch, respectively. The basic idea [120] pursued in section 6.3 should be kept because it is simple, reliable and we have the set-up and the knowledge. We saw that the performance of the switch in the off state is dominated by the switches themselves, whereas the conducting state is limited by the conductions of the silver wires. Hence, we decided to make the switches 'longer'. The prototype switch had a centre line length of 12 mm, the new one was designed to have 19 mm, giving theoretically a 36% higher thermal resistance.

6. Magnets.
   The prototype was operated in a solenoid magnet of 8 T. The switch magnet was home-built. For the 2nd generation stage we ordered a three-stage magnet. It consists from top to bottom of the switch magnet, the demagnetisation magnet and a sample magnet. In this order, they provide 0.5 T, 9 T, and 9 T each solely at maximum field. First tests proved that they actually achieve the specified fields. Hence, we have the opportunity to control the field exerted on the sample independently from the demagnetisation. Furthermore, we saw that the mutual stray fields of the magnets are small. Based on a heat switch map similar to that in figure 7.12, we can say that the stray field of the demagnetisation magnet on the switches is $\sim 2\,\mathrm{mT}$ at 9 T whereas on the prototype it was more like $\sim 7\,\mathrm{mT}$ at 8 T, this compares as $\sim 0.9\text{‰}$ to $\sim 0.2\text{‰}$ of the applied solenoid field. On the other hand, the stray field was $\sim 70\%$ of the critical field of Aluminium on the prototype, whereas now it is more like $\sim 20\%$. Besides, the heat switch map is symmetric.

First Observations

First demagnetisations showed that the new stage achieves about half a millikelvin which is an improvement over the prototype by a factor of 2. Despite this success, the new stage, too, shows a ramp rate dependent heat leak similar to the one observed before.

9.3. Outlook

Although both, the prototype and the 2nd generation stage work and provide low temperatures some questions remain. One of the unsatisfying issues that we can not yet determine the electron temperature directly. On the one hand measurements with LCMN thermometers are in progress but we also have in mind the PtNMR thermometer. The LCMN thermometers are supposed to work into a regime of several $100\,\mu$K but the two on our stage saturate around $1\,$mK so that we can only use them indirectly in a heating curve. Furthermore it is possible that they exhibit thermalisation problems. The wire in the Pt bundle are intended to to be coated with SiO_2, but GE varnish can be considered [66]. Alternatively, it was also observed that the current, i.e. ohmic heating, in the coil during the pulses can heat the Pt bundle as well [139]. Therefore, we are currently working on a new coil and a new support of the coil. We are hoping that this will enable us to use the PtNMR thermometer.

Another open point is the thermalisation of the sample. So far the heat is drained through ohmic contact. The question how to make thermally well-conducting ohmic contact needs to be addressed and appropriate recipes have to be developed. In our labs we used a Au/Ge eutectic instead of evaporating the materials one after another. First, measurements show a clear reduction of the ohmic resistance.

We have also ordered a pulsed-tube cryo cooler [141]. They have become more and more popular in recent years. However, the influence of vibrations in such a system was controversially debated at the Ultra-Low Temperature conference 2008 in Royal Holloway. However, since on such a system it is no longer necessary to transfer helium, we can extend the precooling time and hopefully achieve lower precooling temperatures without having to worry about the influence of vibrations or other interferences during a helium transfer.

Another idea that can be pursued, is to immerse the sample in ^{3}He [85, 86] such as nanostructures are sometimes cooled inside the mixing chamber of a dilution refrigerator [142, 143]. There are pros and cons for that approach. As a matter of fact, the low temperatures achieved seem to indicate that it could give a small boost towards the microkelvin regime. In their experiment [85, 86], simply spoken, they transferred the 'cold' from the nuclear demagnetisation stage into helium-3 and further into the sample. That means that they have to overcome a KAPITZA resistance twice. Nevertheless, they reached a new low temperature record. In our approach, these two resistances do not exist. We almost exclusively cool the 2DEG through the ohmic contacts. Consequently, it seems very obvious to combine the two methods and speculate whether a 'homogenising liquid' around the nanostructure improves the cooling.

There's two cons that seem two speak against the idea. One is the high price of ^{3}He [64]. However, comparing the price to the cost of a good vacuum pump for

a powerful dilution refrigerator, the price looks less scary. The second con is the higher complexity of the experimental set-up. The cryostat has to be equipped with an additional condensing line for the helium. Furthermore, some of the cooling power of the nuclear refrigerators has to be sacrificed to cooling the liquid.

Overall, we could prove that the new cooling scheme enables us to open the microkelvin to mesoscopic physics. This approach is a powerful tool to cool nanostructures into new temperature ranges with room for improvement and development in the future.

Spot Welding

Here, I describe spot welding and in particular the spot welder we used. More information can be found in [144]. The two mating pieces that have to welded together are brought in contact. Subsequently, a current is driven through the pieces which heats the mating pieces locally around their contact point. This melts the pieces and the pieces are pressed together with force. A rule of thumb says that high-conductivity materials such as copper or silver require large power, i.e. a high current, and low pressure. Mediocre conductors like stainless steal require a comparatively low current but a high pressure.

Before spot welding the mating pieces have to be cleaned. This can be done chemically with appropriate etching or mechanically, e.g. with sand paper. A convenient method is to used a rubber one of which is shown in A.1 c). Its blue section is filled with quartz sand and hence coarse enough to polish a metal. In the last step the surfaces should be cleaned with solvents. A drop of solvent during the welding process can help to prevent the joint from oxidising. On the other hand, this creates the risk of flames! If one of the mating pieces is in thermal contact to heat-sensitive parts it can be cooled with a soaked paper towel. We usually used a mixture of water and ethanol. A paper towel soaked purely in ethanol is highly flammable! For example, we had to prevent the superconducting switches from being heated up two much and so we wrapped them, including the silver wire, in a wet paper towel.

The spot welder we used is shown in figure A.1. In a) you can see the control panel. The letters label the weld parametersare according to table A.1. The
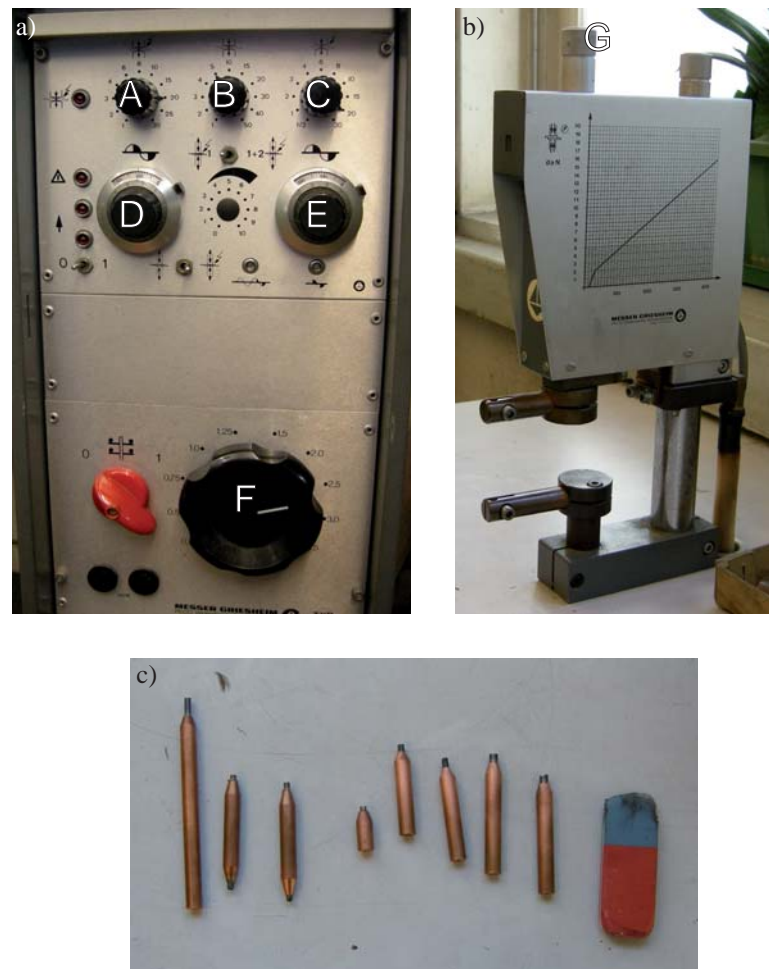
Figure A.1.: The spot welder. a) View of the control panel. b) Side view. The chart gives a correlation between set pressure and the applied force. c) A choice of electrodes and a rubber.

actual welding is initiated with a pedal so that the hands are free two hold the work pieces. The welding parameters can change although the work pieces show only minor differences. In figure A.1 c) a choice of electrodes is shown. They are all made of a copper trunk into which a tungsten tip was pressed. The tip can be grooved or otherwise shaped to fit to the work piece. The electrodes should occasionally be cleaned, e.g. sand blasted.

Table A.2 below gives 'good' parameters for different materials. In any case, spot welding needs a little bit of practise and the parameters should always be checked on a dummy piece. Figure A.2 shows a sketch explaining some details on spot welding. Figure A.2 a) explains how the silver wires were welded to the

A	duration of the first burst in power line cycles (PLC)
B	elay between the two bursts in PLC
C	duration of the second burst in PLC
D	voltage of the first burst in % of F
E	voltage of the second burst in % of F
F	secondary voltage in V
G	pressure (see chart (figure A.1 b) for unit)

Table A.1.: Labels of the spot welder

copper plates. The electrodes, i.e. the weld, should be in the centre of the weld stub which have a length of 10 mm, a width of 3 mm and a thickness of 1 mm. As shown in figure A.2 b) I rolled the Nb foil twice such that three layers of Nb foil were welded.
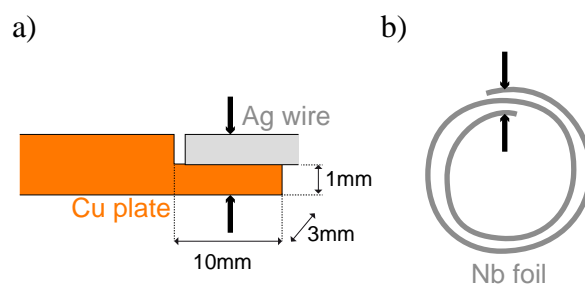
Figure A.2.: Welding sketch. The black arrows show where/how the electrodes should be in contact with the work pieces. a) The silver wires should be welded in the centre of the stub. Further out, the copper melts too much, further inside, the heat drains into the bulk. b) Cross-section of the Nb shield. The Nb foil was double-rolled as shown and three layers were welded.

| A | B | C | D | E | F | G | electrodes | | Comment |
							up.	lo.	
20	5	20	40	70	3.0	50	-	-	silver wire (1.27 mm) to copper plate, see figure A.2 a) for location of placing weld
20	5	20	35	80	2.5	52	B	C	silver wire (1.27 mm) to copper plate, 2nd gen. stage
20	5	20	50	70	3.0	50	B	A	silver wire (1.27 mm) to copper foil (0.2 mm)
20	5	20	40	65	3.0	35	B	D	silver wire (1.27 mm) to silver wire (1.27 mm)
10	81	-	-	-	2.5	65	A	C	silver wire (1.27 mm) to silver wire (1.27 mm)
10	5	10	25	80	2.5	62.5	K	L	silver wire (1.27 mm) to silver wire (1.27 mm), weld CMN to silver wire ON STAGE
10	-	-	95	-	2.5	35	-	-	silver wire (1.27 mm) to silver CMN piece
8	5	10	35	70	2.5	2.5	C	A	silver wire (1.27 mm) to pins of sample carrier
-	-	15	-	75	3.0	60	-	-	Nb shield weld, drops of IPA, see figure A.2 b)
15	-	-	48	-	3.0	50	-	-	Nb shield weld, drops of IPA

Table A.2.: Summary of 'good' weld parameters. Note that the parameters can differ for the same type of work pieces.

Araldite Beam

Production procedure of the Araldite™ beam.

- preheat brass mould to 140 °C

- mixture:
    - part 1: 314 g of CT200
    - part 2: 105 g of HT901

- curing cycle
    - 18.3 h at 140 °C
    - cool from 140 °C to 70 °C within 5 h
    - switch oven to 30 °C, take out mould after ~48 h

- Annealing
    - warm to 140 °C within 60 min
    - switch to 150 °C, stay there for 480 min
    - switch to 20 °C, stay there for 260 min

- machine in shape

- paint with Stycast 1266 (prevents cracking)

Magnet Construction

Field Profile

The calculations below are based on [101]. The model assumes a coil with radius R and length L. The thickness of the coil is treated as infinitesimally small and n is the number of turns per unit length. The radial component B_r and the axial component of the field B_z are thus written

$$B_r = -\frac{R\mu_0 nI}{2\pi} \int_0^\pi \left[\frac{\cos\theta}{\sqrt{\Lambda^2 + r^2 + R^2 - 2rR\cos\theta}} \right]_{\Lambda=L-1/2}^{\Lambda=L+1/2} \mathrm{d}\theta \qquad (C.1)$$

and

$$B_z = \frac{R\mu_0 nI}{2\pi} \int_0^\pi \left[\frac{\Lambda(R - r\cos\theta)}{(r^2 + R^2 - 2Rr\cos\theta)\sqrt{\Lambda^2 + r^2 + R^2 - 2rR\cos\theta}} \right]_{\Lambda=L-1/2}^{\Lambda=L+1/2} \mathrm{d}\theta$$
$$(C.2)$$

We solved the equations using standard IGOR procedures which conduct integration numerically. Figure C.1 shows the field factor as a function of r and z.
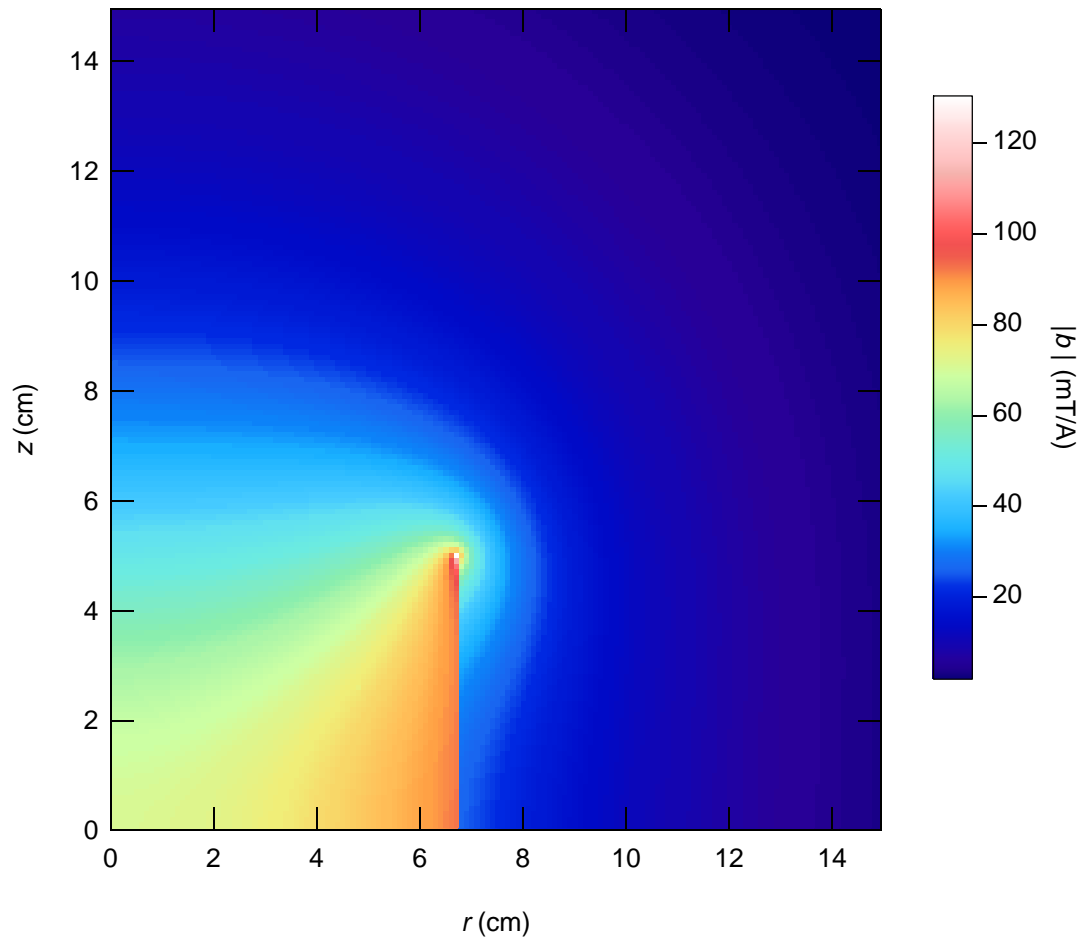
Figure C.1.: Simulation of the magnetic field magnitude as a function of axial coordinate z and radial coordinate r. The profile is symmetric with respect to both axis. The discontinuity corresponds to the solenoid.

Magnet Former

The magnet former was milled out of a section of a solid aluminium tube. Figure C.2 shows a technical drawing onto which we wound the superconduncting wire. For more mechanical strength we applied Sycast 2850 between the windings.
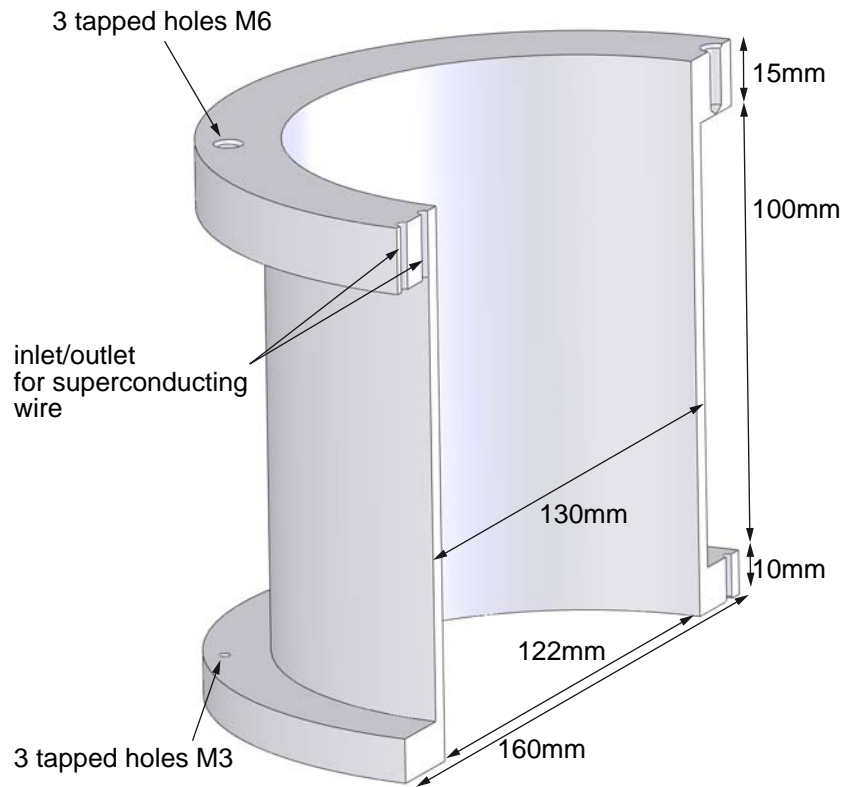
Figure C.2.: Technical drawing of the aluminium former of the heat switch magnet.

Solenoid Field

The field profile of the solenoid is shown in figure D.1. A schematic of the magnet is shown on the right which matches the dimensions given on the axis. The profile itself shows data taken from the magnet's manual (black circles). Moreover, it shows data that was measured at room temperature with a hand-held teslameter (F.W. BELL, Model 5080). It shows the magnetic field for the current directions, each at $0.5\,\text{A}$. The difference is presumably the magnetic field of the earth. The given profile was shifted in z to match the measured data (by $16\,\text{cm}$).

However, the traces are in good qualitative agreement. The positions of the copper plates and the switches are indicated. One can see that the plates experience some inhomogeneities at their ends. On the one hand, the inhomogeneities are larger between the cancellation coils and the main solenoid than between the solenoid. But on the other hand, the plates extend more into the inhomogeneous region at the lower end of the magnet.

Given this information and considering that the field at the end of the plates is of the order 10%, it seems unlikely that the inhomogeneities can explain the heat leaks observed in section 7.6 completely, unless the vibrations are extremely large or the off-axes inhomogeneities are much larger.

Figure D.1 also indicates the position of the heat switches. The residual field, at least on-axis, is of the same order as the critical field of aluminium. This could related to the asymmetric heat switch maps (figure 7.12).
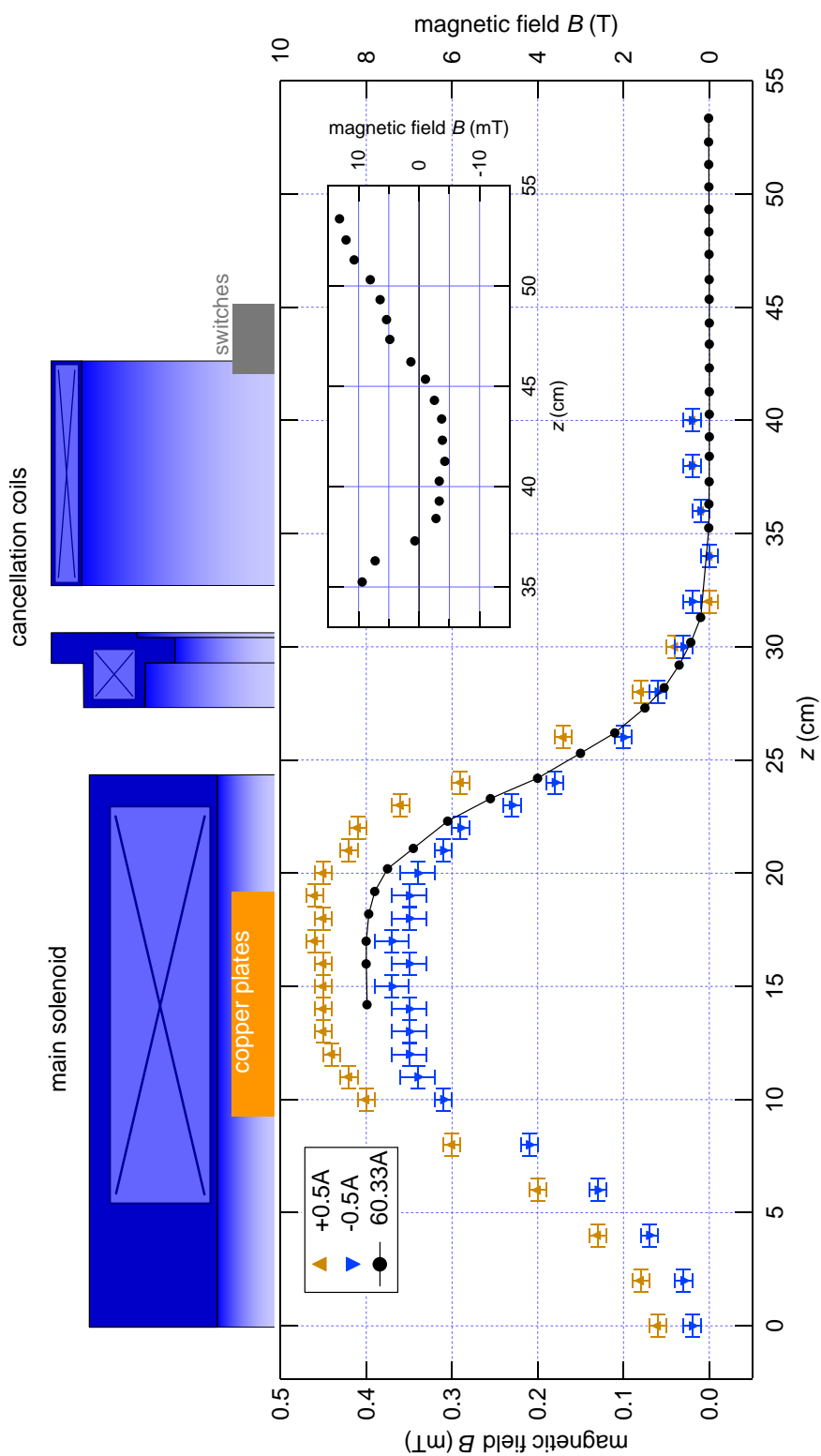
Figure D.1.: Field profile of the 8 T solenoid. The triangles show measurements done at room temperature, the black circles are taken from the manual. The inset shows a zoom into the cancellation region.

Conventional Coldfinger

Before assembling the demagetisation stage we built a 'conventional' coldfinger. Such a coldfinger is used in many set-ups in mesoscopic physics. It has to bring the sample into position mostly in the centre of a magntic field. It was used in Tobias Bandi's masters project [92] to measure a HALL bar sample. The conventional
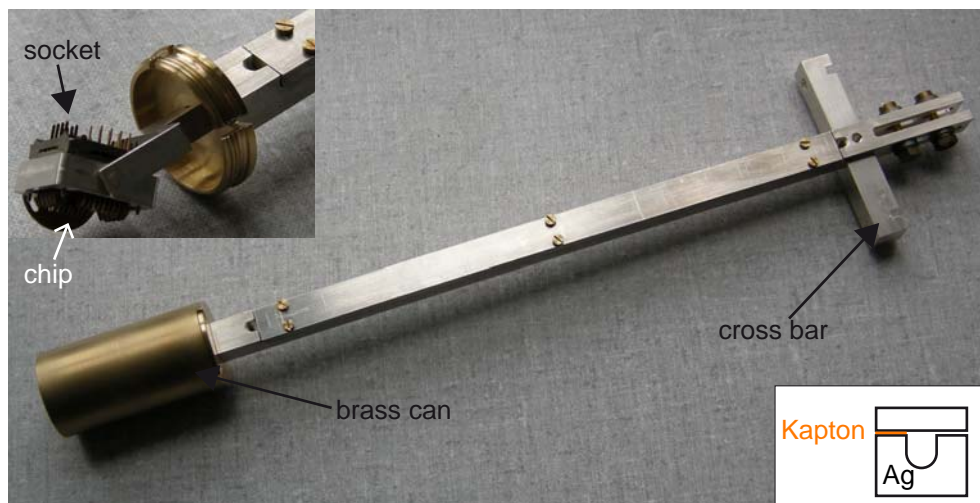
Figure E.1.: The conventional coldfinger that we used for HALL bar measurements. The picture was taken before we mounted the leads.

coldfinger is shown in figure E.1. The centre beam was made out of a 4N silver rod [145]. The cross-section was $12\,mm \times 12\,mm$, further dimensions are given in figure E.2. On the one end it had a fork which was bolted to the small coldfinger extending out of the mixing chamber (see section 6.2). We added molybdenum washers to compensate for different thermal expansion coefficients. Below the fork a cross bar was mounted which had two receptacles for the MCX towers. Two more receptacles were added later to hold CMN thermometers. Along the beam a groove was cut. Some of the leads were mounted inside the groove and secured with copper tabe to enhance thermal contact. The lower left shows a cut through the groove. On one side we put Kapton^{TM} tape to block eddy currents while ramping the magnetic field. The lid of the groove was bolted down with brass screws.

At the other end the socket was mounted on a fork-like structure. The socket was made rotatable to be able to measure in different field directions (upper right). The white arrows indicated the side into which the chip carrier was plugged. The other side shows the pins before soldering the leads. If measureing in a field strong enough the solder doesn't get superconducting. However, we thoroughly wrapped the wire around the pin before soldering to increase thermal conduction. The whole socket was surrounded by a brass can which served as additional protection against radiation.
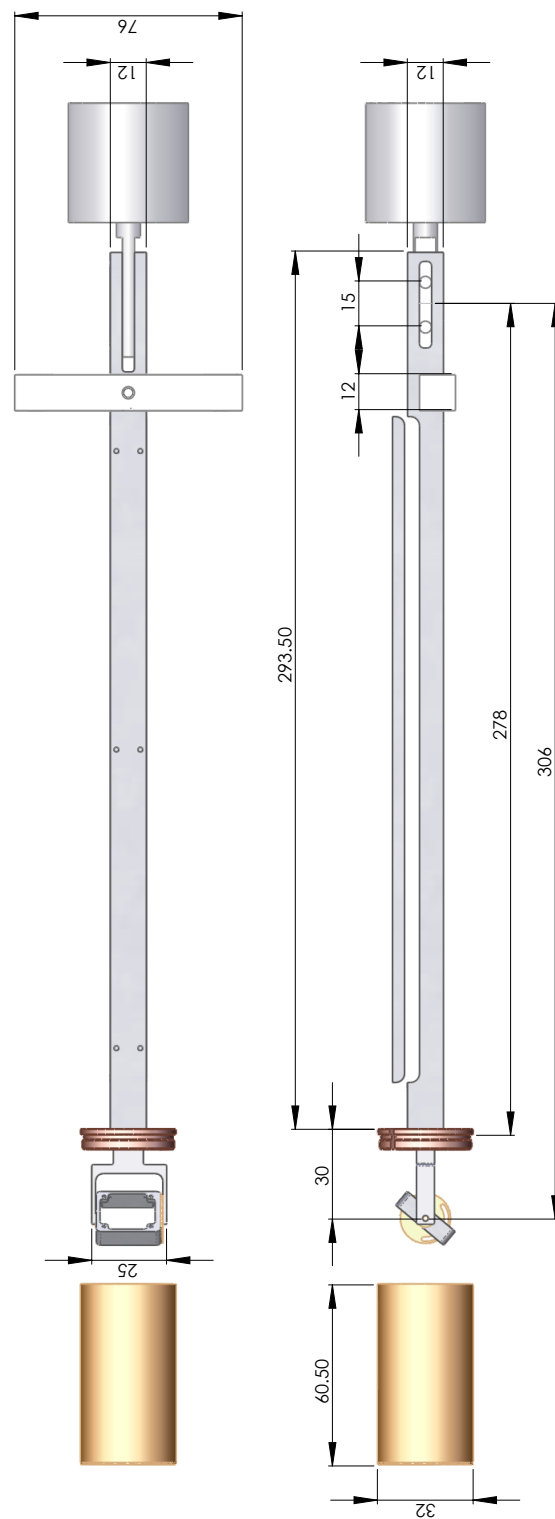
Figure E.2.: Technical drawing showing the dimensions of the conventional coldfinger

List of Figures

List of Tables

Bibliography

[1] G. E. MOORE, *Cramming more components onto integrated circuits*, Electronics **38**, 114–117 (1965).

[2] G. E. MOORE, *Progress in digital integrated electronic ICs*, International Electron Device Meeting, Washington D.C., 11–13 (1975).

[3] M. A. NIELSEN and I. L. CHUANG, *Quantum Computation and Quantum Information*, Cambridge University Press (2000).

[4] D. LOSS and D. P. DIVINCENZO, *Quantum computation with quantum dots*, Phys. Rev. A **57**, 120–126 (1998).

[5] L. P. KOUWENHOVEN, D. G. AUSTING, and S. TARUCHA, *Few-electron quantum dots*, Rep. Prog. Phys. **64**, 701–736 (2001).

[6] R. HANSON, L. P. KOUWENHOVEN, J. R. PETTA, S. TARUCHA, and L. M. K. VANDERSYPEN, *Spins in few-electron quantum dots*, Rev. Mod. Phys. **79**, 1217–1265 (2007).

[7] P. SIMON and D. LOSS, *Nuclear Spin Ferromagnetic Phase Transition in an Interacting Two Dimensional Electron Gas*, Phys. Rev. Lett. **98**, 156401 (2007).

[8] P. SIMON, B. BRAUNECKER, and D. LOSS, *Magnetic ordering of nuclear spins in an interacting two-dimensional electron gas*, Phys. Rev. B **77**, 045108 (2008).

[9] A. S. Oja and O. V. Lounasmaa, *Nuclear magnetic ordering in simple metals at positive and negative nanokelvin temperatures*, Rev. Mod. Phys. **69**, 1–136 (1997).

[10] D. C. Tsui, H. L. Stormer, and A. C. Gossard, *Two-Dimensional Magnetoresistance in the Extreme Quantum Limit*, Phys. Rev. Lett. **48**, 1559–1562 (1982).

[11] D. Goldhaber-Gordon, H. Shtrikman, D. Mahalu, D. Abusch-Magder, U. Meirav, and M. A. Kastner, *Kondo effect in a single-electron transistor*, Nature **391**, 156–159 (1998).

[12] S. M. Cronenwett, T. H. Oosterkamp, and L. P. Kouwenhoven, *A Tunable Kondo Effect in Quantum Dots*, Science **281**, 540–544 (1998).

[13] G. Czycholl, *Theoretische Festkörperphysik*, Vieweg & Sohn (2000).

[14] T. Heinzel, *Mesoscopic Electronics in Solid State Nanostructures*, Wiley-VCH (2003).

[15] B. J. van Wees, H. van Houten, C. W. J. Beenakker, J. G. Williamson, L. P. Kouwenhoven, D. van der Marel, and C. Foxon, *Quantized Conductance of Point Contacts in a Two-Dimensional Electron Gas*, Phys. Rev. Lett. **60**, 848–850 (1988).

[16] D. A. Wharam, T. J. Thornton, R. Newbury, M. Pepper, H. Ahmed, J. E. F. Frost, D. G. Hasko, D. C. Peacock, D. A. Ritchie, and G. A. C. Jones, *One-dimensional transport and the quantisation of the ballistic resistance*, J. Phys. C: Solid State Phys. **21**, L209–L214 (1988).

[17] D. Leonard, M. Krishnamurthy, C. M. Reaves, S. P. Denbaars, and P. M. Petroff, *Direct formation of quantum-sized dots from uniform coherent islands of InGaAs on GaAs surfaces*, Appl. Phys. Let. **63**, 3203–3205 (1993).

[18] B. T. Miller, W. Hansen, S. Manus, R. J. Luyken, A. Lorke, J. P. Kotthaus, S. Huant, G. Medeiros-Ribeiro, and P. M. Petroff, *Few-electron ground states of charge-tunable self-assembled quantum dots*, Phys. Rev. B **56**, 6764–6769 (1997).

[19] S. Takahashi, R. S. Deacon, K. Yoshida, A. Oiwa, K. Shibata, K. Hirakawa, Y. Tokura, and S. Tarucha, *Large Anisotropy of the Spin-Orbit Interaction in a Single InAs Self-Assembled Quantum Dot*, Phys. Rev. Lett. **104**, 246801 (2010).

[20] K. Zaitsu, Y. Kitamura, K. Ono, and S. Tarucha, *Vertical quantum dot with a vertically coupled charge detector*, Appl. Phys. Let. **92**, 033101 (2008).

[21] L. Kouwenhoven and C. Marcus, *Quantum dots*, Physics World **11**, 35–39 (1998).

[22] S. Tarucha, D. G. Austing, T. Honda, R. J. van der Hage, and L. P. Kouwenhoven, *Shell Filling and Spin Effects in a Few Electron Quantum Dot*, Phys. Rev. Lett. **77**, 3613–3616 (1996).

[23] M. Ciorga, A. S. Sachrajda, P. Hawrylak, C. Gould, P. Zawadzki, S. Jullian, Y. Feng, and Z. Wasilewski, *Addition spectrum of a lateral dot from Coulomb and spin-blockade spectroscopy*, Phys. Rev. B **61**, R16315 (2000).

[24] W. R. Smythe, *Static and Dynamic Electricity*, Hemisphere Publishing Corporation (1989).

[25] T. Ihn, *Semiconductor Nanostructures*, Oxford University Press (2010).

[26] E. Bonet, M. M. Deshmukh, and D. C. Ralph, *Solving rate equations for electron tunneling via discrete quantum states*, Phys. Rev. B **65**, 045317 (2002).

[27] C. W. J. Beenakker, *Theory of Coulomb-blockade oscillations in the conductance of a quantum dot*, Phys. Rev. B **44**, 1946–1956 (1991).

[28] E. B. Foxman, U. Meirav, P. L. McEuen, M. A. Kastner, O. Klein, P. A. Belk, D. M. Abusch, and S. J. Wind, *Crossover from single-level to multilevel transport in artificial atoms*, Phys. Rev. B **50**, 14193–14199 (1994).

[29] A. D. Stone and P. A. Lee, *Effect of Inelastic Processes on Resonant Tunneling in One Dimension*, Phys. Rev. Lett. **54**, 1196–1199 (1985).

[30] M. Büttiker, *Role of quantum coherence in series resistors*, Phys. Rev. B **33**, 3020–3026 (1986).

[31] E. B. Foxman, P. L. McEuen, U. Meirav, N. S. Wingreen, Y. Meir, P. A. Belk, N. R. Belk, M. A. Kastner, and S. J. Wind, *Effects of quantum levels on transport through a Coulomb island*, Phys. Rev. B **47**, 10020–10023 (1993).

[32] W. G. VAN DER WIEL, S. DE FRANCESCHI, J. M. ELZERMAN, T. FUJI-SAWA, S. TARUCHA, and L. P. KOUWENHOVEN, *Electron transport through double quantum dots*, Rev. Mod. Phys. **75**, 1–22 (2003).

[33] A. C. JOHNSON, *Charge Sensing and Spin Dynamics in GaAs Quantum Dots*, PhD thesis, Harvard University, Cambridge, Massachusetts, United States of America (2005).

[34] A. BARENCO, D. DEUTSCH, A. EKERT, and R. JOZSA, *Conditional Quantum Dynamics and Logic Gates*, Phys. Rev. Lett. **74**, 4083–4086 (1995).

[35] R. LANDAUER, *Minimal Energy Requirements in Communication*, Science **272**, 1914–1918 (1996).

[36] G. BURKARD, D. LOSS, and D. P. DIVINCENZO, *Coupled quantum dots as quantum gates*, Phys. Rev. B **59**, 2070–2078 (1999).

[37] J. R. PETTA, A. C. JOHNSON, J. M. TAYLOR, E. A. LAIRD, A. YACOBY, M. D. LUKIN, C. M. MARCUS, M. P. HANSON, and A. C. GOSSARD, *Coherent Manipulation of Coupled Electron Spins in Semiconductor Quantum Dots*, Science **309**, 2180–2184 (2005).

[38] I. A. MERKULOV, A. L. EFROS, and M. ROSEN, *Electron spin relaxation by nuclei in semiconductor quantum dots*, Phys. Rev. B **65**, 205309 (2002).

[39] A. V. KHAETSKII, D. LOSS, and L. GLAZMAN, *Electron Spin Decoherence in Quantum Dots due to Interaction with Nuclei*, Phys. Rev. Lett. **88**, 186802 (2002).

[40] D. PAGET, G. LAMPEL, B. SAPOVAL, and V. I. SAFAROV, *Low field electron-nuclear spin coupling in gallium arsenide under optical pumping conditions*, Phys. Rev. B **15**, 5780–5796 (1977).

[41] J. BAUGH, Y. KITAMURA, K. ONO, and S. TARUCHA, *Large Nuclear Overhauser Fields Detected in Vertically Coupled Quantum Dots*, Phys. Rev. Lett. **99**, 096804 (2007).

[42] A. ABRAGAM, *Ordering Nuclear Spins*, Proc. R. Soc. Lond. A **412**, 255–268 (1987).

[43] A. ABRAGAM, *Principles of Nuclear Magnetism*, Oxford University Press (1961).

[44] H. E. VIERTIÖ and A. S. OJA, *Nuclear antiferromagnetism in copper: Interplay of (0,2/3,2/3) and (1,0,0) order*, Phys. Rev. B **42**, 6857–6860 (1990).

[45] A. J. Annila, K. N. Clausen, P.-A. Lindgård, O. V. Lounasmaa, A. S. Oja, K. Siemensmeyer, M. Steiner, J. T. Tuoriniemi, and H. Weinfurter, *Nuclear Order in Copper: New Type of Antiferromagnetism in an Ideal fcc System*, Phys. Rev. Lett. **64**, 1421–1424 (1990).

[46] H. Fröhlich and F. R. N. Nabarro, *Orientation of Nuclear Spins in Metals*, Proc. R. Soc. A **175**, 382–391 (1940).

[47] R. K. Harris, E. D. Becker, S. M. Cabral de Menezes, R. Goodfellow, and P. Granger, *NMR Nomenclature: Nuclear Spin Properties and Conventions for Chemical Shifts*, Solid State Nucl. Magn. Reson. **22**, 458–483 (2002).

[48] W. Buckel and R. Kleiner, *Supraleitung, 6th Ed.*, Viley-VCH (2004).

[49] F. Pobell, *Matter and Methods at Low Temperatures, 3rd Ed.*, Springer (2007).

[50] A. Kent, *Experimental Low-Temperature Physics*, American Institue of Physics (1993).

[51] G. K. White and P. J. Meeson, *Experimental Techniques in Low-Temperature Physics, 4th Ed.*, Oxford University Press (2002).

[52] D. S. Betts, *An Introduction to Millikelvin Technology*, Cambridge University Press (1989).

[53] R. C. Richardson and E. N. Smith, *Experimental Techniques in Condensed Matter Physics at Low Temperatures*, Westview Press (1998).

[54] J. W. Ekin, *Experimental Techniques for Low-Temperature Measurements*, Oxford University Press (2006).

[55] G. R. Pickett, *Microkelvin Physics*, Rep. Prog. Phys. **51**, 1295–1340 (1988).

[56] G. R. Pickett, *Cooling metals to the micokelvin regime, then and now*, Physica B **280**, 467–473 (2000).

[57] G. Frossati, *Experimental Techniques: Methods for Cooling Below 300mK*, J. Low Temp. Phys. **87**, 595–633 (1992).

[58] E. T. Swartz and R. O. Pohl, *Thermal boundary Resistance*, Rev. Mod. Phys. **61**, 605–668 (1989).

[59] C. Enss and S. Hunklinger, *Low Temperature Physics*, Springer (2005).

[60] C. Kittel, *Introduction to Solid State Physics, 8th Ed.*, John Wiley & Sons (2005).

[61] N. W. Ashcroft and N. D. Mermin, *Solid State Physics*, Brooks/Cole Cengage Learning (1976).

[62] A. L. Woodcraft, *Recommended values for the thermal conductivity of aluminium of different purities in the cryogenic to room temperature range, and a comparison with copper*, Cryogenics **45**, 626–636 (2005).

[63] G. S. Kumar, G. Prasad, and R. O. Pohl, *Experimantal determinations of the Lorenz number*, J. Mat. Sci. **28**, 4261–4272 (1993).

[64] A. Cho, *Helium-3 Shortage Could Put Freeze On Low-Temperature Research*, Science **326**, 778–779 (2009).

[65] J. Saunders, contribution to a discussion during ULT 2008 in Royal Holoway, August 17th (2008).

[66] D. Hechtfischer and G. Schuster, *Platinum NMR thermometry below 0.1K*, PTB-Th-1, Physikalisch-Technische Bundesanstalt Braunschweig und Berlin (2004).

[67] P. Horowitz and W. Hill, *The Art of Electronics, 2nd Ed.*, Cambridge University Press (1989).

[68] D. M. Pozar, *Microwave Engineering, 3rd Ed.*, John Wiley & Sons (2005).

[69] W. Yao, T. A. Knuuttila, K. K. Nummila, J. E. Martikainen, A. S. Oja, and O. V. Lounasmaa, *A Versatile Nuclear Demagnetization Cryostat for Ultralow Temperature Research*, J. Low Temp. Phys. **120**, 121–150 (2000).

[70] R. M. Müller, C. Buchal, H. R. Folle, M. Kubota, and F. Pobell, *A double-stage nuclear demagnetization refrigerator*, Cryogenics **20**, 395–407 (1980).

[71] A. Mittal, M. W. Keller, R. G. Wheeler, and D. E. Prober, *Electron Temperature and Thermal Conductance of GaAs 2D Electron Gas Samples Below 0.5 K*, Physica B **194-196**, 167–168 (1994).

[72] A. Mittal, *Electron-Phonon Scattering Rates in GaAs/AlGaAs 2DEGs Below 0.5 K*, PhD thesis, Yale University, New Haven, Connecticut, United States of America (1996).

[73] C. SCHELLER, S. HEIZMANN, and D. M. ZUMBÜHL, *to be published* .

[74] Publications often speak of *the temperature* thereby neglecting the difference in base temperature (of the mixing chamber) and the electron temperature. This statement is also based on private communication and 'reading between the lines'.

[75] W. L. JONES and L. F. EASTMAN, *High-Performance AlGaAs/GaAs MOSFETs with Improved Ohmic Contacts*, IEEE Trans. Elecron Devices **ED-33**, 712 (1986).

[76] A. K. KULKARNI and J. T. LUKOWSKI, *Effect of annealing process parameters on the properties of AuGe ohmic contacts to GaAs*, J. Appl. Phys. **59**, 2901–2904 (1986).

[77] T. S. KUAN, P. E. BATSON, T. N. JACKSON, H. RUPPRECHT, and E. L. WILKIE, *Electron microscope studies of an alloyed Au/Ni/Au-Ge ohmic contact to GaAs*, J. Appl. Phys. **54**, 6952 (1983).

[78] A. KETTERSON, F. PONSE, T. HENDERSON, J. KLEM, and H. MORKOÇ, *Extremely low contact resistances for AlGaAs/GaAs modulation-doped field-effect transistor structures*, J. Appl. Phys **57**, 2305–2307 (1985).

[79] N. BRASLAU, *Alloyed ohmic contacts*, J.Vac.Sci. Technol **19**, 803 (1981).

[80] P. ZWICKNAGL, S. D. MUKHERJEE, P. M. CAPANI, H. LEE, H. T. GRIEM, L. RATHBUN, J. D. BERRY, W. L. JONES, and L. F. EASTMAN, *Very low restistance Au/Ge/Ni/Ag based Ohmic contact formation to $Al_{0.25}/Ga_{0.75}As/GaAs$ and $Al_{0.48}In_{0.52}As/Ga_{0.47}In_{0.53}As$ heterostructures: A behavioral comparison*, J. Vac. Sci. Technol. B **4**, 476–484 (1986).

[81] S. RAISER, *Untersuchung der elektrischen Eigenschaften von AuGe-Kontakten in GaAs/AlGaAs-Heterostrukturen*, Diploma thesis, Universität Tübingen, Tübingen, Germany (2005).

[82] E. J. KOOP, *Electron Spin Transport in Quantum Dots and Point Contacts*, PhD thesis, Rijksuniversiteit Groningen, Groningen, The Netherlands (2008).

[83] A. K. M. WENNBERG, S. N. YTTERBOE, C. M. GOULD, H. M. BOZLER, J. KLEM, and H. MORKOÇ, *Electron heating in a multiple-quantum-well structure below 1 K*, Phys. Rev. B **34**, 4409–4411 (1986).

[84] P. L. Gammel, D. J. Bishop, J. P. Eisenstein, J. H. English, A. C. Gossard, R. Ruel, and H. P. Stormer, *Ultralow-temperature behavior of the $\nu = \frac{5}{2}$ fractional quantum Hall effect*, Phys. Rev. B **38**, 10128–10130 (1988).

[85] W. Pan, J. S. Xia, V. Shvarts, D. E. Adams, H. L. Stormer, D. C. Tsui, L. N. Pfeiffer, K. W. Baldwin, and K. W. West, *Exact Quantization of the Even-Denominator Fractional Quantum Hall State at $\nu = 5/2$ Landau Level Filling Factor*, Phys. Rev. Lett. **83**, 3530–3533 (1999).

[86] J. S. Xia, E. D. Adams, V. Shvarts, W. Pan, H. L. Stormer, and D. C. Tsui, *Ultra-low-temperature cooling of two-dimensional electron gas*, Physica B **280**, 491–492 (2000).

[87] P. J. Price, *Hot electrons in heterolayers*, Phys. Rev. B **30**, 2236–2237 (1984).

[88] G. Gervais and K. Yang, *Adiabatic Cooling with Non-Abelian Anyons*, Phys. Rev. Lett. **105**, 086801 (2010).

[89] W. E. Chickering, J. P. Eisenstein, L. N. Pfeiffer, and K. W. West, *Thermopower of two-dimensional electrons at filling factors $\nu = 3/2$ and 5/2*, Phys. Rev. B **81**, 245319 (2010).

[90] E. Gornik, R. Lassnig, G. Strasser, H. L. Störmer, A. C. Gossard, and W. Wiegmann, *Specific Heat of Two-Dimensional Electrons in GaAs-GaAlAs Multilayers*, Phys. Rev. Lett. **54**, 1820–1823 (1985).

[91] A. Mittal, R. G. Wheeler, M. W. Keller, D. E. Prober, and R. N. Sacks, *Electron-phonon scattering rates in GaAs/AlGaAs 2DEG samples below 0.5 K*, Surface Science **361**/**362**, 537–541 (1996).

[92] T. Bandi, *Ultralow Electron Temperatures in 2D Electron Gases by efficient silver sinter heat exchangers*, Masterthesis, Universität Basel, Basel, Switzerland (2009).

[93] A. de Waard, *MiniGRAIL - The first spherical gravitational wave antenna*, PhD thesis, Universiteit Leiden, Leiden, The Netherlands (2003).

[94] H. N. (Ed.), *Bergmann-Schaefer - Lehrbuch der Experimentalphysk - Band 3: Optik*, Walter de Gruyter (1993).

[95] Db-electronic; Dorfstraße 30; 83088 Kiefersfelden, Germany; http://www.db-electronic.de/.

[96] Y. C. Chung, M. Heiblum, and V. Umansky, *Scattering of Bunched Fractionally Charged Quasiparticles*, Phys. Rev. Lett. **91**, 216804 (2003).

[97] R. M. Potok, I. G. Rau, H. Shtrikman, Y. Oreg, and D. Goldhaber-Gordon, *Observation of the two-channel Kondo effect*, Nature **446**, 167–171 (2007).

[98] I. P. Radu, J. B. Miller, C. M. Marcus, M. A. Kastner, L. N. Pfeiffer, and K. W. West, *Quasi-Particle Properties from Tunneling in the $\nu = {}^5/_2$ Fractional Quantum Hall State*, Science **320**, 899–902 (2008).

[99] Cryogenic Limited; Units 29/30; Acton Park; Industrial Estate; The Vale, Acton; London W3 7QE; United Kingdom; http://www.cryogenic.co.uk/.

[100] Kadel Engineering Company, 1627 East Main Street, Danville, Indiana 46122.

[101] E. E. Callaghan and S. H. Maslen, *The Magnetic Field Of A Finite Solenoid*, NASA Technical Note D-465 (1960).

[102] Leiden Cryogenics B.V., Kenauweg 11, 2331 BA Leiden, The Netherlands, www.leidencryogenics.com.

[103] WaveMetrics, Inc.; P.O. Box 2088; Lake Oswego, OR 97035; USA; http://www.wavemetrics.com/.

[104] National Instruments Switzerland; Sonnenbergstr. 53; CH-5408 Ennetbaden; Switzerland; http://www.ni.com/.

[105] RV-Elektroniikka Oy PICOWATT; Veromiehentie 14; FI-01510 VANTAA, Finland; http://www.picowatt.fi/.

[106] Emitec Messtechnik AG; Birkenstr. 47; CH-6343 Rotkreuz; Switzerland; http://www.emitec.ch/.

[107] TMC - Technical Manufacturing Corporation; 15 Centennial Drive; Peabody, MA 01960 USA; http://www.techmfg.com/.

[108] ACI Alloys; 1985 Las Plumas Avenue; San Jose, CA 95133 USA; http://www.acialloys.com/.

[109] G. R. Pickett, proposed both, to tie the plates together with a (cotton) string and to sacrifice one plate to structural purposes. Private communication.

[110] R. P. H. George R. Pickett, proposed that method and provided a spool of fishing line. Private communication.

[111] KYOWA Electronic Instruments Co., LTD. ;3-5-1, Chofugaoka, Chofu, Tokyo 182-8520, Japan; http://www.kyowa-ei.com.

[112] V. Keith and M. G. Ward, *A recipe for sintering submicron silver powder*, Cryogenics **24**, 249–250 (1984).

[113] H. Franco, J. Bossy, and H. Godfrin, *Properties of sintered silver powders and their application in heat exchangers at millikelvin temperatures*, Cryogenics **24**, 477–483 (1984).

[114] W. Itoh, A. Sawada, A. Shinozaki, and Y. Inada, *New silver powders with large surface areas as heat exchanger materials*, Cryogenics **31**, 453–455 (1991).

[115] T. Bandi, *Silver Sinter Heat Exchangers*, semesterproject, Universität Basel, Basel, Switzerland (2008).

[116] Inframat Advanced Materials LLC; 74 Batterson Park Road, Farmington, CT 06032 USA; http://www.advancedmaterials.us/.

[117] S. Brunauer, P. H. Emmett, and E. Teller, *Adsorption of Gases in Multimolecular Layers*, J. Am. Chem. Soc. **60**, 309–319 (1938).

[118] ESPI Metals; 1050 Benson Way, Ashland, Oregon 97520, USA; http://www.espi-metals.com/.

[119] Y. M. . Bunkov, *Superconducting aluminium heat switch prepared by diffusion welding*, Cryogenics **29**, 938–939 (1989).

[120] N. S. Lawson, *A simple heat switch for use at millikelvin temperatures*, Cryogenics **22**, 667–668 (1982).

[121] R. M. Müller, C. Buchal, T. Oversluizen, and F. Pobell, *Superconducting aluminium heat switch and plated press-contacts for use at ultralow temperatures*, Rev. Sci. Instr. **49**, 515–518 (1978).

[122] P. C. Ho and R. B. Hallock, *A Compact Design for an Indium Heat Switch*, J. Low Temp. Phys. **121**, 797–802 (2000).

[123] Goodfellow GmbH; Postfach 13 43; D-61213 Bad Nauheim, Germany; http://www.goodfellow.com/de.

[124] R. W. Willekers, W. A. Bosch, F. Mathu, H. C. Meijer, and H. Postma, *Impact welding: a superior method of producing joints with high thermal conductivity between metals at very low temperatures*, Cryogenics **29**, 904–906 (1989).

[125] G. R. Pickett, recommended to use that technique. Private communication.

[126] M. Düggelin, Zentrum für Mikroskopie der Universität Basel, Biozentrum/Pharmazentrum, Klingelbergstrasse 50/70, CH-4056 Basel, www.unibas.ch/zmb.

[127] R. P. Haley, from Lancaster University sent us a used switch, that was as described in [120].

[128] CMR-Direct, Britannia House, 19-20 Godesdone Road, Cambridge, CB5 8HR, United Kingdom.

[129] K. Gloos, C. Mitschka, F. Pobell, and P. Smeibidl, *Thermal conductivity of normal and superconducting metals*, Cryogenics **30**, 14–18 (1990).

[130] California Fine Wire Company; 338 So. Fourth Street; Grover Beach, CA 93483-0199 USA, http://www.calfinewire.com/.

[131] J. Tuttle, C. E., and M. DiPirro, *Thermal and electrical conductivity measurements of CDA 510 phosphor bronze*, NASA Goddard Space Flight Center, Code 552, Greenbelt Maryland, 20771, USA.

[132] R. P. Haley, presented the idea at ULT 2008 in Royal Holoway, August 17th.

[133] D. Maradan, *Parallel Nuclear Refrigerators for Cooling Nanoscale Samples to Microkelvin Temperatures*, Masterthesis, Universität Basel, Basel, Switzerland (2010).

[134] Huntsman Advanced Materials (Switzerland) GmbH; Klybeckstrasse 200, 4057 Basel, Switzerland; http://www.huntsman.com/advanced_materials/.

[135] G. Frossati, made us aware of the superconducting pad and recommended to use silver epoxy. Private Communication.

[136] Epoxy Technology, Inc.; 14 Fortune Drive; Billerica, MA 01821; USA; http://www.epotek.com/.

[137] D. HECHTFISCHER, *Homogenisation of magnetic fields by diamagnetic shields*, J. Phys. E: Sci. Instrum. **20**, 143 (1987).

[138] Elektrisola Dr. Gerd Schildbach GmbH&Co. KG; In der Hüttenwiese 2 - 4; D - 51580 Reichshof-Eckenhagen, Germany; http://www.elektrisola.com/.

[139] C. ENSS, J. SAUNDERS, and P. SKYBA, private communication.

[140] S. B. HEIZMANN, *Transport and Charge Sensing Measurements on Few Electron Quantum Dots and going to Ultra Low Electron Temperatures*, PhD thesis, Universität Basel, Basel, Switzerland (2010).

[141] BlueFors Cryogenics Oy Ltd; Arinatie 10; 00370 Helsinki; Finland; http://www.bluefors.com/.

[142] K. KODERA, H. TAKADO, A. ENDO, S. KATSUMOTO, and Y. IYE, *Dispersive lineshape of the resistively-detected NMR in the vicinity of Landau level filling $\nu = 1$*, Phys. Stat. Sol. **3**, 4380–4383 (2006).

[143] The dilution refrigerator that we purchased was delivered with an extension mixing chamber allowing to put a nanostructure inside the mixture and inside a solenoid.

[144] A. D. ALTHOUSE, C. H. TURNQUIST, K. E. BOWDITCH, and M. A. BOWDITCH, *Modern Welding*, The Goodheart-Willcox Company (2004).

[145] Allgemeine Gold- und Silberscheideanstalt AG; Kanzlerstrasse 17; 75175 Pforzheim; Germany; http://www.allgemeine-gold.de/.

Acknowledgement - Danksagung

Zum Schluss möchte ich noch ein paar Danksagungen aussprechen. Vielen Dank an Dominik M. Zumbühl, der mir dieses Projekt ermöglicht hat und der mit mir auf diese Reise in dem auch für ihn neuen Gebiet gegangen ist. I would like to thank Anthony C. Clark for being my personal, assisting post-doc. We solved all the big and the small problems that show up in every-day lab life. We had a great time together, including explosion washers and other humorous encounters. In diesem Zusammenhang gebührt auch Tobias Bandi und Dario Maradan viel Dank, die in ihren Semesterprojekten und Master-Arbeiten eine grosse Unterstützung bei der Herstellung der Silber-Sinter und des Sample-Halters waren.

A special thanks to Sarah Heizmann and Charulata Barge who started with to build a lab in a basically empty hall. Sarah Heizmann und Kristine Bedner möchte ich auch danken, dass sie uns zwei Quantendots und eine Hallbar überlassen haben (Wir haben die Quantenpunkte nicht absichtlich zerstört). Besten dank Christian Scheller für die Filter und auch für die Diskussionen und die Hilfe rund um IGOR. Vielen Dank Daniel Biesinger für die zahlreichen Diskussionen über ... sehr viele Dinge... Besten Dank Lucas Casparis, dass er das Projekt zusammen mit Dario Maradan weiterführt. Einen Dank möchte ich den Doktorierenden im anderen Büro, Florian Dettwiler, Dorothée Hug und Dominikus Koelbl, aussprechen für Hilfe, Inspiration und Zusammenarbeit. Ein weiteres Dankeschön all denen, die in unserer Forschungruppe mitgearbeitet haben: Florian Schweizer, Sandro Erni, Gregor Fessler, Dominic Giss, Lukas Greuter, Petar Jurcevic, Adrian Renfer, Raphael Wagner, Elisa Hemmig, Leon Camenzind

I would like to acknowlegde all the help that we received on low temperature physics: Richard P. Haley, George R. Pickett and Shaun N. Fisher from Lan-

Curriculum Vitae

Kai K. Schwarzwälder

1985-1989	Grundschule Seefelden (elementary school)
1989-1998	Faust-Gymnasium Staufen (high school)
1998-1999	civil service as paramedic at the Red Cross
1999-2006	study at the University of Tübingen
2006	Diploma thesis *Frequenzabhängige, elektrische Eigenschaften von Elektroden in den Neurowissenschaften* in the group of D.A. Wharam
2006-2011	PhD research at the University of Basel in the group of D.M. Zumbühl
2008-2011	lab course supervisor at the Departement Physik
2011	PhD thesis *Towards Cooling Nanoelectronic Devices to Microkelvin Temperatures*

I owe my education to the following lecturers
H. Clement, O. Eibl, H. Fischer, P. Grabmayr, H. Kaul, D. Kern, H. Klaeren, R. Kleiner, D. Kölle, M. Liu, R. Meier, H. Müther, F. Nüsslin, E. Plies, F. Schick, N. Schopohl, J. Schweizer, G.J. Wagner, D.A. Wharam, M. Wolff, C. Zimmermann, D.M. Zumbühl

Publications

- A.C. CLARK, K. K. SCHWARZWÄLDER, T. BANDI, D. MARADAN, AND D. M. ZUMBÜHL, *Method for cooling nanostructures to microkelvin temperatures*, Rev. Sci. Instr. **81**, 103904 (2010)

- L. CASPARIS, M. MESCHKE, D. MARADAN, A.C. CLARK, K.K. SCHWARZWÄLDER, D. M. ZUMBÜHL, AND J. PEKOLA, *The Electron-Phonon Coupling Bottle Neck in Metallic Coulomb Blockade Thermometry*, in preparation
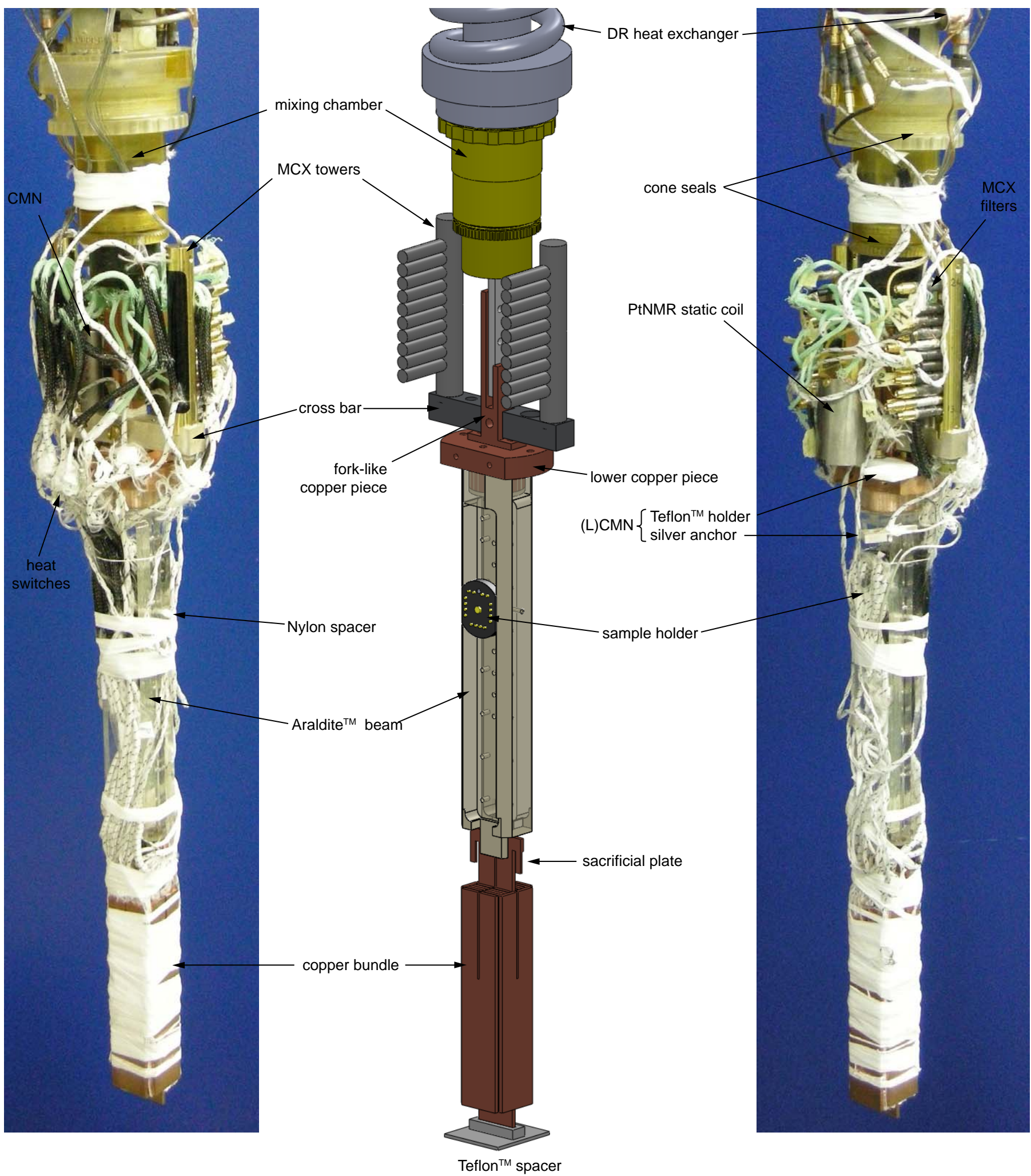
Figure X: The whole demagnetisation stage. This is a zoom of figure 6.16.